THE UNIVERSITY
of ADELAIDE

High-Resolution Molecular Spectroscopy With An Optical Frequency Comb

Sarah Katherine Scholten

Supervisors: Prof. Andre Luiten,
Dr. Christopher Perrella, Dr. Richard White

A thesis submitted for the degree of

Doctor of Philosophy

March 2019

School of Physical Sciences
The University of Adelaide

For my family...

Contents

Publication List

Journal papers are presented in order of publication.

N. Bourbeau Hébert, S. Scholten, R. White, J. Genest, A. Luiten, and J. Anstie, "*A Quantitative Mode-Resolved Frequency Comb Spectrometer*", Optics Express, **23**, 13991 (2015).

S. Scholten, J. Anstie, N. Bourbeau Hébert, R. White, J. Genest, and A. Luiten, "*Complex direct comb spectroscopy with a virtually imaged phased array*", Optics Letters, **41**, 1277 (2016).

S. Scholten, C. Perrella, J. Anstie, R. White, W. Al-Ashwal, N. Bourbeau Hébert, J. Genest, and A. Luiten,"*Number-Density Measurements of CO_2 in Real Time with an Optical Frequency Comb for High Accuracy and Precision*", Physical Review Applied, **9**, 054043 (2018).

S. Scholten, C. Perrella, J. Anstie, R. White, and A. Luiten,"*Accurate optical number density measurement of $^{12}CO_2$ and $^{13}CO_2$ with direct frequency comb spectroscopy* (2019), *submitted.*

F. Karim†, S. K. Scholten†, C. Perrella, and A. N. Luiten, "*High-resolution spectroscopy of $^{12}C_2H_2$ with a tunable rarefied optical frequency comb and virtually imaged phased array spectrometer*" (2019), *in preparation.*

List of Figures

List of Tables

List of Symbols

ℓ	Absolute value of the sum of the vibrational angular momentum quantum numbers l_i.
f_0	Carrier-envelope offset frequency of the optical frequency comb.
Ψ_{total}	Total molecular wavefunction.
λ	Wavelength [m].
f_{rep}	Repetition frequency/repetition rate of the optical frequency comb.
f	Frequency [Hz].
E	Energy [J] (SI) or $\left[\text{cm}^{-1}\right]$ (cgs).
h	Planck's constant [J s] (SI) or [erg s] (cgs).
c	Speed of light in a vacuum [m/s] (SI) or [cm/s] (cgs).
$\widetilde{\nu}$	Wavenumber $\left[\text{cm}^{-1}\right]$.
J	Rotational quantum number of a molecule.
v	Vibrational quantum number of a molecule.
J''	Rotational quantum number of a molecule for the lower state of a ro-vibrational transition.
v''	Vibrational quantum number of a molecule for the lower state of a ro-vibrational transition.
J'	Rotational quantum number of a molecule for the upper state of a ro-vibrational transition.
v'	Vibrational quantum number of a molecule for the upper state of a ro-vibrational transition.
I	The moment of inertia of any molecule through any axis.
m_i	The mass of atom i in a molecule.
r_i	The distance of atom i in a molecule from an axis through the centre of mass of the molecule.
I_a	The moment of inertia about the principal axis a, the smallest of the three principal moments of inertia.
I_b	The moment of inertia about the principal axis b, perpendicular to the two other principal axes.
I_c	The moment of inertia about the principal axis c, the largest of the three principal moments of inertia.
E_r	Quantised rotational energy level.
$F(J)$	Rotational term value for rotational quantum number J.

B	Rotational constant.
T	Temperature; HITRAN database parameter [K].
N_J	The occupation probability of a state with rotational quantum number J.
g_J	Statistical weight of a state with rotational quantum number J.
k_B	Boltzmann constant $\left[\mathrm{m^2\,kg\,s^{-2}\,K^{-1}}\right]$ (SI) or $\left[\mathrm{erg\,K^{-1}}\right]$ (cgs).
D	Centrifugal distortion constant.
r_e	The equilibrium bond length in the diatomic oscillator.
k	Spring constant in the harmonic oscillator approximation.
$\hat{H}$	Hamiltonian (operator).
$\hbar$	The reduced Planck constant; $\hbar = h/2\pi$.
μ	Reduced mass of a diatomic molecule.
E_v	Quantised Vibrational energy level.
$H_v\,(z)$	Hermite polynomial of order v.
$G\,(v)$	Term value for vibrational quantum number v.
ω_e	Harmonic vibration constant.
$\langle \boldsymbol{\mu} \rangle_{nm}$	Dipole transition moment between initial state m and final state n.
μ	Dipole operator.
D_e	Dissociation energy of the Morse potential at the equilibrium position $r = r_e$.
D_0	True dissociation energy of the Morse potential, equal to D_e with the zero point energy subtracted.
χ_e	First-order anharmonic vibration constant.
$\hbar$	Reduced Planck's constant [J s] (SI) or [erg s] (cgs).
v_i	Vibrational quantum number of a molecule associated with the normal mode of vibration i, where $i = 1, 2, 3...$ and specific mode labelling and range of i values is molecular species-dependent.
N	Number of constituent atoms in a molecule.
f_N	The number of normal modes of a system of N point masses.
ℓ_i	The vibrational angular momentum quantum number associated with the degenerate bending mode v_i.
r	The Fermi ranking index as used by the HITRAN database for vibrational levels linked by Fermi resonance.
$S\,(v, J)$	Ro-vibrational term value for vibrational quantum number v and rotational quantum number J.
B_v	Rotational constant with the effects of vibrational coupling.
B_e	Rotational constant for the rigid rotor.
α_e	Rotational-vibrational coupling constant.
D_v	Centrifugal distortion constant including vibrational coupling.
D_e	Centrifugal distortion at the equilibrium of vibration.

β_e	Centrifugal vibrational coupling constant.
HCN	Chemical formula of hydrogen cyanide.
C_2H_2	Chemical formula of acetylene.
CO_2	Chemical formula of carbon dioxide.
ψ_{el}	Electronic component of the molecular wavefunction.
ψ_{vib}	Vibrational component of the molecular wavefunction.
ψ_{rot}	Rotational component of the molecular wavefunction.
ψ_{ns}	Nuclear spin component of the molecular wavefunction.
I	Nuclear spin angular momentum quantum number of an individual particle/atom.
$\hat{P}_{12}$	Pseudo-symmetry operator describing identical nuclei exchange.
$L(x - x_0, \gamma)$	Lorentzian profile.
γ	Lorentzian profile half-width-at-half-maximum.
Δf_L	Lorentzian profile full-width-at-half-maximum.
$G(x - x_0, \sigma)$	Gaussian profile.
σ	Gaussian profile standard deviation.
Δf_G	Gaussian profile full-width-at-half-maximum.
$V(x - x_0, \gamma, \sigma)$	Voigt profile.
G	Gaussian profile (shorthand).
L	Lorentzian profile (shorthand).
$w(z)$	The Faddeeva function evaluated at z.
V	Voigt profile (shorthand).
Δf_V	Voigt profile full-width-at-half-maximum.
Δf_N	The natural line width of a transition (FWHM).
Δf_H	The combined line width of homogeneous broadening mechanisms - the natural line width of a transition and pressure broadening (FWHM).
v	Velocity of a molecule with respect to a reference frame.
f_0	Centre frequency (for a molecule at rest) [Hz]; offset frequency of frequency comb.
σ_D	Doppler broadening Gaussian profile standard deviation.
Δf_D	Doppler broadening Gaussian profile full-width-at-half-maximum.
l	Length.
α	Absorption coefficient.
u	Number density of absorber.
σ	Cross section (of absorber).
$\mathcal{T}$	Transmission - of spectra or transmission function of an optical cavity.
T_{ref}	Reference temperature (296 K); HITRAN database parameter [K].
p_{ref}	Reference pressure (1 atm); HITRAN database parameter [atm].

$S_{\eta\eta'}$	Spectral line intensity for a single molecule, per unit volume, scaled by the natural atmospheric isotopologue abundance for a transition between lower and upper states η and η'; HITRAN database parameter $\left[\mathrm{cm}^{-1}/\left(\mathrm{molecule\,cm}^{-1}\right)\right]$.
$\widetilde{\nu}_{\eta\eta'}$	Wavenumber of the spectral line transition between lower and upper states η and η' in vacuum; HITRAN database parameter $\left[\mathrm{cm}^{-1}\right]$ (cgs).
$Q\left(T\right)$	Total internal partition sum at temperature T.
c_2	Second radiation constant [cm K].
E''	Lower state energy of the ro-vibrational transition; HITRAN database parameter $\left[\mathrm{cm}^{-1}\right]$.
p	Pressure (of a gas); HITRAN database parameter [atm].
n_{self}	Coefficient of the temperature dependence of the self-broadened half-width of each ro-vibrational transition; HITRAN database parameter.
γ_{air}	The air-broadened half-width-at-half-maximum (HWHM) at $T_{\mathrm{ref}} = 296\,\mathrm{K}$ and reference pressure $p_{\mathrm{ref}} = 1\,\mathrm{atm}$; HITRAN database parameter $\left[\mathrm{cm}^{-1}/\mathrm{atm}\right]$.
p_s	Partial Pressure (of a gas); HITRAN database parameter [atm].
γ_{self}	The self-broadened half-width-at-half-maximum (HWHM) at $T_{\mathrm{ref}} = 296\,\mathrm{K}$ and reference pressure $p_{\mathrm{ref}} = 1\,\mathrm{atm}$; HITRAN database parameter $\left[\mathrm{cm}^{-1}/\mathrm{atm}\right]$.
δ_{air}	Pressure shift of the line position at T_{ref} and p_{ref} with respect to the vacuum transition wavenumber $\widetilde{\nu}_{\eta\eta'}$; HITRAN database parameter $\left[\mathrm{cm}^{-1}/\mathrm{atm}\right]$ (cgs).
$f\left(\widetilde{\nu}, \widetilde{\nu}_{\eta\eta'}, T, p\right)$	Unity-integral normalised lineshape function for use with the HITRAN database.
τ	Optical depth.
τ	Round trip time of circulating pulse in the optical cavity of an optical frequency comb.
L	Length [m].
v_g	Group velocity (of an optical cavity).
ω	Angular frequency, $\omega = 2\pi f$.
k	Angular wavenumber, $k = (2\pi)/\lambda$.
v_p	Phase velocity (of an optical cavity).
ϕ_{CE}	Carrier-envelope phase of the frequency comb.
θ_i	Tilt angle of VIPA etalon; angle of input light (general).
θ_m	Diffraction angle of a diffraction grating.
γ_B	Blaze angle of a blazed diffraction grating.
d	Period of a diffraction grating.
$\mathfrak{R}$	Resolving power of a diffraction grating.
$\Delta\lambda_{min}$	Least resolvable wavelength difference of a diffraction grating as defined by the Rayleigh criterion.

N_G	Number of illuminated slits on a diffraction grating.
$\mathfrak{D}$	Angular dispersion of a diffraction grating.
d	Vertical displacement of beams transmitted by the VIPA.
t	Physical thickness of VIPA etalon.
n_r	Refractive index of the VIPA etalon.
θ_{in}	Internal angle of VIPA etalon of incident ray after refraction.
θ_λ	Angle of transmitted VIPA ray from horizontal for a wavelength λ.
n	Refractive index (general).
R	Radius of curvature (of a resonator mirror).
g	Stability parameter of an optical resonator.
r^2	Mirror reflectance (optical cavity).
$\mathcal{F}$	Finesse (of an optical cavity).
$\hat{O}_S$	General symmetry operator.
$\hat{E}^*$	Coordinate inversion symmetry operator.
$\hat{i}$	Inversion symmetry operator (through a centre of symmetry).
$\Delta\nu_{splitting}$	Magnitude of splitting of the J^{th} rotational level for l-type doubling.
q_i	The l-type doubling constant.
ω_c	(Angular) carrier frequency of the optical frequency comb.
t	Time [s].
θ_t	Input angle of ray (to VIPA) with respect to VIPA normal.

Acronyms

VIPA	Virtually Imaged Phased Array.
HITRAN	HIgh-resolution TRANsmission molecular absorption.
FTIR	Fourier Transform Infrared.
CRDS	Cavity Ring Down Spectroscopy.
DCS	Dual-Comb Spectroscopy.
DFCS	Direct Frequency Comb Spectroscopy.
IR	infrared.
NIR	near-infrared.
HWHM	half-width-at-half-maximum.
FWHM	full-width-at-half-maximum.
NPR	Nonlinear Polarisation Rotation.
InGaAs	Indium Gallium Arsenide.
AR	anti-reflection.
FSR	Free Spectral Range.
CW	continuous-wave.
CCD	Charged-coupled Device.
ADC	Analogue-to-Digital Converter.
FP	Fabry-Pérot.

Abstract

Optical spectroscopy provides a window into the world of molecules and their environment by the absorption of electric dipole radiation with frequencies characteristic to each molecular species. The temperature, concentration, and pressures of molecules in a gas sample can theoretically be obtained through examination of optical absorption spectra. This is provided the spectrum is of high enough resolution and sufficient bandwidth that the complicated molecular absorption spectrum may be observed, particularly in cases with multiple molecular species present in a sample.

The invention of a fully-stabilised optical frequency comb in recent decades has revolutionised molecular spectroscopy. It provides a near-ideal spectral interrogation source for the high-resolution study of molecules, combining absolute frequency accuracy, broad single-shot bandwidth, and dense spectral sampling. The comb light is contained within a single beam, and must be dispersed into its component frequencies in order for a molecular spectrum to be extracted. There are numerous methods to perform this, with the technique employed in this thesis utilising a dispersive spectrometer based on a virtually imaged phased array. The spectrometer spreads the comb light from a single beam into a two-dimensional array of its component frequencies, allowing the power of each comb frequency to be measured.

This thesis details the development and construction of a virtually imaged phased array spectrometer system for use with an optical frequency comb. Additionally, code that extracts the traditional absorption spectrum from the two-dimensional arrays of frequencies produced by the spectrometer were developed and demonstrated, along with a model to extract physical parameters of molecules. The theoretical basis to model the characteristic absorption fingerprints is presented for each of the molecules examined in the course of this thesis (hydrogen cyanide, carbon dioxide, and acetylene), as well as the differences in spectra caused by changes to the pressure, temperature, and concentration of molecules in the sample. The results chapters walk through the development of the spectrometer into a reliable system capable of rapidly acquiring high-quality molecular spectra from which highly accurate and precise measurements of concentration and temperature were demonstrated. The capability of the system to easily differentiate between isotopologues of the same species in the same sample makes this spectrometer a powerful spectroscopic tool that, with further development, may find use in out-of-lab applications such as medical breath analysis and environmental monitoring. Additionally, the demonstrated capability to measure extremely high-resolution spectra beyond the resolution limit of the spectrometer may find use in measurements of the thermodynamic properties of molecules.

I certify that this work contains no material which has been accepted for the award of any other degree or diploma in my name at any university or other tertiary institution and, to the best of my knowledge and belief, contains no material previously published or written by another person, except where due reference has been made in the text. In addition, I certify that no part of this work will, in the future, be used in a submission in my name for any other degree or diploma in any university or other tertiary institution without the prior approval of the University of Adelaide.

I give consent to this copy of my thesis when deposited in the University Library, being made available for loan and photocopying, subject to the provisions of the Copyright Act 1968.

The author acknowledges that copyright of published works contained within this thesis resides with the copyright holder(s) of those works.

I also give my permission for the digital version of my thesis to be made available on the web, via the University's digital research repository, the Library Search and also through web search engines, unless permission has been granted by the University to restrict access for a period of time.

I acknowledge the support I have received for my research through the provision of an Australian Government Research Training Program Scholarship.

Sarah Katherine Scholten

17th July, 2019

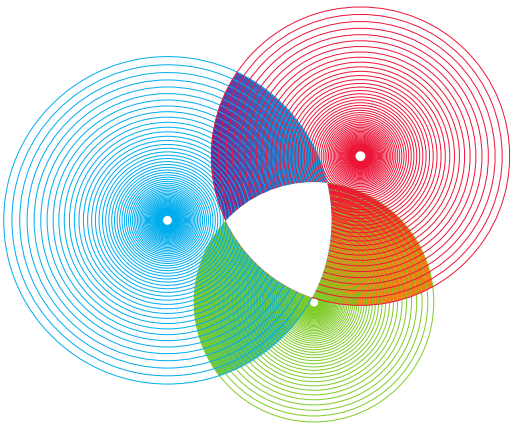

Acknowledgements

I have many people to acknowledge for their contributions and support throughout my PhD, both personally and professionally. Firstly I would like to sincerely thank my supervisors Andre Luiten, Christopher Perrella, and Richard White. The results of this thesis would not have been possible without their endless patient support and guidance. Special thanks must go to Christopher Perrella for taking on a student midway through their PhD studies. I must also thank my original supervisor James Anstie for the inspiration to pursue this project and always believing in its potential.

Thank you to the technical staff at the School of Physical Sciences and the Institute for Photonics and Advanced Sensing (IPAS) workshops for always being happy to assist in the design and manufacture of required custom parts. Special thanks go to Murray Hamilton for the continued lending of critical experimental components. Thanks must go to Eric May and Paul Stanwix for welcoming me to a research exchange at the The Australian Resources Research Centre (ARRC), and to fellow student Kwanghee Jeong for generously allowing me to work with him on his experiment during that time.

I would like to thank the post-docs and fellow students of the group and IPAS for their advice, technical expertise, experimental assistance, and laughter throughout my studies. I am appreciative of their encouragement and contributions to an enjoyable environment that provided a light-hearted escape from temperamental experiments.

I would like to thank all of my friends outside of university for providing a welcome escape from the sometimes turbulent life of a PhD student. You never failed to make me feel better, whether through the consumption of copious amounts of sugar or by the pursuit of hobbies. Thanks especially to Nathanial Wilson. Your equally warped sense of humour never fails to make me laugh. Thank you for sticking with me all this time.

Special thanks to my family for their continued love, support, and encouragement not just during my PhD but for the last 25 years. Without their support, this undertaking would not have been at all possible. Thank you Mum, Dad, and David, I will always be grateful.

Preface

Spectroscopy provides a window into the structure of molecules and their local environment. In contrast to their atomic constituents, the optical spectra of molecules alludes to a complex energy level structure with numerous additional levels due to molecular vibrations and rotations unavailable to lone atoms. With a deep knowledge of the mechanisms that determine such spectra, the local molecular environment may be ascertained. However, this will only be possible with if the spectra are acquired with sufficient resolution and bandwidth. The realisation of optical frequency combs in recent years has provided a near-ideal spectral interrogation source for studying electric dipole radiation transitions in molecules, combining absolute frequency accuracy, broad single-shot bandwidth, and dense spectral sampling. In order to produce a molecular absorption spectrum using an optical frequency comb as the interrogation source, a way must also be found to unravel the hundreds of thousands of simultaneous frequencies of the comb. Numerous methods exist, each with their own pros and cons as will be explored during the course of the thesis.

The first part of the thesis presents motivation for the study of molecules and existing technologies for doing so. Chapter 1 introduces applications of molecular spectroscopy, with a focus on medical breath analysis and environmental monitoring as motivators for the work presented in later chapters. Existing methods for the detection of molecules are explored in Chapter 2, along with their benefits and detractions.

A significant amount of theoretical background is required to understand the shapes and behaviour of molecular spectra, as well as to extract the parameters of interest. The second part of the thesis presents a general physics introduction and overview into the nature of the spectra of molecules presented in later chapters. Chapter 3 provides an introduction to the spectra of molecules seen in this thesis, beginning with conventions and units of the field. The chapter is focused on how the spectra of diatomics and small (less than four-atom) linear polyatomic molecules arise. Rotational spectroscopy and the concept of rotors and their energy level structure is introduced before moving onto vibrational spectra. The harmonic and anharmonic oscillator approximations for vibrational spectra are presented, along with the vibrational transition naming conventions followed throughout the thesis. The combination of rotational and vibrational concepts to produce rotational-vibrational spectra of molecules are then introduced before finishing with discussion of the allowed types of rotational-vibrational transitions and some intensity modifiers that present in spectra examined during the course of this thesis.

The shapes of each line in a molecular spectrum is examined in detail in Chapter 4. The commonly-used Voigt profile is introduced, before the physical cause of the width of each line

is examined. We specifically examine the influences of pressure, temperature, and concentration changes to the shape of the spectral lines. The chapter concludes with consideration of the ways in which these parameters may be extracted from measured spectra using an efficient spectral model, and the effects of the spectral measurement device on the widths of lines.

The experimental part of the thesis is split into three chapters. Chapter 5 describes the generation of the optical frequency comb as used in this thesis. The concepts of mode-locked lasers and mode-locking with non-linear polarisation rotation are introduced before extension to the stabilisation and creation of an optical frequency comb by a self-referencing scheme. The parameters of the base model comb used in this thesis are presented, before the comb spectral bandwidth is increased by the addition of a highly non-linear fibre to target additional molecular species.

Chapter 6 explores the components of a Virtually-Imaged Phased Array (VIPA) spectrometer and its use in unravelling the optical frequency comb into its spectral components. Diffraction gratings and VIPAs are described before their combined output is explained with regards to the broadband comb source. The final component of the spectrometer - an InGaAs camera - is characterised with methods presented to correct the dark current and non-linearity of the camera response within the captured images. Finally, the method by which the imaged comb is converted into a traditional absorption spectrum by this home-built spectrometer is detailed.

The comb rarefication cavity necessary to produce a calibrated frequency axis for the measured molecular spectra is presented in Chapter 7. The construction and stability of this cavity is detailed before discussion of the filtering capabilities and characteristics of the cavity. The chapter concludes with brief discussion of stabilisation for this cavity.

The results section of the thesis is split into chapters based upon individual publications. Each of the publications make use of the optical frequency comb, rarefication cavity, and spectrometer as previously described. The first publication presented in Chapter 8 describes the proof-of-concept demonstration of the VIPA spectrometer system with direct frequency comb spectroscopy as applied to a sample of hydrogen cyanide. This paper describes the first time the system presented in this thesis achieved quantitative detection of a molecular system, comparing favourably with previously published measurements and competing techniques. Additionally, this paper describes how the rarefication cavity may be used to ensure resolution of individual comb modes without loss of the optical frequency comb's dense spectral sampling when the VIPA spectrometer lacks sufficient spectral resolution, while maintaining absolute frequency accuracy.

Chapter 9 details how an additional image containing interference fringes may be used to extract both the phase and absorption data of the molecular sample simultaneously with a Michelson interferometer as demonstrated with hydrogen cyanide. Additionally, this publication describes the matched-filtering techniques that allows the spectrometer to be used

without prior cavity rarefication, and marks the shift towards using the rarefication cavity as a calibrator for the frequency axis.

The publication presented in Chapter 10 describes measurement of the local molecular environment with the undecimated optical frequency comb with high precision and accuracy. It details the use of an efficient molecular model fit based on the Voigt profile and HITRAN spectroscopic parameter database to extract the varied concentration of carbon dioxide along with its temperature from measured spectra all in under a second. The measured concentrations matched those predicted using the Virial-corrected Ideal Gas Law for all examined values. This manuscript is the first demonstration of the system to produce rapid, quantitative results, achieved with a large amount of experimental interfacing and automation. These advancements also opened up the ability to average numerous spectra to improve the signal-to-noise ratio of measurements and allowed measurements of weaker molecular absorption features to be attempted in further work.

Equipping the molecular model fit developed in Chapter 10 to handle multiple isotopologues of carbon dioxide combined with rapid averaging is the basis of the publication presented in Chapter 11. In this paper, the total concentration of carbon dioxide was altered while the absolute concentration of each isotopologue was measured. The linearity of the entire measurement system over a large concentration range is additionally able to be established owing to the drastic difference between the natural abundances of the two fitted isotopologues of carbon dioxide and the disparate depths of their absorptions.

Chapter 12 details how to combine sequential stepping of the comb's repetition rate with a rarefication cavity to produce high-resolution spectroscopic measurements of acetylene beyond the resolution limit of the VIPA spectrometer. In this paper, a low-pressure acetylene cell was probed directly with a rarefied version of the comb as produced by the rarefication cavity detailed in Chapters 7 & 8. This allowed full resolution of the comb frequencies by the spectrometer at the expense of the majority of comb modes. In order to return the missing frequencies, the repetition rate of the comb was sequentially increased. This resulted in a shift of the comb modes at the observed frequency range with the cavity tracking this new comb. This manuscript details the first use of this method with an optical frequency comb and VIPA spectrometer to perform high-resolution spectroscopy, as demonstrated on the narrow features of acetylene.

The final chapter of this thesis presents a summary of the work and planned future work to continue developing the spectrometer system into one suitable for out-of-lab applications such as medical breath analysis or environmental monitoring.

Part I

Introduction and Literature Review

Motivation

The study of light-matter interaction provides great insights into the physical world. An important subset of this field is the unique interactions between light and the molecules that surround us. Measurement of the characteristic ways in which different species of molecules interact with light enables numerous applications. For example, a number of small volatile (airborne at room temperature) molecules can be linked to specific disease states in humans when detected in the breath, while determining the sources of other characteristic molecules that contribute to the pollution and changing climate of Earth can result in a less polluted planet. This chapter aims to introduce some of these important molecules to motivate the necessity of a broadly-applicable detection scheme for such particles [2–10].

1.1 Molecules as Indicators of Disease

It has been known since ancient times that the human breath provides insights into the physiological and pathophysiological processes within the human body [10–12]. For example, A fruity-sweet smell is associated with uncontrolled diabetes, while a fishy smell accompanies liver disease [13,14]. Evidently certain volatile molecules contained within the breath of these patients are characteristic of these diseases, and these molecules are then known as *biomarkers* for that disease [5]. However neither liver disease nor diabetes stem from dysfunction of the lungs or airways, so the presence of these biomarkers in the breath must be explained by another mechanism [15,16].

1.1.1 Physiological Mechanism

In order for a biomarker to be found within the breath, it must have passed through the respiratory system. Excluding inhalation, if the biomarker does not originate directly from disease within the mouth cavity, upper airway, or the lungs themselves, it will have entered the respiratory system by diffusion through the lungs. The lungs are a collection of millions of small expandable air sacs called alveoli [17–19]. The alveoli walls are surrounded by capillaries fed by pulmonary arterial blood returning from the tissues of the body, with the blood and alveoli separated by a thin barrier called the pulmonary alveolar membrane, also more simply known as the 'blood-air barrier' [17–20]. Oxygen drawn into the alveoli during inhalation is then diffused into the surrounding capillaries, while at the same time carbon dioxide diffuses into the alveoli for exhalation [18,19,21]. However, if the molecule is small enough, it may

cross the alveolar membrane and be exhaled along with carbon dioxide [16,22,23]. A cross-sectional diagram of an alveolus depicting gas exchange is shown in Fig 1.1.

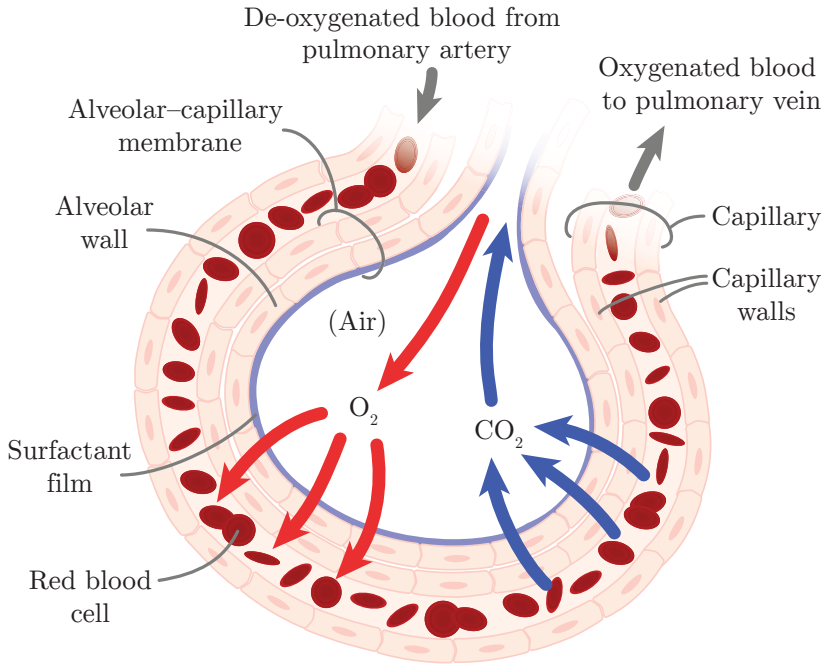

Figure 1.1: Cross-section of an alveolus depicting gas exchange in the lung. Inhaled oxygen is diffused through the alveolar-capillary membrane, oxygenating red blood cells carried in the surrounding capillary on their way to the pulmonary vein. Simultaneously, de-oxygenated blood from the pulmonary artery diffuses carbon dioxide - and biomarkers - through the alveolar-capillary membrane into the air cavity for exhalation [24–26].

1.1.2 Biomarkers

An ever-growing number of biomarkers are being correlated to particular disease states as seen in Table 1.1 [27]. Additionally, some diseases are now able to be diagnosed via a commercially-available breath test e.g. the presence of *Helicobacter pylori* (*H. pylori*) - the cause of several gastrointestinal diseases - can be ascertained based on the $^{13}C/^{12}C$ ratio of carbon dioxide [28–31].

Analysis of the exhaled breath is an appealing method for disease diagnostics as it is inherently non-invasive. In addition, these techniques have the potential to detect diseases in their early stages in a painless manner, as well as in critical care scenarios [16,58,59]. The human breath is a mixture of predominantly nitrogen, oxygen, carbon dioxide, water vapour, and other inert gases with trace concentrations of biomarkers [60,61]. However, the wide-spread adoption of breath analysis for disease diagnostics is hampered by the expense, accuracy, sensitivity, technical difficulty and time required by current methods. These current methods include selected ion flow tube mass spectrometry or gas chromatographymass spectrometry [62,63]. Another class of detectors - electrochemical-based sensors - are an active area of research but are typically specialised to a specific target species and do not provide a true

Disease	**Related exhaled biomarker**	**Reference(s)**
Asthma, COPD*, oxidative stress	(Fractional) nitric oxide, carbon monoxide	[32–36]
H. pylori infection	$^{13}C/^{12}C$ ratio of carbon dioxide	[37,38]
Lung cancer	Benzene, ethane, formaldehyde, isoprene, propanol, etc.	[39–43]
Renal disease	Ammonia, isoprene	[44–47]
Diabetes	Acetone	[48,49]
Oesophageal cancer	Phenols	[50–52]
Liver disease	Carbonyl disulfide, methanol, limonene etc.	[53–56]

Table 1.1: Common diseases and their correlated exhaled biomarkers [27]. *Chronic Obstructive Pulmonary Disease (COPD) is an umbrella term that includes numerous long-term lung conditions such as chronic bronchitis and emphysema [57].

broad-scale detection technique. In addition, many suffer from molecular cross-sensitivities or non-specificity issues [64–66]. A broad-scale breath-screening device requires high sensitivity, low response time, species selectivity of biomarkers in the complex human breath, relatively low cost, and ease of use with minimal specialised training to find widespread adoption in a clinical setting [16,50,60,61,67].

1.2 Pollution and the Environment

Anthropogenic sources and absolute levels of volatile pollutants and greenhouse gases are of major concern to the environmental monitoring and medical communities [68,69]. Both are linked with reduced life expectancy and detrimental effects on the environment [69]. Additionally, with increasing global industrialisation, the levels of airborne pollutants and greenhouse gases are growing [70,71]. Unfortunately, the long term effects of such emissions are now becoming apparent in the human environment in regards to the health of the global population and climate.

1.2.1 Pollution

The levels of particular volatile molecules in the environment can be indicative of anthropogenic pollution, many of which have detrimental effects to the health of the human population. This is particularly important in urban environments, where exhaust fumes from engines and burning of fossil fuels leads to higher incidences of respiratory, cardiovascular, and central nervous system disease from the release of carbon monoxide, sulphur dioxide and nitrogen dioxide [6,35]. Additionally, an increased likelihood of cancer is linked with elevated pollution levels [72–75]. It is estimated that the yearly death toll from air pollution is in the millions, with the majority of deaths in rapidly industrialising areas such as Asia [76,77].

Global food supply is also at risk, with groundwater and soil also affected by contamination from anthropogenic pollution sources [78]. Sources of air pollution may be traced by detection of characteristic molecules, for example leak detection in natural gas pipelines, industrial emissions, and automotive fumes [79–82]. Once traced back to their source, polluters may be encouraged to implement solutions to reduce the pollution toll on the environment [83–85].

1.2.2 Anthropogenic Global Warming

In addition to the more immediate human health effects of pollution, emission of large volumes of greenhouse gases such as carbon dioxide and methane are major causes of anthropogenic global warming [86]. The majority of Earth's atmosphere is comprised of three major gases - oxygen, nitrogen, and argon. [87]. Trace amounts of other gases such as water vapour, carbon dioxide, nitrogen dioxide, and methane can have a large impact on the climate of the planet, owing to their effective capture of infrared radiation [88,89]. Water vapour, carbon dioxide, nitrogen dioxide, and methane are the major greenhouse gases, with the latter three most heavily influenced in their atmospheric concentrations by anthropogenic activities [89,90].

Solar radiation passes through the Earth's atmosphere and heats the terrestrial surface, which re-emits this energy as infrared radiation. Greenhouse gases are very effective at absorbing and re-emitting this infrared radiation in all directions - including back into the atmosphere - and act as a 'blanket' around the planet by preventing the escape of this transformed solar energy [89,90]. While this is a natural process, known as the greenhouse effect, rising levels of greenhouse gases from anthropogenic sources increases the amount of infrared radiation trapped in the atmosphere, heating the planet as a whole [88,90]. This increase in global mean temperature then evaporates surface water, increasing the amount of atmospheric water vapour and causing more warming [88,89]. Unchecked, emissions of greenhouse gases and the consequent global warming is expected to produce severe climate change, rising sea levels with the melting of glaciers and permafrost, ocean acidification and warming, and an increase in the frequency and severity of extreme weather events such as storms systems, heat waves, and droughts [89,91–100].

To reduce emissions globally, an effort must be made to monitor the levels at which anthropogenic activity is releasing these greenhouse gases and identify the specific practices that are the main contributors. Industry was responsible for approximately 20% of greenhouse gas emissions in 2010 from the burning of fossil fuels for energy and industrial processing [97,101,102]. Production of electricity and heat by burning of fossil fuels was the largest contributor in the same year, accounting for the greatest source of emissions [97,102]. Agriculture and deforestation is also responsible for a large proportion of emissions (25%), while transportation and fuel refining are the predominant remaining sources of anthropogenic greenhouse gas emissions [97,101–103].

1.3 The Ideal Measurement Device

Both applications explored in Sections 1.1 and 1.2 share similar requirements for an ideal detection system. A non-invasive measurement technique for disease diagnostics and patient monitoring would inherently benefit all patients, in particular those that are critically or chronically ill. Similarly, industrial monitoring or environmental applications benefit from a stand-off detector that does not need to be exposed directly to possibly hazardous environments. In addition, detection of multiple gas species and their isotopologues simultaneously with high specificity in a complex mixture reduces the need for multiple detectors in either application. The ideal detection system would also be small in physical size, highly sensitive, relatively cost-effective, and produce high-resolution and rapid results. While there are many established detection systems and yet more in development, all have both benefits and shortcomings as will be explored in the next chapter.

Molecular Measurement Techniques

The ideal molecular detector would rapidly produce highly accurate and precise results for the concentration of each molecular species in the sample. Ideally, other characteristics such as the temperature and pressure of the sample would be returned simultaneously, and the detector would have no cross-sensitivities between molecular species. For use in industrial environments, an ideal detector would avoid direct exposure to the environment under test. These characteristics would also benefit biomedical applications such as breath testing, being inherently non-invasive in nature. There are a number of techniques used to measure the properties and contents of gas samples. Some methods such as electrochemical sensors measure the electrochemical reactions of the target molecule with the sensor, while others utilise the absorption of light by the molecular sample, such as in Fourier Transform Infrared (FTIR) spectroscopy, Cavity Ring Down Spectroscopy (CRDS), and Dual-Comb Spectroscopy (DCS) [104–107]. The most commonly used lab-based technique, Mass Spectrometry, is also examined together with the complimentary technique of Gas Chromatography. A distinction will be made between optical spectroscopy-based techniques and other common methods of interrogating gas samples.

2.1 Non-Optical Measurement Techniques

2.1.1 Electrochemical Sensors

Electrochemical sensors return information about the sample by interaction of a chemically-selective layer (containing an electrolyte) to some form of electrochemical transducer to produce a measurable current or other measurable change. These changes are then proportional to the amount of target chemical in the sample [108–110]. While these type of sensors are quite common (including in blood glucose detectors), cheap, and can be extremely sensitive, there are some applications in which such sensors are unsuitable. Additionally, the chemically-selective layer has a finite lifetime and becomes less sensitive over time [111–114]. Another major downfall of electrochemical sensors is their cross-sensitivity of target and non-target species [115–117]. These combine to make electrochemical sensors useful for specifically-targeted applications rather than a broad-scale detector.

2.1.2 Gas Chromatography - Mass Spectrometry

Gas Chromatography - Mass Spectrometry (GC-MS) is a combination of two techniques. The first technique, gas chromatography, involves injecting the sample into the gas chromatograph where it is vaporised. A carrier gas, known as the *mobile phase*, sweeps the vaporised sample into a chromatographic column of which the inner surface is specially-coated (the *stationary phase*). The carrier gas is often an inert gas, most commonly helium. The compounds of interest are separated by their relative interactions with the stationary phase due to their differing chemical and physical properties. This leads to a chemically-specific retention time in the column. The compounds emerge from the end of the column, where the amount of each compound is detected. Each compound is then identifiable by the time taken to reach the outlet. In a GC-MS instrument, the gases emerging from the column are then sent to the inlet of the mass spectrograph, bypassing this detector [118,119].

The second technique folded into GC-MS is mass spectrometry, which uses the differential deflection of charged particles to separate them based on their mass-to-charge ratio for compositional analysis [120]. In a typical mass spectrometer, a solid, liquid, or gaseous sample is ionised by bombardment with electrons, which may fragment molecules of the sample into charged pieces. After ionisation, the charged particles are first accelerated then deflected by an applied electric or magnetic field, with the amount of deflection dependent on their charge and mass. A charged particle detector such as an electron multiplier detects the landing points - and therefore the amount of deflection - of each ionised fragment, with results displayed as the number of detections (relative abundance) as a function of mass-to-charge ratio. The composition of the original sample is then inferred using known masses of molecules or by characteristic fragmentation patterns [120,121].

The two techniques of gas chromatography and mass spectrometry are combined to form the final GC-MS instrument. The gas chromatography segment of the spectrometer provides a continuous flow of molecules to be analysed by the mass spectrometer component. GC-MS is capable of high sensitivities and isotopic detection, and may produce high resolution spectra. However, GC-MS machines are relatively expensive to procure and maintain, and require training to operate correctly. In addition, care must be taken not to contaminate the column of the gas chromatograph portion, or allow the carrier gas to become ionised and introduced to the mass spectrometer part of the instrument. For similar reasons, the sample may also require some degree of pre-treatment prior to its injection into the chromatograph, and the mass spectrometer must be maintained at a high vacuum. Finally, and in particular for biochemical samples, the sample itself may decompose or chemically react during the gas chromatography phase of the spectrometer [120–122]. A GC-MS device is not suited for use outside of a laboratory setting, and cannot be used in-situ for applications such as continuous critical patient monitoring.

2.2 Optical Measurement Techniques

Optical measurement techniques are extremely useful for probing molecular systems, particularly in cases where remote measurements are required. In addition, optical measurements can be rapid and performed *in situ* as they require only optical access. This allows applications of optical detectors in environments where sample extraction is unwanted or hazardous conditions, as well as continuous monitoring applications. The most common optical measurement techniques including Fourier Transform Infrared (FTIR) spectroscopy, Cavity Ring-Down Spectroscopy (CRDS), and systems based on optical frequency combs. Each have their own advantages and disadvantages which must be explored.

2.2.1 Fourier Transform Infrared (FTIR) Spectroscopy

Fourier Transform Infrared (FTIR) spectroscopy uses the interference of a collimated broadband infrared light source in combination with an optical beam splitter and two mirrors - one fixed and one movable - in an arrangement known as a Michelson interferometer. The sample to be interrogated is placed in the infrared beam, typically just prior to a detector. A typical FTIR apparatus may be seen in Fig. 2.1. As the movable mirror is scanned, the detector observes a complex interference pattern as the wavelengths of the broadband light interfere constructively and destructively. A Fourier transform is used to convert the signal (consisting of the absorption of light by the sample as a function of mirror position) into a frequency-dependent absorption of light.

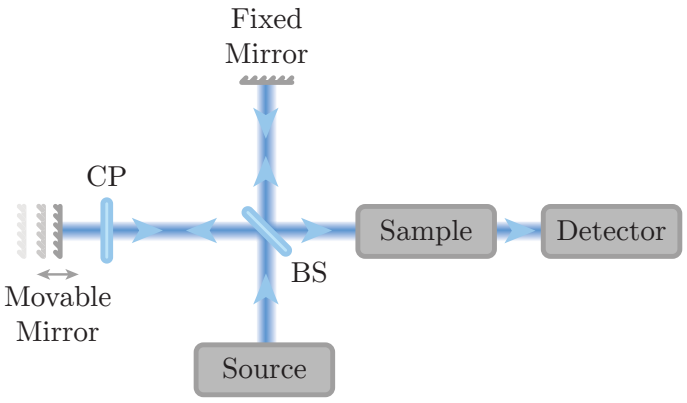

Figure 2.1: A typical FTIR setup. A collimated broadband infrared light source is evenly split by a beam splitter (BS). Half of the light is directed toward the fixed mirror, and the other half towards the movable mirror. A compensation plate (CP) is often present in one or both arms to compensate for the phase delay that one arm of the spectrometer acquires by travelling through the beam splitter material twice. Both paths are recombined before passing through the sample. The interference signal of the two beams is encoded with the absorption spectrum of the sample, which is revealed after a Fourier transform is performed [123].

These spectrometers are capable of providing high-resolution and broadband spectra.

The spectrometer resolution is mainly defined by the maximum path difference between the interferometer arms, while the total spectral width depends on the spectral width of the source [105,120]. However, these devices are limited by the speed of data collection, as the signal must be sampled at a rate at least twice as high as the highest-frequency component as dictated by the *Nyquist criterion* to prevent aliasing of the spectrum. Additionally, high spectral resolution requires a relatively large scan range, and the incoherent nature of the light often used in these spectrometers precludes the use of common sensitivity enhancement techniques such as the use of optical enhancement cavities [123–125].

2.2.2 Cavity Ring-Down Spectroscopy

Cavity Ring-Down Spectroscopy (CRDS) exploits the coherent nature of laser light to increase sensitivity of molecular measurements by utilising an optical enhancement cavity. Such cavities increase the sensitivity of detection by increasing the effective path length of the system by bouncing light between the cavity mirrors many times. The simplest optical cavity is formed of two opposing mirrors. A coherent light source of wavelength λ is introduced to the cavity through the input mirror. In CRDS, a tunable laser source is used with a high finesse optical cavity. If the mirror separation is equal to an integer multiple of $\lambda/2$, the light will be resonant with the cavity, and the intensity of light within the cavity builds as it circulates due to constructive interference while the input light source continues to feed the cavity.

The light bounces back and forth between the mirrors, with a small portion of the light leaking out of the output mirror each time the circulating light strikes the output mirror. A fast photodetector is placed behind this mirror and monitors the light leaking from the cavity. Once a certain signal threshold is met at this detector, the laser source is deactivated. The detector continues to monitor the light as the signal follows an exponential decay while the remaining light leaks out of the cavity. CRDS measures the time taken for the output light to decay to $1/e$ of its initial output intensity - known as the *ringdown time*.

If a gaseous sample is introduced to the space between the cavity mirrors, a new loss mechanism (absorption by the sample) is introduced. This shortens the ringdown time compared to the empty cavity, with the intensity of light measured at the detector decaying more rapidly as the light makes fewer bounces between the mirrors. The ringdown time for the empty cavity and sample run are then used to calculate the concentration of the gas in the sample at λ. The laser is then tuned to a new wavelength, the cavity length adjusted to suit, and the two required runs repeated for as many wavelength points as desired.

While CRDS is extremely sensitive due to its long path lengths, and capable of very high resolution measurements, it is limited by the speed of spectral acquisition. In order to cover a broad bandwidth with sufficient resolution, long acquisition times are required. Additionally, the tunability of the laser source and spectral bandwidth of the mirror coatings affect the bandwidth of achievable results. These factors usually make CRDS unsuited to rapid, spectrally-broad out-of-lab measurements [106,126–128].

2.2.3 Dual Comb Spectroscopy

Dual-comb spectroscopy (DCS) is a powerful technique that utilises the unique properties of optical frequency comb lasers. An in-depth description of combs and their properties appears in Chapter 5, but the output of a comb can be essentially described as many hundreds to thousands of individual lasers appearing simultaneously at very well-defined frequencies or comb 'teeth' over a large frequency span. These individuals lasers have a high degree of spectral coherence. The separation of each frequency from its neighbour is known as the repetition rate of the comb, f_{rep}. In DCS, two combs of slightly different repetition rates f_{rep} and $f_{\text{rep}} + \Delta f_{\text{rep}}$ are interfered and detected on a photodiode as seen in Fig. 2.2. The mixing of the two optical combs in this way produces a new comb in the radio-frequency (RF) domain with a repetition rate equal to the difference in repetition rates between the optical combs, Δf_{rep}. To perform spectroscopy, either one or both of the optical combs are passed through the sample prior to their interference, encoding an absorption (or phase) signature onto the teeth of the RF comb [105,129–131].

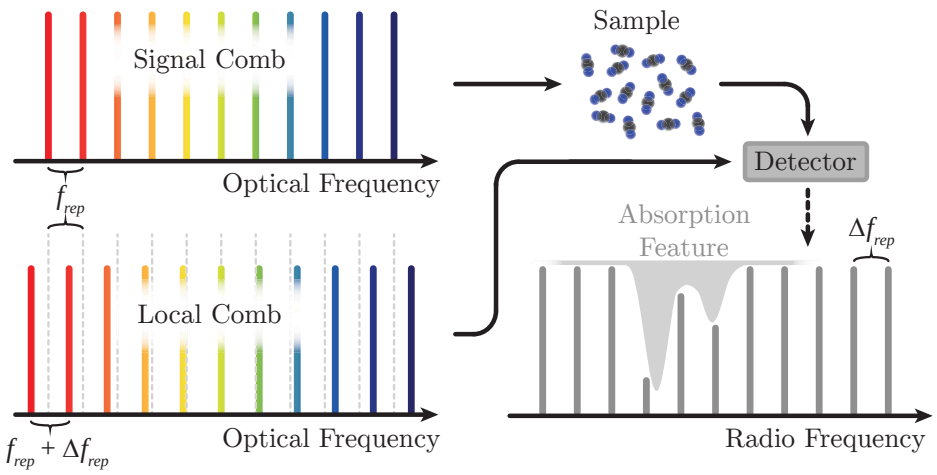

Figure 2.2: The concept of dual-comb spectroscopy. Two combs of slightly different repetition rates f_{rep} and $f_{\text{rep}} + \Delta f_{\text{rep}}$ are mixed and detected on a photodetector. The mixing of the two optical combs produces a new comb in the radio-frequency (RF) domain with teeth spaced by Δf_{rep}. To perform spectroscopy, either one or both combs are passed through the sample, encoding an absorption signature onto the teeth of the resulting RF comb.

Dual-comb spectroscopy is a burgeoning field, with demonstrations in both enhancement-cell and open-air paths, trace gas analysis, and gas turbine exhaust [130,132–138]. The increasing availability and recent reductions in the expense and size of optical frequency combs make DCS and comb spectroscopy in general a popular choice. However, the need for two optical frequency combs can make DCS a relatively costly and complex technique. Additionally, there is a trade off between the optical bandwidth and acquisition speed for DCS, with increased speed coming at the cost of single-spectrum signal-to-noise ratios. In practice this issue is overcome by averaging numerous spectra together, however it makes time-critical measurements difficult. Furthermore, the stability of Δf_{rep}, and hence the sta-

bility and synchronisation of the original optical combs, must be precisely controlled. Despite this, DCS is an extremely powerful technique capable of high-resolution broadband spectra, which contributes to its popularity [105,139–141]. We note that recent work aimed at developing compact chip-based combs can remove some of the cost and complexity of this technique [142].

2.2.4 Direct Frequency Comb Spectroscopy

Direct Frequency Comb Spectroscopy (DFCS) uses the properties of optical frequency combs to measure the absorption signatures of molecules. As optical frequency combs are coherent sources, optical tricks such as enhancement cavities may be used to increase the sensitivity of such systems [139,143]. In the simplest architecture the comb is shone through a gas sample which leaves a characteristic absorption fingerprint on the comb teeth. The transmitted comb light that has passed through the sample is compared to comb light (originating from the same comb) that did not interact with the sample. Comparison of these two paths then extracts the absorption fingerprint of the molecule, usually employing a spectrometer to disperse the comb light into its component frequencies before measurement by a detector [144–147].

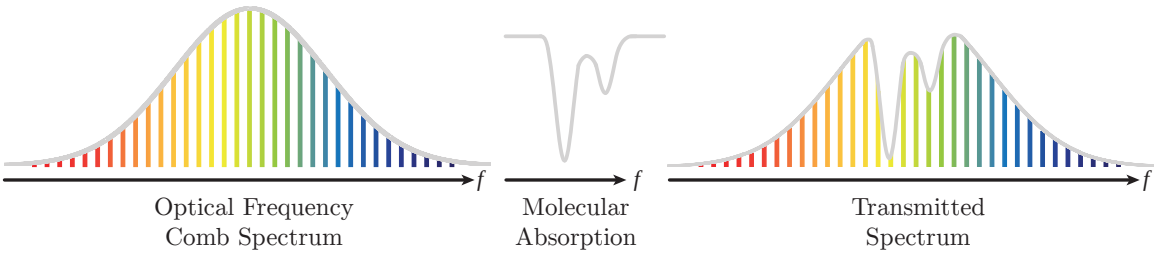

Figure 2.3: The principle of direct frequency comb spectroscopy. The comb is directed through a molecular sample, which absorbs frequencies characteristic to the sample composition. The transmitted light is compared to light that has not passed though the sample and unravelled into its frequency components using a spectrometer, producing an absorption spectrum.

A commonly-used type of spectrometer is based on a Virtually-Imaged Phased Array (VIPA) as will be described further in Chapter 6. These spectrometers are based on two spatially-dispersive elements - the virtually imaged phased array and a diffraction grating - which work in conjunction to spread the comb frequencies into a two-dimensional array of light. This array is then imaged by a sensitive camera, and analysed to produced the absorption fingerprint. Such spectrometers have the capability to be quite high-resolution, and benefit from the requirement of only a single comb, simplicity of operation, and lack of moving parts [143,144]. It is for these reasons and the general benefits that follow the use an optical frequency comb that the DFCS technique combined with a VIPA-based spectrometer was chosen as the spectroscopic method of choice throughout the course of this thesis.

Part II

Background and Theory

Molecular Spectroscopy

Spectroscopy with electromagnetic radiation has provided important insights into the structure and dynamics of the molecules that surround us. If the energy of light incident on a molecule corresponds to a difference in energy between two states of the molecule, the molecule may be excited to the higher state through the absorption of a photon [148,149]. This absorption of photons with specific energies leaves a characteristic modulation in the intensity of the light. Molecular absorption features are more complex than those of their individual atomic constituents, due to the bonds between the atoms that make up the molecule. Because of these bonds, the energy levels of the molecule are numerous, formed from a combination of many related molecular vibrational and rotational states. Correspondingly, the patterns produced by looking at the energies missing from a broadband incident light source - an optical absorption spectrum - are also complex in nature. This chapter aims to provide a guide for the reader to understanding basic molecular spectroscopy through the physical phenomena behind the unique absorption spectra of some simple linear molecules.

3.1 Foundations of Molecular Spectroscopy

It is important to first define the commonly used conventions in the field of molecular spectroscopy. Firstly, the relations between energy and frequency of the photons used to excite the molecules must be defined.

3.1.1 Molecular Spectroscopy Unit Conventions

For historical reasons, there are a variety of units used to measure the frequencies and wavelengths of light in the field of molecular spectroscopy. It is common to see a mixture of units depending on the field of scientific study utilising spectroscopic methods. Laser physicists often prefer working with frequency, f, in Hz due to its direct link with the energy of each photon:

$$E = hf \qquad \text{[J]} \quad (3.1)$$

where h is Planck's constant and the energy is measured in Joules [120,148,149]. Another favoured unit is wavelength, λ, as it is easily linked with frequency through:

$$\lambda = \frac{c}{f} \qquad \text{[m]} \quad (3.2)$$

where c is the speed of light in vacuum [120,148,149]. Another unit commonly used in molecular parameter databases is wavenumber, $\widetilde{\nu}$, which has units cm^{-1} and is related to wavelength and frequency in Hz by:

$$\widetilde{\nu} = \frac{1}{\lambda} = \frac{f}{c} \qquad \left[\mathrm{cm}^{-1}\right] \quad (3.3)$$

where caution must be taken to ensure correct unit propagation [120,148–150]. Energy may also be expressed with units of cm^{-1}, with widespread use due to ease of incorporation into molecular parameter databases. Throughout this thesis a preference for SI units will be used, excepting where use of databases based in cgs units is required.

3.1.2 Fundamentals of Molecular Spectroscopy

Due to the presence of bonds between the atoms constituting a molecule, there are additional ways in which a molecule may absorb energy compared to those available to its individual atoms. An incident photon's energy and momentum may be transferred to the molecule, exciting it through an optical transition into a higher rotational, vibrational, and/or electronic state. The molecule may rotate in space, appearing different to the incoming light depending on its orientation at time of the photon collision. The bonds between the atoms in the molecule also may vibrate in a number of ways depending on the arrangement and strength of these bonds in the molecule. Finally the molecule's electrons may be excited directly to a higher state by a high-energy photon. The state of a molecule is then described by its molecular quantum numbers, with selection rules governing the allowed changes to these numbers during an optical transition.

To a good approximation, the total wavefunction or excitation energy of the molecule may be expressed as the sum of its individual rotational, vibrational, and electronic excitations [151–153]. This is known as the Born-Oppenheimer approximation, and is most commonly used to express the total excitation energy of a molecule as the sum of its rotational, vibration, and electronic energies:

$$E = E_{\mathrm{el}} + E_{\mathrm{vib}} + E_{\mathrm{rot}} \quad (3.4)$$

where the subscripts 'el', 'vib', and 'rot' refer to electronic, vibrational, and rotational excitations of the molecule respectively [149,154]. This approximation also implies the existence of three types of optical spectra:

- *Rotational spectra* are transitions between different rotational levels in a given electronic and vibrational state. Only the rotational quantum number, J, changes in such transitions. This type of spectrum is usually in the microwave or far-infrared, consisting of a large number of densely-packed spectral features, and are observable with Raman spectroscopy [149,155,156].
- *Rotational-vibrational spectra* or *ro–vibrational spectra* are those consisting of transitions between rotational levels of one vibrational state to another set of rotational levels of another vibrational state in the same electronic level. The rotational, J, and

vibrational, v, quantum numbers change in a quantised manner following selection rules. These transitions are typically in the infrared (IR) spectral region, and form absorption 'bands' – spectra containing a structure of closely-spaced absorption lines. These bands may be examined with either IR or Raman spectroscopy [149,155,156].

- *Electronic spectra* are those consisting of transitions between the rotational and vibrational energy levels of one electronic state and the electronic and vibrational states of another electronic state. All three quantum numbers may change in such transitions, with this type of spectra normally occurring in the near-infrared, visible, or ultraviolet regions [149,155,156].

It is conventional in molecular spectroscopy to list the upper state before the lower state when referring to a particular transition [150,156]. The lower state is denoted by a double-prime superscript, e.g. J'' or v'', while the upper state is denoted by a single prime, e.g. J' or v' [149,156,157]. A transition or change between states is denoted by a Δ symbol [150,156,158], for example:

$$\Delta J = J' - J''. \tag{3.5}$$

Returning to our consideration of the types of transitions, the following conditions hold [152,155]:

$$\Delta E_{\mathrm{el}} \gg \Delta E_{\mathrm{vib}} \gg \Delta E_{\mathrm{rot}}. \tag{3.6}$$

In this thesis, the spectra presented are all results of ro–vibrational transitions in small (less than five-atom) linear polyatomic molecules, occurring in the near-infrared (NIR). The spectra of such molecules are often explained though selection rules derived from the rotating anharmonic oscillator model [155]. We will firstly consider the rotational component of this model.

3.2 Rotational Spectroscopy of Diatomic and Linear Polyatomic Molecules

The first and simplest approach to explaining rotational features of in spectra of linear polyatomics is the rigid rotor approximation or 'dumbbell' model of a diatomic molecule. As will be shown in the coming sections, this approximation cannot fully explain the observed features of such spectra. However, it remains a good starting point to understanding the more complicated systems.

3.2.1 Rigid Rotor Approximation

The rigid rotor approximation of a linear molecules, including diatomics and linear polyatomics, is the first step to understanding the rotational spectra of such molecules. The approximation assumes that the molecules are formed by rigid bonds connecting the nuclei

together, with the molecule in its entirety being free to rotate about its centre of mass [159]. In order to discuss the rotational motion and spectra of any molecule, the principal axes and moments of inertia must first be defined.

3.2.1.1 Principal Axes and Inertia

The moment of inertia I of any molecule about any axis through the molecule's centre of mass is given by

$$I = \sum_i m_i {r_i}^2 \tag{3.7}$$

where m_i and r_i are the mass and distance of atom i from the axis [153,156,160]. By convention one of these axes, labelled the c axis, will have the largest moment of inertia about it. A second axis, known as the a axis, is the axis about which the moment of inertia is minimum and is perpendicular to the c axis. The final axis with the label b is then perpendicular to the other two. These three axes together are known as the principal axes of inertia and correspond to the principal moments of inertia I_a, I_b, and I_c [150,153,156,159]. According to these definitions the general rule is then

$$I_c \geq I_b \geq I_a. \tag{3.8}$$

For a linear polyatomic molecule, this can be further refined to

$$I_c = I_b > I_a = 0 \tag{3.9}$$

by Eq. 3.7 since $r_i = 0$ for the a axis as can be seen for the case of hydrogen cyanide in Fig. 3.1 [153,159]. The inertia of molecules about their principal axes is then directly relatable to the rotational energy levels and transition frequencies.

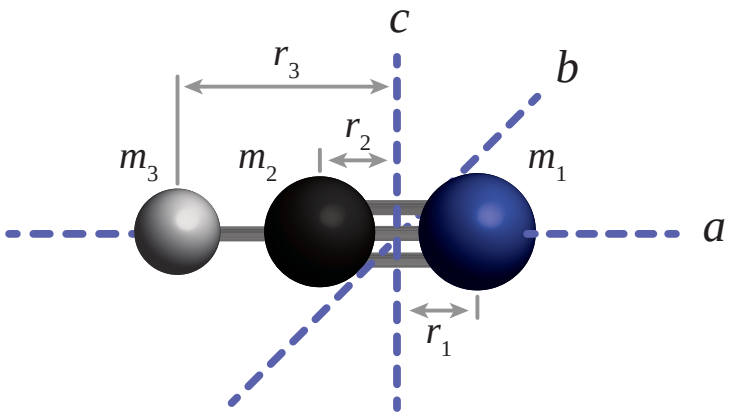

Figure 3.1: A molecule of hydrogen cyanide (HCN) showing its principal axes through the centre of mass. Hydrogen, carbon, and nitrogen atoms are light grey, dark grey, and dark blue respectively. As is true for all linear polyatomics, $I_a = 0$ as $r_i = 0$ [155].

3.2.1.2 Rotational Energy Levels

The solution of the Schrödinger equation for the rigid rotor model of a linear polyatomic gives quantised values for the rotational energy levels E_r of

$$E_r = \frac{h^2}{8\pi^2 I} J(J+1) \tag{3.10}$$

where $J = J'' = 0,1,2...$ is the rotational quantum number, and each energy level is $(2J+1)$-fold degenerate in the absence of an electric or magnetic field [159,161]. Note that as the moment of inertia of the molecule I is proportional to mass (Eq. 3.7), this indicates that the energy levels of a rigid rotor are further apart for a diatomic molecule compared to a higher-mass linear polyatomic. Additionally, different isotopologues - molecules that differ only in their isotopic composition - will have a slightly different mass and so slightly different energy levels, allowing differentiation between isotopologues [155,162]. However the wavenumbers or frequencies of rotational transitions are what is actually measured rather than the energy levels directly, and are represented by (rotational) *term values*, $F(J)$, given by

$$F(J) = \frac{E_r}{hc} = \frac{h}{8\pi^2 Ic} J(J+1) = BJ(J+1) \tag{3.11}$$

where

$$B = \frac{h}{(8\pi^2 Ic)} \qquad \left[\mathrm{cm}^{-1}\right] \tag{3.12}$$

is the *rotational constant* [153,155,157,158]. This representation of B has units of wavenumber $\left(\mathrm{cm}^{-1}\right)$, while if it is defined as $h/\left(8\pi^2 I\right)$, the units are of frequency (Hz) [157,159]. Unfortunately, the same symbol is used for two different quantities with different units, but this use is now widespread. This thesis will define the particular units of B on each occasion it is used.

3.2.1.3 Transition Intensities

The intensities of each line in the rotational spectrum depends on three factors: the degeneracy of each rotational energy level; the selection rules of each transition; and the thermal occupation probabilities of each rotational level [149,152,153,155,158,159,163]. In the absence of an external electric or magnetic field, each rotational level of quantum number J is $(2J+1)$-fold degenerate, and the statistical weight of the state corresponds to this value providing the degeneracy is not lifted [163]. Without delving too far into symmetries and time-dependent perturbation theory, the selection rules for infrared rotational transitions may be understood in the following ways:

- The molecule must posses a non-zero dipole moment, whether permanent or induced by molecular vibrations [120,153,155,161].
- Only rotational transitions with $\Delta J = \pm 1$ are allowed so that conservation of angular

momentum is obeyed. This is because one photon must carry one unit of angular momentum, and can therefore transfer one unit to a molecule in a single-photon transition. This selection rule is obeyed unless the photon momentum is transformed into another type of molecular momentum (cf. Section 3.4.2) [155,163,164].

As a side note, the first condition forbids homonuclear diatomics such as N_2 from possessing a pure rotational (or for that matter ro-vibrational) infrared spectrum [165]. This makes them excellent buffer gases for spectroscopic experiments in which an additional transparent gas is required for concentration adjustment purposes. More widely, it also forbids centrosymmetric linear polyatomic molecules such as carbon dioxide (CO_2) or acetylene (C_2H_2) from having purely rotational infrared spectra [155].

The thermal occupation of the initial state in a transition is the final factor in determining the intensities of each rotational line. The thermal occupation is described by the Boltzmann distribution at a temperature T [153,155,163]. At room temperature in thermal equilibrium many rotational states are occupied, with the occupation probability N_J of the rotational state with quantum number J given by

$$\frac{N_J}{N_0} = \frac{g_J}{g_0} e^{-(E_J - E_0)/kT} \tag{3.13}$$

$$= \underbrace{(2J+1)}_{\text{Degeneracy}} \underbrace{e^{-BhcJ(J+1)/kT}}_{\text{Thermal}} \tag{3.14}$$

where $g_J = (2J+1)$ is the degeneracy of the J^{th} level for a non-symmetric linear molecule [149,152,153,155,158,161]. The two bracketed terms are opposing factors - the degeneracy term increasing with increasing J while the thermal term decreases rapidly. This means the N_J/N_0 increases at low values of J until the exponential thermal factor becomes more dominant at high J values and N_J/N_0 approaches zero [159,163]. A theoretical maximum intensity occurs at $J = J_{\max}$ which corresponds to

$$\frac{\mathrm{d}\left(N_J/N_0\right)}{\mathrm{d}J} = 0 \tag{3.15}$$

which yields

$$J_{\max} = \left(\frac{k_B T}{2hB}\right)^{\frac{1}{2}} - \frac{1}{2} \tag{3.16}$$

when B has units of frequency [155,157,162]. However, the $J_{\max}$ predicted by Eq. 3.16 produces incorrect results for the maximum intensity value for J when compared to experimental results, due to effects so far neglected in the rigid rotor approximation [155].

3.2.1.4 Transition Frequencies or Wavenumbers

The transition wavenumbers are given by considering the difference in term values for $\Delta J = \pm 1$ [157,158]:

$$\widetilde{\nu} \text{ (or } f) = F(J+1) - F(J) = 2B(J+1). \tag{3.17}$$

Equation 3.17 indicates that the spacing of the rotational transitions should be constant and equal to $2B$ with increasing J values as seen in Fig. 3.2 [161]. However, the spacing of

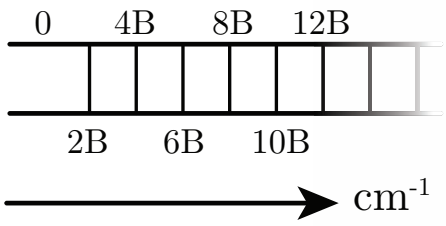

Figure 3.2: The equidistant $2B$ spacing of rotational energy levels as predicted by the rigid rotor approximation and Eq. 3.17.

rotational lines (and rotational energy levels) observed in experimental data is not constant, again due to additional effects that are neglected in the rigid rotor approximation [155].

3.2.2 Centrifugal Distortion and the Nonrigid Rotor

Experimentally it is observed that the line spacings decrease with increasing values of J. As the molecule rotates, particularly as J increases, centrifugal forces tend to throw the constituent atoms outwards from the centre of mass [160,166]. A more accurate representation of the rotating molecule is that of a nonrigid rotor, in which the solid bonds between atoms are instead represented by springs connecting the nuclei. As the nuclei are thrown outward by the centrifugal forces, the 'springs' stretch, the bond lengths r_i in Eq. 3.7 increase, and B decreases (Eq. 3.12). The effects of the centrifugal forces may be included in the term values by addition of the *centrifugal distortion constant*, D [157,159]:

$$F(J) = BJ(J+1) - DJ^2(J+1)^2 . \tag{3.18}$$

The transition wavenumbers or frequencies are also modified from Eq. 3.17 to

$$\widetilde{\nu} \text{ (or } f) = F(J+1) - F(J) \tag{3.19}$$

$$= 2B(J+1) - 4D(J+1)^3 . \tag{3.20}$$

The value of D is dependent upon the stiffness of the spring/bond. The effects of the centrifugal distortion on the spacing of the rotational energy levels is summarised in Fig. 3.3.

As previously mentioned in discussion about the intensities of rotational transitions, molecules that do not posses a dipole moment - such as centrosymmetric carbon dioxide and acetylene - are forbidden from having purely rotational spectra in the infrared. Yet these molecules do display infrared spectra with rotational features. This is because a temporary dipole moment may be induced by *molecular vibrations* [155,166].

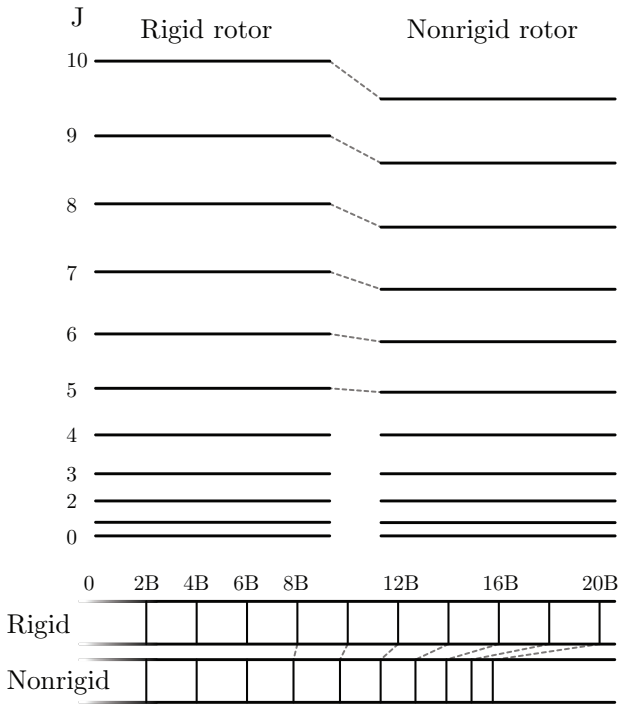

Figure 3.3: Comparison diagram of the spacing of rotational energy levels between the rigid and nonrigid rotor approximations, as reproduced from Ref. [155]. Unlike the equidistant $2B$ spacing predicted by the rigid rotor approximation, energy levels for the nonrigid rotor show a shift towards lower energies (and closer lines) with the amount of shift increasing with increasing J [155].

3.3 Vibrational Spectroscopy of Diatomic and Linear Polyatomic Molecules

In contrast to individual atoms, molecules posses an additional degree of freedom - the excitation of vibrational states about their equilibrium positions. The complicated nature of molecular vibrations is most easily understood by first considering the case of a diatomic molecule, which produces results that also apply to linear polyatomics as considered in this thesis. The simplest of model of a diatomic is that of the *harmonic oscillator*.

3.3.1 The Harmonic Oscillator Approximation

A good first approximation to aid in the understanding of the vibrations of molecules is the one-dimensional harmonic oscillator, or 'ball and spring' model, in which the two nuclei, separated by their equilibrium bond length r_e are joined by a spring representing the bond between them, as seen in Fig. 3.4 [148,149,167].

The spring freely stretches and contracts, and for small displacements of the bond, the spring obeys Hooke's Law:

$$F = \frac{-\mathrm{d}V(x)}{\mathrm{d}x} = -kx \tag{3.21}$$

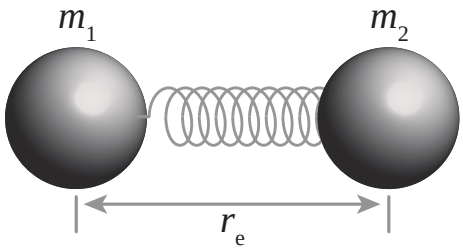

Figure 3.4: The 'ball and spring' model of a diatomic harmonic oscillator, in which the two nuclei of masses m_1 and m_2 are separated by a spring equal to the equilibrium bond length r_e [148,149,164,167].

where $x = r - r_e$ is the displacement from the equilibrium bond length, r is the bond length, $V(x)$ is the potential energy at x, and k is the spring constant, with the magnitude of k proportional to the bond strength [148,149,153,155,167]. Integration of Eq. 3.21 gives the potential energy curve of the oscillator:

$$V(x) = \frac{1}{2}kx^2 \tag{3.22}$$

which is evidently parabolic in nature [148,149,155,167]. This potential can be used in combination with the time-independent Schrödinger equation to find the quantised vibrational energy levels of the harmonic oscillator [149]. Firstly, the quantum mechanical Hamiltonian $\hat{H}$ for a one-dimensional harmonic oscillator is given by

$$\hat{H} = -\frac{\hbar}{2\mu}\frac{\mathrm{d}^2}{\mathrm{d}x^2} + \frac{1}{2}kx^2 \tag{3.23}$$

where μ is the reduced mass of the system of two masses m_1 and m_2 and

$$\mu = \frac{m_1 m_2}{m_1 + m_2}. \tag{3.24}$$

Note that by Eq. 3.23 and 3.24, different isotopologues will produce slightly differing final spectra owing to their slightly differing masses [148,149,167]. Substituting $\hat{H}$ into the one-dimensional time-independent Schrödinger equation - also known as the 'wave equation'

$$\hat{H}\psi(x) = E\psi(x) \tag{3.25}$$

gives

$$-\frac{\hbar}{2\mu}\frac{\mathrm{d}^2\psi_v(x)}{\mathrm{d}x^2} + V(x)\,\psi_v(x) = E_v\psi_v(x) \tag{3.26}$$

which when combined with Eq. 3.22 and rearranged, becomes:

$$\frac{\mathrm{d}^2\psi_v(x)}{\mathrm{d}x^2} + \left(\frac{2\mu E_v}{\hbar^2} - \frac{\mu k}{\hbar^2}\right)\psi_v(x) = 0 \tag{3.27}$$

in which E_v are the quantised vibrational energy levels, and $\psi_v(x)$ are the vibrational wavefunctions of the harmonic oscillator [148,153,168]. The energy eigenvalues of this equation,

and hence the (quantised) energy levels of the harmonic oscillator, are found to be

$$E_v = hf\left(v + \frac{1}{2}\right) \tag{3.28}$$

in which $v = 0, 1, 2, 3...$ is the vibrational quantum number and f is the classical oscillator frequency:

$$f = \frac{1}{2\pi}\sqrt{\frac{k}{\mu}}. \tag{3.29}$$

Equation 3.28 may also be written in terms of wavenumber as

$$E_v = hc\widetilde{\nu}\left(v + \frac{1}{2}\right) \tag{3.30}$$

or angular frequency:

$$E_v = \hbar\omega\left(v + \frac{1}{2}\right) \tag{3.31}$$

where ω is related to the classical oscillator frequency f through [148,153,155,164]

$$\omega = 2\pi f = \sqrt{\frac{k}{\mu}}. \tag{3.32}$$

Equation 3.28 predicts an even spacing of the allowed vibrational energy levels [149,153]. Another interesting feature of this equation is that it predicts a non-zero energy for $v = 0$, which is known as the *zero-point energy* [149,155,164,167]. This zero-point energy is the minimum energy a molecule may possess - even at absolute zero of temperature, and is a consequence of the Heisenberg uncertainty principle [148,169] .

3.3.1.1 Wavefunctions of the Harmonic Oscillator Approximation

The wavefunctions in Eq. 3.27 take the form of increasing orders of Hermite polynomials, $H_v(z)$ (where in this formalism we have performed the coordinate transformation of $z = \sqrt{\alpha}x$), multiplied by a Gaussian factor $e^{-\frac{\alpha x^2}{2}}$, and the normalisation constant $\left(\frac{\alpha}{\pi}\right)^{\frac{1}{4}}$ [153,164,167]:

$$\psi_n(x) = \left(\frac{\alpha}{\pi}\right)^{\frac{1}{4}} H_n\left(\sqrt{\alpha}x\right) e^{-\frac{\alpha x^2}{2}}. \tag{3.33}$$

The Hermite polynomials up to $v = 4$ are given in Table. 3.1, and may be computed with the recursion relation [170]:

$$zH_m(z) = mH_{m-1}(z) + \frac{1}{2}H_{m+1}(z). \tag{3.34}$$

It is important to note for future discussion of the vibrational transition selection rules for the harmonic oscillator (Appendix A) that the Hermite polynomials form an orthonormal

$H_v(z)$
$H_0(z) = 1$
$H_1(z) = 2z$
$H_2(z) = 4z^2 - 2$
$H_3(z) = 8z^3 - 12z$
$H_4(z) = 16z^4 - 48z^2 + 12$

Table 3.1: The first five Hermite polynomials, where $z = \sqrt{\alpha}x$. Hermite polynomials form the solutions, when multiplied by a Gaussian term, for the allowed wavefunctions $\psi_v(x)$ in the differential equation (Eq. 3.27) for the quantum harmonic oscillator [157,164,167].

vector space. That is:

$$\int_{-\infty}^{\infty} \psi_i(x)\,\psi_j(x) = \delta_{ij} = \begin{cases} 1, & \text{if } i = j \\ 0, & \text{if } i \neq j \end{cases} \tag{3.35}$$

and δ_{ij} is the Kronecker delta [166,170,171]. The harmonic oscillator potential with its quantised energy levels, wavefunctions $\psi_v(x)$, and occupation probabilities $|\psi_v(x)|^2$ of each state up to $v = 3$ may be seen in Fig. 3.5.

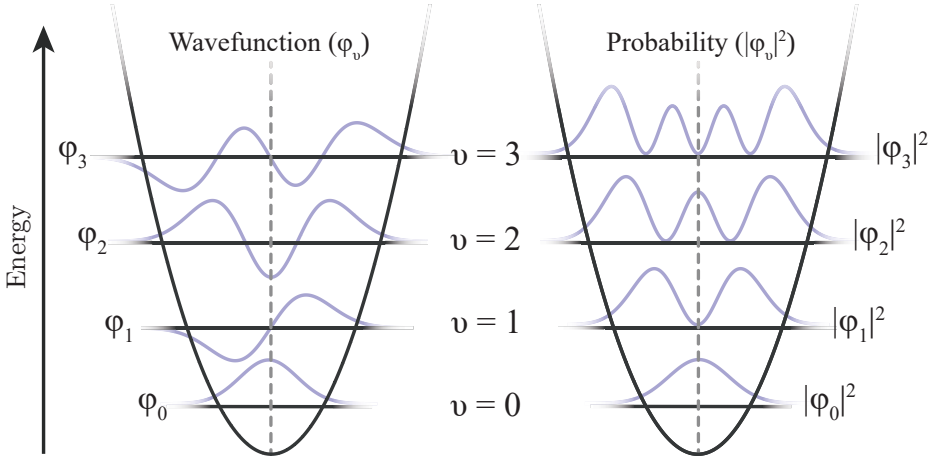

Figure 3.5: The first four wavefunctions $\psi_v(x)$ (left) that are the solutions to (Eq. 3.27) and quantised vibrational energy levels in the harmonic oscillator approximation. The dashed grey line shows the equilibrium position of the harmonic oscillator. The occupation probability ($|\psi_v(x)|^2$) for each vibrational state is seen on the right [153,155,157,164].

3.3.1.2 Harmonic Oscillator Term Values

Just as in the discussion of rotational spectroscopy, division of Eq. 3.28 by hc yields the vibrational term values, $G(v)$, in units of cm^{-1}:

$$G(v) = \frac{E_v}{hc} = \omega_e \left(v + \frac{1}{2}\right) \tag{3.36}$$

and ω_e is then known as the harmonic vibrational constant, and is equal to the harmonic vibrational wavenumber $\widetilde{\nu}$ [153,155].

3.3.1.3 Harmonic Oscillator Approximation Vibrational Selection Rules

In order for a vibrational transition between an initial vibrational state ψ_m and final vibrational state ψ_n to be allowed for a single photon transition, there must be an associated change to the molecule's dipole moment [120,153,160]. Whether or not this is the case for a particular vibrational transition may be found by evaluation of the dipole transition moment $\langle \boldsymbol{\mu} \rangle_{nm}$:

$$\langle \boldsymbol{\mu} \rangle_{nm} = \int \psi_n^* \mu \psi_m d\tau = \langle \psi_n | \mu | \psi_m \rangle \neq 0. \tag{3.37}$$

in which μ is the dipole operator and Eq. A.1 is evaluated over all space (τ) [148]. The asterisk implies complex conjugation. To be an allowed transition Eq. 3.37 must be non-zero [120,153,160]. Consideration of the dipole transition moment for transitions between two vibrational states described by the wavefunctions introduced in Subsection 3.3.1.1 gives rise to the selection rule for vibrational transitions of

$$\Delta v = \pm 1. \tag{3.38}$$

For a full derivation of the vibrational selection rule for the harmonic oscillator approximation, see Appendix A [155,167,171]. Equation 3.38 indicates that vibrational transitions in the harmonic oscillator approximation are only allowed if the vibrational quantum number changes by one unit, i.e. adjacent vibrational energy levels. However, molecular spectra in which this rule is broken are routinely observed in experiment due to anharmonicity of the molecular oscillator [120,133,172].

3.3.2 The Anharmonic Oscillator

Certain aspects of measured molecular spectra cannot be explained by application of the harmonic oscillator approximation to the potential. Namely, the presence of higher harmonic vibrational transitions and the non-equal spacing of the observed vibrational energy levels. These effects may only be explained when the anharmonicity of the true potential energy curve is taken into account [173]. The harmonic oscillator approximation is actually the result of truncation of a Taylor expansion around $x = r - r_e$ of $V(x)$:

$$V(x) = V(0) + x\left(\frac{\mathrm{d}V}{\mathrm{d}x}\right)\Bigg|_{x=0} + \frac{1}{2}x^2\left(\frac{\mathrm{d}^2V}{\mathrm{d}x^2}\right)\Bigg|_{x=0} + \ldots \tag{3.39}$$

where we have made the assumption that x is small so that the second term goes to zero, and the first term is an arbitrary constant taken to be zero [166,174,175]. In the harmonic approximation, we then truncate the Taylor series at cubic terms and above, leaving the third

term to be written in the familiar form of the harmonic oscillator potential:

$$\frac{1}{2}x^2\left(\frac{\mathrm{d}^2V}{\mathrm{d}x^2}\right)\Bigg|_{x=0} = \frac{1}{2}kx^2. \tag{3.40}$$

However for larger displacements - and higher vibrational excitations - the higher-order terms of the potential have an increasing importance, and introduce anharmonicity into the system [148]. A more physical and better approximation is the *Morse potential*:

$$V(x) = hcD_e\left(1 - e^{-ax}\right)^2 \tag{3.41}$$

where

$$a = \left(\frac{k}{2hcD_e}\right)^{\frac{1}{2}}, \tag{3.42}$$

$x = r - r_e$, D_e is the equilibrium dissociation energy, also known as the depth of the molecule's potential well, at $r = r_e$, and $V(x) \to 0$ as $r_e \to \infty$ [155,166,176,177]. The true energy required for dissociation, D_0, is equal to D_e with the anharmonic oscillator zero-point energy subtracted [149,166]. A comparison between the harmonic oscillator and Morse potentials is seen in Fig. 3.6. The Morse potential predicts energy levels that become less widely spaced

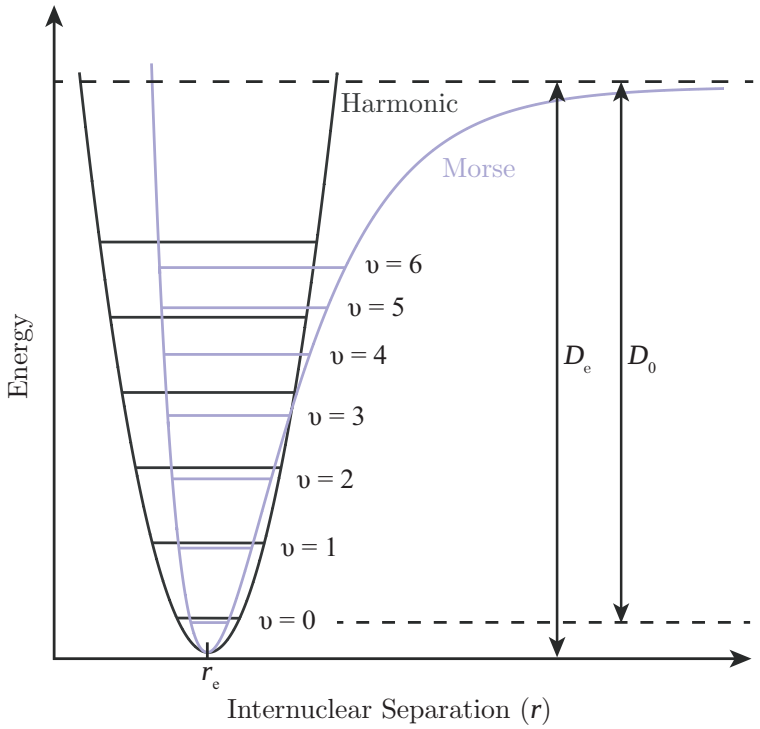

Figure 3.6: The harmonic oscillator potential (dark grey) and the Morse potential (light purple). In contrast to the evenly-spaced energy levels of the harmonic oscillator, the energy level spacing decreases with increasing excitation in the case of the Morse potential [149,157].

as the level of vibrational excitation increases. This is shown by solving the Schrödinger

equation analytically using perturbation theory, giving energy levels of:

$$E_v = \left(v + \frac{1}{2}\right)\hbar\omega_e - \left(v + \frac{1}{2}\right)^2 \hbar\omega_e\chi_e + ... \tag{3.43}$$

in which χ_e is the unitless first anharmonic vibrational constant:

$$\chi_e \approx \frac{\hbar\omega_e}{4D_e} \tag{3.44}$$

which is always positive and may also be seen as $\omega_e\chi_e$ in units of cm^{-1} [149,155,166]. We can also then define D_e with the introduction of χ_e:

$$D_e \approx D_0 + \frac{1}{2}\hbar\omega_e + \frac{1}{4}\hbar\omega_e\chi_e. \tag{3.45}$$

The quadratic term in Eq. 3.43 acts to lower the energy levels compared to the harmonic oscillator, with the levels getting more closely spaced as v increases as seen in Fig. 3.6 [157]. Division of Eq. 3.43 by hc yields the vibrational term values, $G(v)$, with anharmonicity included in units of cm^{-1} [157]:

$$G(v) = \omega_e\left(v + \frac{1}{2}\right) - \omega_e\chi_e\left(v + \frac{1}{2}\right)^2 + ... \tag{3.46}$$

Additionally to perturbing the energy levels, the anharmonicity affects the selection rules for vibrational transitions. This is because the wavefunctions of the anharmonic oscillator are no longer symmetric or antisymmetric with respect to the equilibrium position r_e [148]. The selection rule is modified to allow higher harmonics:

$$\Delta v = \pm 1, \pm 2, \pm 3... \tag{3.47}$$

where those transitions with $\Delta v = \pm 2, \pm 3, ...$ are called 'overtone' transitions, and occur with increasingly weaker intensities as Δv increases [149,155,157]. Those transitions with $\Delta v = \pm 1$ are termed 'fundamental' transitions are and the strongest in intensity [149]. Transitions to a higher vibrational state originating from states other than the ground state are termed *hotbands*, as the probability of a non-ground vibrational state having appreciable population - and therefore the strength of the hotband originating from that state - is related to the temperature of the system [148,149,157]. These three types of vibrational transitions are summarised in Fig. 3.7. The theory of both rotational and vibrational transitions for diatomic molecules introduced so far in the course of this thesis may also be applied to the case of simple linear polyatomics, and extended more generally into three dimensions [149,155]. However, in contrast to diatomics wherein there is only one possible mode of vibration, linear polyatomic molecules have additional bonds as the number of atoms increase, and will therefore have a number of new possible vibrations which must be classified for broader discussion.

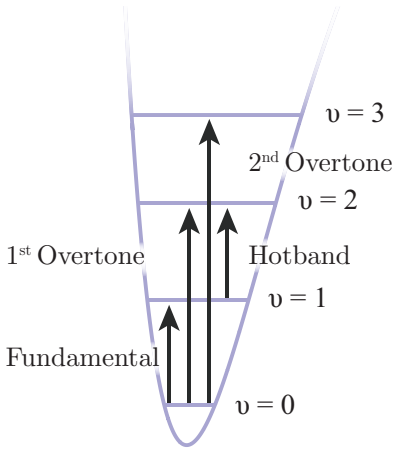

Figure 3.7: The types of vibrational transitions observed within this thesis and their names [157].

3.3.3 Vibrational Transition Naming Conventions

In order to describe the vibrational motions of larger molecules, we will define the *normal modes* of vibration. These normal modes are vibrations of the total molecule that can be considered to be orthogonal - that is, any of the normal modes of vibration may be excited without causing excitation to any of the other normal modes provided the level of excitation is not so great as to introduce nonlinearities [148,166]. The i^{th} normal mode of vibration of a molecule is denoted v_i [156]. Depending on the composition and shape of the (linear) molecule, two types of vibration may occur: *bending* vibrations in which the bond angles between the atoms comprising the molecule change, and *stretching* vibrations, in which the bond angles do not change, but rather stretch as the atoms move along a line joining their nuclei [148,149,153,155,162].

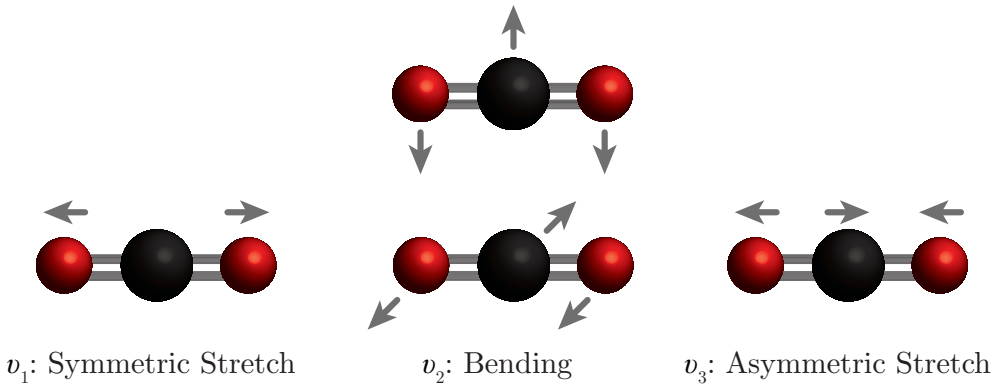

Figure 3.8: The normal modes of vibration of CO_2 [149,153,155,162]. Oxygen atoms are red, carbon atoms are dark grey. The bending mode is doubly degenerate and may occur in the plane of the page or perpendicular to it.

In a system of N uncoupled point masses, the number of normal modes (also known as the *degrees of freedom* of the system), f_N, is simply given by $3N$ [148,160]. If the masses are coupled however, as they are in a molecule, then there are 3 translational degrees of freedom

(in which the centre of mass of the whole molecule moves) together with three degrees of freedom for rotations. It is important to note that there are only two degrees of freedom for a linear molecule, as rotation about the cylinder axis is not counted [151,178]. Therefore the number of normal modes of vibration for a molecule is $f_N = 3N - 6$, or $f_N = 3N - 5$ in the case of a linear molecule [148,155,160].

Consider the CO_2 molecule in which $N = 3$. As this is a linear molecule, we expect to describe the molecular motion by the superposition of $f_N = 9\text{-}5 = 4$ normal modes of vibration. Note that in this particular case that the bending mode is doubly degenerate (two modes with the same energy) as the bending motion may occur within the plane of the molecule or perpendicular to it [149]. The remaining two modes are the *symmetric stretch* and *antisymmetric stretch* [149,162]. The normal modes of vibration of CO_2 are summarised in Fig. 3.8.

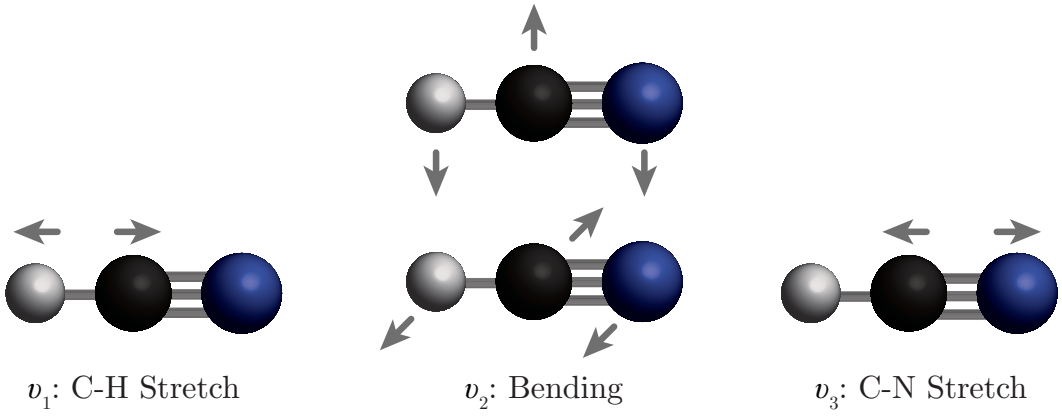

Figure 3.9: The normal modes of vibration of HCN [153]. Hydrogen atoms are light grey, carbon atoms are dark grey, and nitrogen atoms in blue. The bending mode is doubly degenerate and may occur in the plane of the page or perpendicular to it.

The naming conventions of the vibrational modes of a molecule are unfortunately rather species-dependent, and relate to the molecule's structure (linear, trigonal planar, tetrahedral etc.), whether the molecule possesses a centre of symmetry, effects of Fermi resonance, and the symmetry of the vibration [150,156,179–181]. In some cases, such as for HCN, it does not make physical sense to describe the stretching motions along the internuclear axis as symmetric or antisymmetric as was the case for CO_2 where there is a centre of symmetry. In this case the convention is to denote the motion as a stretching vibration whilst also describing the particular atoms involved. For example, υ_1 of HCN corresponds to the C-H stretch, while it corresponds to the symmetric stretching mode in CO_2. The naming conventions for the molecules seen in this thesis are summarised in Fig. 3.9 and Fig. 3.10 for HCN and C_2H_2 respectively.

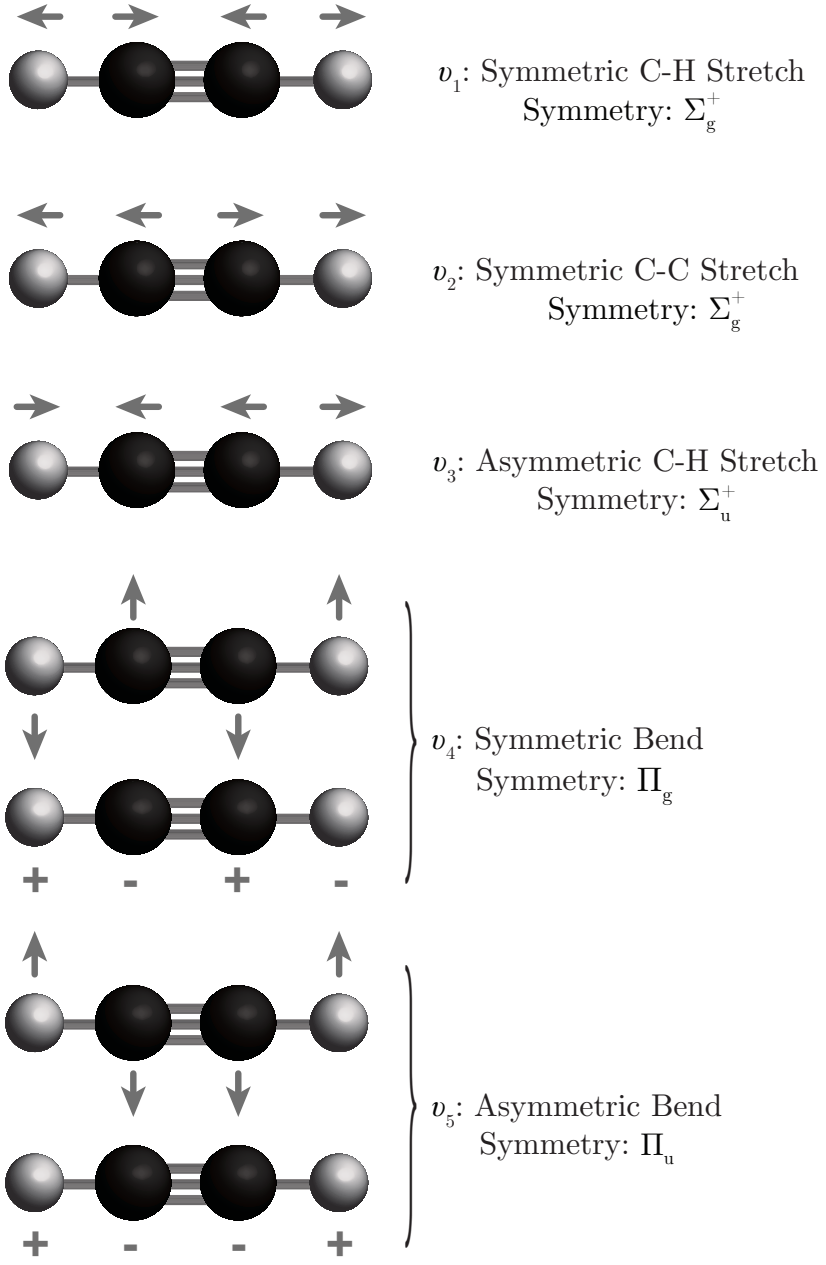

Figure 3.10: The normal modes of vibration of C_2H_2 [149,153]. Hydrogen atoms are light grey, carbon atoms are dark grey. Both the symmetric and asymmetric bending mode are doubly degenerate and may occur in the plane of the page or perpendicular to it. Also shown are the symmetries of each normal mode of vibration - explained further in Section 3.5.1 - which gives rise to the symmetric (subscript g) or antisymmetric (subscript u) vibration classification (cf. Appendix B).

The HITRAN database used in this thesis has its own nomenclature for naming vibrational transitions, though their normal mode labelling follows the conventions laid out in Fig. 3.8, 3.9, and 3.10. HITRAN separates molecules into classes based on their structure and some cases, such as CO_2, by the effects of Fermi resonance (see Section 3.4.2.2). The labelling conventions of HITRAN for each of these classes are summarised in Table 3.2.

HITRAN Molecular Class Definitions	Upper/Lower State Global Quanta
Class 4: Linear triatomic (HCN)	$v_1 v_2 \ell_2 v_3$
Class 5: Linear triatomic with large Fermi resonance (CO_2)	$v_1 v_2 \ell_2 v_3 r$
Class 7: Linear tetratomic (C_2H_2)	$v_1 v_2 v_3 v_4 v_5 \ell \pm r$

Table 3.2: A summary of the HITRAN class definitions of the molecules mentioned in this thesis, and their associated state-labelling conventions. v_i is the vibrational quantum number of a molecule associated with the normal mode of vibration i, where $i = 1, 2, 3...$ and specific mode labelling and range of i values is molecular species-dependent. ℓ_i is the vibrational angular momentum quantum number associated with the degenerate bending mode v_i. ℓ is the absolute value of the sum of the vibrational angular momentum quantum numbers ℓ_i. r is the ranking index for vibrational states that are members of a Fermi resonance polyad. $r = 1$ for the highest-energy vibrational state involved, with decreasing rank (2,3,4...) as the energy values decrease. $\pm$ is the symmetry type for Σ vibrational states ($\ell = 0$) as explained in Appendix B [150,156,179–181].

For example, a member of a CO_2 Fermi tetrad is examined closely in Chapter 10, in which the transition is denoted in HITRAN notation as $30012 \leftarrow 00001$, which corresponds to a transition from the vibrational ground state of CO_2 (in which $r = 1$ as it is not a member of a Fermi polyad) to the $3v_1 + v_3$ excited vibrational state and the second-highest energy member of the associated Fermi tetrad. Note that transitions are denoted with the excited state first followed by the ground or initial state, with the direction of the arrow indicating the direction of the transition (emission to the right, absorption to the left) [156,182].

As mentioned previously in Section 3.2, molecular vibrations may induce temporary dipole moments, allowing rotational transitions to occur. This indicates that both rotational and vibrational excitations should not be looked at in isolation, but instead together in *rotational-vibrational* or *ro-vibrational* spectroscopy.

3.4 Rotational-Vibrational Spectroscopy

Spectra arising from transitions involving both a change in rotational and vibrational state of a molecule are called *rotational-vibrational* or *ro-vibrational* spectra [183]. This type of spectroscopy allows observation of rotational characteristics in molecules that do not posses permanent dipole moments such as CO_2 in which pure rotational spectra are forbidden. A vibrational transition may induce a temporary dipole moment, allowing a coupled rotational-vibrational transition to occur even in these molecules [120,153,155]. As the separation between rotational energy levels is small in comparison to both the thermal population distribution and to the vibrational energy levels, the vibrational ground state is often the most populous at room temperature with a number of rotational levels filled [155]. This produces a stack of rotational energy levels associated with each vibrational state, and of vibrational transitions being accompanied by rotational ones.

The result is a spectrum showing a vibrational transition with fine structure from the accompanying rotational transitions which is collectively called a *band*. The rotational transitions are arranged into 'branches' classified depending on the change in rotational quantum number [162]. Ro-vibrational transitions with $\Delta J = -1$ occur to the lower-wavenumber side of the band centre are termed the P-branch [151,153,166]. Those transitions with $\Delta J = +1$ form the R-branch are to the higher wavenumber side of the band centre, while $\Delta J = 0$ transitions are known as the Q branch clustered around the band centre [153,162,163]. Note that the same rotational and vibrational selection rules so far derived are still applicable to ro-vibrational spectra, and so the Q-branch is not always observed. Additionally, individual lines in a band are defined by their branch and lower-state J value as P(1), R(1) etc [163]. Recalling that the lower state in a transition is indicated by a double prime superscript and the upper by a single prime, an example transition diagram showing these conventions omitting the Q-branch may be seen in Fig. 3.11.

The term values of ro-vibrational spectra are given by addition of the term values for the rotational and vibrational cases previously derived [157]:

$$S(v, J) = G(v) + F(J). \tag{3.48}$$

Some modification is required however, owing to the fact that the rotations and vibrations of a molecule are not completely separable, but are instead coupled together [148].

3.4.1 Rotational-Vibrational Coupling

Along with centrifugal distortion as discussed in Section 3.2.2, there is another effect that modifies the spacing of the rotational lines in a ro-vibrational spectrum. It can be seen in Fig. 3.11 that the R-branch lines get closer together as J increases, while the spacing increases with J for the P-branch. This is due to *rotational-vibrational coupling*, and demonstrates the breakdown of the Born-Oppenheimer approximation. Essentially, as the molecule vibrates, the lengths of the bonds comprising the molecule change. Recalling Eq. 3.7, the moment of inertia I is dependent on the length of this bond. By definition (Eq. 3.12), the rotational constant B is inversely proportional to the inertia. This means that B is coupled to any molecular vibrations, leading to rotational-vibrational coupling of the ro-vibrational lines [148,166]. This is accounted for by modification of the definition of B to become:

$$B_v = B_e - \alpha_e \left(v + \frac{1}{2}\right) + ... \tag{3.49}$$

in which α_e is the vibration-rotation coupling constant and B_e is the rotational constant for a rigid rotor [153,155,157]. Note that this changes slightly if the vibration involved is degenerate to include a degeneracy factor that is unity for non-degenerate transitions [153].

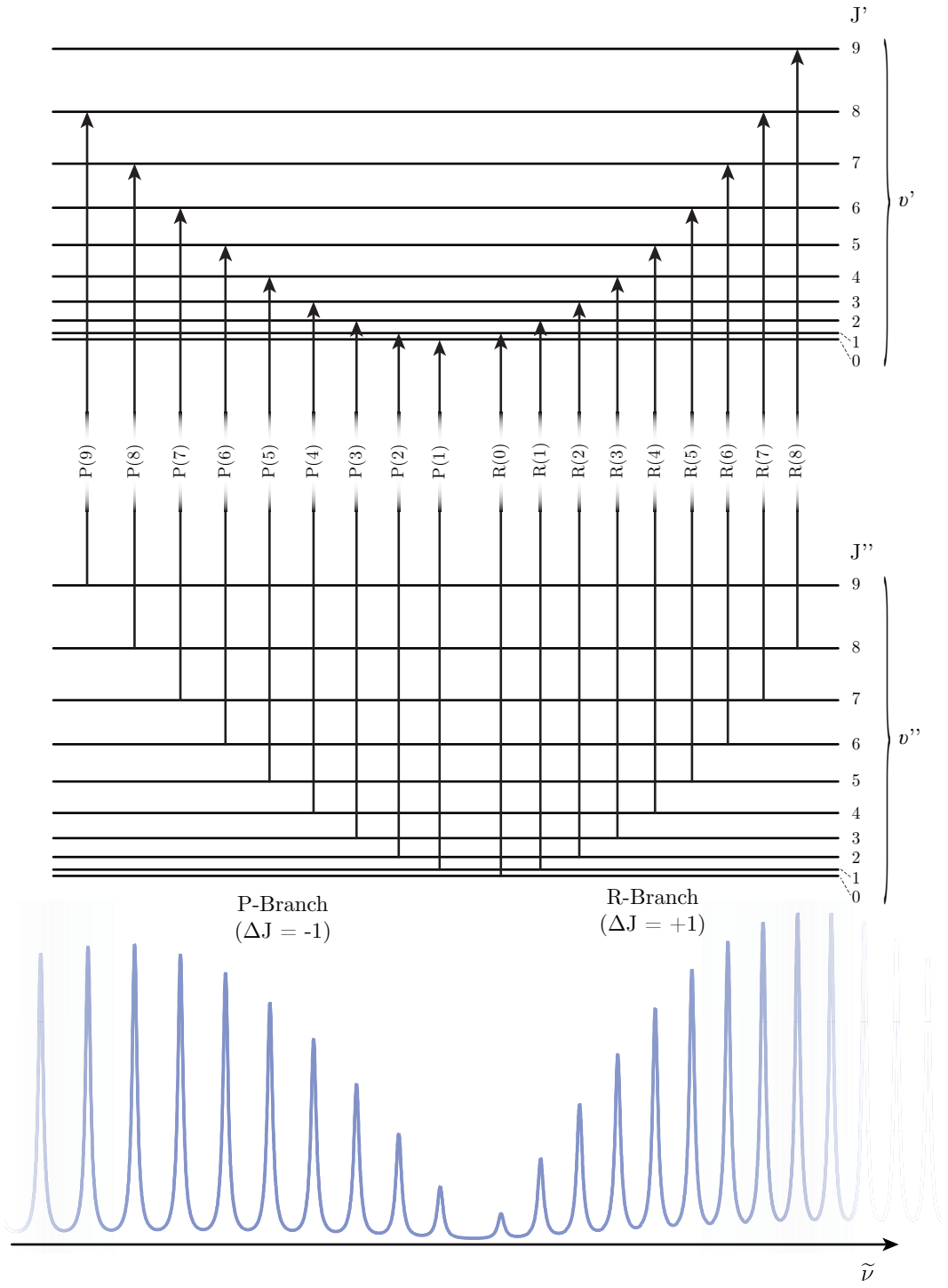

Figure 3.11: A portion of an example ro-vibrational energy level schematic for a simple linear molecule showing the peak labelling conventions (top) and the observed ro-vibrational spectrum (bottom). Energy is increasing with increasing J. Recalling that the double prime indicates the lower energy state of the transition, and a single prime for the upper state. The R-branch contains transitions in which $\Delta J = +1$, while the P-branch contains transitions in which $\Delta J = -1$. Some molecules may additionally posses a Q-branch, in which $\Delta J = 0$, falling between the P and R branches in the spectrum. By convention, the lower state J value is used for a transition's P, Q, or R branch numerical designation [155].

The centrifugal distortion constant D is also affected by the coupling, and is redefined as

$$D_v = D_e + \beta_e \left(v + \frac{1}{2}\right) + ... \tag{3.50}$$

where β_e is the centrifugal distortion vibrational coupling constant, and D_e is the centrifugal distortion constant at the equilibrium state of the molecule on the potential energy curve [151,155,157]. This means the final rotational-vibrational term values are given by [155]:

$$\begin{aligned} S(v,J) &= G(v) + F(J) && (3.51)\\ &= \omega_e \left(v + \frac{1}{2}\right) - \omega_e \chi_e \left(v + \frac{1}{2}\right)^2 + ... + B_v J(J+1) - D_v J^2 (J+1)^2 . && (3.52) \end{aligned}$$

3.4.2 Types of Bands

To understand which ro-vibrational bands are allowed for a particular molecular species, and indeed the variation in the structure of such bands, the symmetry of each vibrational mode must be considered. The symmetries of a particular vibrational state is summarised in a molecule's *molecular term symbol*. For homonuclear diatomics and linear molecules with an inversion centre (known as belonging to symmetry point group $D_{\infty h}$), the molecular term symbol is of the form:

$$^{(2S+1)}\Lambda^{(+/-)}_{\Omega,(g/u)} \tag{3.53}$$

where S is the nuclear spin of the molecule; Λ is the projection of the orbital angular momentum along the internuclear axis and may take values of $0, 1, 2, 3...$ which are represented by their corresponding symbols $\Sigma, \Pi, \Delta, \Phi...$; Ω is the projection of the total angular momentum along the internuclear axis; g/u, $+/-$ are types of symmetry/parity of the molecule (See Appendix B) [156,159,166,184]. If there is no centre of inversion of the molecule, such as in the symmetry point group $C_{\infty h}$ (linear molecules), the g/u subscript is dropped [165].

There is an additional classification of bands related to the vibrational angular momentum quantum number ℓ, and whether ℓ is changed in the transition. If $\Delta\ell = 0$, the band is a *parallel* band, while if $\Delta\ell = \pm 1$, it is a *perpendicular* band [171,185]. The vibrational energy states in which $\ell = 0, 1, 2, 3, ...$ are classified as species or term symbols as being of type Σ, Π, Δ, Φ,... respectively [166,184]. The selection rules for vibrational transitions are derivable by calculation of the transition dipole moment integral (see Appendix A.1), but may be summarised as $\Delta\ell = 0, \pm 1$, $g \leftrightarrow u$, and $\Sigma^+ \nleftrightarrow \Sigma^-$ (see Appendix B) [153,166]. The three types of bands for a linear polyatomic are:

1. $\Delta\ell = 0$ with $\ell = 0$. This is termed a *parallel* transition of $\Sigma^+ - \Sigma^+$ type. This type of transition produces parallel bands with both P and R branches ($\Delta J = \pm 1$) [153,157].

2. $\Delta\ell = \pm 1$. This is termed a *perpendicular* transition, such as $\Pi - \Sigma$, $\Delta - \Pi$ etc. This type of transition produces perpendicular bands with both P and R branches ($\Delta J = \pm 1$), along with a strong Q branch ($\Delta J = 0$) [153,157].

3. $\Delta\ell = 0$ with $\ell \neq 0$. This includes transitions of the type $\Pi - \Pi$, $\Delta - \Delta$ etc. These bands posses both P and R branches ($\Delta J = \pm 1$), along with a weak Q branch ($\Delta J = 0$). These bands are also known as *parallel* bands [153,157].

Additionally, only rotational transitions for which of $\Delta J = 0, \pm 1$, $s \nleftrightarrow a$, and $+ \nleftrightarrow -$ are allowed [153,157]. There are also cases in which a particular vibrational transition is forbidden for symmetry reasons. In such cases, a *combination* band or the effects of *Fermi resonance* may be observed.

3.4.2.1 Combination Bands

A combination band is observed when two or more of the normal modes of vibration are excited simultaneously, combining to form a single vibrational transition [148,149,153]. There are two types of combination bands depending on how the vibrations combine. The first type is a *sum* band, such as the $3v_1 + v_3$ excited vibrational state of CO_2, in which the excited state occurs at a frequency of approximately the sum of the $3v_1$ overtone and v_3 fundamental levels [186]. The other type of combination band is the *difference* band, where as the name suggest the band centre will occur at approximately the difference between the two vibrations involved [148,186]. The transition moment integral may again be used to determine whether a combination band may occur, using the appropriate excited state vibrational wavefunction that sums (or subtracts) the involved vibrations. Another method is to consider the direct products of the irriducible representations of the involved vibrations, which will not be explored in this thesis [171].

3.4.2.2 Fermi Resonance

Another way in which typically forbidden vibrational transitions may be observed is through the effects of Fermi resonance. If a molecule contains vibrational states that are accidentally degenerate or nearly degenerate (of very similar energy) and possessing the same symmetry, the states may mix, share population, and perturb the positions of the energy levels by forcing them apart [148,149,152,153,162]. These interacting states are then known as members of a Fermi polyad. As the states are mixed, they cannot be assigned to any of the original states, and are instead assigned according to their energy/wavenumber position of the Fermi polyad of which they are a part [149,159,163,187].

For example, the lower-energy member of the $(2v_2)$, (v_1) dyad in CO_2 is denoted v_-, and the higher as v_+ (see Fig. 3.12), while in the tetrad formed of the $(3v_1 + v_3)$, $(2v_1 + 2v_2 + v_3)$, $(v_1 + 4v_2 + v_3)$ and $(6v_2 + v_3)$ vibrational states, the resulting mixed states are labelled with the Fermi ranking index r [163,187]. The highest-energy vibrational state involved has rank $r = 1$, with decreasing rank for each state (2,3,4...) as the energy/wavenumber values decrease as seen in Fig. 3.13 [163,187] . Some transitions, such as the symmetric stretch vibration (v_2) in the aforementioned Fermi dyad, which is forbidden in the infra-red due to its lack of

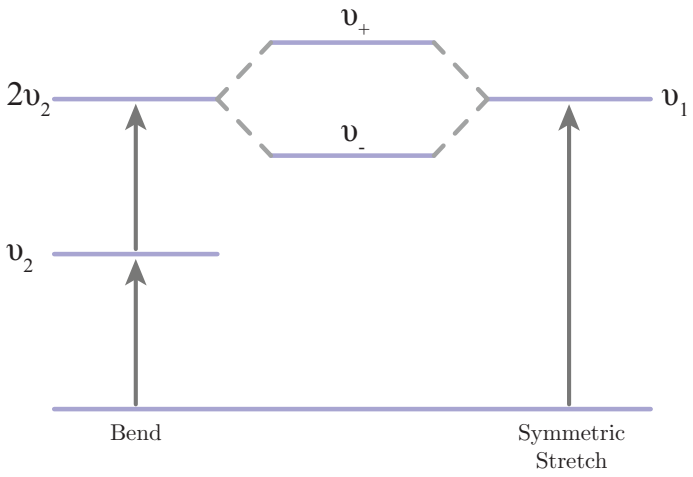

Figure 3.12: The vibrational energy level diagram of CO_2, showing the Fermi resonance mixing and splitting of the $2v_2$ bending overtone and v_1 symmetric stretch fundamental vibrational excited states, and the resulting mixed states. The symmetric stretch is IR-inactive in isolation, but contributes as part of the Fermi resonance dyad [148,149].

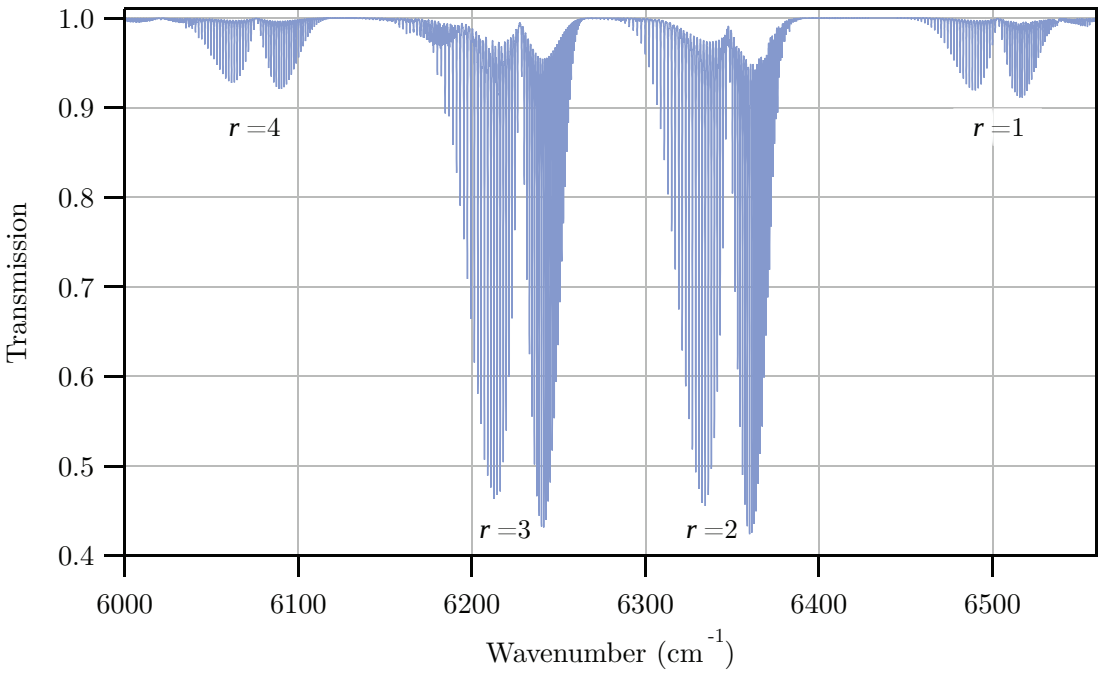

Figure 3.13: A spectrum of the $^{12}CO_2$ Fermi tetrad centred at $\sim 6300\,\mathrm{cm}^{-1}$ generated by SpectralCalc commercial molecular modelling software at 296 K at 1 atm over 6 m for 100 % $^{12}CO_2$. The ranking index of each of the members of the tetrad is shown. This thesis has a particular focus on the two strongest members with $r = 2$ and $r = 3$.

dipole moment, may interact and contribute as part of a Fermi resonance [148,149,153]. Additionally, the mixing of the states has somewhat of an equalising effect on the intensities of the involved transitions, with weaker transitions 'borrowing' intensity from the stronger ones [148,149,153]. Additionally, Fermi resonance may only occur between vibrational levels of the same molecular species [153].

3.5 Intra-band Intensity Modifiers

Another influence on the spectra of linear polyatomic molecules is that of *nuclear spin statistics*. More generally, the effects of nuclear spin statistics are apparent in the spectra of molecules that posses a centre of inversion symmetry, such as CO_2 [166]. Molecules without a centre of inversion symmetry such as hydrogen cyanide (HCN) are unaffected [154]. Affected ro-vibrational spectra display characteristic intensity variations between transitions arising from either even or odd values of the rotational quantum number J. The effect may produce alternating intensity patterns as is the case in acetylene (C_2H_2), or cause lines originating from even or odd-numbered J rotational levels to be absent entirely as is the case with carbon dioxide (CO_2) [153,166,188]. The cause of the observed intensity variations is an alteration of the relative probability with which particular molecular states occur. To understand these effects, we must again consider the Born–Oppenheimer approximation introduced in Subsection 3.1.2 which states that the total wavefunction of the molecule may be written as a product of its separate spatial functions [153,189]. That is, in terms of the electronic (ψ_{el}), vibrational (ψ_{vib}), rotational (ψ_{rot}), and nuclear spin (ψ_{ns}) wavefunctions:

$$\Psi_{\text{total}} = \psi_{\text{el}}\psi_{\text{vib}}\psi_{\text{rot}}\psi_{\text{ns}}. \tag{3.54}$$

The parity behaviour of the various components of Ψ_{total} under certain symmetry operations give rise to these intra-band intensity modifications. Extended discussion of the concepts of parity and nuclear spin statistics for molecular spectra presented in this thesis are explored in more detail in Appendix B for the interested reader, but a short summary is presented here.

3.5.1 Nuclear Spin Statistics

Nuclear spins of identical nuclei may couple together and form either symmetric or antisymmetric net spin states. The number of symmetric and antisymmetric spin states possible from the exchange of two identical nuclei is dependent on the nuclear spins of the individual particles [189]. The Pauli exclusion principle requires that the total wavefunction of a molecular state be symmetric or antisymmetric with respect to the exchange of two identical nuclei depending if the exchanged nuclei are bosons or fermions respectively [162,190].

3.5.1.1 Bosonic and Fermionic Nuclei

If the identical nuclei to be exchanged are bosons, which have integer nuclear spin quantum numbers I, then the total wavefunction is symmetric with respect to the exchange. For fermions, with half-integer I, the total wavefunction must be antisymmetric with respect to exchange of the identical nuclei [166]. So we have

$$\hat{P}_{12}\left(\psi_{\mathrm{el}}\psi_{\mathrm{vib}}\psi_{\mathrm{rot}}\psi_{\mathrm{ns}}\right) = +\left(\psi_{\mathrm{el}}\psi_{\mathrm{vib}}\psi_{\mathrm{rot}}\psi_{\mathrm{ns}}\right) \tag{3.55}$$

for bosons and

$$\hat{P}_{12}\left(\psi_{\mathrm{el}}\psi_{\mathrm{vib}}\psi_{\mathrm{rot}}\psi_{\mathrm{ns}}\right) = -\left(\psi_{\mathrm{el}}\psi_{\mathrm{vib}}\psi_{\mathrm{rot}}\psi_{\mathrm{ns}}\right) \tag{3.56}$$

for fermions, where $\hat{P}_{12}$ is the pseudo-symmetry operator that describes the exchange of identical nuclei [191]. Nucleons (protons and neutrons) are fermions, with the total amount of nucleons composing the atomic nucleus being equal to its *mass number* [192,193]. Three scenarios are then possible [194]:

- The mass number is even, with even number of protons and even number of neutrons, resulting in bosonic nuclei with I= 0 such as for ^{16}O and ^{12}C.
- The mass number is even, with odd number of protons and odd number of neutrons, produces bosonic nuclei with integer spin (I= 1, 2, 3...) such as ^{14}N where I=1.
- The mass number is odd, indicating fermionic nuclei with half-integral nuclear spins (I = 1/2,3/2,5/2...) such as ^{1}H where I = 1/2.

The nuclear spins of some common nuclei are summarised in Table 3.3. For molecules with a centre of symmetry, such as those belonging to the $D_{\infty h}$ molecular point group like CO_2 and C_2H_2, the even-J rotational levels are symmetric, and the odd-J rotational levels are antisymmetric for vibrational levels of g symmetry (Σ_g^+, Σ_g^-, Π_g,...) [153,159,165]. The reverse is true for vibrational levels of u symmetry (Σ_u^+, Σ_u^-, Π_u,...) [152,153].

Spin I	**Nuclei**	**Statistics**
0	^{12}C, ^{14}C, ^{16}O, ^{18}O, ^{32}S	Bose-Einstein
$\frac{1}{2}$	^{1}H, ^{3}H, ^{13}C, ^{13}N, ^{15}N, ^{15}O, ^{31}P, ^{19}F	Fermi-Dirac
1	^{2}H (D), ^{14}N	Bose-Einstein
$\frac{3}{2}$	^{11}B, ^{33}S, ^{35}Cl, ^{37}Cl	Fermi-Dirac
$\frac{5}{2}$	^{17}O	Fermi-Dirac
3	^{10}B	Bose-Einstein

Table 3.3: Some common nuclei, their spin quantum numbers, and statistics classification [154,189].

3.5.1.2 Statistical Weights of States

For the spin quantum number I of the identical nuclei, the number of symmetric and antisymmetric final states are given by:

$$\text{total symmetric states} = (I+1)\,(2I+1) \tag{3.57}$$

$$\text{total antisymmetric states} = (2I+1)\,I \tag{3.58}$$

where the number (or *statistical weights*) of symmetric and asymmetric states are known as g_s and g_a respectively [166,189]. The ratio of g_a to g_s gives the intensity ratio variation observed in some spectra [153,155]:

$$\frac{g_a}{g_s} = \frac{I}{(I+1)} \tag{3.59}$$

In general, the electronic ground states of most molecules (with which we are working in this thesis) are symmetric with respect to exchange of identical nuclei [154]. The vibrational state symmetry is dependent on the symmetry of the vibrational mode being excited, and to what excited state it is elevated. The final consideration is the symmetry of the rotational wavefunction with respect to exchange of identical nuclei, and is determined by the lower state rotational quantum number, J. Quite simply: If $J = \text{even}$, the rotational wavefunction is symmetric with respect to exchange, and for $J = \text{odd}$, the wavefunction is antisymmetric [189]. Centrosymmetric acetylene for example, shows a 1:3 variation in ro-vibrational absorption peak heights for the $101000 \leftarrow 0000000$ vibrational band under exchange of identical H^1 nuclei from ro-vibrational transitions originating from even-J and odd-J rotational levels [153]. For some transitions and molecules such as CO_2, lines originating from entire subsets of rotational levels may be forbidden entirely by the effects of nuclear spin statistics [152,153,155,162,189].

Molecular Modelling

In the previous chapter the fundamental origins of the band shapes in molecular absorption spectra were derived. However, the shapes of the individual tens to hundreds of ro-vibrational lines comprising such a band was not discussed. Additionally, the effects of the local molecular environment - temperature, pressure, and concentration for example - were not discussed. In order to extract the physical properties of the molecular system from an absorption spectrum, it is typical to construct a model of the spectrum which is then fit to the data. Provided the model is based on physical phenomena, the fitted parameters may then be related to properties of interest of the system. This chapter will explore the lineshapes of the individual ro-vibrational lines in an absorption band and their physical origins, before delving into the effects of pressure, temperature and concentration on the molecular spectrum. Finally, the HITRAN database and its usefulness in fitting the numerous lines in a molecular absorption spectrum will be discussed.

4.1 Lineshapes

While the individual ro-vibrational absorption features in molecular spectra are known as lines, they are not delta-functions, rather they have a frequency width related to fundamental physical properties of the molecular species as well as the local environment of the molecule [161]. An important consideration in any spectral model - molecular or otherwise - is the shape of each line, known as the *lineshape*. In the case of molecules, this refers to the lineshapes of each of the ro-vibrational feature that comprise the absorption band. There are numerous approximations to the real lineshapes, and most are derived from fundamental physical effects. One such lineshape often used for molecular spectra is the Voigt profile. This profile takes a large number of physical effects into account and is comprised of the convolution of two profiles: the Lorentzian and Gaussian lineshapes. Unfortunately, there are a number of varying definitions for these profiles. The functions used in this thesis are normalised such that the integral of the final Voigt profile is unity. The following definitions of each profile will be used in this thesis unless stated otherwise.

4.1.1 Lorentzian Profile

The Lorentzian profile, $L\left(x - x_0, \gamma\right)$, is defined as:

$$L\left(x - x_0, \gamma\right) = \frac{\gamma}{\pi\left(\left(x - x_0\right)^2 + \gamma^2\right)} \tag{4.1}$$

where γ is defined as the half-width-at-half-maximum (HWHM) value of $L\left(x - x_0, \gamma\right)$, and x_0 is the centre [195–197]. The Lorentzian profile is shown in Fig. 4.1. The full-width-at-half-maximum (FWHM), Δf_L, of this profile is simply given by $\Delta f_L = 2\gamma$. This definition of the Lorentzian is area-normalised to one, e.g.:

$$\int_{-\infty}^{\infty} L\left(x - x_0, \gamma\right)\, dx = 1.$$

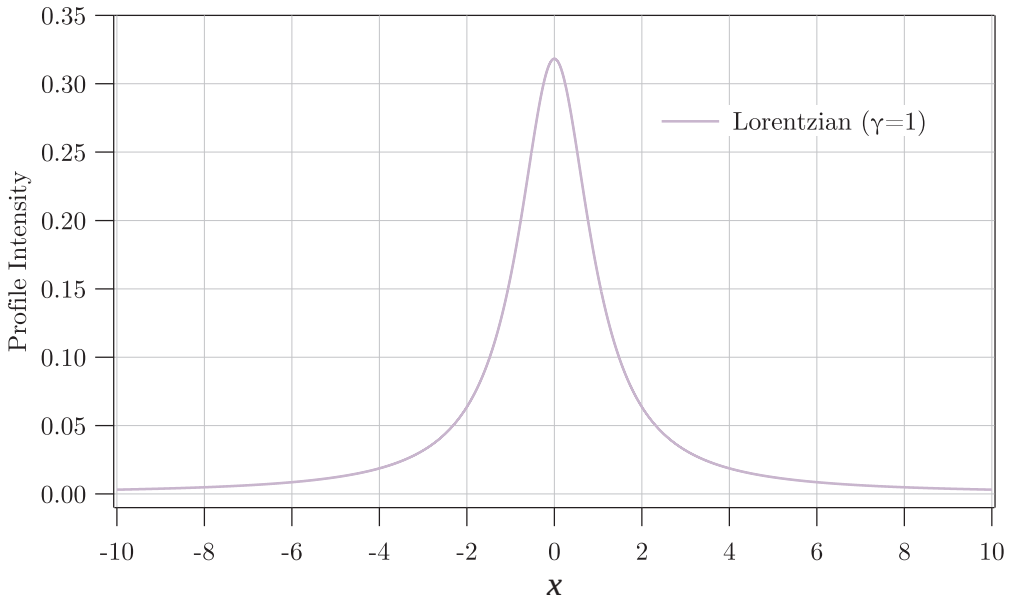

Figure 4.1: The area-normalised Lorentzian profile with $\gamma = 1$ and $x_0 = 0$.

4.1.2 Gaussian Profile

The Gaussian profile, $G\left(x - x_0, \sigma\right)$, is defined as:

$$G\left(x - x_0, \sigma\right) = \frac{1}{\sigma\sqrt{2\pi}} e^{\frac{-(x-x_0)^2}{2\sigma^2}} \tag{4.2}$$

where σ is the standard deviation (square root of the variance) and x_0 is the centre of the Gaussian profile [167,195,196]. A comparison between the Gaussian and Lorentzian profiles is shown in Fig. 4.2. Again, this definition is area-normalised to one:

$$\int_{-\infty}^{\infty} G\left(x - x_0, \sigma\right)\, dx = 1.$$

While this definition uses the standard deviation, the FWHM (Δf_G) is also commonly used to describe the Gaussian profile, and is related to σ by $\Delta f_G = 2\sigma\sqrt{2\ln 2}$.

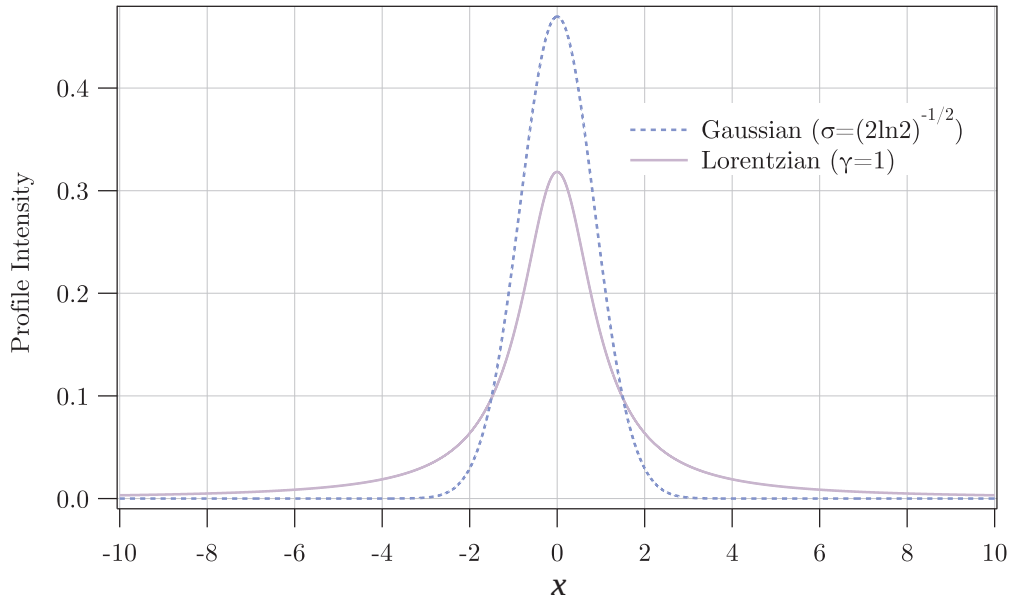

Figure 4.2: The area-normalised Lorentzian profile with $\gamma = 1$ (purple solid line) and area-normalised Gaussian profile (blue dashed line) of the same HWHM ($\sigma = (2\ln 2)^{-\frac{1}{2}}$). Both profiles are centred on $x_0 = 0$.

4.1.3 Voigt Profile and the Faddeeva Function

The normalised Voigt profile, $V(x - x_0, \gamma, \sigma)$, is a convolution of the previously defined unity-area-normalised Lorentzian and Gaussian profiles [196,197]:

$$V(x - x_0, \gamma, \sigma) = G(x - x_0, \sigma) * L(x - x_0, \gamma) \tag{4.3}$$

$$= \int_{-\infty}^{\infty} G(x' - x_0, \sigma)\, L(x - x', \gamma)\, dx'. \tag{4.4}$$

A comparison between the Voigt, Gaussian, and Lorentzian profiles is shown in Fig. 4.3. Once again, the integral of this profile is unity as it is a convolution of normalised profiles:

$$\int_{-\infty}^{\infty} V(x - x_0, \gamma, \sigma)\, dx = 1. \tag{4.5}$$

This definition is required for compatibility with several spectral databases, including HITRAN as presented in this thesis [195]. However, computation of the Voigt profile, particularly in cases where multiple Voigt profiles are required such as in molecular spectra, is computationally expensive [196,198,199]. To improve computation times the Faddeeva function, $w(z)$, where

$$z = \frac{x + i\gamma}{\sigma\sqrt{2}},$$

is often employed due to the availability of rapid computational packages. The Faddeeva function is a scaled complex complementary error function that is decomposable into real and imaginary parts:

$$w\left(x+iy\right)=V\left(x,y\right)+iL_{\mathrm{V}}\left(x,y\right) \tag{4.6}$$

Where $V\left(x,y\right)$ and $L_{\mathrm{V}}\left(x,y\right)$ are the real and imaginary Voigt functions, up to prefactors [199,200]. The Faddeeva function and Voigt profile, prefactor included, are related through

$$V\left(x,\gamma,\sigma\right)=\frac{\mathrm{Re}\left[w\left(z\right)\right]}{\sigma\sqrt{2\pi}}. \tag{4.7}$$

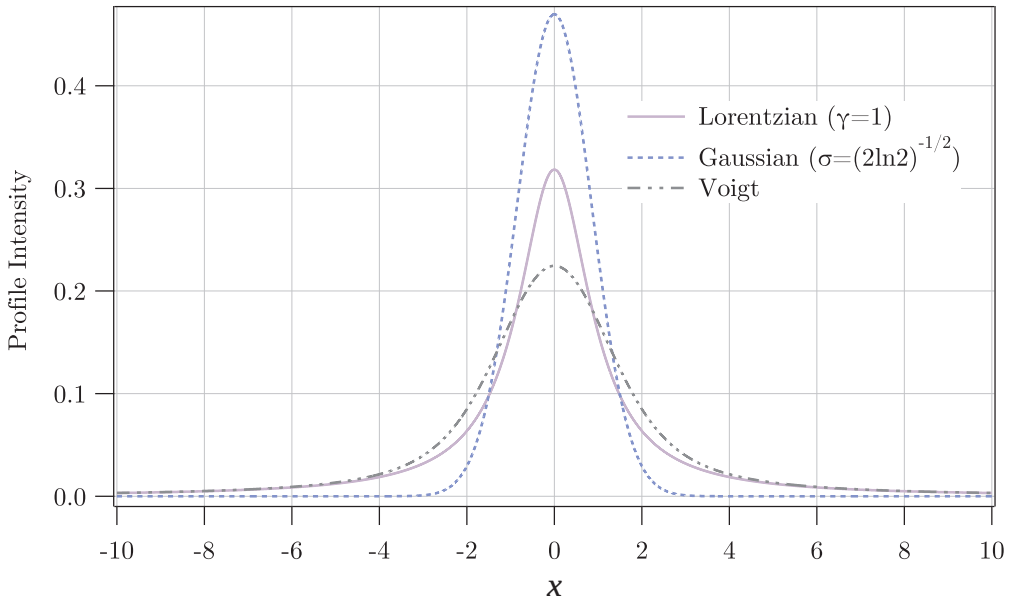

Figure 4.3: The area-normalised Lorentzian profile (purple solid line) and Gaussian profile (blue dashed line) of the same width. The grey dot-dashed line is the corresponding area-normalised Voigt profile as calculated using the Faddeeva function. All profiles are centred on $x_0 = 0$.

The FWHM of the Voigt profile, Δf_V, may be approximated by the widths of the Lorentzian and Gaussian profiles to an accuracy of 0.02 % by the relation [201]

$$\Delta f_V \approx 0.5346\Delta f_L + \sqrt{0.2166{\Delta f_L}^2 + {\Delta f_G}^2}. \tag{4.8}$$

4.2 Line Width

As flagged in Section 4.1, using the term 'line' to describe a peak in observed optical spectra is historical. The lines forming absorption spectra are not infinitely narrow, even in the case where the instrument measuring the spectrum can be assumed to have no broadening effect on the lines. Firstly, a distinction between *homogeneous* and *inhomogeneous* broadening mechanisms must also be made. As suggested by their names, homogeneous broadening mechanisms are those in which each molecule's frequency response is broadened in exactly

the same way in the entire ensemble, while inhomogeneous broadening mechanisms affect different groups of molecules in the ensemble in differing ways. Homogeneous broadening results in Lorentzian profiles, while inhomogeneous broadening results in Gaussian line profiles [124,202,203]. We will now consider several effects that contribute to the line width and shape of the absorption features observed.

4.2.1 Natural Line Width

The natural line width is the result of a fundamental quantum mechanical limit to the precision to which the energy (E) and natural lifetime (t) of a particular state of a particle can be known. This is known as the Heisenberg uncertainty principle:

$$\Delta t \Delta E \sim \frac{\hbar}{2} \tag{4.9}$$

where Δ refers to the uncertainty in that variable and $\hbar = h/2\pi$ is the reduced Planck constant (h) [158,167]. This uncertainty or 'fuzziness' in the energy of a state translates to an uncertainty or range in the frequency of a photon (FWHM) that is exciting a transition of [204]:

$$\Delta f_N \sim \frac{\Delta E}{\hbar} \sim \frac{1}{2\pi\Delta t}. \tag{4.10}$$

This 'smearing out' of the energy levels results in homogeneous broadening of an optical transition also known as *lifetime broadening*, and a Lorentzian line shape characterised by the natural line width, Δf_N, or equivalently the natural lifetime, of the state involved in the transition [124,151,157,158,204]. The direct consequence of Eq. 4.10 is that a shorter-lived state will correspond to a larger natural line width.

4.2.2 Pressure Broadening

The effects of pressure broadening, also known as collisional broadening, on molecular spectra may be modelled in a variety of ways, depending on assumptions made about the nature of the collisions as well as properties of the molecules themselves [205]. Collisional broadening is so named as collisions between absorbers, or with other perturbing molecules, interrupts the natural absorption or emission process [124,206,207]. This shortens the effective lifetime of the energy states involved in the transition, increasing uncertainty in the energy states and broadening of the lines via the Heisenberg uncertainty principle. Additionally, the close proximity of molecules creates a shift in the position of the absorption lines. When a molecule A approaches another molecule B, the energy levels of both A and B are shifted by the interaction of their electrons, with the degree of shift depending on their electron configurations and the separation of their centres of mass during the collision [197,202,208]. As the density of the gas increases, the effects of these collisions becomes more pronounced, leading to the alternate name of pressure broadening [202]. Additionally, the degree of pressure broadening and shift is different for each ro-vibrational line in the spectrum, owing to the non-constant

spacing of rotational lines. Collisional broadening is homogeneous, resulting in a Lorentzian line shape [202,209]. The combination of the collisional and natural broadening profiles is then characterised by the homogeneous FWHM line width, Δf_H, as seen in Fig. 4.4.

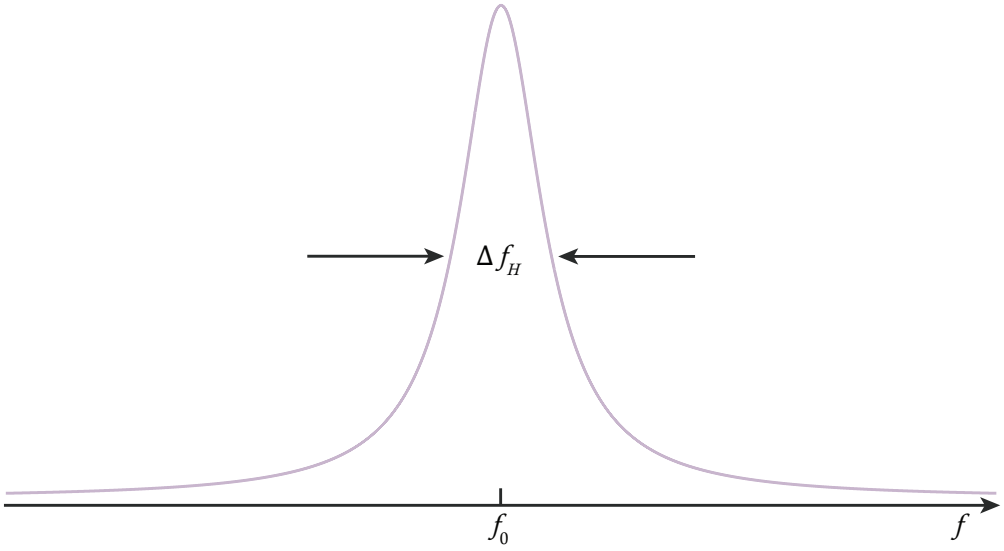

Figure 4.4: The Lorentzian line shape showing the homogeneous line width, Δf_H, that is the combination of the natural and collisional broadening.

4.2.3 Doppler Broadening

Doppler broadening, also known as thermal broadening for reasons that will become apparent, is broadening caused by the relative velocities of the molecules with respect to the photons with which they will interact in either absorption or emission [151]. Consider a photon of frequency f being absorbed by a molecule that is at rest. From the previous discussion of the natural line width, we expect to see a Lorentzian absorption profile centred at f. Now consider a single molecule and photon travelling toward one another, with the molecule having velocity v_a toward the direction of laser propagation. The molecule sees the photon as having a higher frequency through the Doppler effect, and if the photon is absorbed by the molecule, an observer in the laboratory rest frame would see a Lorentzian profile centred at that higher frequency:

$$f_a = f_0 \left(1 - \frac{v_a}{c}\right) \tag{4.11}$$

where c is the speed of light and f_0 is the transition frequency of the stationary molecule [158,197]. Conversely, if the molecule was moving away from the laser, the photon appears to have lower energy and frequency, causing another Lorentzian profile to be observed at this new lower frequency. Now consider the entire system of molecules in motion with a spread of velocity values as dictated by the Maxwell-Boltzmann distribution. As each molecule in the sample behaves individually the broadening is inhomogeneous, resulting in a Gaussian line

shape characterised by the standard deviation

$$\sigma_D = \sqrt{\frac{k_B T}{mc^2}} f_0 \tag{4.12}$$

where k_B is the Boltzmann constant, T is the temperature of the sample, and m is the mass of the particle [202,204]. It may also be characterised by its FWHM:

$$\Delta f_D = \sqrt{\frac{8 k_B T \ln 2}{mc^2}} f_0 \tag{4.13}$$

as shown in Fig. 4.5 [157,204,210]. It can be seen from Eq. 4.13 that the governing factor for the extent of Doppler broadening is the temperature of the sample, with higher temperatures inducing more broadening. It should also be noted that it is the component of velocity parallel to the observer that should be considered in regards to Doppler broadening. Those particles with no parallel velocity component, such as molecules travelling perpendicular to the observer or not at all, will not show the effects of Doppler shift [157,206].

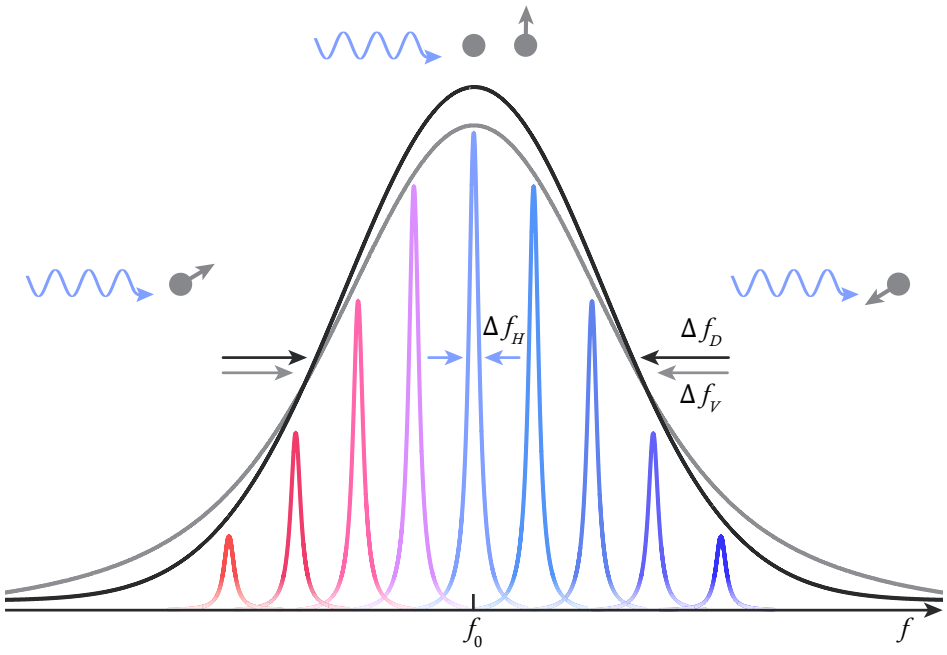

Figure 4.5: The Doppler profile (dark grey) of FWHM Δf_D around f_0 as weighted by the Gaussian Maxwell-Boltzmann temperature-velocity distribution. Molecules with components of velocity toward the incoming photon encounter a higher-frequency ('blue-shifted') photon and produce an absorption feature at a frequency higher than f_0 due to the Doppler effect. Those particles with velocity components away from the incoming photon encounter a lower-frequency ('red-shifted') photon and produce an absorption feature at a frequency lower than f_0. Particles with velocity perpendicular to the direction of photon travel, or lacking velocity at all, are unaffected by the Doppler effect, and produce an absorption feature at f_0. The Voigt profile (light grey, FWHM of Δf_V) is the cumulative result of a near-continuum of overlapping Lorentzian profiles of width Δf_H (red to blue) convolved with a Gaussian profile due to Doppler broadening [157].

The width of the Gaussian profile derived from Doppler broadening Δf_D is much larger than that of the homogeneous line width Δf_H at room temperature and atmospheric pressure [203]. All broadening mechanisms are convolved with the natural line width to produce the final lineshape - a Voigt profile of width Δf_V as seen in Fig. 4.5 [203]. However, broadening is not the only mechanism in which a molecule's local environment impacts upon its spectrum.

4.3 Pressure, Temperature, and Concentration Influence on Spectra

As was first introduced in Section 4.2, the local environment in which the molecules reside impact upon their absorption spectrum. Once the underlying physical phenomena behind these changes to the spectrum are understood, they provide a window through which the local environment may be monitored. Of particular interest are the spectroscopic changes induced by variations in temperature, concentration, and pressure.

4.3.1 Temperature

Changes in the local temperature of the sample can have dramatic effects on the shape of the absorption spectrum. In particular, the relative peak heights have a strong dependence on the absolute temperature of the sample. Recalling the discussion about population distribution amongst rotational levels and the effect on ro-vibrational line intensities in Section 3.2.1.3, it was noted that the equation predicting relative populations of the rotational levels (Eq. 3.14) included a thermal term:

$$\begin{aligned} \frac{N_J}{N_0} &= \frac{g_J}{g_0} e^{-(E_J - E_0)/kT} \\ &= \underbrace{(2J+1)}_{\text{Degeneracy}} \underbrace{e^{-BhcJ(J+1)/kT}}_{\text{Thermal}}. \end{aligned}$$

This thermal term is the Maxwell-Boltzmann distribution of the population, and governs the probability of a particle occupying a particular state at a temperature T [162,211]. Recalling also that the energy separation between rotational states is much less than that between vibrational states, changes in temperature are unlikely to produce a change in vibrational state, but may much more readily produce a change in the rotational population distribution. This leads to a shift of the population towards higher rotational states as T increases [207]. This results in stronger molecular absorption towards the wings and lessening absorptions in the band centre as the population in redistributed at higher temperatures. This effect may be seen in the spectrum of $^{12}CO_2$ as the temperature is changed in Fig. 4.6.

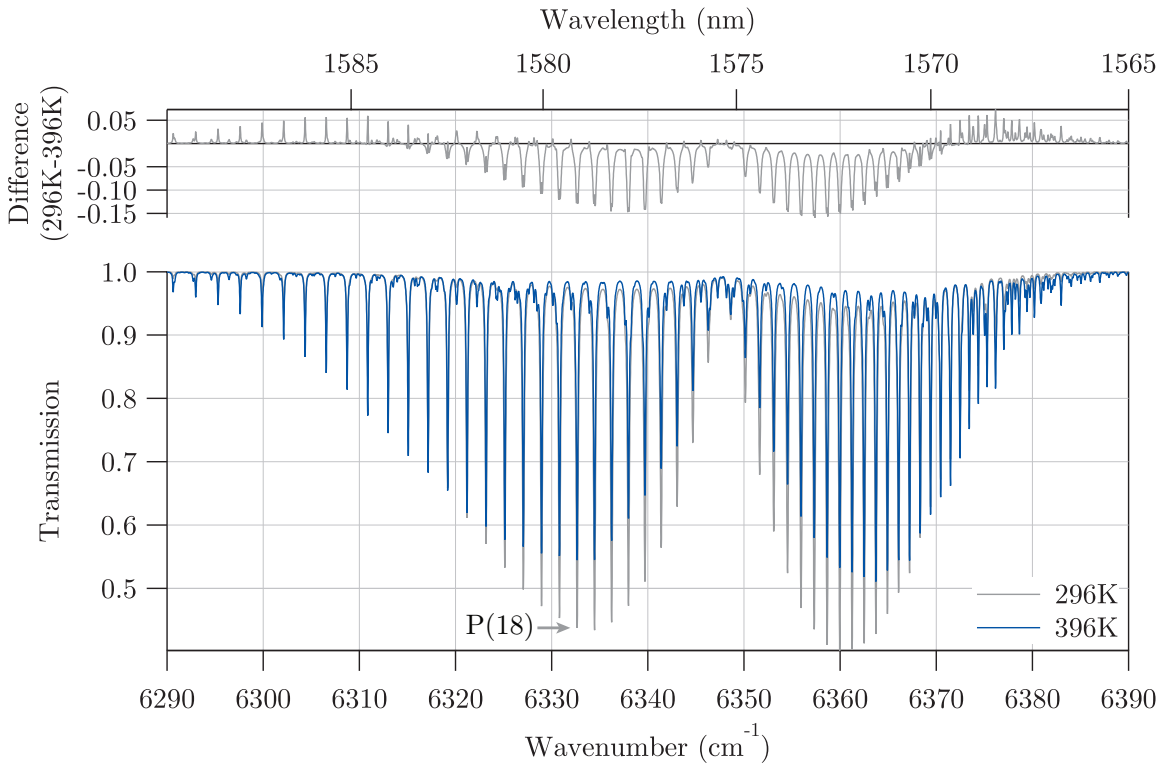

Figure 4.6: $^{12}CO_2$ spectra generated by SpectralCalc commercial molecular modelling software at 296 K (grey) and 396 K (blue) at 1 atm over 6.5 m for 100 % $^{12}CO_2$ (bottom) for the 30012 ← 00001 and 31112 ← 01101 main and hot-band transitions respectively. Also shown (top) is the difference between the two spectra, showing the shift of population to higher ro-vibrational levels and the resultant shift of absorption to the wings of the spectra with increasing temperature for the main transition. The hotband transition also follows this trend, along with the expected relative increase in absorption as the lower state of the hotband transition garners more of the population due to the temperature change. This is clearly seen in Fig. 4.7.

The origin and type of band is also an important factor. We have so far been considering the effects on the absorption spectra for a vibrational transition originating in the ground state - a fundamental or overtone (combination) band. However, hotbands - vibrational transitions originating from a vibrational state other than the ground state and exciting to a higher vibrational state - actually increase in overall intensity as the temperature is increased. This is because there is usually a small amount of the molecular population that is excited into a hotband's originating vibrational state as the temperature is increased [207]. This is seen in Fig. 4.7, in which the P(18) line of the 30012 ← 00001 band shown in Fig. 4.6 is seen to decrease with increasing temperature, while the adjacent 31112 ← 01101 hot band (P27) line increases in intensity with increasing temperature.

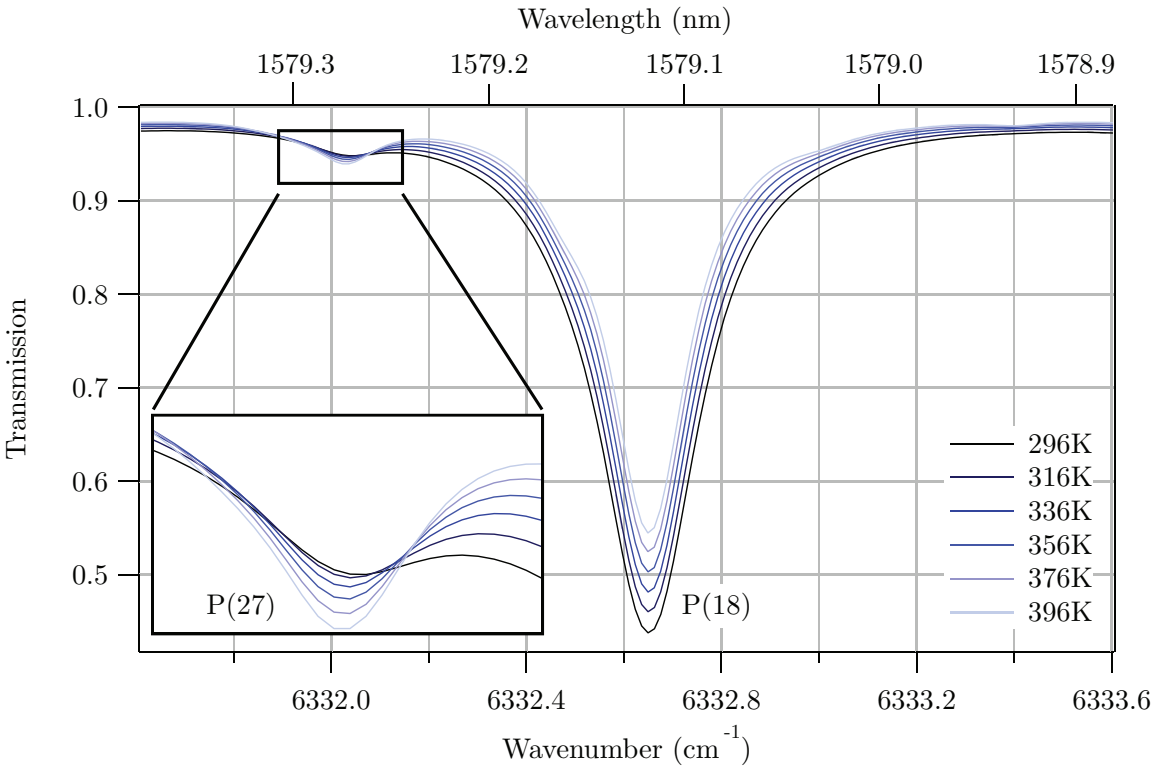

Figure 4.7: Mid-P-branch peaks (P18) and (P27) of $^{12}CO_2$ spectra seen in Fig. 4.6 generated by SpectralCalc commercial molecular modelling software between 296 K and 396 K at 1 atm over 6.5 m for 100 % $^{12}CO_2$ for the 30012 ← 00001 and 31112 ← 01101 main (larger peak) and hotband (smaller peak) transitions respectively. The main peak decreases in height with increasing temperatures as the vibrational ground state population shifts to higher rotational levels, increasing the magnitude of the far wings of the spectrum while decreasing magnitude of the central lines. The hotband peak shows a reversed trend increasing in magnitude with increasing temperature as thermal redistribution means a larger population in the higher vibrational level from which the hot band originates.

Finally, as mentioned previously in Section 4.2.3, a change in temperature will affect the widths of each ro-vibrational line through the effects of Doppler broadening. As the temperature is increased, so too is the Doppler width of each ro-vibrational line Δf_D as defined by Eq. 4.13.

4.3.2 Concentration and the Beer-Lambert Law

The concentration of the absorber in a sample determines the integrated absorptions of each line over the whole band. Before analysing the effect of concentration on the sample, first we must consider a laser of frequency f and intensity $I_0(f, 0)$ on its passage through a sample of length l. After passing through the sample, some of the light is absorbed, with an intensity $I(f, l)$ remaining at the far side of the sample. The loss of intensity due to passage through

the sample is described by the Beer-Lambert Law:

$$I(f,l) = I_0(f,0)\, e^{-\alpha l} = I_0(f,0)\, e^{-u\sigma l} \tag{4.14}$$

where α is the frequency-dependent linear absorption coefficient of the sample [120,157,158,212]. Additionally, the ratio I/I_0 is known as the *transmittance* of the sample, $\mathcal{T}(f)$ [120]. The absorption coefficient itself is the result of the multiplication of the concentration or number density of molecules of the absorber, u, and the frequency-dependent *cross section*, σ [120]. Equation 4.14 indicates that as either the concentration or path length of absorbers (or both) is increased, the amount of light transmitted by the sample decreases exponentially as a greater proportion of the input light is absorbed. This corresponds to deeper features in an absorption spectrum when considered in transmission, as can be seen in Fig. 4.8.

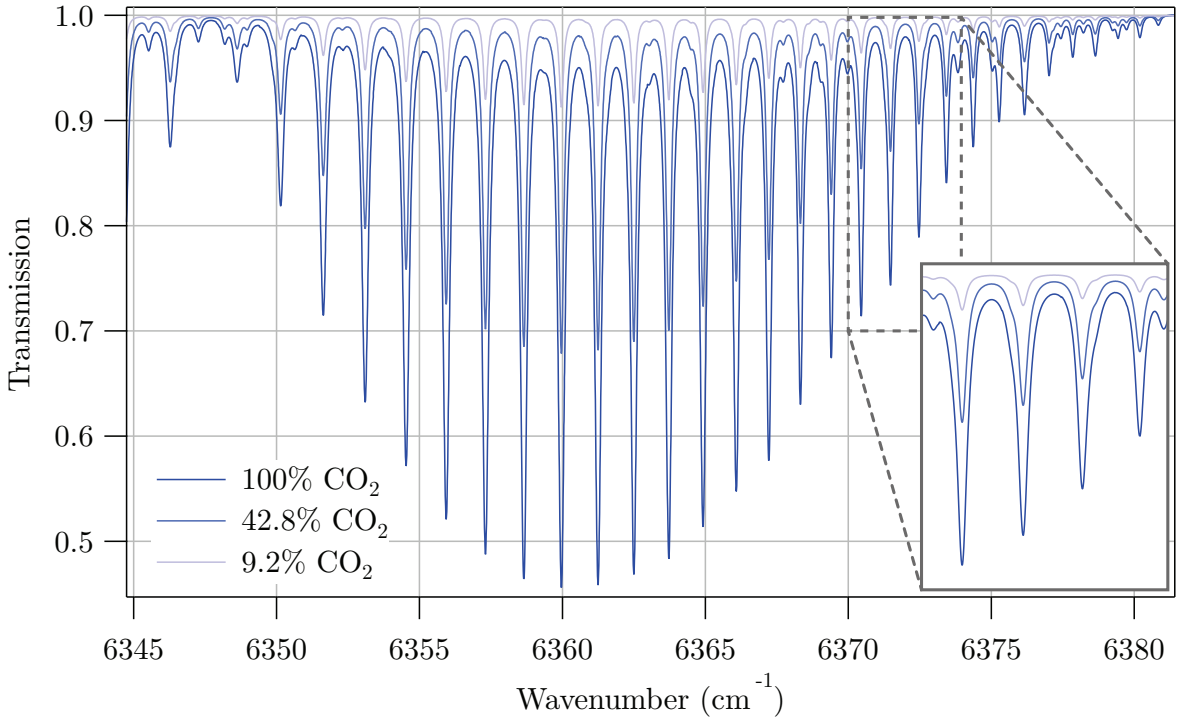

Figure 4.8: The effect on spectra of changing absorber concentration on the R-branch of the 30012 ← 00001 transition of CO_2 with 31112 ← 01101 hotband, for a fixed path length (6.5 m) and temperature (296 K). As the concentration of the absorber increases, the absorption of all types of bands become deeper until saturation conditions. These spectra are the result of fitting some of the measured spectra presented in Chapter 10.

4.3.3 Pressure

Changes in pressure affect molecular absorption spectra through collisional or pressure broadening, and the associated pressure shift as described in Section 4.2.2. However, this effect is dominated by Doppler broadening until relatively high pressures are considered [160,203]. This is evident by observation of Fig. 4.5.

4.4 The HITRAN Database and Modelling Molecular Spectra

The HITRAN database, short for HIgh-resolution TRANsmission molecular absorption database, is an online compilation of spectroscopic parameters of molecules with atmospheric significance. The parameters available on the HITRAN database are a mixture of direct observations, theoretical calculations, and semi-empirical values [1,213]. These parameters are used in a variety of computer codes for simulation of the transmission or emission of light in the atmosphere, and are also used in the course of this thesis to create and fit models of $^{12}CO_2$, $^{13}CO_2$, and $^{12}C_2H_2$ to allow extraction of physical parameters of interest.

4.4.1 The HITRAN Database: Line Strength

HITRAN spectroscopic parameters are available for each ro-vibrational line and isotopologue of molecules included in the database. Additionally, the online interface allows one to sort by vibrational mode, allowing for identification of molecular absorptions when there is some uncertainty. The parameters are provided at a reference temperature (T_{ref}) of 296 K and pressure (p_{ref}) of 1 atm. Some of the most important parameters available on the database are the line strength $S_{\eta\eta'}$ of a ro-vibrational transition between lower and upper states η and η' respectively, along with the wavenumber of that transition $\widetilde{\nu}_{\eta\eta'}$. Values of ($T_{\text{ref}}$) come preweighted by the natural terrestrial isotopic abundances as listed in Ref. [214]. It is important to note that as with the previously mentioned HITRAN parameters $S_{\eta\eta'}$ is provided at T_{ref}, but may be converted to any other temperature T by:

$$S_{\eta\eta'}(T) = S_{\eta\eta'}(T_{\text{ref}}) \frac{Q(T_{\text{ref}})}{Q(T)} \frac{e^{-c_2 E''/T}}{e^{-c_2 E''/T_{\text{ref}}}} \frac{\left(1 - e^{-c_2 \widetilde{\nu}_{\eta\eta'}/T}\right)}{\left(1 - e^{-c_2 \widetilde{\nu}_{\eta\eta'}/T_{\text{ref}}}\right)} \tag{4.15}$$

where $Q(T)$ is the total internal partition sum at temperature T, E'' is the lower state energy of the transition, and c_2 is the second radiation constant ($c_2 = hc/k_B = 1.4387770\,\text{cm K}$) [153,215]. It is at this point useful to note that the native units of HITRAN are cgs rather than SI. To simplify the modelling, this preference has been maintained in the fitting code and resulting spectra that are derived from it. Equation 4.15 introduces temperature dependence to the model. Furthermore, in order to calculate the correct line strength in Eq. 4.15, the temperature dependence of $Q(T)$ must be calculated. The full equation for $Q(T)$ for linear polyatomics in the ground electronic state is given by

$$Q(T) = \frac{1}{\sigma} \sum_{\text{all levels}} (2J+1)(g_n)\, e^{-\frac{E}{k_B T}} \tag{4.16}$$

were σ is 2 for homonuclear diatomics and 1 otherwise, g_n is the full nuclear spin degeneracy factor, and the summation is over all ro-vibrational levels of the molecule [216]. As this is quite time-consuming to calculate in full, the authors of the HITRAN database recommend

utilising a cubic polynomial approximation:

$$Q(T) = a + bT + cT^2 + dT^3 \tag{4.17}$$

where the coefficients a, b, c, d are species and isotopologue-dependent and listed in Ref. [216]. This approximation is accurate to within 1% in the $70 - 500\,\mathrm{K}$ temperature range [213,216]. However, $S_{\eta\eta'}$ is not the only HITRAN parameter which has a temperature dependence.

4.4.2 The HITRAN Database: Shifts and Broadening

The width of each ro-vibrational absorption line is also temperature dependent, due to the physical phenomena discussed in Section 4.2. This leads to another of the HITRAN parameters - the line halfwidth $\gamma(p, T)$ - needing adjustment when considered away from T_{ref}:

$$\gamma(p, T) = \left(\frac{T_{\mathrm{ref}}}{T}\right)^{n_{\mathrm{self}}} \left[\gamma_{\mathrm{air}}(p_{\mathrm{ref}}, T_{\mathrm{ref}})(p - p_s) + \gamma_{\mathrm{self}}(p_{\mathrm{ref}}, T_{\mathrm{ref}})\, p_s\right], \tag{4.18}$$

where p is the pressure of the system in atmospheres, p_{ref} is the reference pressure (1 atm), γ_{air} is the air-broadened half-width-at-half-maximum (HWHM), γ_{self} is the self-broadened half-width-at-half-maximum (HWHM), n_{self} is the coefficient of the temperature dependence of the self-broadened half-width, and p_s is the partial pressure of the gas [213].

Additionally, if the system is not at atmospheric pressure, Eq. 4.18 introduces a pressure dependence into the model. Additionally, the line position is shifted by this change in pressure, with the new shifted position given by

$$\widetilde{\nu}_{\eta\eta'}{}^{*} = \widetilde{\nu}_{\eta\eta'} + \delta_{\mathrm{air}}(p_{\mathrm{ref}})\, p \tag{4.19}$$

where δ_{air} is the pressure shift of the line position in units of $\left[\mathrm{cm}^{-1}/\mathrm{atm}\right]$ and is another parameter provided in the database. Doppler broadening of each line must also be included. All width contributions must be included prior to the calculation of the Voigt profile, with Lorentzian widths combined via direct summation, and Gaussian widths added in quadrature [217].

4.4.3 Molecular Modelling and Fitting

The final consideration when using the HITRAN database is how to convert the shifts, line strengths, and broadening values so far discussed into a model which may be compared to a measured quantity. The HITRAN lineshape function for each ro-vibrational line forming the absorption band, $f\left(\widetilde{\nu}, \widetilde{\nu}_{\eta\eta'}, T, p\right)$, includes the widths and shifts discussed in Section 4.4.2[1]. Multiplication of $f\left(\widetilde{\nu}, \widetilde{\nu}_{\eta\eta'}, T, p\right)$ by the corrected linestrength $S_{\eta\eta'}(T)$ from Section 4.4.1 and

[1] While this thesis makes use of a Voigt lineshape, more recent iterations of HITRAN are now beginning to include parameters for use with more sophisticated lineshape functions that account for subtle collisional dynamics, such as the Hartmann-Tran profile [218,219].

u, the number density of absorbers results in the unitless quantity of *optical depth*, τ:

$$\tau\left(\widetilde{\nu},T,p\right)=u\times S_{\eta\eta'}\left(T\right)\times f\left(\widetilde{\nu},\widetilde{\nu}_{\eta\eta'},T,p\right) \tag{4.20}$$

where u has an overall depth scaling effect on the spectrum. The optical depth is then related to a measured transmission spectrum $\mathcal{T}\left(\widetilde{\nu}\right)$ simply through

$$\tau\left(\widetilde{\nu},T,p\right)=-ln\left(\mathcal{T}\left(\widetilde{\nu},T,p\right)\right). \tag{4.21}$$

Therefore if the transmission spectrum is able to be measured, a fitting function may be constructed out of parameters sourced from the HITRAN database. In this case the only free parameters of the fit are the temperature, pressure, and (essentially) concentration in the form of u. Multiple overlapping spectral bands from the same molecular species and isotopologue are simply included in the fit as extra lines. Inclusion of differing isotopologues of the same species, or indeed differing species, requires that they be considered separately before being combined in the final stages of the fitting procedure. This method was used to extract T and u from the measured spectra in the papers presented in Chapters 10 & 11.

Part III

Experimental

Molecular Spectroscopy with an Optical Frequency Comb

One important factor of note in performing molecular spectroscopy is the spectral width and complexity of molecular absorption bands. As seen in Part I, there is an abundance of information to be gained about a molecular species from its absorption spectrum, including its pressure, temperature, and concentration. However, recovery of this information is reliant upon the use of a densely-sampled and broadband spectral source able to acquire molecular spectra on rapid time scales with large enough spectral coverage to cover the majority of the targeted vibrational band. High-resolution spectra are also required to provide differentiability between molecular species or isotopologues of the same species in more complex samples more akin to those found in real-world applications. There are a number of ways to achieve these requirements, though all have their drawbacks to some extent. A widely tunable source may require too much time to acquire or lack the tuning range required for a broadband spectrum, making it unsuited to rapid measurements of complex spectra [220]. A broadband source such as an incandescent light bulb is incoherent and unable to be efficiently coupled into an enhancement cavity for trace gas analysis [221,222], while Fourier transform infrared (FTIR) requires an impractically-long scanning distance of the moveable arm to achieve high resolution results [124]. The invention of the optical frequency comb has however provided an elegant solution to these problems.

Optical frequency combs are highly stabilised lasers with a spectrum formed of a series of equally-spaced, discrete and coherent frequency lines or *comb modes* occurring at extremely well-defined frequencies. Additionally, they posses a large bandwidth on the order of tens to hundreds of nanometres, making them near-ideal interrogation sources in laser spectroscopy [223].

There are a number of known methods to create such a comb, including four-wave mixing, periodic phase or amplitude modulation, and via the stabilisation of the output of a mode-locked laser [223,224]. The latter method is utilised to generate the frequency comb used throughout this thesis (Menlo Systems FC1500). It was the development of this method that garnered one half of the 2005 Nobel Prize in Physics shared between John L. Hall and Theodor W. Hänch [225,226]. To understand the generation of a frequency comb created using a mode-locked laser, one must first understand the general operating principles of a laser resonator.

5.1 Frequency Comb Generation: Mode-Locked Lasers

The simplest laser resonator is constructed of a pump beam as an input to a laser cavity of some sort such as two opposing mirrors. The input mirror is partially transmissive to the pump wavelength, while the output mirror is partially transmissive to the wavelength generated within the resonator itself. This results in the amount of light present in the cavity steadily building over time [227,228]. This may be understood as a multitude of standing waves existing within the cavity, constructively interfering to a pulse that circulates around the resonator cavity as the standing waves evolve in time. Each time the circulating pulse strikes the output mirror, a small amount of light is transmitted. Within a laser cavity, there is also a gain medium present to generate the coherent photons via population inversion that form the laser. Finally, modulator of some sort is typically present within the cavity to control the output of the laser [204,224,229].

For now we ignore the gain medium and modulator, and return to consideration of the longitudinal modes within the cavity. In such a cavity, each of the longitudinal modes is independently oscillatory, with no relation between each mode. Similarly, the phase of each mode has no fixed relation to any other longitudinal mode of the cavity [204,224]. If only a few such modes are considered, the time-evolving phase differences between them will cause uncontrolled interference effects leading to a resonator output that varies in intensity as the cavity - and hence the phases of the longitudinal modes - are affected by external forces such as thermal expansion of the cavity components [224]. The result of this process may be seen in Fig. 5.1. When many longitudinal modes of the cavity are considered, the output tends towards a relatively constant intensity as the modes interfere toward an average value.

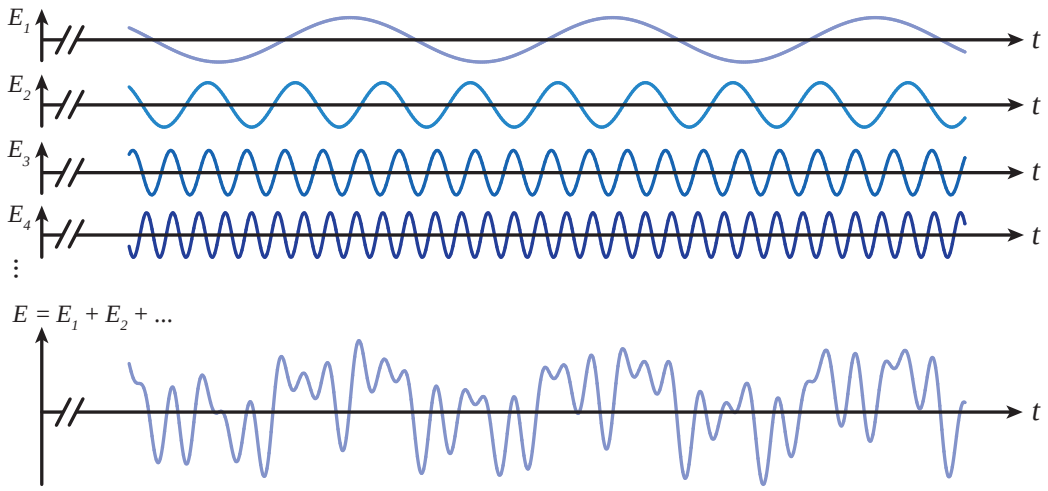

Figure 5.1: Time-dependent evolution of the intracavity longitudinal modes (top) with random phases creates an electric field at the output (bottom) which evolves in time as the modes interfere without a fixed phase relation. A relatively constant intensity may result with enough contributing longitudinal modes [224].

In a mode-locked laser by contrast, the phase relation between the longitudinal modes of the cavity are locked to a fixed value. Instead of the near-constant output of the non-mode-locked laser resonator with thousands of longitudinal modes of random phase, the output of a mode-locked laser is a series of periodic light pulses corresponding to times when the longitudinal modes all constructively interfere with each other, as seen in Fig. 5.2. That laser is then termed to be *mode locked* or *phase locked*, with the process of ensuring the fixed phase difference between the interfering longitudinal modes termed *mode locking* [204,224].

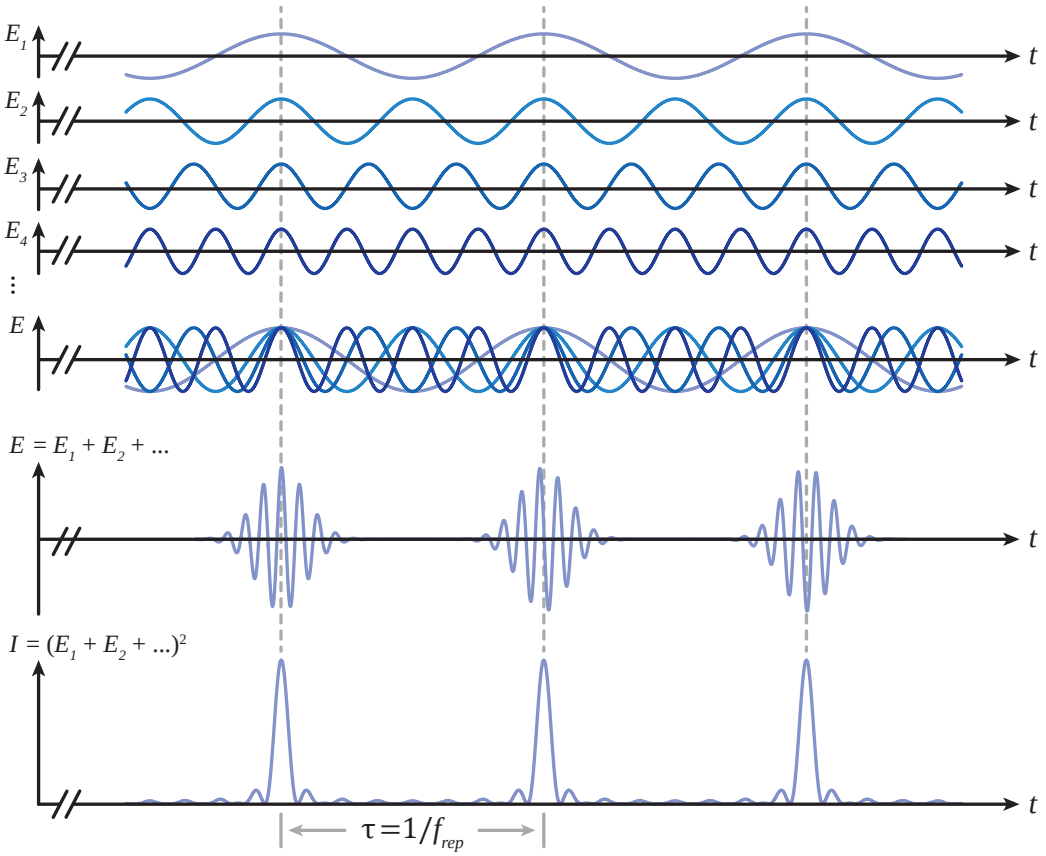

Figure 5.2: The phase-locked intracavity longitudinal modes (top) interfere constructively at multiples of the cavity round-trip-time, τ, resulting in pulsed intensity output (bottom) characteristic of mode-locked operation. The output pulses are separated by τ in the temporal domain [224,229].

The output of a mode locked laser is a periodic series of pulses separated by a time

$$\tau = \frac{2L}{c} \tag{5.1}$$

where L is the length of the cavity, c is the speed of light, and τ is known as the *round trip time* or the time taken for a pulse to circulate around the cavity once [224,228,229]. This round trip time is also inversely related to the frequency spacing or *repetition rate* of the pulses:

$$f_{\text{rep}} = \frac{1}{\tau}, \tag{5.2}$$

where the cavity length is also stabilised to maintain f_{rep} [223,224,228,229]. Additionally, just

as in any other laser cavity, a gain medium is also present. The purpose of the gain medium is to act as an amplifier of the light within the cavity. Amplification of the light is achieved through incoming photons - normally from a pump diode or laser - driving stimulated emission from the gain media by creating a population inversion [204,230]. There are a number of ways to achieve mode locking, including active mode locking and the method used for the comb used in this thesis, passive mode locking [231–235].

5.1.1 Passive Mode Locking: Nonlinear Polarisation Rotation

Nonlinear Polarisation Rotation (NPR) is the result of the nonlinear Kerr effect in non-polarisation-maintaining fibre, and is a popular method to mode-lock a laser. In essence, high intensity light, such as that confined to the core of an optical fibre, causes an intensity-dependent refractive index variation and birefringence within the fibre proportional to the intensity of the light. The medium in which this occurs is then referred to as a *Kerr medium* [224].

A series of waveplates can be used to optimise the maximum transmission of the cavity (minimum loss conditions) for the highest optical intensity i.e. the peak of the desired circulating pulse within the cavity. The addition of a polarising optical element, such as a polarising beam splitter, allows the power-dependent polarisation change to be converted into a power-dependent transmission through the polariser [224]. As the polarisation rotation is intensity-dependent, the un-rotated wings of the pulse to either side of the peak encounter more loss than the high-intensity peak, and are suppressed at the polariser. This has the effect of shortening the circulating pulse or *pulse-shaping*. This produces an ultra-short, high-intensity circulating pulse that is sampled each time upon striking the output coupler, leading to a mode-locked pulsed output [204,233,234,236–238] .

When considered in the frequency domain, the pulse train output of the mode locked laser is seen to be a series of discrete lines occurring at frequencies separated by f_{rep} [223]. Additionally, shorter pulse durations result in wider spectral bandwidths, so it is advantageous to target a short pulse duration on femtosecond or shorter time-scales when aiming to produce a frequency comb [224,229].

5.2 Frequency Comb Stabilisation

A frequency comb built around a mode-locked laser requires additional stabilisation to enable the frequency of each of its modes to be known. This requires control of the cavity dispersion whose origin lies in the differing dependence upon frequency of two important intracavity velocities - the *group* and *phase* velocities.

5.2.1 Intracavity Velocities

Within any resonator cavity there are two important velocities that must be considered. The origin of these two velocities is related to the formation of the pulses from a superposition of the lasing longitudinal modes (resonant waves) of the laser cavity. Each pulse therefore contains a multitude of light waves and a spread of frequencies, each of which travel at slightly different speeds through different media - a phenomenon known as *dispersion* - depending on the frequency of the wave. As discussed in Section 5.1, the crest of the pulse envelope will occur each time the longitudinal modes are in phase. In a cavity without dispersion all waves travel at the same speed, and so the maxima of the pulse envelopes, and the pulses themselves, travel at the same speed. With dispersion however, the conditions for constructive interference are now dependent upon the speeds and phase differences between the various waves [124].

The group velocity, v_g, is the speed at which the overall envelope of a wave travels through space and is related to the angular frequency of the wave, $\omega = 2\pi f$, and angular wavenumber, $k = (2\pi)/\lambda$, by:

$$v_g \cong \frac{d\omega}{dk}. \tag{5.3}$$

The phase velocity, v_p, is the speed at which the phase and *carrier frequency* ω_c of the wave travels is given by:

$$v_p \cong \frac{\omega_c}{k}. \tag{5.4}$$

In a dispersive medium such as the laser cavity $v_p \neq v_g$, leading to a 'slipping' between the output pulse envelope and the carrier wave whose peaks and troughs form the envelope of each pulse [223]. This slipping is known as the *carrier-envelope phase shift*, $\Delta\phi_{CE}$, and is shown in Fig. 5.3. The carrier-envelope phase shift may be related to ω_c along with the phase and group velocities through

$$\Delta\phi_{CE} = \left(\frac{1}{v_g} - \frac{1}{v_p}\right) L_c \omega_c \tag{5.5}$$

where L_c is the round-trip length of the laser cavity [223,224]. Without stabilisation $\Delta\phi_{CE}$ will be unstable on a pulse-to-pulse basis subject to external factors affecting the laser cavity such as thermal expansion [239]. When considered in the frequency domain via the shift theorem of Fourier transforms, $\Delta\phi_{CE}$ results in each of the comb modes deviating from falling on exact harmonics of the pulse repetition rate. This is known as the *carrier-envelope offset frequency* f_0 as described by [223,224,240]:

$$f_0 = \frac{\Delta\phi_{CE}}{2\pi} f_{\text{rep}}. \tag{5.6}$$

Thus in the frequency domain we have a 'comb' around ω_c - the lasing frequency in the angular domain - with discrete lines separated by f_{rep} [241]. The frequency of the nth mode can be described by:

$$f_n = n f_{\text{rep}} + f_0 \tag{5.7}$$

where n is a large, positive integer [223,224,229]. A full derivation of this result may be found in Appendix D for the interested reader. This equation is extremely powerful if f_0 can be stabilised, providing knowledge of the absolute frequency of every line in the spectrum of the comb. Stabilisation of $\Delta\phi_{CE}$, and hence f_0, is what differentiates the optical frequency comb from a mode-locked laser, and is achieved through what is known as f-$2f$ locking [223,242].

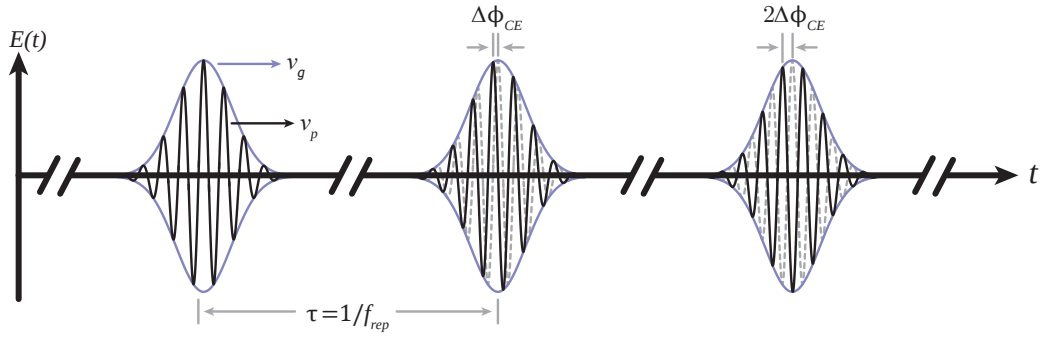

Figure 5.3: The τ-periodic pulsed output of a mode-locked laser. The envelope of the pulse (purple) travels at the group velocity v_g while the carrier wave of travels at the phase velocity v_p (black). This representation shows a constant pulse-to-pulse phase 'slippage' between the envelope and carrier wave known as the *carrier-envelope phase shift* $\Delta\phi_{CE}$.

5.2.2 Carrier-Envelope Offset Stabilisation: f-$2f$ Locking

An optical frequency comb may be measured and $\Delta\phi_{CE}$ stabilised through a feedback loop by means of an f-$2f$ self-referencing scheme. In such a scheme, a beat note is created between a comb mode from the lower-frequency end of the spectrum at a frequency $nf_{\text{rep}}+f_0$ that is frequency-doubled via second harmonic generation to $2(nf_{\text{rep}} + f_0)$ and a comb mode from the higher-frequency end of the spectrum $(2nf_{\text{rep}}+f_0)$ as seen in Fig. 5.4. As an aside, it must be noted that this is only possible if the comb spans what is known as an 'octave' (a factor of two in frequency) as the second comb mode that forms the beat signal must be one octave away from the first [223,242–245]. This is often performed by the addition of a nonlinear photonic crystal fibre to broaden the initial output into the octave-spanning regime [223,242–244].

Returning to the f-$2f$ stabilisation scheme, the result of the beat note is [223,242,244,245]:

$$2\,(nf_{\text{rep}} + f_0) - (2nf_{\text{rep}} + f_0) = f_0. \tag{5.8}$$

This allows direct measurement of f_0 using a fast photodetector. The signal from this photodetector is then used as the input to a feedback loop to actuate a dispersion-compensating component within the laser cavity, maintaining $\Delta\phi_{CE}$ on a pulse-to-pulse basis and results in the production of a fully stabilised optical frequency comb as seen in Fig. 5.5 [242].

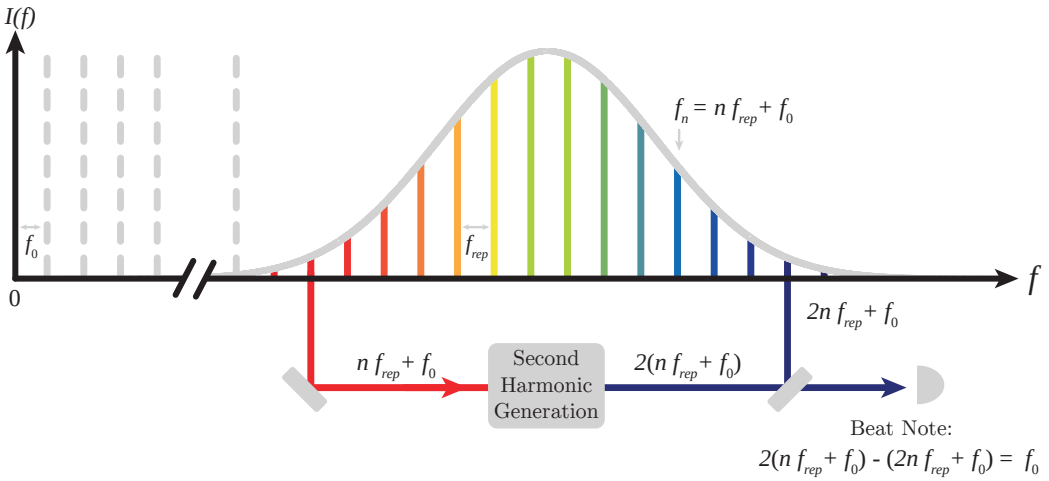

Figure 5.4: Operating principle of an f-$2f$ lock in an optical frequency comb to stabilise the carrier-envelope offset f_0.

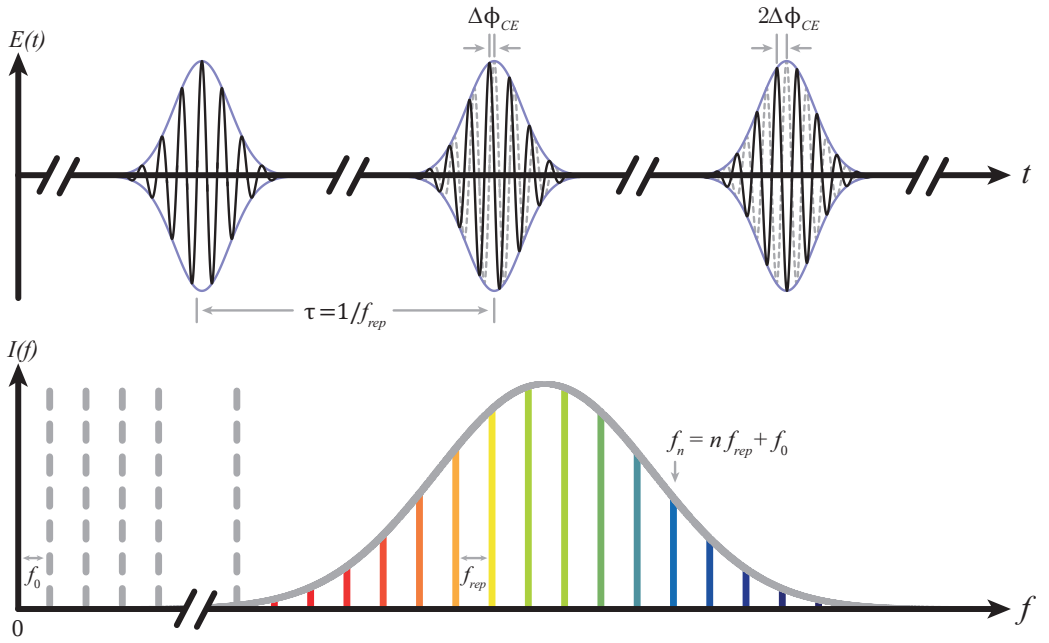

Figure 5.5: The output of a fully-stabilised optical frequency comb in the temporal (top) and spectral domains (bottom). The comb spectrum is a series of equidistant lines spaced by the repetition rate f_{rep} offset from DC by f_0. The frequency of the nth comb modes is described by Eq. 5.7 [223,229].

5.3 Menlo Systems FC1500 Optical Frequency Comb

The optical frequency comb used throughout the course of this thesis is a commercial comb from Menlo Systems (FC1500) and is based on a NPR mode-locked femto-second (fs) erbium-doped (Er^{3+}) fibre laser. The mode-locked laser is generated in a ring cavity depicted in Fig. 5.6, and has an adjustable repetition rate via intracavity electro-optic modulator (EOM) and mirror equipped with both a translation stage and piezoelectric transducer (PZT) for cavity length control. The Er^{3+}-doped fibre acts as the laser gain medium, with the pump supplied by multiple 980 nm laser diodes. This produces a comb spectrum centred around 1550 nm. The entire fibre laser is temperature-controlled for additional stability and an intracavity wedge allows active control of f_0.

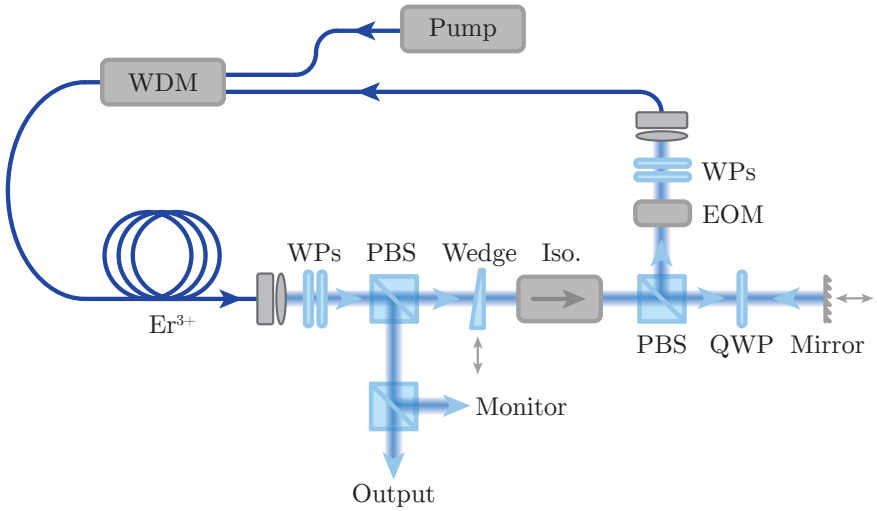

Figure 5.6: Schematic of the optical frequency comb's ring cavity. Fibre paths shown in dark blue, free-space optical paths in light blue, WPs: Waveplates, EOM: Electro-Optic Modulator, PBS: Polarisation Beam Splitter, QWP: Quarter-Wave Plate, Iso: Optical Isolator, WDM: Wavelength Division Multiplexer. Note that the QWP is a fixed element, while the remaining waveplates are computer-controllable. The Er^{3+}-doped fibre amplifies the intensity of the circulating pulse (driven by multiple 980 nm diodes), while the laser is passively mode-locked using NPR.

The pulse duration of this comb is ∼100 fs, which produces a broad-bandwidth frequency envelope (∼ 10 THz, ∼ 50 nm). The round-trip time of the cavity is ∼4 ns, or equivalently $f_{rep} = 250$ MHz, which is stabilised by adjusting the comb cavity length as part of a phase lock between a single nearby comb mode and a cavity-stabilised CW laser [223]. The stability of the laser (∼2 Hz with 1 s of averaging) is imposed onto each comb mode, which are in turn exceedingly narrow (∼ kHz) [246]. The carrier-envelope offset frequency f_0 is locked at 20 MHz after being referenced to a caesium beam clock (Datum CsIII) with a frequency instability of 0.2 mHz with 1 s of averaging [243,244]. The end result is a comb spanning approximately 100 nm between 1500-1600 nm. While this spectral bandwidth is adequate to observe some transitions of HCN and CO_2 as seen in Chapters 8, 9 & 10, there is a relatively easy way to extend the spectrum of the comb to target additional molecular absorption bands.

5.4 Extending the Comb Spectrum: Highly Non-Linear Fibre

While the output of the frequency comb is quite broad, there are additional interesting molecular absorptions from molecules such as methane (CH_4) and acetylene (C_2H_2) that fall outside its natural spectral band. The addition of a highly nonlinear optical fibre at the output of the comb broadens the spectral output to cover from below 1480 nm to above 1700 nm as may be seen in Fig. 5.7 in which the comb spectrum was measured on an optical spectrum analyser [247–250]. The broad spectral coverage of the optical frequency comb, along with its dense spectral sampling and absolute frequency accuracy as described by Eq. 5.7 makes the comb a nearly-ideal spectral interrogation source. When fully stabilised, it allows massively-parallel spectroscopy without the need for a widely-tunable laser source [223].

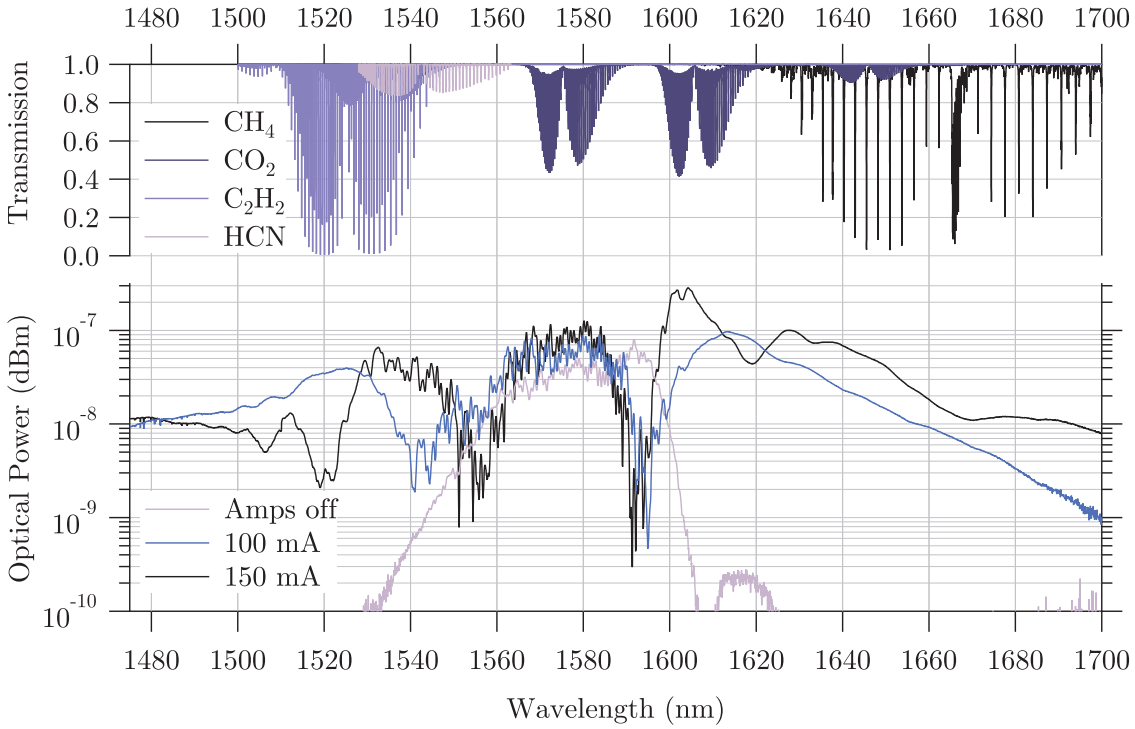

Figure 5.7: The measured spectral-broadening effect of the highly-nonlinear fibre allows access to additional molecular absorption bands and species depending on applied amplifier diode currents within the comb.

One complication is that all of the comb's frequencies are contained within a single beam. In order to obtain the frequency-dependent absorption of a sample, this beam must be unravelled into its component frequencies using a *spectrometer*.

Virtually-Imaged Phased Array Spectrometers

The optical frequency comb is a nearly-ideal light source for molecular spectroscopy, with its broad bandwidth, dense spectral sampling, and absolute frequency accuracy. However, all of the comb's frequency components are contained within one laser beam. This poses a problem for spectroscopic measurement, in which the absorption of light of each frequency must be carefully measured. This necessitates a method of unravelling the multi-frequency laser beam into its component frequencies. Additionally, to take full advantage of the dense frequency spacing of the comb, this unravelling must be of sufficiently high-resolution so that the individual comb modes are, ideally, separable. The experimental method to perform the unravelling in this thesis uses a home-built spectrometer based on a Virtually Imaged Phased Array in combination with a diffraction grating to spatially disperse the comb frequencies prior to imaging with an Indium Gallium Arsenide (InGaAs) camera. The arrangement of components that form the VIPA spectrometer may be seen in Fig. 6.1. Firstly, it is crucial to consider the design of the diffraction grating and its fundamental limitations with regards to spatial dispersion of multi-wavelength light.

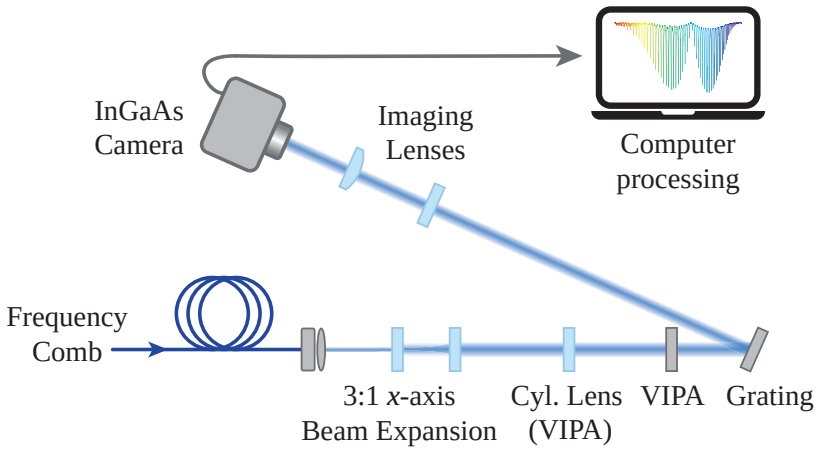

Figure 6.1: Top-down view of the spectrometer, showing the arrangement of the diffraction grating, VIPA etalon, and InGaAs camera.

6.1 Diffraction Gratings

Diffraction gratings are often used to disperse multi-wavelength optical beams into their component wavelengths by means of optical interference. Gratings are available in optically transmissive and reflective varieties which are comprised of a glass plate with periodic, parallel etchings into the specialised coating on its surface. The structure embedded within the grating surface affects the phase and/or amplitude of the incident light, which causes interference in the output light. A third type of grating - the blazed or echelette diffraction grating - is a specific type of reflective or transmissive grating specially optimised for maximum efficiency in a particular diffraction order. The diffraction order and the wavelength-dependent dispersive properties of all gratings may be described by the grating equation as discussed below [124,251,252].

6.1.1 The Grating Equation

A diffraction grating disperses multi-wavelength light incident at an input angle θ_i spatially into angles θ_m as a function of wavelength. The diffraction gratings used in the course of this thesis are all of the blazed reflection-type variety, which are manufactured to have a high efficiency for a particular diffraction order and wavelength range. The large grating used predominantly in this thesis has a blaze angle, γ_B, of 29°, highest efficiency at a wavelength of 1.6μm, and has 600 grooves/mm. Angular definitions for diffraction gratings may be seen in Fig. 6.2.

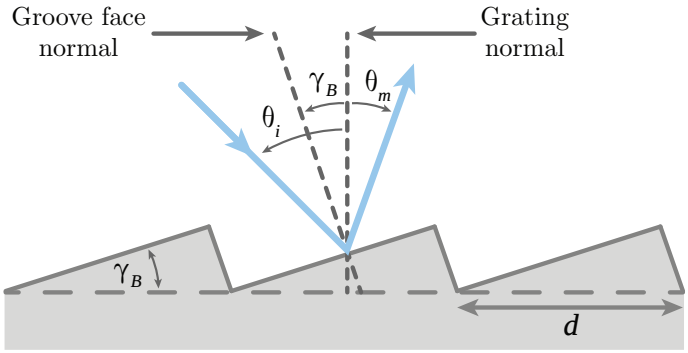

Figure 6.2: A section of the blazed face of a reflection-type diffraction grating. the blaze angle, γ_B, incident light angle, θ_i, diffraction angle, θ_m, grating period, d, and the two surface normals are shown [252,253].

The relation between the grating period, d (the distance between adjacent grooves on the grating face) and the incident (θ_i) and diffracted output (θ_m) angles is given by the grating equation:

$$d\left(\sin\left(\theta_i\right)+\sin\left(\theta_m\right)\right)=m\lambda \tag{6.1}$$

where all parameters are as defined in Fig. 6.2 and $m=0,\pm1,\pm2,...$ is the order of diffraction [124,167,253]. Note that there is a sign convention associated with the angles θ_m and θ_i. When

θ_m and θ_i are on opposite sides of the grating normal, as in Fig. 6.2, θ_m is negative [253]. Additionally, in order to ensure the highest efficiency is achieved, the blaze angle must obey the relation $\gamma_B = \frac{1}{2}(\theta_i - \theta_m)$ [124,253]. While the setup of the spectrometer was modified over the duration of experiments covered in this thesis, it was endeavoured to fulfil this high-efficiency criterion in all cases.

6.1.2 Resolving Power

Another important parameter of diffraction gratings in the *resolving power* ($\mathfrak{R}$), which is the ability of the grating to resolve closely-spaced wavelengths of incident light. The resolving power is dependent on the central wavelength to be resolved λ, the minimum resolvable wavelength separation $\Delta\lambda_{min}$ (as defined by the Rayleigh criterion), and the illuminated area of the grating through its definition of:

$$\mathfrak{R} = \frac{\lambda}{\Delta\lambda_{min}} \tag{6.2}$$

$$= mN_G \tag{6.3}$$

where m is again the order of diffraction, and N_G is the number of illuminated grating lines [252–254]. This can be rewritten in terms of the input and output angles θ_i and θ_m by substitution of the grating equation (Eq. 6.1) for m:

$$\mathfrak{R} = \frac{N_G d\left(\sin\left(\theta_i\right) + \sin\left(\theta_m\right)\right)}{\lambda} \tag{6.4}$$

where $N_G d$ is the illuminated area of the grating. It is important to note however that $\Delta\lambda_{min}$ is defined by the Rayleigh criterion, which allows for a relatively large overlap between adjacent diffraction signals as seen in Fig. 6.3 [124]. This is undesirable when performing quantitative spectroscopy, particularly with a dense spectral sampling as when using a frequency comb, as preferably each come mode should be individually resolvable with no or very little overlap. Therefore for quantitative spectroscopy, the resolving power of a grating must ideally be greater than that predicted by Eq. 6.4.

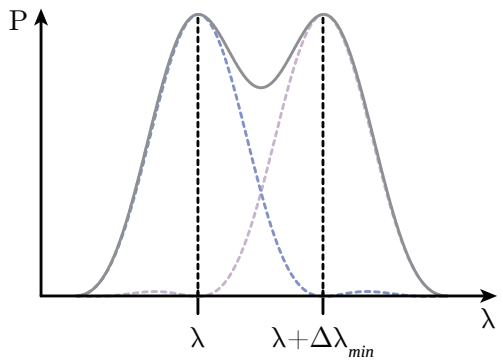

Figure 6.3: The Rayleigh criterion for the limit of resolution for two adjacent diffraction patterns. The peaks are spaced by the minimum resolvable wavelength separation $\Delta\lambda_{min}$.

6.1.3 Angular Dispersion

The final parameter that requires consideration when choosing a diffraction grating is its angular dispersion, $\mathfrak{D}$. This parameter describes the angular spread of an input multi-wavelength beam as a function of wavelength by the grating, and is defined as [124,253,254]:

$$\mathfrak{D} = \frac{d\theta_m}{d\lambda}. \tag{6.5}$$

When combined with the grating equation, Eq. 6.5 can be written as [124,254]:

$$\mathfrak{D} = \frac{m}{\cos(\theta_m)\, d} \tag{6.6}$$

in which d is again the grating period [124,254]. It can be seen from examination of the equations governing the angular dispersion, grating efficiency, and resolving power that these parameters are dependent on the physical characteristics of the grating, the illuminated grating area, and the input and output angles. When using a blazed grating, the diffraction order m is fixed to a specific diffraction order, and so this contribution to the equations is essentially fixed. The illuminated area and input/output angles are therefore the only variables, and are chosen for all experiments such that the angular dispersion, grating efficiency, and resolving power were maximised. However it must be noted that these equations are interdependent upon shared parameters, so not all may be maximised to their full extent. To increase $\mathfrak{R}$, which by Eq. 6.4 has a direct dependence on the width of the grating illuminated, the horizontal beam width was expanded by a factor of three prior to reaching the grating. However, even once fully optimised, the angular dispersion of the diffraction grating is not adequate to disperse the densely-packed modes of the frequency comb, necessitating the introduction of a greater angular dispersion element - the Virtually Imaged Phased Array.

6.2 Virtually-Imaged Phased Arrays

A Virtually Imaged Phased Array (VIPA) consists of a cylindrical lens and a tilted plane-parallel glass plate as seen in Figures 6.4 and 6.5. The front face of the VIPA etalon is coated with an $\sim 100\%$ reflective optical coating, with the exception of an anti-reflection (AR)-coated input window at the bottom of the plate, while the back face is completely coated by a relatively high reflectivity coating ($\geq 95\%$) [255]. The cylindrical lens is used to line-focus the beam of multi-wavelength light into the VIPA etalon, such that the beam waist is located at the back face of the VIPA etalon. Additionally, focusing with the cylindrical lens provides the multiple input angles for every wavelength required for the VIPA to function [255,256].

Consider the case where the back face of the etalon is 95% reflective, and we have a single-wavelength input beam. Upon striking the back face, 5% of the incident light will be transmitted out of the etalon and diverges after the beam waist. The remaining 95% of the light is internally reflected from the back face and strikes the front face, is 100%

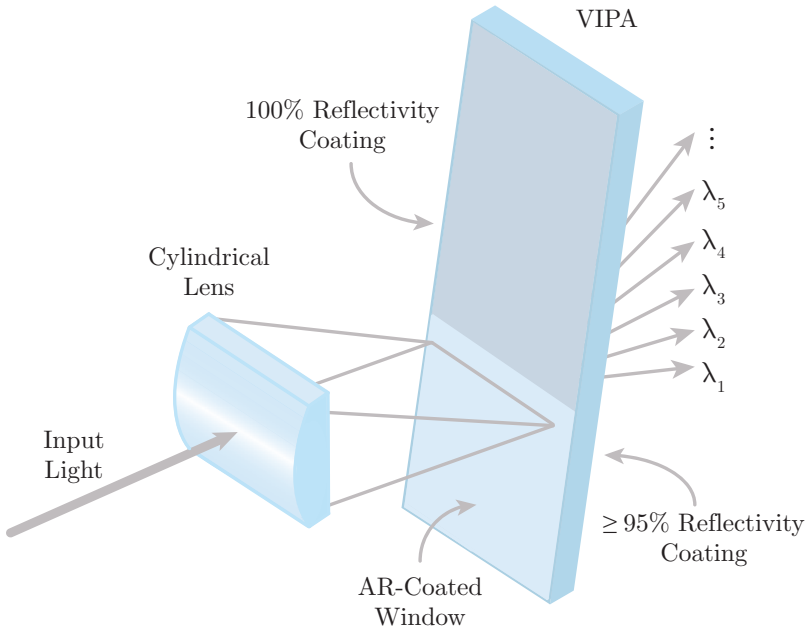

Figure 6.4: The principle of wavelength dispersion by a VIPA, showing the locations of the various optical coatings. The cylindrical lens line-focuses collimated multi-wavelength light in the horizontal plane into the glass plate through the AR-coated window section. The vertical angle of the output light is a function of wavelength [255,257].

reflected, and the light again strikes the back face displaced by a vertical distance d as seen in Fig. 6.5. This process repeats up the VIPA etalon, yielding an exponentially decreasing amount of transmitted light as the number of reflections increases for a single wavelength. When considered with a plane wave ray-tracing approach neglecting beam divergence, the output light is a series of beams separated by d. However, as the input light was focused by the cylindrical lens into the back face of the VIPA, the transmitted light is also diverging, resulting in a series of divergent virtual images of the beam waist. These virtual images are spaced by a distance $2t$, where $t = 2\,\text{mm}$ is the thickness of the etalon, along a line normal to the glass plate as seen in Fig. 6.5. The transmitted beams then undergo either constructive or destructive interference depending on the relative phases of the transmitted beams. In regions where the beams are in-phase with one another, constructive interference occurs and these beams continue on into the far field, while if the beams are out of phase, destructive interference occurs and these portions of the beam are removed. The end result is a collimated output consisting of the in-phase portions, as can be seen in Fig. 6.5.

6.2.1 VIPA Multiple Input Wavelength Behaviour - Wavelength-Dependent Dispersion

When considering multi-wavelength input light it is more convenient to think in terms of the ray-tracing perspective on beam propagation through the VIPA. In the case where only one wavelength at a specific angle is incident on the VIPA, the only restriction was that

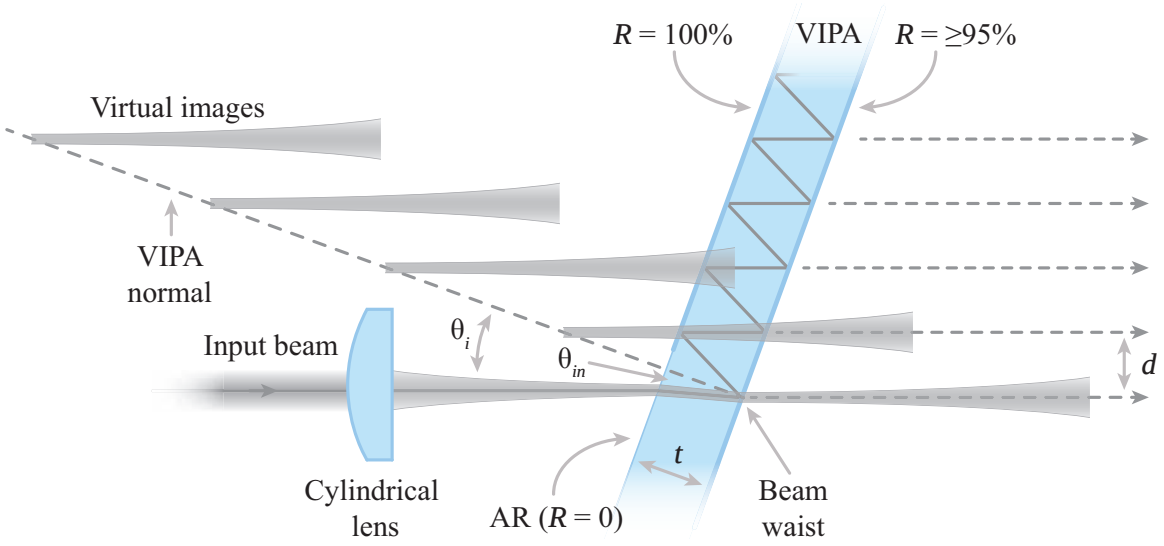

Figure 6.5: Side view of the VIPA system for a *single* input wavelength, showing the internal reflections of the etalon. The glass plate creates many beams diverging from many virtual images of the beam waist. These multiple beams interfere, leaving a collimated beam to be seen in the far-field [255,258].

the transmitted beams must be in phase in order to yield a non-zero output in the far field. When multi-wavelength light is considered, such as that supplied by an optical frequency comb, the input angle of the light is also important. In general, a new wavelength incident at the same angle as the wavelength considered in the single-wavelength case will not satisfy the phase condition, and will destructively interfere away to nothing at the output. However, when presented with a collimated beam, the cylindrical lens provides a large number of incident angles for every wavelength in the beam, and there will therefore be a new set of input and output angles such that the phase criterion is satisfied for the new wavelength and is transmitted. The VIPA therefore acts as a wavelength-dependent dispersion element, in the case of the experimental work presented here arranged to disperse in the vertical direction. The angular dispersion of a solid VIPA etalon of refractive index n_r as a function of wavelength, discussed in a more in-depth manner in Appendix F.1, is given by

$$2kt\left(n_r\cos\left(\theta_{in}\right)-\tan\left(\theta_{in}\right)\cos\left(\theta_i\right)\theta_\lambda-\frac{1}{2n_r}\cos\left(\theta_{in}\right)\theta_\lambda{}^2\right)=2\pi m \quad \text{for } m=1,2,3... \tag{6.7}$$

where $k=(2\pi)/\lambda$ is the angular wavenumber, m is the resonance order, $n_r\sin\left(\theta_{in}\right)=\sin\left(\theta_i\right)$ (Snell's Law), θ_{in} is the internal angle inside the solid etalon resulting from the refraction, θ_i is the VIPA tilt angle, and θ_λ is the angle of the transmitted ray from horizontal as per Xiao *et al.* [259] (c.f. Fig. 6.5). Equation 6.7 describes the phase criterion for a specific wavelength to be transmitted by a solid VIPA etalon, and thus describes the spectral dispersion of the VIPA with angle, with a unique output angle assigned to each wavelength per VIPA Free Spectral Range (FSR).

6.2.2 VIPA Multiple Input Wavelength Behaviour - VIPA Free Spectral Range

The VIPA Free Spectral Range (FSR) is important when interpreting the frequency response in the far-field. Again consider the single-wavelength input into the VIPA system. With enough angular range on the input, it is possible to achieve the phase-matching condition of the transmitted beams for multiple angles of incidence (and hence multiple output angles) as is shown for comb modes A and B in Fig. 6.6 [144,260]. The span of frequencies for a single input angle for a change in VIPA mode order by one $\Delta m = 1$ is then known as the VIPA FSR, given by

$$\mathrm{FSR} = \frac{c}{2t\left(n_r \cos\left(\theta_{in}\right) - \tan\left(\theta_{in}\right)\cos\left(\theta_i\right)\theta_\lambda - \frac{1}{2n_r}\cos\left(\theta_{in}\right)\theta_\lambda{}^2\right)} \tag{6.8}$$

as derived from the VIPA dispersion relation (Eq. 6.7) (see Appendix F.2 for derivation). The VIPA FSR may be estimated by sending a single-frequency source, such as a continuous-wave (CW) laser, through the VIPA system. The CW source will appear once per mode order m, and produce multiple vertical spots at the output of the system corresponding to values of θ_λ that fulfil Eq. 6.8, allowing an estimate of the VIPA FSR. For an input beam with a spectral bandwidth greater than the VIPA FSR, the VIPA output orders are spatially superimposed on one another, leading to a bright vertical stripe of overlapping modes. This peculiarity of the VIPA is dealt with by the introduction of an orthogonally-positioned secondary dispersive element - the diffraction grating - as introduced in Sec. 6.1 at the output of the VIPA etalon. For frequencies separated by one VIPA FSR, the diffraction grating disperses them in the horizontal dimension, converting the superimposed frequencies into many parallel, slightly-tilted stripes separated horizontally by one VIPA FSR. The combination of VIPA and diffraction grating converts the optical frequency comb beam into a two-dimensional spectrograph with complex 'wrapping' behaviour as summarised in Fig. 6.6 [144,257,260].

In the ideal case, each comb mode within a vertical stripe is separated and fully resolved into the repetition rate of the comb (250 MHz in the case of this thesis). Additionally, each of the modes in the horizontal direction is separated by one VIPA FSR (∼50 GHz for these experiments). Each comb mode appears once per VIPA FSR, per VIPA order. One consequence of this is the presence of additional comb modes above those shown in Fig. 6.6, however, this is merely repeated information [144,260].

The comb modes with frequencies f_0 and $f_0 + \mathrm{FSR}$ as shown in Fig. 6.6 are modes with the same input (and hence output) angles with regards to the VIPA etalon. Both frequencies (f_0 and $f_0 + \mathrm{FSR}$) fulfil the VIPA dispersion relation (Eq. 6.7) simultaneously and are spatially superimposed until their separation by the diffraction grating in the horizontal dimension. Additionally, the mode of frequency $f_0 + \mathrm{FSR}$ appears for a second time in the vertical direction as a member of the next VIPA order as shown. The drastically different scales for the VIPA FSR in the horizontal and vertical axes is due to the much higher dispersion

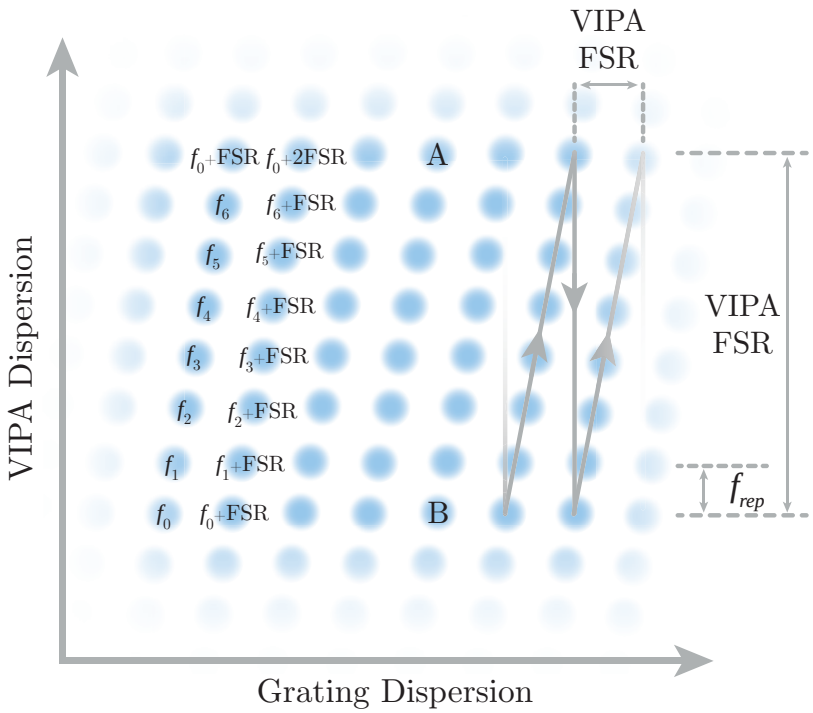

Figure 6.6: The output of the spectrometer system for a frequency comb input is a two-dimensional array of comb modes with frequency indexing as shown. The y-axis, dictated by the VIPA, has a much higher angular dispersion than the x-axis, controlled by the diffraction grating. The comb modes labelled A and B are the same mode, with the same frequency, separated by one VIPA FSR. In this case, full resolution of each comb mode has been assumed for clarity. It has also been assumed that the VIPA FSR is an integer multiple of the comb repetition rate [144,257,260].

of the VIPA compared to the diffraction grating. This shows the reason for including the VIPA etalon in the spectrometer over two orthogonal diffraction gratings. Additionally, the wrapping behaviour of the VIPA precludes the use of two etalons arranged orthogonally, as unravelling the coupled behaviour of two etalons for the sheer number of frequencies in an optical frequency comb would be problematic. Discussion so far has focused on a system in which each comb mode is individually resolvable. Though the dispersion of the VIPA is much larger than that of the diffraction grating by a factor of 10-20, the comb modes spaced by 250 MHz are not able to be resolved by the VIPA, with an experimentally measured resolution of 2 GHz [255,257,259]. For this reason the modes of the frequency comb are often rarefied during the course of this thesis by use of an optical cavity as will be discussed in Chapter 7 to produce fully-resolved modes. After the combination of VIPA and diffraction grating disperses the comb light into a two-dimensional array, the dispersed beam is sent to the final element of the spectrometer - the InGaAs camera.

6.3 InGaAs Camera

The camera is the final component of the spectrometer, and is used to record the images that are later processed into spectrographs. Care must be taken with the calibration and use of the camera to ensure accuracy of the images and the final results, and the camera chosen carefully to ensure high sensitivity in low photon-count regimes. The camera used throughout this thesis is a Xenics XEVA-1.7-320 InGaAs Charged-coupled Device (CCD) array, with sensitivity between $0.9 - 1.7\,\mu$m. The distance between the centres of each pixel, known as the *pixel pitch*, is 30μm for this camera [261]. Each of the 320×256 pixels is formed of a InGaAs photodiode bonded to a CCD. The InGaAs photodiode converts an incoming photon into charge, which is then collected in the potential 'well' of the CCD. This collection continues for an amount of time known as the *integration time*, which may be changed to suit the amount of light falling on the camera. After this integration phase the charges are read out of the wells of the CCD [262].

Readout of CCD arrays is performed either column-wise or row-wise depending on the arrangement of electrodes within the array. Assuming the CCD is read column-wise beginning with the right-most row, the readout begins with the charges being shifted one well to the right, pushing the right-most column off of the array and onto the *serial register* column. The serial register column is then amplified and read one pixel at a time by an Analogue-to-Digital Converter (ADC). The process is repeated, shifting and reading out one column at a time, until all pixels have been read out [263,264]. Each pixel well is capable of handling only a certain amount of charge, known as the *full-well capacity*, and exceeding this amount leads to imaging problems that are discussed in the next section [264,265].

6.3.1 Pixel Saturation and Leakage

The CCD of each pixel may only collect up to the full-well capacity of charge. If the amount of charge exceeds this amount, then the extra charge may leak into adjacent pixels in the row [265]. This scenario should be avoided particularly when imaging high-contrast scenarios within a confined number of pixels as is the case in this thesis.

In addition to this type of saturation, the readout ADC may also become saturated when the conversion of the analogue number to a digital one requires a digital number larger than is able to be stored in the available number of bits [264]. The camera used in this thesis is 12-bit. The maximum number able to be stored in an n-bit unsigned integer is $2^n - 1$ assuming counting beginning at zero [266]. Therefore the maximum digital number able to be handled by the camera used in this thesis is $2^{12} - 1 = 4095$. Care must be taken to avoid these two saturation scenarios, with the integration time adjusted to ensure operation away from these regimes. Conversely, the integration time should not be drastically reduced, as this compromises the signal-to noise ratio of results. However, even with no photons falling onto the camera there is signal recorded across the CCD array, due to what is known as *dark*

current.

6.3.2 Dark Current

Dark current is the result of operating a CCD at a temperature above 0 K, and occurs without the presence of light on the camera. Thermal excitation causes electrons from the bulk material part of the CCD array to become free, and some may be collected in the potential wells of the pixels [265]. This results in a charge in each pixel even in the absence of light, and is indistinguishable from the real photo-electrons. There is typically some spatial variation across the array with regards to this dark current, which results in a background pattern overlay on the measured image for a constant temperature and integration time [264]. As this dark current is thermal in nature, cooling the CCD array reduces the generation of free electrons and therefore the dark current [265,267]. For this reason the camera used in this thesis makes use of active cooling. Additionally, a reduction in integration time gives less time for this charge to accumulate, but must be balanced with adequate signal to noise [264]. In order to remove the residual effects of the dark current from images, dark frames - those in which no light falls onto the camera - were acquired with integration times matching the 'bright' image. The dark image was subtracted from the bright image, resulting in a dark-current corrected final image [264]. This process is shown in Fig. 6.7. Additionally, there is some variation between the response of each pixel, and a certain proportion will respond abnormally. These pixels are known as *dead* or *bad* pixels.

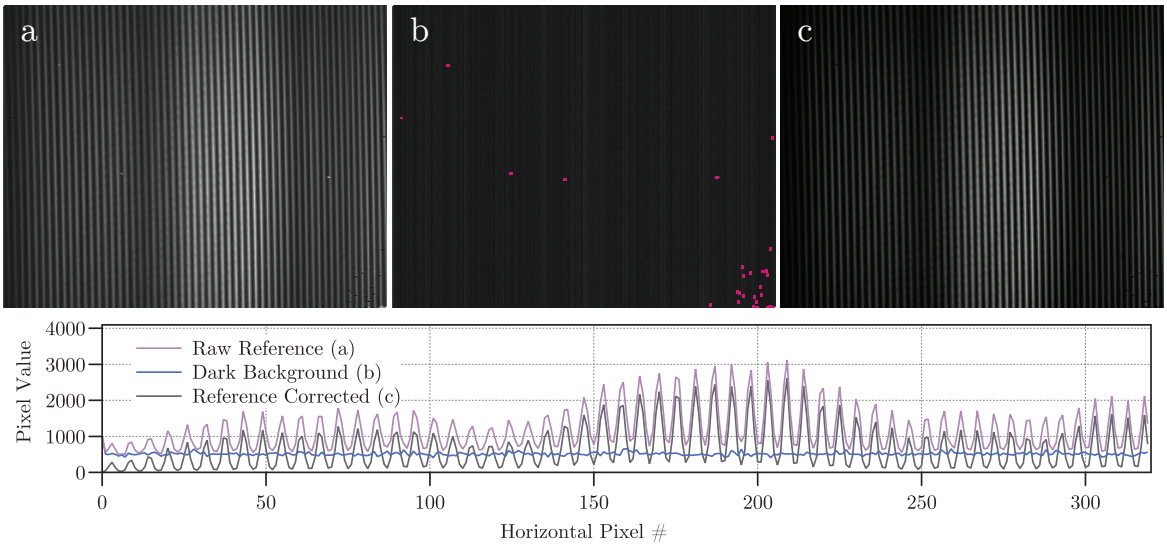

Figure 6.7: a) The raw bright image from the experiment, b) the raw dark image acquired at the same integration time, c) the bright image with the dark image subtracted to remove the effects of the dark current. Some dead and bad pixels may be seen in all three images, highlighted in pink in b). A graph of the horizontal cross section for vertical pixel 150 (bottom) shows the effects of dark current and its correction.

6.3.3 Dead Pixels and Bad Pixels

Each CCD array will posses some pixels that respond abnormally. If a pixel is completely unresponsive to light falling upon it, it is known as a dead pixel. Such pixels often return zero or infinite values when readout is attempted. Another type of abnormal pixel is commonly referred to as a *bad* pixel. These pixels are those that still respond to photons, but not in a consistent manner that is useful. Such pixels include those that flicker rapidly between random values, or have such high background values that the dynamic (useful) range of the pixel is reduced to little worth [265]. The native software of the camera attempts to remove these pixels in a 'bad pixel map' and replaces their values with the average of the surrounding pixels [268]. When the camera was interfaced with the acquisition code, this was abandoned in favour of removing the dead pixels from the final spectral results, as their location is extremely evident at that stage. In addition to dealing with the dead pixels, the acquisition code also corrects for slight nonlinearities in pixel response.

6.3.4 Nonlinearity Correction - Averaged Correction

CCD arrays have extremely good linearity over the majority of their range, with the degree of nonlinearity increasing as saturation conditions are approached [265,267]. However, for quantitative imaging such as that performed in this thesis, the degree of linearity must be exceptionally high so that the molecular absorption features are of the correct depth. This is particularly an issue in regions of the camera where the absorption features are strong. For single-shot images and the spectra generated from them, a 'screen-averaged' linearity correction is adequate to ensure the correct depths of the absorption features.

To determine the correction curve, many images were acquired (bright along with their dark counterparts with matched integration times) for different laser powers directed at the camera with the same integration time. The camera was equipped with a Teflon diffusion screen and the laser was directed out of a fibre with no collimator connected, such that the laser light was relatively evenly spread across the CCD array. A fibre-coupled variable attenuator allowed control of the beam power incident on the camera, and was measurable with a photodetector. As energy is defined as power multiplied by time, the average pixel value recorded may be assigned an energy value, resulting in the correction curve seen in Fig. 6.8. Note that the dark background removal reduces the dynamic range of the camera.

If the camera response was linear, this response function would be a straight line. However, a fifth-order polynomial fit to this line makes the nonlinearity apparent. In order to correct the images with this averaged correction, as is performed in Chapter 10, the dark background must first be subtracted. A custom program then takes the dark current corrected images and uses the fit to Fig. 6.8 to return the corrected energy for each pixel value. This results in a high degree of linearity, as is also demonstrated by the linearity of returned concentration values of $^{12}CO_2$ over the entire concentration (and hence absorption depth) range as examined

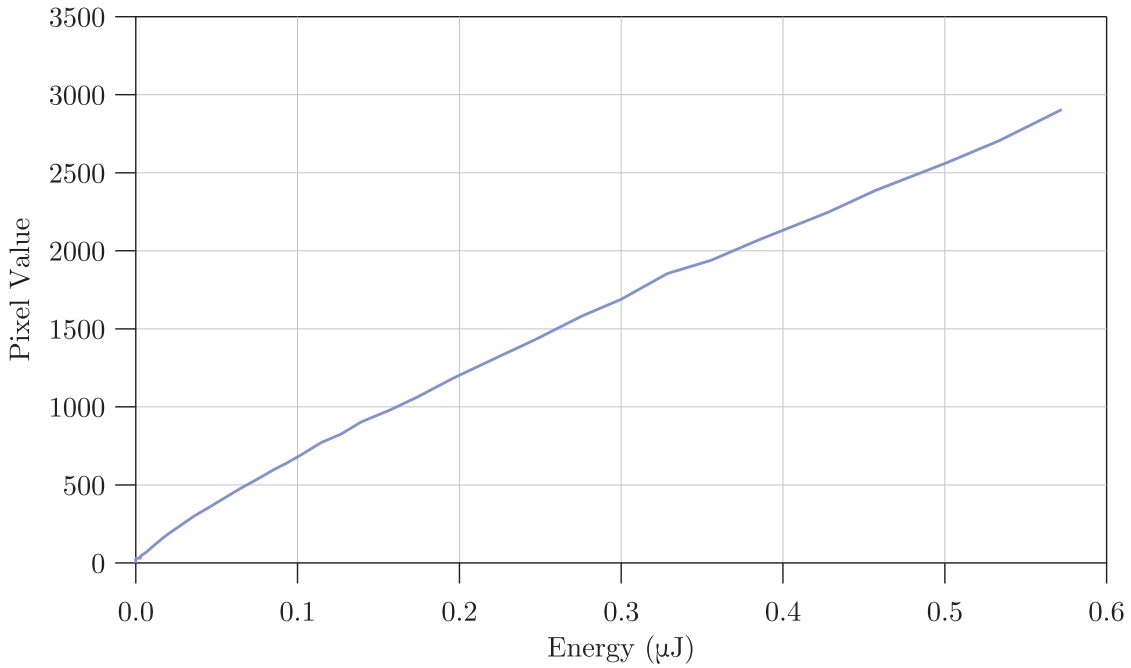

Figure 6.8: The camera nonlinearity correction curve resulting from taking a screen-average of pixel values for each measured optical power and a fixed integration time. Note that the dark background subtraction makes the graph pass through zero, but reduces the dynamic range of the camera.

in Chapter 10. It is only when averaging many hundreds to thousands of results that the noise is suppressed to levels in which the failure of this type of nonlinearity correction becomes apparent, pointing to the need for a pixel-by-pixel approach.

6.3.5 Nonlinearity Correction - Pixel-By-Pixel

Each pixel in the CCD array responds in a slightly different manner. While an average nonlinearity correction is adequate in most scenarios, the different responses of each pixel becomes apparent in the spectra produced from many images averaged together, where differing the molecular absorption relative peak heights become distorted on the $\sim 0.5\%$ level. Again returning to the definition of energy as power multiplied by time, the nonlinearity correction curve may be acquired for each pixel by maintaining the power level on the camera during calibration and changing the camera integration time. This method was applied, producing 1400 calibration points for each pixel from 1400 images taken over the entire range of integration times used with the camera ($100 - 140,000\,\mu$s). The response for each pixel was then fitted with a seventh-order polynomial. This resulted in 320×256 linearity correction polynomials, with their coefficients stored in a matrix for later correction computation efficiency.

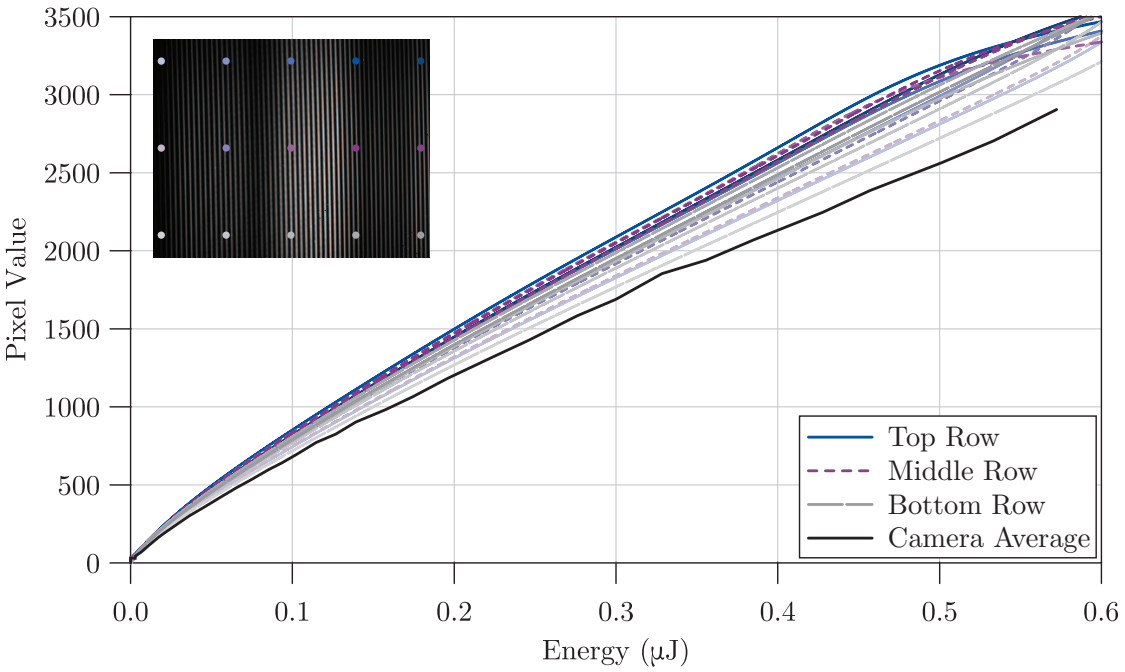

Figure 6.9: Nonlinearity correction curves for 15 pixels spread across the CCD array compared to the screen-average correction (black solid line). Each pixel is colour coded to its correction graph (inset), shown with the top row (solid line), middle row (short dash) and bottom row (long dash) corrections. Each pixel requires a different correction for nonlinearity, applied after dark background subtraction.

The correction is then applied in the same way as for the averaged case, except with each pixel having its own correction polynomial. The pixel-to-pixel variation in the nonlinearity correction is appreciable, as can be seen in Fig. 6.9, which shows the correction polynomials for 15 individual pixels spread across the CCD array compared to the old correction. The pixel-by-pixel correction to the nonlinearity was applied to achieve the results in Chapter 11. Now that the final piece of the spectrometer has been introduced, operation of the spectrometer as a whole and may be considered, particularly how the individual pictures are converted into more traditional absorption spectra.

6.4 Converting 2D Images into Spectra

The three vital components of the VIPA spectrometer introduced in this Chapter - the diffraction grating, VIPA etalon, and the InGaAs camera, combine together to form the VIPA spectrometer as seen in Fig. 6.1. Communication with the camera and control of light reaching the spectrometer is coordinated by a series of wrapper functions called by an overarching Matlab script. This script controls the optical shutters on each of the possible spectrometer paths and all communications with the camera including automatic integration time adjustment and image acquisition. The set of images are then converted into a traditional spectrum. At a minimum, four images are required to produce this spectrum - a bright and

dark image of the comb passing through the gas sample (the signal path) with matched integration times, and the same for a reference path that bypasses the gas and is used for optical comparison.

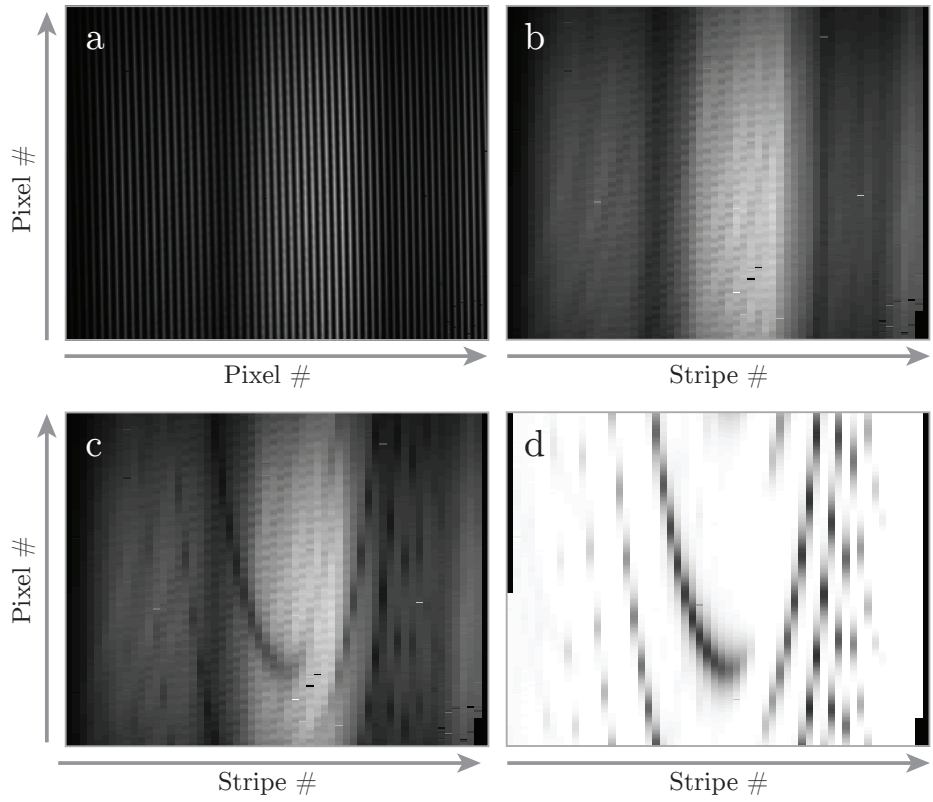

Figure 6.10: a) A reference path image after background subtraction and nonlinearity correction. b) The same image after matched filtering, with each VIPA vertical stripe collapsed down into one horizontal pixel. c) The signal path image after the same filtering has been applied. d) The filtered transmission image created by the division of the filtered signal image by the filtered reference image. Any errant optical aberrations and background issues common to the reference and signal paths are removed by this division, resulting in a clear molecular absorption signature (dark regions) against a clean background (white). This image may then be unwrapped into a traditional absorption spectrum as seen in Fig. 6.11.

As mentioned in Subsection 6.3.2, the first step is to subtract the dark images to reduce the effects of dark current. Each image must then be corrected for nonlinearities in the pixel response, either by a screen-averaged correction (Subsection 6.3.4) or the pixel-by-pixel case (Subsection 6.3.5). What happens next depends exactly on the comb light presented to the spectrometer and whether the spectrometer is able to fully resolve the frequency comb. In the case where the full comb is presented and the spectrometer is not able to resolve the individual comb modes, the images consist of a series of bright slightly-tilted vertical stripes. The tilt of the stripes is found using a spatial Fourier transform, from which the centres of each stripe may be found across the entire image. Fitting indicates that the horizontal cross-section of each stripe is well approximated by a Gaussian profile that spans several pixels, centred on the previously found stripe centres. A series of Gaussian functions are created for

each stripe in each pixel row, and are used as matched filters for both the signal and reference images. This results in one representative brightness point for each row of each stripe as seen in Fig. 6.10b. The use of matched filtering minimises any possible cross-talk effects between adjacent stripes to below the level of measurement noise, and maximises the signal to noise ratio.

The set of matched filters derived from the reference path image are then applied to the corresponding background and nonlinearity-corrected signal path image (Fig. 6.10c), resulting in a filtered image for each path. Division of the filtered signal image by the filtered reference image divides out optical aberrations that are common to both paths. This results in a transmission image with clear molecular absorption features, and a clean background as seen in Fig. 6.10d. The final filtered transmission image may then be unwrapped and plotted to deliver the traditional molecular transmission spectrum. This image analysis process converts the bright vertical VIPA stripe images into an absorption spectrum, with each VIPA stripe contributing 50 GHz of the spectrum as seen in Fig. 6.11.

This chapter has focused on acquiring a correctly calibrated absorption measurement of the gas. In the next chapter we consider how to obtain a high quality mapping of position on the CCD array to frequency.

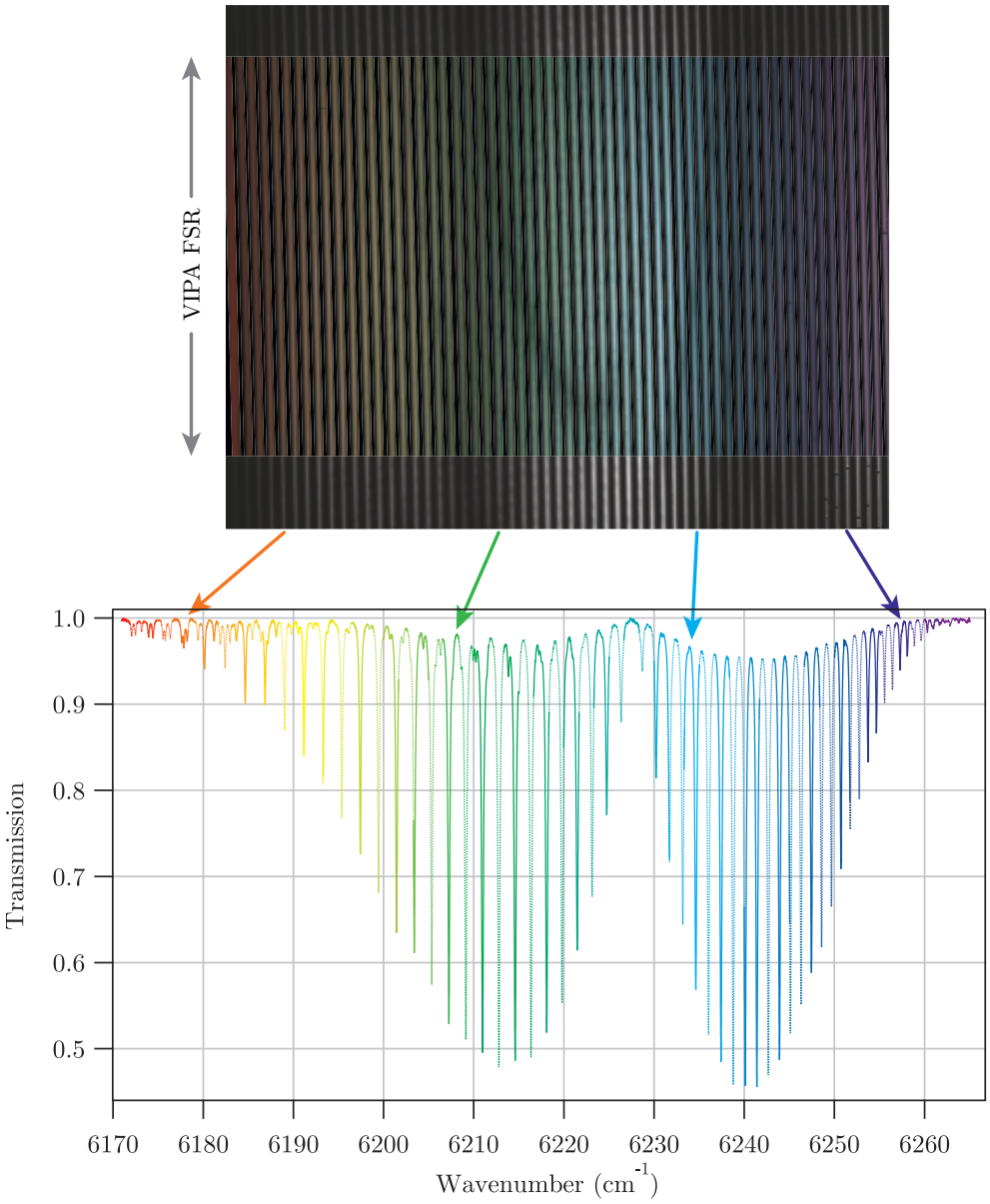

Figure 6.11: Each VIPA stripe contributes one VIPA FSR (50 GHz) to the final transmission spectrum. Each VIPA stripe has been colour-coded to match the segment of transmission spectrum it becomes after the image analysis process. Every second FSR segment is dashed for clarity. There are typically on the order of 60 VIPA stripes in one image.

Frequency Axis Calibration and Comb Decimation: Fabry-Pérot Optical Cavities

Optical cavities are useful tools for both spectral absorption enhancement by increasing the interaction path length or, as used in this thesis, to perform spectral filtering [269]. The physical arrangement of the cavity mirrors that form the optical resonator along with their reflectivity are of particular importance to understand the spectral filtering behaviour of an optical cavity. This chapter focuses on the design and behaviour of Fabry-Pérot (FP) cavities, and their application as spectral filters to enable relative frequency calibration of the VIPA spectrometer when used with an optical frequency comb.

7.1 Cavity Construction and Stability

In a similar fashion to the resonant cavities discussed in the creation of an optical frequency comb in Chapter 5, the FP cavity is constructed of two high-reflectivity mirrors spaced by a specific distance L [227,228,230]. A partially-reflective input coupler (one of the mirrors) allows light into the cavity, which then traverses the cavity length, and strikes the far mirror. At this point a portion of the light leaks out the far mirror while the majority is reflected back toward the input mirror, interfering with the oncoming light. In order for light to resonate within the cavity this interference must be constructive, which occurs when the cavity length is equal to an integer number of half-wavelengths. That is, when

$$L = m\frac{\lambda}{2n}, \tag{7.1}$$

where m is a positive integer (the resonant longitudinal mode order) and n is the refractive index of the intracavity medium [204,224,227,230].

7.1.1 Resonator Stability

The stability of an optical cavity is related to the divergence of light within the cavity. Consider a cavity with two opposing flat mirrors. Initially, resonant light bounces between the mirrors. However, due to diffraction the beam diverges, growing wider with every pass of the optical cavity. Eventually its width exceeds the dimensions of the mirrors and is lost [162,204]. The use of two curved mirrors with radii of curvature R_1 and R_2 respectively ensure that the beam is periodically refocused within the cavity and so never exceeds the

mirror dimensions. If this is the case, the resonator is called *stable* [204]. The stability of a FP optical cavity is summarised by its stability criterion:

$$0 \leq g_1 g_2 \leq 1 \tag{7.2}$$

in which g_1 and g_2 are the *stability parameters* of the two mirrors that form the cavity [202,204,228,230]. The stability parameters are related to the mirror separation and radii of curvature through

$$g_1 = 1 - \frac{L}{R_1},\ g_2 = 1 - \frac{L}{R_2}. \tag{7.3}$$

In the case of a symmetric cavity where the mirrors are identical ($R_1 = R_2$), this simplifies further to $0 \leq g^2 \leq 1$. Any resonator design that fulfils Eq. 7.2 will be stable.

7.1.2 Construction

The cavity used throughout this thesis is of symmetric construction with $L = 1.58\,\text{cm}$, which may be finely tuned by use of a piezoelectric transducer affixed to one mirror, and coarsely tuned by screwing the second mirror in and out of the main cavity housing. Both mirrors have a radius of curvature of $R = 50\,\text{mm}$ and a reflectance $r^2 = 98 \pm 0.75\,\%$, yielding a stability criterion of a $g^2 = 0.468$. Both mirrors are plano-concave with a 12.7 mm diameter. Now that a stable optical cavity has been created, we must now consider the behaviour of such a cavity in terms of its output.

7.2 Output of a Fabry-Pérot Optical Cavity

When considered in the frequency domain, the transmission function of a FP cavity, $\mathcal{T}(f)$, is a series of peaks with strictly defined width and frequency-separation [124]. There are two important parameters that govern $\mathcal{T}(f)$, the first of which is the free spectral range.

7.2.1 Free Spectral Range

The free spectral range (FSR) is the separation in frequency between adjacent transmission peaks (or longitudinal modes) of the cavity [124]. Equivalently, it is the difference between adjacent longitudinal mode orders m in Eq. 7.1, which when converted to frequency gives the defining equation of the FSR:

$$\text{FSR} = \frac{c}{2nL} \tag{7.4}$$

in which n is the intracavity refractive index, c is the speed of light in vacuum, and L is the cavity length [227]. The rarefication cavity is specifically-designed to have an FSR of 9.5 GHz for optimal spectral filtering of the frequency comb. The final parameter required to understand the transmission function of the optical cavity is the bandwidth of each transmission mode, which is determined by the *finesse*.

7.2.2 Cavity Full-width-at-half-maximum and Finesse

The finesse $\mathcal{F}$ of an optical cavity is the ratio of the separation between the transmittance peaks of the optical cavity - i.e. the FSR - to the full-width-at-half-maximum (FWHM) of said peaks [124]. For a spectral filter, we are interested in the FWHM of the cavity transmission function at different mode orders more so than $\mathcal{F}$, so the equation for $\mathcal{F}$ is often seen as [228,229]:

$$\text{FWHM} = \frac{\text{FSR}}{\mathcal{F}}. \tag{7.5}$$

The finesse and hence FWHM is related to the reflectance of the mirrors, assuming a symmetric cavity, by

$$\mathcal{F} = \frac{\pi r}{1 - r^2}. \tag{7.6}$$

The relation between the FSR, $\mathcal{F}$, and FWHM of the transmission peaks for a FP optical cavity may be seen in Fig. 7.1 [204,228,229].

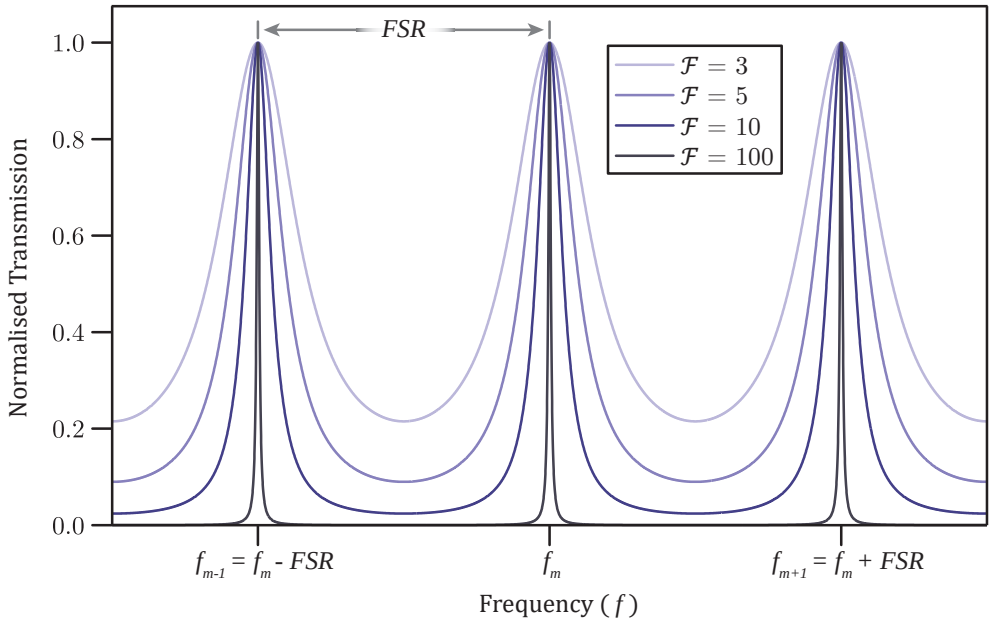

Figure 7.1: The normalised Fabry-Pérot transmission function $\mathcal{T}(f)$ for various $\mathcal{F}$ values for cavity longitudinal mode order m. Increasing $\mathcal{F}$ produces narrower transmission features. The FSR is also shown.

The optical cavity must therefore be carefully designed in terms of the length, curvature and coatings of the mirrors, and refractive index of the intracavity medium in order to achieve the desired result. For the required comb rarefication presented in this thesis, the finesse must be relatively low, while the FSR must be carefully controlled to equal a specific integer multiple of the optical frequency comb's repetition rate.

7.2.3 Optical Cavity Transmission Function - Spectral filtering

One of the major uses of optical cavities is their ability to act as spectral filters, whereby they only transmit those frequencies that are resonant with the cavity. As seen in Chapter 6, the VIPA spectrometer does not have sufficient resolution to resolve individual comb modes. This prevents accurate assignment of the frequencies of the comb to positions on the camera, and precludes a calibrated frequency axis. However, use of an optical cavity to sufficiently rarefy the comb such that the spectrometer may resolve individual comb modes restores this ability. With such knowledge, a relative frequency may then be assigned to each comb mode on the rarefied image captured by the spectrometer, and an accurate frequency approximation made for the non-rarefied images. In order to achieve this, the FSR of the cavity must be set to an integer multiple of the comb's repetition rate f_{rep}:

$$\text{FSR} = n f_{\text{rep}} \tag{7.7}$$

where n is a positive integer [269]. Through experimental investigation, it was found that there are two values of n for which optimum comb mode separation occurs with minimum cross-talk with the current apparatus: $n = 36$ and $n = 38$, corresponding to FSRs of 9 GHz and 9.5 GHz respectively. Other values of n such as $n = 37$ and $n = 40$ that are within tuning range of the cavity produce inadequate separation of transmitted modes with respect to adjacent VIPA stripes. The cavity-rarefication process and result is summarised in Fig. 7.2.

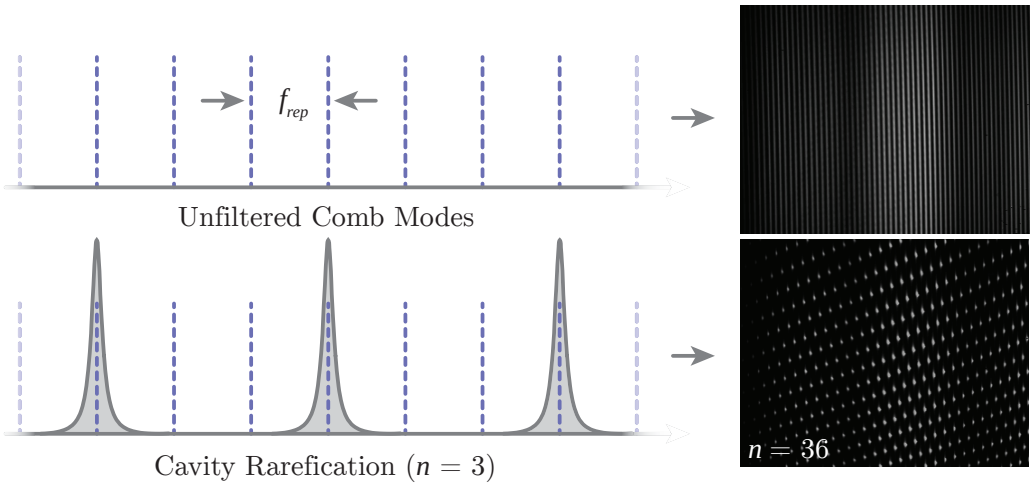

Figure 7.2: The process and imaged results of rarefying the frequency comb using an optical cavity.

Additionally, the finesse of the cavity must be carefully chosen. As seen in Fig. 7.1, if $\mathcal{F}$ is too low, the large wings of the cavity transmission function do not approach zero. If such as low finesse cavity were used with the comb, adjacent comb modes would not be completely suppressed, leading to adjacent comb modes leaking through together with the targeted modes. Conversely, increasing $\mathcal{F}$ reduces the range of comb modes simultaneously resonant with the cavity (see Appendix E).

7.2.4 Cavity Transmission Function

The full expression for $\mathcal{T}(f)$ of a Fabry-Pérot cavity is known as the Airy Function:

$$\mathcal{T}(f) = \frac{\mathcal{T}_{max}}{1 + \left(\frac{2\mathcal{F}}{\pi}\right)^2 \sin^2\left(\frac{\pi f}{\mathrm{FSR}}\right)} \tag{7.8}$$

where $\mathcal{T}_{max}$ is the maximum transmission fraction of the cavity at resonance [124,221,269]. Equation 7.8 may be used to determine the minimum value for $\mathcal{F}$ to achieve adjacent comb mode rejection is at least 98%. Setting $\mathcal{T}(f) = 0.02$ (2% in transmission) at a frequency $f = 250\,\mathrm{MHz}$, with $\mathcal{T}_{max} = 1$ and $\mathrm{FSR} = 9.5\,\mathrm{GHz}$ gives $\mathcal{F} = 133$. Therefore a finesse of at least 133 is required to achieve 98% rejection of adjacent comb modes. Rearrangement of Eq. 7.6 indicates this is achieved with a mirror reflectance of $r^2 \geq 97.7\%$. The mirrors that form the cavity have a stated reflectance of $r^2 = 98\% \pm 0.75\%$, producing an expected finesse of $\mathcal{F} = 155^{+92}_{-42}$ within the wavelength range of $1450\text{-}1650 \pm 10\,\mathrm{nm}$, which falls within the errors of the experimentally measured value of $\mathcal{F} = 192 \pm 5$ [270]. This results in an optical cavity with suitable adjacent comb mode extinction and allows rarefication of the optical frequency comb, with the result at the spectrometer shown in Fig. 7.3. The frequency spacing between each transmitted comb mode is then the FSR of the cavity. Combined with knowledge of the spatial locations of unrarefied VIPA lines this can then be used to generate a calibrated frequency axis across the whole image, and therefore the transmission spectrum. However, in order for the cavity to be used to generate a rarefied frequency comb the FSR of the cavity must be maintained. This is achieved by active stabilisation of the length of the cavity.

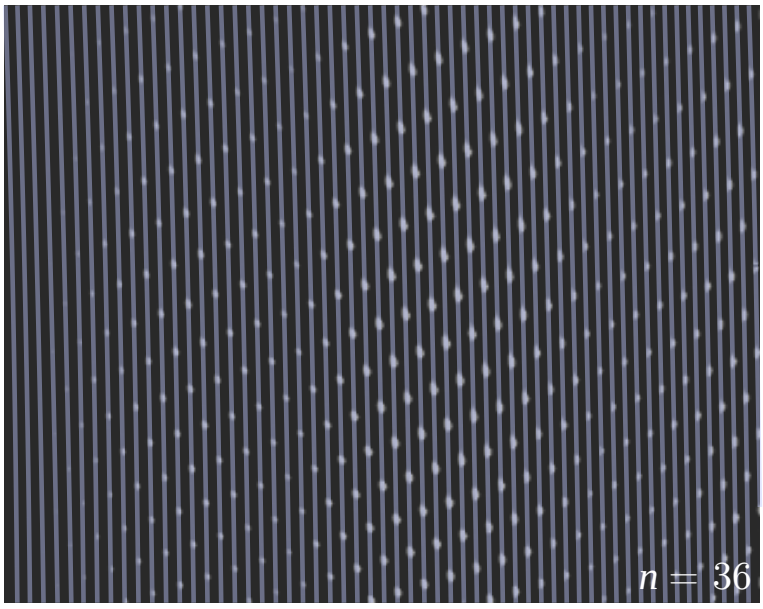

Figure 7.3: The rarefied optical frequency comb with $n = 36$ as imaged by the spectrometer (greyscale), with the positions of unrarefied VIPA lines overlayed. The rarefied image, combined with knowledge of the VIPA line position in the unrarefied case, allows generation of a calibrated frequency axis in transmission spectra.

7.3 Rarefication Cavity Stabilisation

In order to ensure maximum and stable transmission through the rarefication cavity, an active feedback loop is employed to maintain its length. As mentioned in Sec. 7.1, one of the cavity mirrors is mounted on a voltage-controlled piezo-electric transducer, which allows rapid control of the length of the cavity over a short range. If the length of the cavity is then slowly swept, a characteristic envelope with fine structure may be measured using a photodetector at the output of the cavity. The output of the photodetector during one such scan is shown in Fig. 7.4.

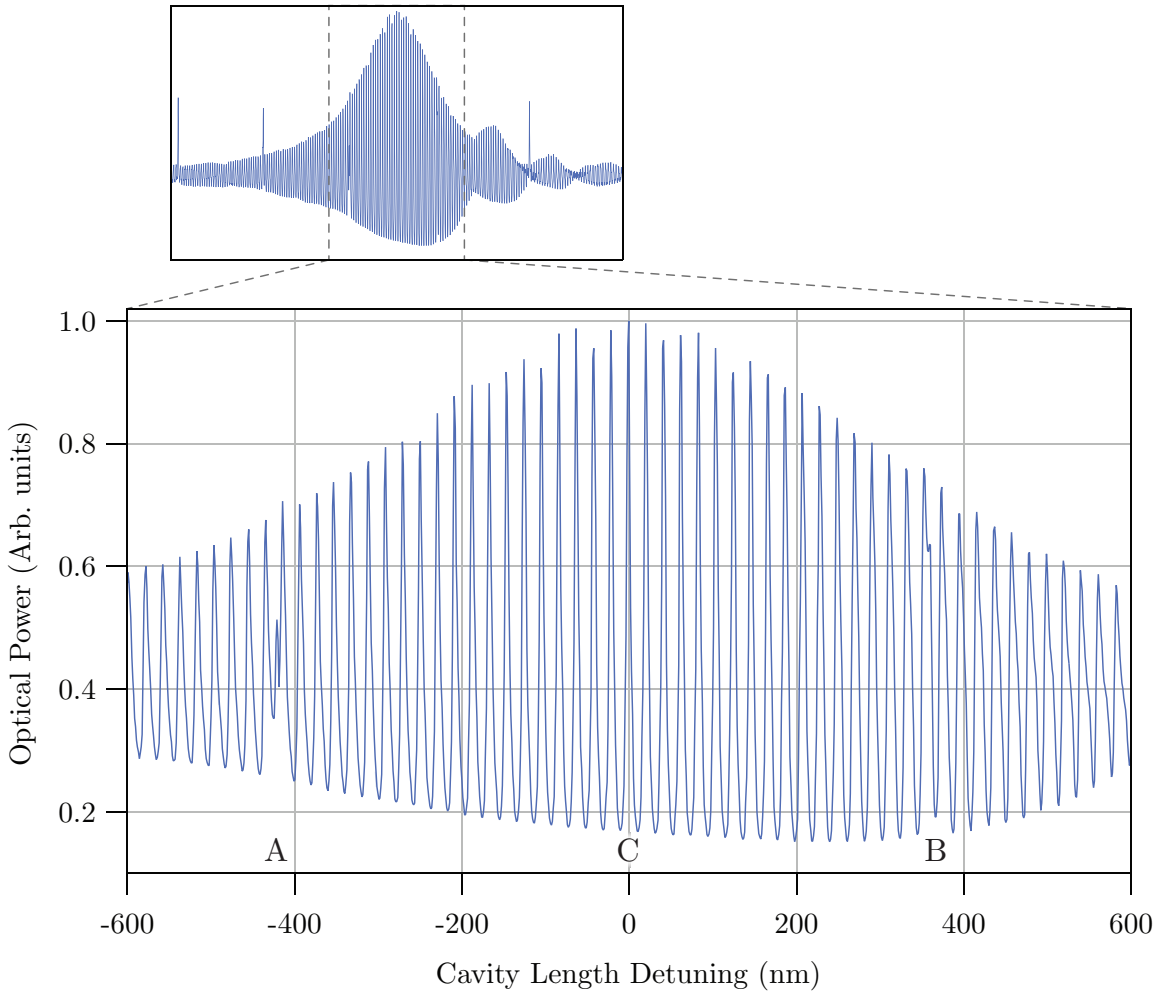

Figure 7.4: Rarefication-cavity transmission as a function of cavity length detuning from $L = c/(2\text{FSR})$ for FSR= 9.5 GHz. Positions A and B denote transmission of the 1560 nm laser by the cavity, and there are 38 local maxima between A and B corresponding to optimal transmission of the 38 unique decimated comb subsets with 9.5 GHz mode separation. Position C corresponds to the maximum number of comb modes being resonant with the optical cavity at an FSR of exactly 9.5 GHz.

In order to deduce the FSR of the cavity, a 1560 nm laser (Koheras Adjustik) is introduced to the cavity along with the comb, producing obvious disruptions to the smoothly varying

fine structure features in Fig. 7.4. The regions between two such disruptions is the FSR of the cavity, and there are 38 such peaks between each transmission of the 1560 nm laser. A detailed discussion about the generation of this envelope and its fine structure may be found in Appendix E. In simpler terms and assuming a perfect filter cavity, the fine structure observed in Fig. 7.4 corresponds to the 38 individual comb subsets (for a cavity FSR of 9.5 GHz) each separated by f_{rep}.

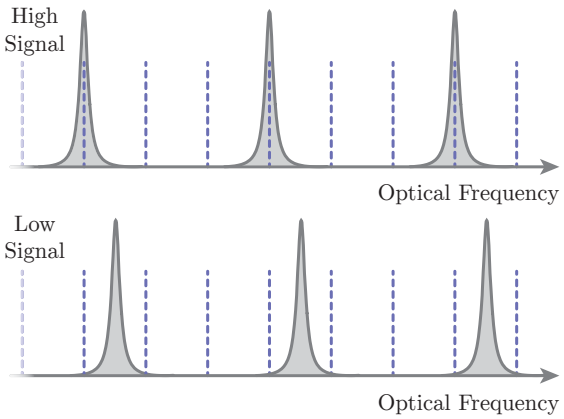

Figure 7.5: Top: matching every 3$^{\text{rd}}$ mode of the optical frequency comb (dotted) with the modes of an idealised filter cavity (solid), in a position corresponding to good alignment, a high signal at the photodetector at the cavity output, and a peak in Fig. 7.4. Bottom: the filter cavity's passbands shifted to poor alignment and low photodetector signal, corresponding to a trough in Fig. 7.4.

As seen in Fig. 7.5, when the modes of the frequency comb align well with the maxima of the idealised cavity transmission function for every n^{th} comb mode, a high signal is produced at the photodetector. This corresponds to a peak in the fine structure and the majority of a cavity-rarefied image being 'bright' (though still decimated). Conversely, when the cavity length is changed slightly, producing a poor alignment between the comb modes and cavity transmission function, the photodetector signal is low and a trough in Fig. 7.4 results. There will be 38 such peaks in the case of a cavity FSR of ~ 9.5 GHz, with an optimally tracking FSR of 9.5 GHz corresponding to position C in Fig. 7.4. In order to achieve the largest number of rarefied modes simultaneously resonant with the cavity for the chosen FSR, the photodetector signal at the output of the cavity is used to generate an error signal for a cavity dither lock to maintain cavity transmission around the global maximum (labelled C) in Fig. 7.4. The slow scan is disabled while locking and the drop off of the overall envelope in Fig. 7.4 is explained in Appendix E.

The length of the FP cavity is dithered around the global maximum position using a 10 kHz signal generated by an Arduino Due board. We use this board to also implement the cavity stabilisation. A photodetector at the output of the cavity detects the cavity transmission power, which is directed through a band-pass filter before sampling by the Arduino board. The Arduino then digitally mixes this signal with a copy of the 10 kHz dither to demodulate the photodetector signal before a low-pass filter is applied. This generates an error signal with zero crossings at each of the 38 cavity transmission maxima of Fig. 7.4. This

error signal is then passed through a proportional-integral (PI) loop filter in the Arduino before being combined with the 10 kHz dither signal, which are then sent together to the piezo-electric transducer on which one of the cavity mirrors is mounted. In this way, any deviation from the maxima of cavity transmission is corrected via the feedback loop moving the cavity mirror, maintaining a high and stable cavity transmission.

This rarefication cavity and its stabilisation system is used for each of the experiments presented in Part IV, though the manner in which the cavity is utilised in each experiment differs greatly. It was most commonly used to generate a calibrated frequency axis, but has also seen use to effectively produce a comb with a larger f_{rep} for fully-resolved comb spectroscopy. The stabilisation code running on the Arduino is presented in Appendix G.

7.3.1 Spectrometer Instrumentation Broadening

Until now, we have assumed that the measured spectrum is determined by the molecules themselves responding to their local environment. The experiment actually measures the convolution of the molecular response with that of the instrumental response function [271,272]. The rarefication cavity allows the instrumental response function to be measured and quantified by fitting each comb mode as analysed by the image analysis code with a 2D Voigt profile across the entire CCD array. In this thesis, the instrumental broadening was measured to have both Gaussian and Lorentzian components of $0.01 \pm 0.001\,\mathrm{cm}^{-1}$ ($1/e$ half-width) and $0.006 \pm 0.001\,\mathrm{cm}^{-1}$ (half-width-at-half-maximum) respectively, as measured by this fitting of rarefied comb images.

Part IV

Results

A Quantitative Mode-resolved Frequency Comb Spectrometer

This chapter is based on the published article:

N. Bourbeau Hébert, S. K. Scholten, R. T. White, J. Genest, A. N. Luiten, and J. D. Anstie, "A Quantitative Mode-Resolved Frequency Comb Spectrometer", *Optics Express* **23**, 13991-14001 (2015).

8.1 Overview and Motivation

The aim of this paper was to demonstrate the direct comb spectroscopy technique described in Chapter 6. Additionally, new image processing software was needed and developed in the course of this paper to convert images of the optical frequency comb as they appeared at the output of the spectrometer into more traditional molecular absorption spectra. VIPA spectrometers had been used previously with optical frequency combs spanning different spectral regions [144,260,273], however the larger repetition rate of such combs allowed for immediate resolution of individual comb modes. This paper used a tunable rarefied version of the comb to interrogate the sample by use of a Fabry-Pérot optical cavity. This allowed us to overcome the VIPA resolution limit and provide higher-resolution spectra. Other cavity-comb systems known as Vernier comb spectrometers had seen use previously, with a dispersive spectrometer based on moving optical elements rather than a VIPA spectrometer [146,147].

Additionally, the cavity-stabilisation procedure used in this paper and many that follow was developed. More papers performing spectroscopy with a rarefied optical frequency comb as described in this paper were published [274] and it remains an active field of research. The performance of the spectrometer in terms of the expected line centres and line widths of the hydrogen cyanide sample was verified by comparison to previous high-precision absorption measurements in the same molecular absorption band. Additionally, the rapidity of direct comb spectroscopy was demonstrated, with a full spectrum of 250 MHz resolution acquired in under 8.2 seconds.

The stabilisation procedure for the optical cavity and knowledge of the spatial dispersion behaviour of the VIPA spectrometer were utilised in future papers presented in upcoming chapters. Additionally, the analysis code from this paper was developed further after the publication of this paper so that the rarefied optical frequency comb could be used to cali-

brate the frequency axis in measurement cases below the VIPA resolution limit. This is also demonstrated in future papers.

8.2 Statement of Contribution

8.2.1 Conceptualisation

The idea of using a tunable optical cavity to produce a rarefied optical frequency comb with an essentially increased repetition rate was conceptualised by James Anstie. The method to achieve this was conceptualised by James Anstie and Sarah Scholten.

8.2.2 Realisation

The first iteration of the spectrometer and analysis code was created by James Anstie and Richard White. The bulk amount of construction, design, and characterisation of the remaining optical experiment was performed by Sarah Scholten, with modification by Nicolas Bourbeau Hébert. The initial stabilisation system was joint effort between James Anstie and Sarah Scholten, with the final Arduino-based locking system the work of Nicolas Bourbeau Hébert under the supervision of Jérôme Genest and James Anstie. The theory of the cavity filtering behaviour as to how the cavity-rarefication functions was a joint effort between James Anstie, Richard White, and Sarah Scholten. The data acquisition procedure, initial camera interface, and a significant addition to the data analysis code was written by Nicolas Bourbeau Hébert under the guidance of Jérôme Genest and James Anstie. Nicolas Bourbeau Hébert additionally acquired the data that appears in the published manuscript.

8.2.3 Documentation

This paper was written primarily by Nicolas Bourbeau Hébert, James Anstie, and Jérôme Genest, with editing by all other authors.

Candidate overall percentage contribution: 50%.

Sarah K. Scholten

8.2.4 Co-author Contributions

By signing below, each co-author certifies that:

- The candidate's stated contribution to the publication is accurate (as stated above).
- Permission is granted for the candidate to include the publication in the thesis.

Co-author certifications are in order of published authorship unless otherwise specified. Nicolas Bourbeau Hébert is the primary author of this paper.

Nicolas Bourbeau Hébert

Richard T. White

Jérôme Genest

Andre N. Luiten

James D. Anstie

A Quantitative Mode-Resolved Frequency Comb Spectrometer

Nicolas Bourbeau Hébert[2], Sarah K. Scholten[1], Richard T. White[1], Jérôme Genest[2], Andre N. Luiten[1] and James D. Anstie[1,*]

[1] *Institute for Photonics and Advanced Sensing, School of Physical Sciences, The University of Adelaide, Adelaide SA 5005, Australia*

[2] *Center d'optique, photonique et laser, Université Laval, Québec, G1K 7P4, Canada*

[*] *james.anstie@adelaide.edu.au*

Abstract:
We have developed a frequency-comb spectrometer that records 35-nm (4 THz) spectra with 2-pm (250 MHz) spectral sampling and an absolute frequency accuracy of 2 kHz. We achieve a signal-to-noise ratio of ∼400 in a measurement time of 8.2 s. The spectrometer is based on a commercial frequency comb decimated by a variable-length, low-finesse Fabry Pérot filter cavity to fully resolve the comb modes as imaged by a virtually imaged phased array (VIPA), diffraction grating and near-IR camera. By tuning the cavity length, spectra derived from all unique decimated combs are acquired and then interleaved to achieve frequency sampling at the comb repetition rate of 250 MHz. We have validated the performance of the spectrometer by comparison with a previous high-precision absorption measurement of $H^{13}C^{14}N$ near 1543 nm. We find excellent agreement, with deviations from the expected line centers and widths of, at most, 1 pm (125 MHz) and 3 pm (360 MHz), respectively.

OCIS codes: (120.6200) Spectrometers and spectroscopic instrumentation; (140.4050) Mode-locked lasers; (300.1030) Spectroscopy, absorption; (300.6390) Spectroscopy, molecular.

References and links

1. S. Spuler, M. Linne, A. Sappey, and S. Snyder, "Development of a cavity ringdown laser absorption spectrometer for detection of trace levels of mercury," Appl. Opt. **39**, 2480–2486 (2000).
2. F. Couto, M. Sthel, M. Castro, M. da Silva, M. Rocha, J. Tavares, C. Veiga, and H. Vargas, "Quantum cascade laser photoacoustic detection of nitrous oxide released from soils for biofuel production," Appl. Phys. B **117**, 897–903 (2014).
3. L. Nugent-Glandorf, F. Giorgetta, and S. A. Diddams, "Open-Air, Broad-Bandwidth Trace-Gas Sensing with a Mid-Infrared Optical Frequency Comb," ArXiv e-prints (2014).
4. S. Y. Lehman, K. A. Bertness, and J. T. Hodges, "Detection of trace water in phosphine with cavity ring-down spectroscopy," Journal of Crystal Growth **250**, 262 – 268 (2003). Proceedings of the Fourteenth American Conference on Crystal Grow th and Epitaxy.
5. H. H. Funke, B. L. Grissom, C. E. McGrew, and M. W. Raynor, "Techniques for the measurement of trace moisture in high-purity electronic specialty gases," Rev. Sci. Instr. **74**, 3909–3933 (2003).
6. M. R. McCurdy, Y. Bakhirkin, G. Wysocki, R. Lewicki, and F. K. Tittel, "Recent advances of laser-spectroscopy-based techniques for applications in breath analysis," Journal of Breath Research **1**, 014001 (2007).
7. M. J. Thorpe, D. Balslev-Clausen, M. S. Kirchner, and J. Ye, "Cavity-enhanced optical frequency comb spectroscopy: application to human breath analysis," Opt. Express **16**, 2387–2397 (2008).
8. T. H. Risby and F. K. Tittel, "Current status of midinfrared quantum and interband cascade lasers for clinical breath analysis," Optical Engineering **49**, 111123–111123–14 (2010).

9. D. Moore, "Recent advances in trace explosives detection instrumentation," Sensing and Imaging: An International Journal **8**, 9–38 (2007).
10. K. C. Cossel, D. N. Gresh, L. C. Sinclair, T. Coffey, L. V. Skripnikov, A. N. Petrov, N. S. Mosyagin, A. V. Titov, R. W. Field, E. R. Meyer, E. A. Cornell, and J. Ye, "Broadband velocity modulation spectroscopy of HfF+: Towards a measurement of the electron electric dipole moment," Chemical Physics Letters **546**, 1 – 11 (2012).
11. F. Adler, M. J. Thorpe, K. C. Cossel, and J. Ye, "Cavity-enhanced direct frequency comb spectroscopy: Technology and applications," Annual Review of Analytical Chemistry **3**, 175–205 (2010).
12. M. J. Thorpe, K. D. Moll, R. J. Jones, B. Safdi, and J. Ye, "Broadband cavity ringdown spectroscopy for sensitive and rapid molecular detection," Science **311**, 1595–1599 (2006).
13. S. Schiller, "Spectrometry with frequency combs," Opt. Lett. **27**, 766–768 (2002).
14. I. Coddington, W. C. Swann, and N. R. Newbury, "Coherent multiheterodyne spectroscopy using stabilized optical frequency combs," Phys. Rev. Lett. **100**, 013902 (2008).
15. J. Roy, J.-D. Deschênes, S. Potvin, and J. Genest, "Continuous real-time correction and averaging for frequency comb interferometry," Opt. Express **20**, 21932–21939 (2012).
16. A. Zolot, F. Giorgetta, E. Baumann, W. Swann, I. Coddington, and N. Newbury, "Broad-band frequency references in the near-infrared: Accurate dual comb spectroscopy of methane and acetylene," Journal of Quantitative Spectroscopy and Radiative Transfer **118**, 26 – 39 (2013).
17. G. Villares, A. Hugi, S. Blaser, and J. Faist, "Dual-comb spectroscopy based on quantum-cascade-laser frequency combs," Nat. Comm. **5**, 6192 (2014).
18. C. Gohle, B. Stein, A. Schliesser, T. Udem, and T. W. Hänsch, "Frequency comb vernier spectroscopy for broadband, high-resolution, high-sensitivity absorption and dispersion spectra," Phys. Rev. Lett. **99**, 263902 (2007).
19. F. Zhu, J. Bounds, A. Bicer, J. Strohaber, A. A. Kolomenskii, C. Gohle, M. Amani, and H. A. Schuessler, "Near infrared frequency comb vernier spectrometer for broadband trace gas detection," Opt. Express **22**, 23026–23033 (2014).
20. L. Rutkowski and J. Morville, "Broadband cavity-enhanced molecular spectra from vernier filtering of a complete frequency comb," Opt. Lett. **39**, 6664–6667 (2014).
21. M. Siciliani de Cumis, R. Eramo, N. Coluccelli, M. Cassinerio, G. Galzerano, P. Laporta, P. De Natale, and P. Cancio Pastor, "Tracing part-per-billion line shifts with direct-frequency-comb vernier spectroscopy," Phys. Rev. A **91**, 012505 (2015).
22. S. A. Diddams, L. Hollberg, and V. Mbele, "Molecular fingerprinting with the resolved modes of a femtosecond laser frequency comb," Nature **445**, 627–630 (2007).
23. N. R. Newbury, I. Coddington, and W. Swann, "Sensitivity of coherent dual-comb spectroscopy," Opt. Express **18**, 7929–7945 (2010).
24. L. Nugent-Glandorf, T. Neely, F. Adler, A. J. Fleisher, K. C. Cossel, B. Bjork, T. Dinneen, J. Ye, and S. A. Diddams, "Mid-infrared virtually imaged phased array spectrometer for rapid and broadband trace gas detection," Opt. Lett. **37**, 3285–3287 (2012).
25. L. C. Sinclair, I. Coddington, W. C. Swann, G. B. Rieker, A. Hati, K. Iwakuni, and N. R. Newbury, "Operation of an optically coherent frequency comb outside the metrology lab," Opt. Express **22**, 6996–7006 (2014).
26. M. Shirasaki, "Large angular dispersion by a virtually imaged phased array and its application to a wavelength demultiplexer," Opt. Lett. **21**, 366–368 (1996).
27. A. Ferguson and R. Taylor, "Active mode stabilization of a synchronously pumped mode locked dye laser," Optics Communications **41**, 271 – 276 (1982).
28. T. Udem, J. Reichert, R. Holzwarth, and T. W. Hänsch, "Absolute optical frequency measurement of the cesium D_1 line with a mode-locked laser," Phys. Rev. Lett. **82**, 3568–3571 (1999).
29. G. Turin, "An introduction to matched filters," Information Theory, IRE Transactions on **6**, 311–329 (1960).
30. W. Demtröder, *Laser spectroscopy: basic concepts and instrumentation*, 2674 (Springer Science & Business Media, 2003).
31. S. L. Gilbert, W. C. Swann, and C.-M. Wang, "Hydrogen cyanide h13c14n absorption reference for 1530 nm to 1565 nm wavelength calibration–srm 2519a," NIST special publication **260**, 137 (2005).

1. Introduction

Molecular absorption spectroscopy has many applications, including: environmental monitoring [1, 2, 3], measurement of contaminants in industrial processes [4, 5], human breath analysis [6, 7, 8], detection of contraband and warfare agents [9] and fundamental science [10]. There are several mature competing techniques for measuring molecular absorption spectra, including tunable laser spectroscopy, cavity-ringdown spectroscopy (CRDS) and Fourier-transform infrared spectroscopy (FTIR). The best approach depends on the requirements of the application and there is usually a trade-off between measurement parameters such as spectral coverage, sensitivity, spectral resolution, spectral accuracy, measurement speed, simplicity and cost.

In recent years, frequency combs have been demonstrated to be ideal sources for absorption spectroscopy because they combine broad spectral coverage, dense spectral sampling, high accuracy and fast measurement [11]. Frequency combs allow simultaneous interrogation at thousands of precisely known optical frequencies and – as they are coherent sources – resonant enhancement within a high-finesse cavity can be employed for high sensitivity [12].

Several methods have been developed to measure absorption spectra using frequency combs; most notably: multiheterodyne detection using two frequency combs with slightly different repetition rates [13, 14, 15, 16, 17]; vernier detection using a resonant optical cavity to scale the comb's repetition rate [18, 19, 20, 21]; and using dispersive elements such as a diffraction gratings and virtually imaged phase arrays (VIPAs) [22, 7]. These three methods offer similar performance in terms of spectral coverage, spectral sampling density and measurement time. The figure of merit introduced by Newbury *et al.* [23] (the product of the SNR, normalized by the square root of the acquisition time, and the number of resolved frequency elements) is typically $\sim 10^6 - 10^7$ for these spectrometers.

The combination of a VIPA, a diffraction grating and an imaging array is attractive because it requires only a single frequency comb and it minimizes the number of moving parts. To date; however, VIPA-based spectrometers have only been able to resolve decimated comb modes [22, 24] or have been unable to resolve comb modes at all [7, 3]. For the latter, the spectrometer cannot take advantage of the inherent accuracy and stability of the comb mode frequencies, negating that benefit of using a comb.

We have developed a quantitative frequency-comb absorption spectrometer that delivers broad spectral coverage ($\sim$4 THz) and utilises the full spectral sampling and frequency accuracy available from a stabilised optical frequency comb. It is based on a commercial frequency comb in conjunction with an imaging system consisting of: VIPA, diffraction grating and near-IR camera. The imaging system has a resolution of 1.2 GHz; so, in order to fully resolve the 250-MHz-spaced comb modes, an external resonant optical cavity with a free spectral range (FSR) of $\sim$9.5 GHz is used as a tunable spectral filter to decimate the frequency comb modes, producing a 2-dimensional array of well separated bright spots when imaged by the camera. A fully automatic control system dynamically locks the filter cavity to the frequency comb and sequentially measures all unique decimated comb subsets, which are interleaved to produce complete spectra with 250-MHz spectral sampling over $\sim$4 THz in a total measurement time of 8.2 s. The comb is locked to an ultra-stable laser that gives stability and accuracy of the frequency axis of $<$10 Hz and $<$2 kHz, respectively, for measurement times of 1 – 10 s.

The spectrometer requires only one frequency comb, unlike similarly performing dual-comb spectrometers, and its only moving part is a PZT-scanned filter-cavity mirror, making it a useful tool for applications requiring fast, quantitative spectra. In conjunction with new portable high-performance frequency combs [25], this automated system may easily evolve into a useful tool for field applications and is consistent with world-wide efforts to bring frequency-comb applications out of the metrology laboratory.

The spectrometer's performance was evaluated by measuring the $^2\nu_3$ vibrational overtone band of $H^{13}C^{14}N$ centered at $\sim$1543 nm. The measured line centers and widths are in excellent agreement with a previous high-precision measurement.

2. Methods

2.1. Optical System

Figure 1 shows the experimental setup. The frequency comb (Menlo Systems FC1500) has a repetition rate of 250 MHz and spans $\sim$1500 – 1600 nm. Its carrier-envelope-offset frequency (f_{CEO}) and repetition rate (f_{RR}) are locked to a cesium beam clock and a cavity-stabilized continuous-wave reference laser (NKT Koheras BoostiK E15), respectively. The resulting sta-

bility of each comb mode is ∼10 Hz for an observation time of 1 – 10 s and its absolute frequency is known to ∼2 kHz.

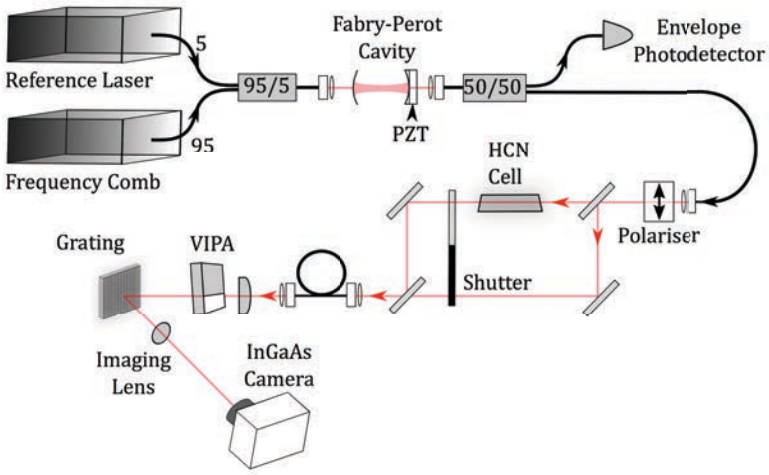

Fig. 1. Simplified schematic of the experimental system.

The frequency comb is combined with the reference laser, which provides a marker for calibrating the frequency scale. We use two optical paths alternately: a sample path that contains a $H^{13}C^{14}N$ reference cell at 100 Torr, and an empty reference path for calibration. Light from the two paths is passed through an optical fiber to ensure they are colinear before introduction to the imaging optics. The light is line-focused into the AR-coated access window of the VIPA (Light Machinery). The VIPA is a specialized étalon with a free spectral range (FSR) of 50 GHz and a finesse of ∼100 that disperses the comb light vertically [26]. To avoid frequency ambiguity, it is used in combination with a 600 lines/mm diffraction grating (Thorlabs GR25–0616) oriented to disperse the light horizontally [22]. The resulting beam is imaged on an InGaAs camera (Xenics Xeva-1.7-320). The camera captures just over one VIPA FSR in the vertical direction and ∼35 nm (∼4 THz) of spectral width in the horizontal direction. The algorithm used to extract the absorption spectrum from the image is described in detail in Section 2.3.

By measuring the vertical width of an imaged spot due to the reference laser, we estimated the resolution of the VIPA spectrometer to be ∼1.2 GHz, which is significantly larger than the comb mode separation (250 MHz). In order to resolve the comb modes, we use a variable-length, low finesse (∼200) Fabry-Pérot cavity to decimate the comb. We chose a cavity FSR (ν_{FSR}) of 9.5 GHz (transmitting every 38^{th} comb mode) because it is significantly larger than the spectrometer resolution and produces the optimum two-dimensional distribution of imaged modes on the camera (see Fig. 5). A longer cavity would result in closer spacing of imaged modes, leading to cross-talk in the extracted spectra. Scanning the cavity length allows access to all unique subsets of 9.5 GHz-spaced decimated combs. However, as demonstrated in Fig. 2, when detuned from the best match between comb and cavity, the pass-bands of the cavity transfer function acquire an accumulating offset from the comb mode frequencies that reduces the transmitted optical power of modes far from the center of the camera image. The finesse of the cavity was chosen to provide enough selectivity to suppress unwanted comb modes, yet was low enough to transmit sufficient optical power ($P > 0.1P_{\mathrm{max}}$) for all imaged modes when maximally detuned from the best match.

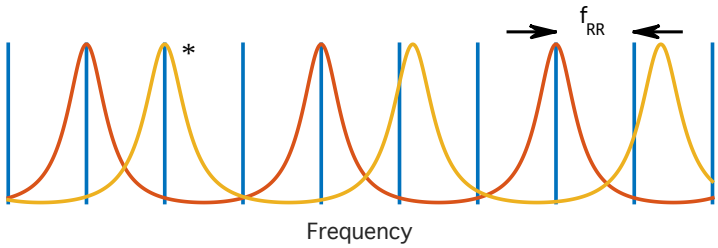

Fig. 2. Depiction of overlap of comb modes (blue vertical lines) with modes of a Fabry-Pérot cavity with a FSR of $4 \times f_{\mathrm{RR}}$, showing transmission of every fourth comb mode (c.f. every 38$^{\mathrm{th}}$ in the experiment). The red curve describes the best possible match between comb and cavity. Scanning the cavity length allows transmission of the adjacent subset of comb modes (orange), but transmission of modes far from the optimally matched mode (*) is reduced.

2.2. *Cavity Locking and Data Acquisition*

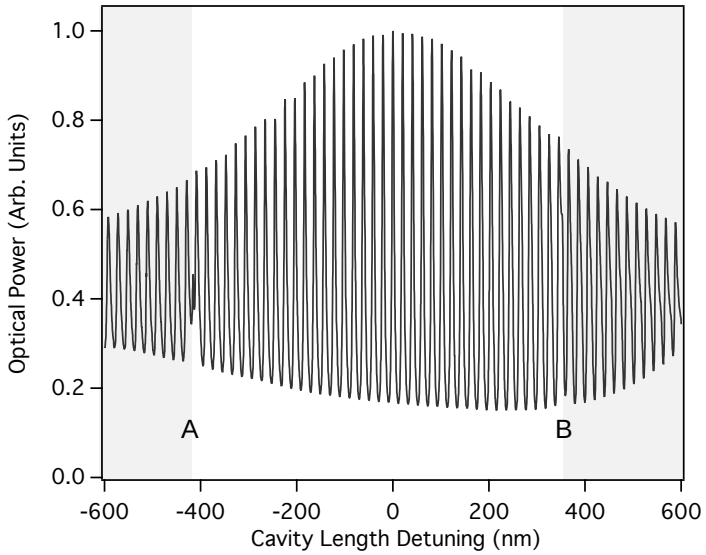

Fig. 3. Filter-cavity transmission as a function of cavity length detuning from $L = c/(2 \times \nu_{\mathrm{FSR}})$. Positions A and B indicate reference laser transmission by the filter cavity. The 38 local maxima between A and B correspond to optimal transmission of the 38 unique decimated comb subsets with 9.5 GHz mode separation.

Figure 3 shows the integrated cavity transmission (measured by the photodetector positioned after the Fabry-Pérot cavity) as a function of cavity length. This curve is similar to previous observations [27, 28]. Local maxima occur when cavity resonances (separated by $\sim$9.5 GHz) are optimally aligned with a 9.5 GHz subset of comb modes. The peak of the envelope corresponds to $\nu_{\mathrm{FSR}} = 38 \times f_{\mathrm{RR}}$ and, as the cavity is detuned from this optimum length, the increasing mismatch between f_{RR} and ν_{FSR} leads to lower transmission of some modes and thus a reduction in the amplitude of successive maxima. The asymmetry of the envelope is due to dispersion

in the mirrors combined with an asymmetric distribution of comb power around the central wavelength.

To measure a complete spectrum, we record two camera images (one for the sample and one for the reference path) for each of the central 38 adjacent peaks in the cavity transmission pattern in Fig. 3. A dither lock stabilizes the cavity length during the acquisition of each image to ensure that the cavity transmission intensity profile for each image pair is identical which allows accurate normalization. Coordinating the acquisition requires control of the cavity length, the dither locking electronics and the camera triggering. Our control system is based on an Arduino Due board, which provides sufficient flexibility to create a completely automated acquisition system.

Figure 4 shows a schematic of the cavity length control and dither locking system. The Arduino Due board has a program loop rate of 20 kHz. It generates a 10 kHz dither signal by toggling a digital output at each program loop. The signal is filtered, amplified and sent to a piezoelectric transducer (PZT) behind one filter-cavity mirror (also shown on Fig. 1). The amplitude of the resulting oscillation in the transmitted optical power is proportional to the local derivative of the pattern in Fig. 3 and its phase indicates the sign of the same derivative. The signal from the photodetector (D) is band-pass filtered (BPF) and sampled by the Arduino, which performs digital demodulation and low-pass filtering (LPF) to generate an error signal with zero crossings at cavity transmission peaks. The error signal is passed to a digital proportional-integral (PI) loop filter in the Arduino, the output of which is passed through an on-board 12-bit digital-to-analog converter (DAC), attenuated to give fine control, and summed with the dither signal. A second 12-bit DAC coarsely controls the cavity length to ensure the servo control stays within its range. It is also used to step between cavity resonances.

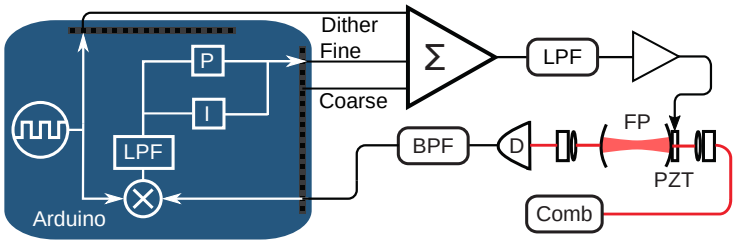

Fig. 4. Schematic of the locking system. The length of the Fabry-Perot (FP) filter cavity is dithered at 10 kHz and the transmitted comb power is detected. The resulting signal is used to lock the cavity length via a proportional-integral (PI) controller implemented on an Arduino Due microcontroller.

The Arduino board also controls the automatic acquisition of the 38 consecutive pairs of camera images. Digital outputs are used to cycle the position of the shutter between the sample and reference paths (shown in Fig. 1) and trigger the camera. Sample and reference images are acquired alternately using a camera integration time of 8 ms. Successive images are separated by intervals of 100 ms, dominated by the shutter settling time. The measurement time for a complete spectrum (38 image pairs) is 8.2 s. By using a high-speed shutter, we expect the measurement time would be reduced to less than 2 s.

2.3. Image Analysis

The modes of each decimated comb subset are dispersed vertically (by the VIPA) and horizontally (by the diffraction grating) before being focused onto the InGaAs camera, yielding images similar to that shown at the top left of Fig. 5. For the sample-path images, each bright spot

corresponds to a cavity-resolved comb mode with brightness dependent of the degree of absorption by the gas sample. The reference path image is required to normalize common-mode brightness variations in the optical system. A sample image normalized by its corresponding reference image is shown on the top right of Fig. 5 with the characteristic absorption fingerprint clearly visible. Each image pair (sample and reference) is analysed to extract a traditional one-dimensional absorption spectrum.

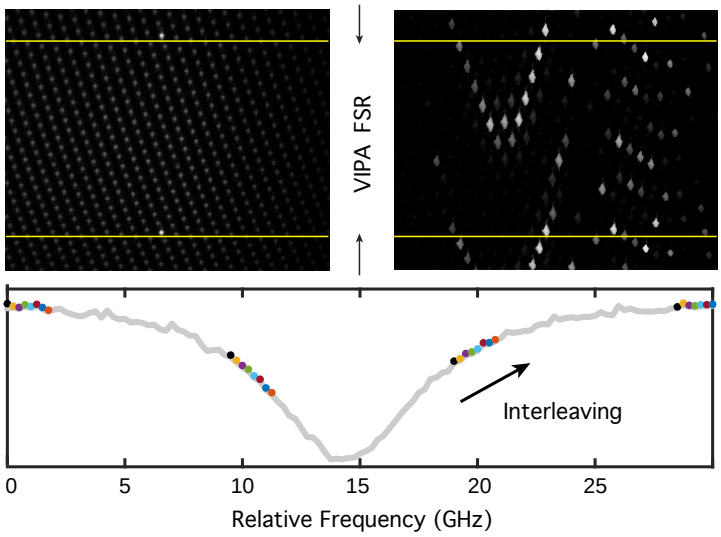

Fig. 5. Top left: Raw camera image showing resolved comb modes. The two brightest spots correspond to the reference laser and horizontal yellow lines mark out one VIPA FSR containing unique spectral data. Top right: Sample image normalized by its corresponding reference image. Bottom: Interleaving multiple spectra derived from filtered comb subsets. Eight adjacent subsets are shown here, with different colors for clarity. Adjacent points are spaced by $f_{RR} = 250\,\text{MHz}$ and points of the same color are spaced by $\nu_{FSR} = 9.5\,\text{GHz}$. The fully reconstructed spectrum is outlined in grey.

The integrated power of each comb mode was determined by applying a matched filter to the images. This step can be understood as a cross-correlation of the images with a kernel based on a single imaged mode that best approximates the profile of all modes. The cross-correlation is a weighted integration at all possible kernel positions, and thus the amplitude of the maxima are proportional to the power of the respective comb modes. It can be shown that the matched filter is the optimal linear technique to detect the presence of a signal contaminated by white noise [29]. Therefore, the spots that are only partially transmitted by the cavity and appear dimmer on the image are easily extracted from the image. The filter also serves to reduce cross-talk from adjacent spots. For each image pair, the ratio of corresponding cross-correlation maxima is computed to find the normalized transmittance of the corresponding comb mode.

The local maxima of the cross-correlation image closely correspond to the centroid positions of the spots, allowing a very accurate determination of the position of each comb mode in an image. Knowing the dispersion in both the vertical and horizontal directions, and keeping in mind that adjacent modes are separated by precisely $38 f_{RR}$, allows the relative frequency of each imaged mode to be determined and an absorption spectrum for a single frame to be constructed. Also, knowing that the subset of modes in each successive image pair is offset f_{RR} from the last, allows us to interleave a set of 38 consecutive spectra to reconstruct a full absorption spec-

trum, as shown in the bottom panel of Fig. 5. Due to environmental fluctuations affecting the free-space beams, slight power fluctuations occur during the time interval separating the acquisition of the reference and sample images. A robust (bi-square), first-order polynomial fit was used to individually renormalize individual spectra before interleaving. Using a faster shutter or reducing alignment fluctuations would eliminate the need for this step.

Finally, within each set of 38 consecutive image pairs there is a single pair that also shows the reference laser (see Fig 5). If the position of the reference laser is used as a proxy for the nearest comb mode, and the optical frequency of this mode is known, then an absolute frequency can be assigned to every imaged mode. The optical frequency ν_{ref} of the reference laser was independently measured using a wave meter (HighFinesse WS/7) and the optical frequency of the nearest comb mode, ν_n, was deduced by minimizing $|\nu_{ref} - \nu_n|$ where: $\nu_n = n \times f_{\mathrm{RR}} + f_{CEO}$ and n is the mode index. A measurement of f_{CEO} and f_{RR} using a frequency counter referenced to a Cs beam clock (Datum CsIII) allowed the optical frequency of each comb mode to be determined with an absolute accuracy of $\sim$2 kHz.

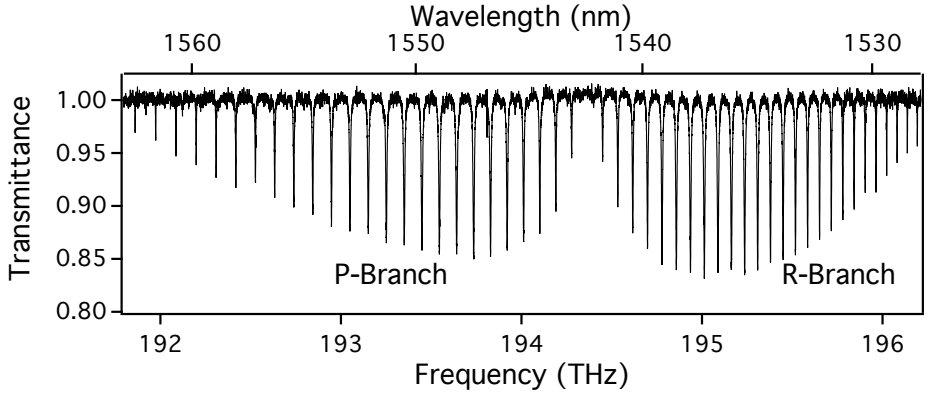

Fig. 6. The complete spectrum formed by interleaving the 38 individual spectra obtained by varying the cavity length.

The full reconstructed spectrum is shown in Fig. 6. It spans $\sim$4 THz (35 nm) with 250-MHz (2 pm) spectral sampling and 2-kHz (10 am) absolute accuracy. The signal to noise ratio varies slightly across the interleaved spectrum primarily because individual modes have a range of intensities when imaged by the camera. Data points are therefore limited either by relative intensity noise for the brighter spots or by additive noise from the camera for dimmer spots. At all intensities the noise is white with an average signal-to-noise ratio across the interleaved spectrum of $\sim$400. This gives a figure of merit [23] of $2.2 \times 10^6 \sqrt{\mathrm{Hz}}$, which compares well with other comb spectroscopy techniques.

3. Spectral Analysis

The full spectrum presented in Fig. 6 was used to determine the line centers and the Lorentzian components of the linewidths of 48 $2\nu_3$ rotational-vibrational absorption lines of $H^{13}C^{14}N$. The sample was contained in a nominally 100$\pm$10 Torr, 50 mm long reference cell (Wavelength References; HCN-13-100) at room temperature (22.5$\pm$1° C).

Regions of the absorption spectrum were approximated by fitting functions of the form:

$$\left(\sum_{i=0}^{j} a_i \nu^i\right) \exp\left(-\sum_{n=1}^{m} b_n V\left[\nu; \nu_n, \sigma_n, \gamma_n\right]\right) \tag{1}$$

where $V[\nu;\nu_n,\sigma_n,\gamma_n]$ represents a Voigt profile centered on ν_n, with Gaussian (Doppler) component FWHM, $\sqrt{8\ln(2)}\sigma$ (determined by calculation [30]), and Lorentzian component FWHM, 2γ.

An initial estimate of the parameter set was found by moving to each absorption line, windowing the spectrum to include the immediately adjacent lines, and performing a linear least-squares fit using Eqn. 1 with $j = 2$ and $m = 3$ ($m = 2$ for the edge cases). Parameters ν, σ and γ for the line of interest for each fit were retained. This initial parameter set was used to suppress the main absorption lines in the spectral data, revealing the residual broadband background structure. A robust (bi-square) fourth-order polynomial fit to this structure allowed it to be removed before performing a final linear least-squares fit of all lines simultaneously using Eqn. 1 with $j = 0$ and $m = 51$, seeded by the initial parameter set. Fig. 7 shows a closeup of the fitted spectrum around the P(16) feature.

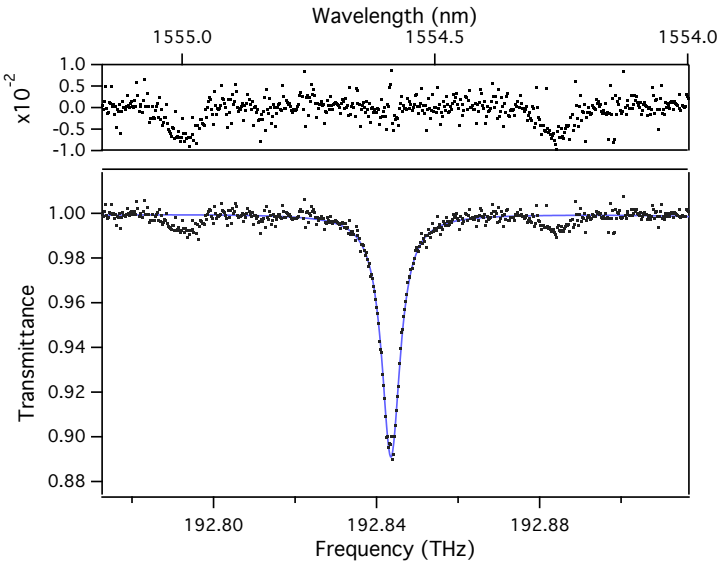

Fig. 7. Close-up of the spectrum presented in Fig. 6 near the P(16) absorption line. The background structure has been removed and the fit (blue) and residuals (top panel) are also shown. Hot-band absorption lines can be seen either side of the main line.

To validate the quality of the spectrometer, line centers and widths derived from the fit were compared with those expected at 100 Torr (calculated from [31]). Significant deviation from the expected Lorentzian linewidth (up to $\sim$8 pm or 1 GHz) suggested that the reference cell pressure was lower than than the nominal pressure of 100 Torr. Least-squares optimization was used to minimize deviation from the expected linewidths, giving an estimate of 92.5 ± 0.8 Torr, which is within the $\pm10\%$ tolerance quoted by the manufacturer. Fig. 8 displays a comparison of selected line centers and linewidths to expected values at 92.5 Torr. Measurement uncertainties are the 2σ confidence intervals obtained from the least-squares fit.

We find good agreement with the expected values predicted by [31]. Line center and width measurements using this analysis exhibited repeatability consistent with the 2σ confidence intervals derived from the fit. Repeatability also corresponded well to the uncertainty in these parameters predicted by a modelled spectrum with added Gaussian noise of SNR = 400. We do, however, see deviations from calculated expected values of up to $\sim$1 pm and up to $\sim$3 pm, respectively – exceeding the 2σ confidence intervals and thus presenting a strong indication of

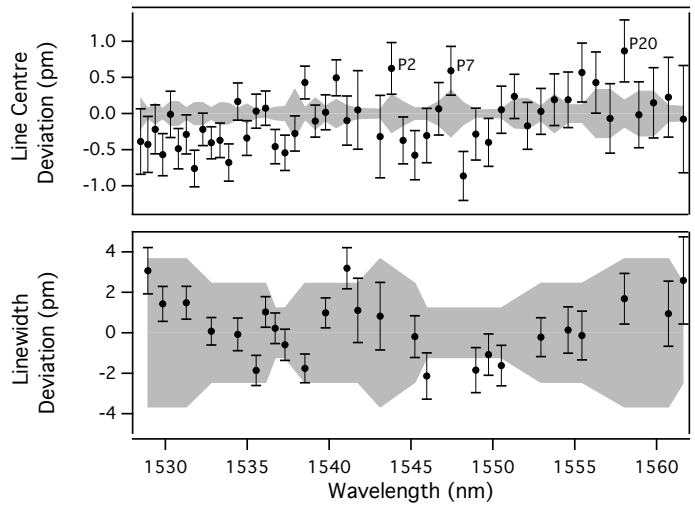

Fig. 8. Deviation of our line centers and widths from expected values at 92.5 Torr. Displayed uncertainties are 2σ confidence intervals. Solid grey regions indicate uncertainties estimated according to [31]. Small wavelength shifts due to nearby hot-band features can be seen for the P(2), P(7) and P(20) features.

underlying systematic errors. One source of such errors are the smaller hot-band features visible in the spectrum. These were not included in this analysis and, consequently, some of the main absorption lines experienced small shifts from the expected line centers. This was particularly noticeable for the P(2), P(7) and P(20) features, which was also noted by [31]. We also observe broader structure that may indicate pressure shifts and pressure broadening introduced by a buffer gas in the reference cell. We are confident that a more detailed analysis will result in closer agreement with previous work.

4. Conclusion

We have demonstrated a quantitative frequency comb spectrometer with 35-nm (4 THz) bandwidth around 1543 nm, 2-pm (250 MHz) spectral sampling and an absolute frequency accuracy of 2 kHz. We achieve a signal-to-noise ratio $\sim$400 in 8.2 seconds, giving a figure of merit of $2.2 \times 10^6 \sqrt{\text{Hz}}$, which compares favourably with other comb spectroscopy techniques. We have validated the performance of the spectrometer by comparing our measurement of the $^2\nu_3$ vibrational overtone of $H^{13}C^{14}N$ to a previous high-precision measurement; finding excellent agreement with line centers and Lorentzian linewidths exhibiting deviation of, at worst, 1 and 3 pm, respectively.

Our approach has demonstrated a practical spectrometer that harnesses the full potential of a stabilized frequency comb and can be easily deployed for a range of high-precision spectroscopic measurements.

Complex Direct Comb Spectroscopy With A Virtually Imaged Phased Array

This chapter is based on the published article:

S. K. Scholten, J. D. Anstie, N. Bourbeau Hébert, R. T. White, J. Genest, and A. N. Luiten, "Complex Direct Comb Spectroscopy With A Virtually Imaged Phased Array", *Optics Letters* **41**, 1277-1280 (2016).

9.1 Overview and Motivation

The aim of this paper was to demonstrate simultaneous capture of both absorption and phase information using direct optical frequency comb spectroscopy combined with a Michelson interferometer. Dual-comb spectroscopy may capture both in certain configurations, while this was the first demonstration of acquiring the same information with a single optical frequency comb to construct the sample's full optical transfer function using a stabilised Michelson interferometer and VIPA spectrometer [105,275]. In addition, it was also the first demonstration of the newer analysis code designed to function with the full, unrarefied comb. This code utilised the Faddeeva function as introduced in Sec. 4.1.3 for the rapid generation of Voigt profiles. The method described in this paper required four images in total - one each for the sample and reference paths, one interferogram, and a cavity-rarefied image. The rarefication cavity was also re-purposed in this paper to act as a frequency calibration for the unrarefied images. The results maintain their high-resolution and broadband character, being acquired and analysed within a rapid time frame.

An important change to the spectrometer performed in the course of this experiment was the replacement of the original imaging lenses to physically-larger and longer focal-length lenses to remove aberrations. At the same time, the spectral width of results was reduced from $\sim 35\,\mathrm{nm}$ to $\sim 25\,\mathrm{nm}$ to increase the spacing between adjacent VIPA stripes on the spectrometer images. Additionally, the diffraction grating was changed to a double-pass arrangement to improve the resolution of VIPA stripes in the horizontal dimension under grating control. Both of these changes were necessary to prevent leakage of adjacent VIPA stripes and an associated zero-error. It was also during the course of this paper that the nonlinearity of the spectrometer camera response using the built-in camera software first became apparent. This was rectified in future publications with the addition of dark background and nonlinearity correction procedures.

9.2 Statement of Contribution

9.2.1 Conceptualisation

The idea of applying using the undecimated system to simultaneously measure both the phase and transmission spectrum of hydrogen cyanide was a joint effort between James Anstie and Sarah Scholten, as was the conceptualisation of the method with which to achieve these measurements.

9.2.2 Realisation

James Anstie and Richard White developed the spectrometer analysis code further to function with the undecimated optical frequency comb output, with assistance from Sarah Scholten. The construction of the experiment detailed in this paper was primarily performed by Sarah Scholten. Literature review, the mathematics, and the code required to extract the phase was also the work of Sarah Scholten under the guidance of James Anstie.

9.2.3 Documentation

This paper was primarily written by Sarah Scholten, with editing by all other authors, mainly James Anstie, Richard White, and Andre Luiten. The data presented in the paper was acquired and analysed by Sarah Scholten.

Candidate overall percentage contribution: 75%.

Sarah K. Scholten

9.2.4 Co-author Contributions

By signing below, each co-author certifies that:

- The candidate's stated contribution to the publication is accurate (as stated above).
- Permission is granted for the candidate to include the publication in the thesis.

Co-author certifications are in order of published authorship unless otherwise specified.

James D. Anstie

Nicolas Bourbeau Hébert

Richard T. White

Jérôme Genest

Andre N. Luiten

Optics Letters

Complex direct comb spectroscopy with a virtually imaged phased array

Sarah K. Scholten,[1,*] James D. Anstie,[1] Nicolas Bourbeau Hébert,[2] Richard T. White,[1] Jérôme Genest,[2] and Andre N. Luiten[1]

[1]Institute for Photonics and Advanced Sensing, School of Physical Sciences, The University of Adelaide, Adelaide SA 5005, Australia
[2]Centre d'Optique, photonique et laser, Université Laval, Québec GIV 0A6, Canada
*Corresponding author: sarah.scholten@adelaide.edu.au

Received 21 January 2016; revised 15 February 2016; accepted 16 February 2016; posted 17 February 2016 (Doc. ID 257968); published 15 March 2016

We demonstrate a simple interferometric technique to directly measure the complex optical transmittance over a large spectral range using a frequency-comb spectrometer based on a virtually imaged phased array. A Michelson interferometer encodes the phase deviations induced by a sample contained in one of its arms into an interferogram image. When combined with an additional image taken from each arm separately, along with a frequency-calibration image, this allows full reconstruction of the sample's optical transfer function. We demonstrate the technique with a vapor cell containing $H^{13}C^{14}N$, producing transmittance and phase spectra spanning 2.9 THz (~23 nm) with ~1 GHz resolution.

OCIS codes: (140.4050) Mode-locked lasers; (300.1030) Absorption; (300.6390) Spectroscopy, molecular; (120.5050) Phase measurement; (110.5100) Phased-array imaging systems.

http://dx.doi.org/10.1364/OL.41.001277

Optical frequency combs have been a revolutionary development for spectroscopy, allowing fast measurements, broad spectral coverage, dense spectral sampling, and absolute frequency accuracy [1]. Further, in contrast to many other broadband sources, frequency combs are also spatially and temporally coherent, making comb sources useful for measurements of both a sample's amplitude and phase response. In this Letter, we exploit these properties to make direct, high quality measurements of the complex transmittance of a molecular sample.

The magnitude of the optical response of some samples, whether transmittance, absorbance, or reflectance, is the most commonly reported spectroscopic measurement. It is much easier to obtain than the phase response, and it is conventionally held that the Kramers–Kronig relations [2,3] provide a means to derive both the real and imaginary components of the complex transfer function from the magnitude measurement. However, this is only formally true for causal, linear, and time-invariant systems that have the property of minimal phase [4]. For nonminimal phase systems, the spectral phase cannot be retrieved from the amplitude spectrum, and thus a distinct measurement of the phase response is required to determine the complete optical transfer function. There are numerous optical measurements that can benefit from the separate acquisition of phase, including: dispersion measurements of optical fibers and components [5], reflectivity characterization of optical thin films [6], detailed lineshape perturbation analysis [7], and the probing of certain cavity configurations, most notably microresonators [8,9].

Interferometric spectrometers, such as Fourier-transform [10,11], dual-comb [12] and frequency modulated continuous wave (FMCW) spectrometers [5,13,14] can be configured to yield complex measurements; however, spectrometers based on spatial dispersion are in general simpler and more robust. Gohle *et al.* [15] have achieved phase measurements using a Fabry–Perot (FP) cavity-based discriminator but, to our knowledge, high-quality direct phase measurements with a spatially resolved spectrometer have yet to be demonstrated.

In this Letter, we demonstrate a technique suitable for simultaneously measuring both amplitude and phase spectra using a comb in conjunction with a virtually imaged phased array (VIPA) spectrometer [16,17]. The $2\nu_3$ vibrational overtone band of $H^{13}C^{14}N$ is used as a minimal-phase optical system to demonstrate accurate phase retrieval. Measurement of the full optical transfer function is achieved with the addition of a Michelson interferometer. One arm of the interferometer is actively length-stabilized, such that a $\lambda/4$ offset from the path matched condition is maintained. Working at this point ensures that all comb modes experience essentially the same phase shift due to the length mismatch (to within a small linear factor) and leaves the phase shift due to molecular interaction simply encoded within three camera images.

The experimental setup is shown in Fig. 1. The frequency comb (Menlo Systems FC1500) spans ~1500–1600 nm. Its carrier-envelope-offset frequency (f_{CEO}) is locked to a cesium beam clock (Datum CsIII), while the comb repetition rate (f_{RR}) of ~250 MHz is stabilized by locking the nearest comb mode to a cavity-stabilized reference laser (NKT Koheras Boostik E15). The comb is combined with the reference laser, which acts as a marker for optical frequency calibration. The

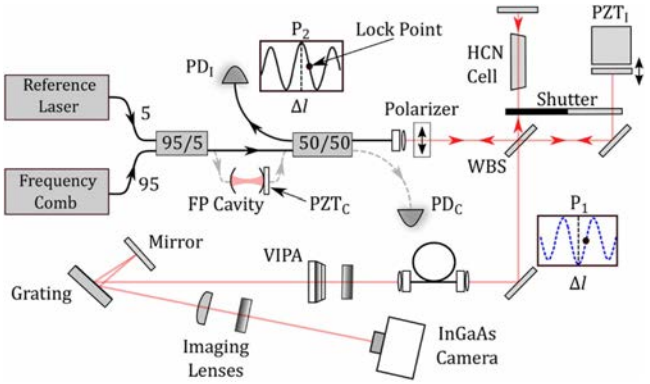

Fig. 1. Simplified schematic of the experiment. Also shown is the power at the two output ports of the interferometer, P_1 and P_2, as a function of length detuning (Δl) from the global interference maximum at P_2 at the path-matched condition.

light then follows one of two paths: either it travels through a stabilized low finesse (~200) FP cavity (gray dashed path), or it bypasses the cavity (solid path) and enters the rest of the experiment. The cavity, with a free spectral range (FSR) of $35 \times f_{RR} = 8.75$ GHz is set to transmit every 35th comb mode and is used to calibrate the optical frequency axis. The beam is then sent, via a four-port 50:50 coupler and Glan-Thompson polarizer (to ensure identical beam polarizations), into a wedged beam splitter (WBS) that feeds the two arms of a Michelson interferometer.

One arm of the interferometer (sample path) contains a 50 mm-long cell of $H^{13}C^{14}N$ at 100 ± 10 Torr (Wavelength References HCN-13-100) at room temperature (22.5 ± 1°C). The second arm (reference path) controls the interference condition between the two arms of the interferometer via a mirror on a piezoelectric (PZT) stage (PZT_I). After recombination, light from the retroreflected output port (P_2) is directed back to a photodetector (PD_I) for use in locking the interferometer. Light from the other output port (P_1) is directed through an optical fiber to enforce beam overlap, before being line-focused into the AR-coated input window of a VIPA etalon (Light Machinery). The VIPA is a specialized étalon with a FSR of ~50 GHz and a finesse of ~100 that disperses the comb light vertically as a function of wavelength [18]. To avoid frequency ambiguity [19], the VIPA is used in combination with a 600-lines/mm diffraction grating, oriented to disperse the light horizontally. The grating is double-passed to provide higher angular resolution [20]. The resulting beam is imaged on an InGaAs camera (Xenics Xeva-1.7-320) with a ~2.9 THz (~23 nm) spectral range in the horizontal direction and just over one VIPA FSR in the vertical direction.

Retrieval of the transmittance and phase data may be understood by considering the recombination of a single comb mode at the imaged output of the interferometer (P_1). For a light field of form: $E_0 \exp[i(\omega t + \phi)]$, where E_0 is the electric field amplitude, ϕ is the optical phase, and ω is the angular optical frequency, feeding the interferometer through an ideal 50:50 beam splitter. In this case, the magnitude of the interference (P_1) is

$$P_1 = E_1^2 + E_2^2 - 2E_1E_2 \cos\left(\Delta\phi - \frac{2\pi\Delta l}{\lambda}\right), \quad (1)$$

where $E_1 = \alpha E_0/\sqrt{4}$, α^2 is the attenuation from a double pass through the sample, $E_2 = E_0/\sqrt{4}$, Δl is the change in round-trip optical path length of the sample arm with respect to the reference arm, λ is the wavelength, and $\Delta\phi$ is the phase shift from a double pass through the sample. $\Delta\phi$ is thus

$$\Delta\phi = \arccos\left(\frac{E_1^2 + E_2^2 - P_1}{2E_1E_2}\right) + \frac{2\pi\Delta l}{\lambda}. \quad (2)$$

In order to obtain the largest unambiguous phase range and highest phase sensitivity, the interferometer should be tuned such that $\Delta l = \lambda/4$. If we now consider the full ensemble of comb modes, then this length tuning can only be exact for one central wavelength (λ_c). If the interferometer is locked such that it satisfies $\Delta l = \lambda_c/4$, an additional term dependent on detuning from λ_c is required to fully describe the phase shift of an individual comb mode. When working with optical frequency combs, it is more natural to use optical frequency, so we introduce $\Delta\nu = (\nu - \nu_c)$ with $\nu_c = c/\lambda_c$. Expressed in terms of frequency, and with the additional detuning dependent term, the equation for the sample phase shift becomes

$$\Delta\phi(\nu) = \arcsin\left(\frac{E_1^2 + E_2^2 - P_1}{2E_1E_2}\right) + \Phi(\Delta\nu), \quad (3)$$

where $\Delta\phi(\nu)$ is the phase shift of an individual comb mode due to interaction with the sample, and $\Phi(\Delta\nu) = [\pi/(2\nu_c)]\Delta\nu$ is the additional term due to the mode's deviation from ν_c, which dominates linear dispersion effects from other optical components. Note that Eqs. (1)–(3) imply that deviation from a 50:50 split ratio does not impact phase recovery.

We now describe the process for deriving the complex transmittance. First, we measure two separate VIPA images from the sample and reference paths alone (by blocking the alternative path), which yield E_1^2 and E_2^2, respectively. We then measure an interferogram image when operating at $\Delta l = \lambda_c/4$ to find P_1. The transmittance (T) is found from $T = E_1^2/E_2^2 = \alpha^2$ and the phase from Eq. (3).

As previously stated, to obtain a high quality interferogram image, the interferometer length imbalance must be tuned and stabilized such that $\Delta l = \lambda_c/4$. This is achieved by measuring the retroreflected interferometer output port (P_2 on Fig. 1) using a photodetector (PD_I), which is used to lock the interferometer at half of its global maximum, as shown in Fig. 2. The error signal is then passed to a proportional-integral (PI) filter, the output of which is passed via a piezo controller to the PZT actuator (PZT_I) to stabilize the reference-arm length.

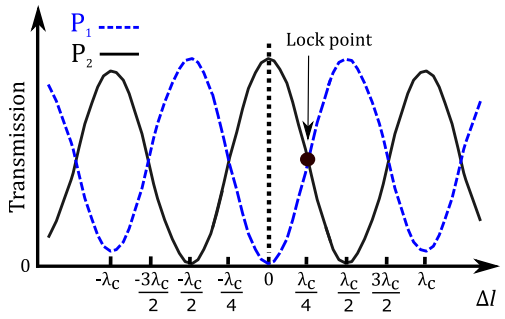

Fig. 2. Output of both ports (P_1 and P_2 in Fig. 1) of the interferometer as a function of length detuning (Δl) from the path-matched condition (dashed vertical line).

With the interferometer length locked, the interferogram image is recorded [Fig. 3(a)]. The interferometer lock is then disabled, and the reference and sample paths are alternately blocked, recording a sample and reference image, respectively. The interferogram image is acquired with 1 ms of integration time, while the sample and reference images are integrated for 2 ms in order to make best use of the available camera intensity resolution. In the current configuration, switching among the three image states is done manually, but this can easily be automated to reduce acquisition times to ∼100 ms.

In order to ensure frequency accuracy of the measurement, a final frequency calibration image is acquired by imaging the decimated, fully resolved, comb that results from passing through the FP cavity. This image is taken with the sample path blocked, and with the FP cavity length stabilized such that it transmits only the subset of comb modes containing the mode nearest to the reference laser, as well as the reference itself. This point is found by scanning the cavity length and monitoring the photodetector (PD_C), stopping at the appropriate local maximum. The cavity length is dithered around this point and the demodulated transmission signal is used as an error signal to lock the cavity length [21]. This delivers a decimated version of the comb with every 35th mode transmitted through the cavity, as shown in Fig. 3(b). The VIPA resolution is sufficient to fully resolve the decimated comb, and thus allows us to identify and assign a frequency to every imaged comb mode. This in turn allows us to make a high-quality calibration of the frequency at every location on the images.

The reference, sample, and interferogram images contain a series of near vertical stripes [see Fig. 3(a)], with each stripe encoding just over one VIPA FSR of spectral information limited by the VIPA resolution (∼1 GHz). The vertical stripes are spaced horizontally by one VIPA FSR (∼50 GHz). The use of the double-pass grating confers sufficient horizontal resolution to ensure that these features are well separated, minimizing potential cross talk between adjacent stripes. It is possible to calculate the transmittance and (uncorrected) phase directly from the image data, shown in Fig. 4, which may be useful for optical fingerprinting applications, where a detailed understanding of the spectra is not so important. For more quantitative applications we have developed a process to reconstruct the underlying spectra in a more robust way.

The reference image is used as a key to extract the spectral information from all three images. The horizontal cross section

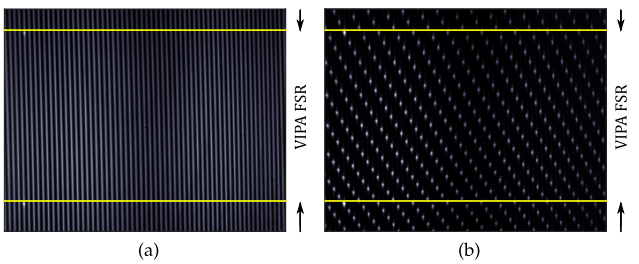

Fig. 3. Left: a typical raw interferogram. The two brightest spots correspond to the reference laser, and the yellow horizontal lines mark out one VIPA FSR containing unique spectral data. The horizontal separation of adjacent bright vertical stripes is also one VIPA FSR [19]. Right: raw cavity-decimated image showing fully resolved comb modes.

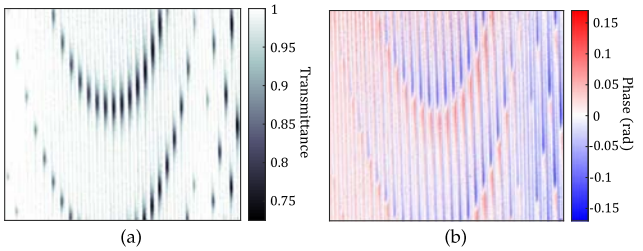

Fig. 4. Two-dimensional molecular fingerprints for absorption (left) and phase (right). The effects of the phase ramp are evident in the phase data.

of each stripe within the reference image is essentially Gaussian, with each pixel contributing a signal proportional to the amount of optical power falling within its borders. By averaging a large number of these cross sections, we can find an approximation to the underlying Gaussian intensity profile (point spread function). We use this width approximation, along with an estimate of the center position, to construct a set of matched filters that mimic the observed cross sections. We then calculate the sum of the pixel-by-pixel products between each cross section and its corresponding filter, producing a weighted sum that maximizes the available signal-to-noise ratio and suppresses any residual cross talk between adjacent stripes to well below the noise floor of the measurement. Applying this process to the entire image allows efficient extraction of the spectral data, with one data point per row per stripe. The set of matched filters derived from the reference image is also used to extract spectral information from the sample and interferogram images.

As mentioned previously and shown in Fig. 3(b), an image of the decimated comb and reference laser is used to generate an optical frequency axis for the spectral data extracted from each image. Measurements of the wavelength of the reference laser (HighFinesse WS/7, accurate to ∼10 MHz), comb repetition rate, and carrier-envelope-offset frequency, allow for each imaged mode to be identified [21]. Least-squares fitting of the identified modes to a mapping function determines the relationship between optical frequency and position on the image.

Finally, the transmittance ($T = E_1^2/E_2^2$) and phase [Eq. (3)] are calculated with E_1^2, E_2^2, and P_1 supplied by the spectral data determined from the sample, reference, and interferogram images, respectively. The central frequency (ν_c) for the phase correction can be estimated by choosing ν_c such that the off-resonance phase is zero; in this case, ∼176.2 THz. For non-minimal phase systems, determination of ν_c is more difficult, leading to uncertainties in phase offset and slope, governed by Eq. (3). In this case ν_c may be determined, for example, by using a CW laser of known λ to lock the path length imbalance and thus set ν_c.

Figure 5 shows the measured transmittance and phase for a single measurement of the P1–P24 and R0–R4 lines of the $2\nu_3$ vibrational overtone band of $H^{13}C^{14}N$, and Fig. 6 shows a close-up of the P8 and P9 features. Also visible in these spectra are a series of smaller hot-band features [22]. The recorded transmittance spectrum has a signal-to-noise ratio of ∼500 (with sensitivity of ∼1000 ppm at 1 atm). It corresponds well to a model based on previous high-resolution measurements of $H^{13}C^{14}N$ [21,23], represented by the solid red curve, with the optical path length through the sample and a linear background

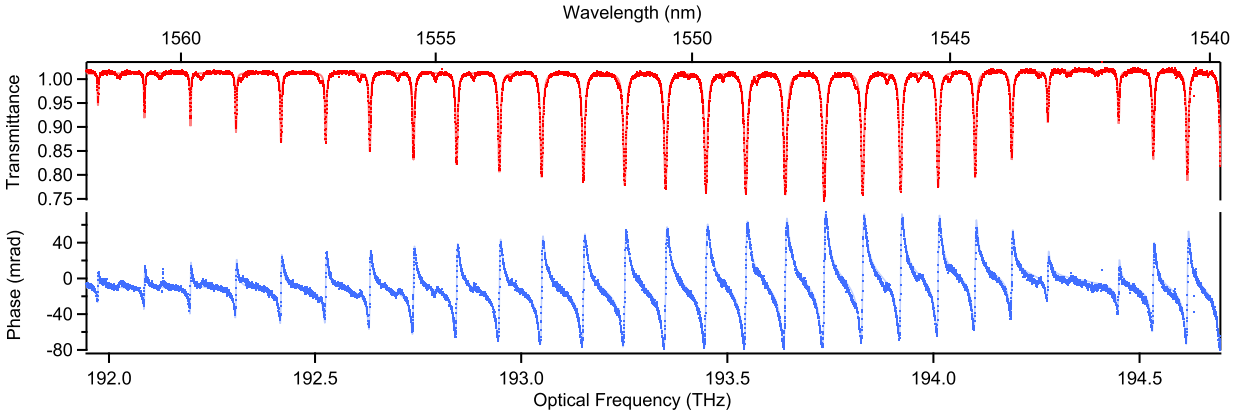

Fig. 5. Extracted transmittance and phase spectra for the P1–P24 and R0–R3 features of $H^{13}C^{14}N$. The solid lines show the modeled transmittance (red) and phase (blue) based on a previous high-resolution absorption measurement [21,23]. Small (unmodelled) hot-band features can also be seen in both the transmission and phase data.

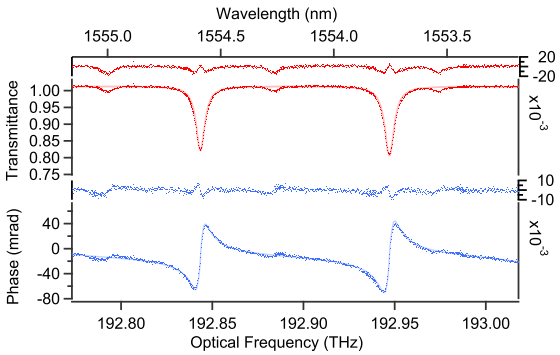

Fig. 6. Close-up of the P8 and P9 features of $H^{13}C^{14}N$ of Fig. 5. Smaller (unmodelled) hot-band features and instrumental broadening can be seen in both spectra and residuals.

correction as the only free parameters. The phase spectrum exhibits a slightly reduced signal-to-noise ratio (phase sensitivity of ~1 mrad), primarily due to nonlinearity of the camera. It also corresponds well to the expected phase response (blue solid curve) modeled by a Faddeeva function approximation to the complex Voigt profile applied to the high-resolution data. Instrumental broadening of the measured features with respect to the high-resolution measurement is due to the resolution limit of the VIPA.

In conclusion, we have demonstrated a direct interferometric measurement of the complex transmittance of $H^{13}C^{14}N$ using a VIPA-based frequency comb spectrometer. Though powerful in its current form, this technique is best suited to phase variations of <1 rad, which can be overcome by locking to a range of path imbalances to determine relative phase unambiguously. It is also currently limited by the VIPA resolution, which can be improved by fully resolving individual comb modes and thus taking advantage of the intrinsic frequency accuracy of the stabilized optical frequency comb. This technique demonstrates a simple, fast, accurate, and practical way to directly extract broadband amplitude and phase spectra, with potential application to a diverse range of optical systems.

Funding. Australian Research Council (ARC) (LP120200605, LP140100674); Department of Further Education, Employment, Science and Technology, Government of South Australia (DFEEST) (Catalyst Research Grant, Premiers Science and Research Fund).

REFERENCES

1. F. Adler, M. J. Thorpe, K. C. Cossel, and J. Ye, Annu. Rev. Anal. Chem. **3**, 175 (2010).
2. R. de L. Kronig, J. Opt. Soc. Am. **12**, 547 (1926).
3. H. A. Kramers, in *Atti Cong. Intern. Fisica (Transactions of Volta Centenary Congress)* (1927), pp. 545–557.
4. J. Bechhoefer, Am. J. Phys. **79**, 1053 (2011).
5. T. Ahn, Y. Jung, K. Oh, and D. Kim, Opt. Express **13**, 10040 (2005).
6. P. Grosse and V. Offermann, Appl. Phys. A **52**, 138 (1991).
7. J. Wang, P. Ehlers, I. Silander, and O. Axner, J. Opt. Soc. Am. B **28**, 2390 (2011).
8. H. Bergeron, J. R. Carrier, V. Michaud-Belleau, J. Roy, J. Genest, and C. Allen, Phys. Rev. A **87**, 063835 (2013).
9. V. Michaud-Belleau, J. Roy, S. Potvin, J. Carrier, L. Verret, M. Charlebois, J. Genest, and C. Allen, Opt. Express **20**, 3066 (2012).
10. J. Birch, Mikrochim. Acta **93**, 105 (1987).
11. J. Mandon, G. Guelachvili, and N. Picqué, Nat. Photonics **3**, 99 (2009).
12. I. Coddington, W. C. Swann, and N. R. Newbury, Phys. Rev. Lett. **100**, 013902 (2008).
13. A. Cygan, P. Wcisło, S. Wójtewicz, P. Masłowski, J. T. Hodges, R. Ciuryło, and D. Lisak, Opt. Express **23**, 14472 (2015).
14. A. Foltynowicz, F. M. Schmidt, W. Ma, and O. Axner, Appl. Phys. B **92**, 313 (2008).
15. C. Gohle, B. Stein, A. Schliesser, T. Udem, and T. W. Hänsch, Phys. Rev. Lett. **99**, 263902 (2007).
16. L. Nugent-Glandorf, T. Neely, F. Adler, A. J. Fleisher, K. C. Cossel, B. Bjork, T. Dinneen, and S. A. Diddams, Opt. Lett. **37**, 3285 (2012).
17. L. Nugent-Glandorf, F. R. Giorgetta, and S. A. Diddams, Appl. Phys. B **119**, 327 (2015).
18. M. Shirasaki, Opt. Lett. **21**, 366 (1996).
19. S. A. Diddams, L. Hollberg, and V. Mebele, Nature **445**, 627 (2007).
20. D. Derickson, *Fiber Optic Test and Measurement*, 1st ed. (Prentice-Hall, 1998).
21. N. B. Hébert, S. K. Scholten, R. T. White, J. Genest, A. N. Luiten, and J. D. Anstie, Opt. Express **23**, 13991 (2015).
22. H. Sasada and K. Yamada, Appl. Opt. **29**, 3535 (1990).
23. S. L. Gilbert, W. C. Swann, and C. Wang, NIST Spec. Publ. **260**, 137 (2005).

Rapid Number Density Measurements of CO_2 with an Optical Frequency Comb

This chapter is based on the published article:

S. K. Scholten, C. Perrella, J. D. Anstie, R. T. White, W. Al-Ashwal, N. Bourbeau Hébert, J. Genest, and A. N. Luiten, "Rapid Number Density Measurements of CO_2 with an Optical Frequency Comb", *Physical Review Applied* **9**, 054043 (2018).

10.1 Overview and Motivation

The aim of this paper was firstly to determine if molecular parameters of interest could be extracted from spectra acquired using the VIPA spectrometer in a quantitative manner. Secondly, it was of interest to determine the accuracy and precision of the returned parameters. In doing so, many improvements were made to the spectrometer system overall. Carbon dioxide was chosen as the demonstration sample gas due to its importance to both medical breath analysis as a major component of the human breath, and to environmental monitoring as a greenhouse gas and anthropogenic pollutant.

This paper describes the method to rapidly acquire and analyse spectra acquired using direct optical frequency comb spectroscopy with a VIPA spectrometer to extract the absolute concentration and temperature of a pure sample of carbon dioxide as the concentration was deliberately changed. This was achieved in part by improving the efficiency of the code responsible for converting spectrometer images into absorption spectra, along with full automation of the spectrometer system and data acquisition. This included interfacing of the spectrometer camera and newly-implemented high-speed optical shutters with the acquisition algorithms. As the 6.5 m optical path length of the cell was of sufficient length to observe beam-alignment fluctuations when gas was injected into the cell, the sample path was equipped with a computer-controlled two-stage spatial stabilisation system formed of a two mirrors: one mounted on a piezo-electric transducer for correction of fast alignment fluctuations and a second affixed to a stepper motor for slow corrections. The stabilisation system utilised a second laser at 780 nm in order to avoid influencing the spectroscopic results.

Additionally, as was identified soon after the publication of the previous paper, the native camera software was deemed unsuitable for continued use for two reasons. Firstly, the software was unable to be utilised when automation of the spectrometer was required, and

secondly, did not produce a linear camera response in relation to the power of incoming light. The second point in particular required a solution as a linearity error will directly translate into a retrieved concentration error as the spectral peaks become more affected as the absorption features deepen. In addition, dark current effects were not taken into account by the native software correctly. These two issues were corrected as described in Sections 6.3.2 and 6.3.4 with the introduction of dark frames and a screen-averaged camera nonlinearity correction respectively.

This paper also saw the introduction of an efficient spectral modelling code based on parameters from the HITRAN database combined with the previously introduced rapid computation package for the Faddeeva function as described in Section 4.4 [1,179,213,276]. This was the first demonstration of the continuous-monitoring capability of a DFCS system based on a VIPA spectrometer, with data acquisition, spectral analysis, and parameter extraction all performed in under one second. In addition, the results were highly precise and accurate, with returned concentrations having accuracy within 1% and precision of 0.04% in under a second.

10.2 Statement of Contribution

10.2.1 Conceptualisation

The concept of applying the spectrometer system to rapidly measure the concentration of carbon dioxide was a joint effort between Sarah Scholten, James Antie, Richard White, Christopher Perrella, and Andre Luiten. The idea of applying spectral fitting to the aqcuired spectra in the manner presented in the paper was that of Sarah Scholten.

10.2.2 Realisation

James Anstie was responsible for the design and realisation of the sample cell that is presented in this paper, along with the initial experimental design and construction. Sarah Scholten, Christopher Perrella, and James Anstie began work on the path-stabilisation system, with Sarah Scholten and Christopher Perrella finalising this system with the inclusion of 780 nm light paths and components. Characterisation of the spectrometer camera's non-linearity, interfacing of the camera and other components using MATLAB, image correction procedures, and data acquisition were performed by Sarah Scholten with guidance from Christopher Perrella and Andre Luiten. Creation and implementation of the fitting code was primarily the work of Sarah Scholten, with assistance from Christopher Perrella.

10.2.3 Documentation

This paper was primarily written by Sarah Scholten, with editing by all other authors, mainly Christopher Perrella and Andre Luiten.

Candidate overall percentage contribution: 70%.

Sarah K. Scholten

10.2.4 Co-author Contributions

By signing below, each co-author certifies that:

- The candidate's stated contribution to the publication is accurate (as stated above).
- Permission is granted for the candidate to include the publication in the thesis.

Co-author certifications are in order of published authorship unless otherwise specified.

Christopher Perrella

James D. Anstie

Richard T. White

Waddah Al-Ashwal

Nicolas Bourbeau Hébert

Jérôme Genest

Andre N. Luiten

Number-Density Measurements of CO_2 in Real Time with an Optical Frequency Comb for High Accuracy and Precision

Sarah K. Scholten,[1,*] Christopher Perrella,[1] James D. Anstie,[1] Richard T. White,[1] Waddah Al-Ashwal,[1] Nicolas Bourbeau Hébert,[2] Jérôme Genest,[2] and Andre N. Luiten[1]

[1]*Institute for Photonics and Advanced Sensing, School of Physical Sciences, The University of Adelaide, Adelaide, South Australia 5005, Australia*

[2]*Centre d'optique, photonique et laser, Université Laval, Québec G1V 0A6, Canada*

(Received 11 December 2017; published 29 May 2018)

Real-time and accurate measurements of gas properties are highly desirable for numerous real-world applications. Here, we use an optical-frequency comb to demonstrate absolute number-density and temperature measurements of a sample gas with state-of-the-art precision and accuracy. The technique is demonstrated by measuring the number density of $^{12}C^{16}O_2$ with an accuracy of better than 1% and a precision of 0.04% in a measurement and analysis cycle of less than 1 s. This technique is transferable to numerous molecular species, thus offering an avenue for near-universal gas concentration measurements.

DOI: 10.1103/PhysRevApplied.9.054043

I. INTRODUCTION

Many industrial applications have an acute need for rapid, accurate, and precise measurements of gas properties such as density, temperature, concentration, and pressure. Examples can be found in liquid natural-gas processing and quality assurance [1], medical breath analysis [2–4], and environmental monitoring of greenhouse gases or air quality [5–8]. A particular example in this latter category is the current call to develop atmospheric CO_2 measurements with a precision in the 10^{-3}–10^{-4} range [9–12].

In this paper we demonstrate an optical spectroscopic technique that meets this desired precision. Optical spectroscopy comes with a number of other advantages in that it can be rapid, performed *in situ*, and allow the equipment to be some distance from the system under test. These can be highly beneficial when compared with conventional gas measurement techniques such as mass spectrometry and gas chromatography—particularly when operating in environments in which sample extraction is unwanted or where conditions are hazardous.

The field of optical molecular spectroscopy is proceeding rapidly, with major developments in dual-comb, Fourier-transform infrared (FTIR), and direct-comb spectroscopy techniques occurring in the past decade. Dual-comb techniques have been used to measure molecular spectra in both enhancement-cell and open-air paths, as well as measurements of gas turbine exhaust, trace gas analysis, and spectroscopy of near-infrared frequency [7,8,13–18]. However, this technique typically requires two optical-frequency combs, making them relatively costly and complex systems. FTIR measurements of air with optical-frequency combs have also been demonstrated [19]. Direct-frequency comb spectroscopy has been successfully applied to temperature measurements of CO_2 on the time scale of milliseconds [20]. The direct-frequency comb spectroscopy method used in this paper has the benefits of requiring only a single comb, operation in the eye-safe spectral band, and use of a simple, fixed, and robust spectrometer based on spatial dispersion. This reduction in complexity makes the system appealing for use outside of the laboratory.

Measurements in real-world environments typically involve numerous molecular species. Each species presents a complicated absorption spectrum, with a large number of rovibrational transitions observable under typical conditions [21]. Related absorption lines (arising from transitions from one vibrational state to another) in the unique spectra of a molecule are categorized into "bands" [22]. The relative intensities of rovibrational molecular absorption features within such bands are predominantly governed by temperature as a result of population distribution in the quantized rotational energy levels of the molecular system [23]. Overall scaling of the total absorption envelope is a function of absorber concentration in the sample, while pressure dependence results in shifting of line centers and line-shape broadening.

In principle, it is possible to simultaneously extract the temperature, pressure, and number density of molecules in a single spectrum provided the measurement has sufficient spectral range and resolution to resolve the individual absorption line shapes across the majority of a band. The particular properties of optical-frequency combs (OFCs) deliver a nearly ideal interrogation source for molecular spectroscopy. The broadband nature of an OFC's spectrum allows for interrogation of a large number of the quantized

*sarah.scholten@adelaide.edu.au

energy levels of a molecule simultaneously, producing a characteristic rovibrational absorption spectrum specific to the molecular species under examination. Additionally, they also allow rapid measurements with dense spectral sampling and absolute frequency accuracy [24]. This allows multiple absorption peaks to be examined simultaneously, resulting in fast and accurate measurements.

In this paper we demonstrate a technique for accurate and real-time $^{12}C^{16}O_2$ number-density determination using an OFC measured with a virtually imaged phased array (VIPA) spectrometer. An approximately 25-nm high-resolution $^{12}C^{16}O_2$ transmission spectrum is extracted from six images acquired by the spectrometer. A model of the expected spectrum using parameters from the high-resolution transmission molecular absorption (HITRAN) database [25] is combined with an efficient approximation of the total molecular partition function [26]. The model is used in a fitting procedure to rapidly extract concentration and temperature from the measured spectra. The process is demonstrated with the 30012 ← 00001 spectral band of $^{12}C^{16}O_2$ in a flow cell containing varying partial pressures of CO_2 and N_2. The entire measurement and fitting procedure generates a number density on average every 0.9 s with a concentration precision of 0.04%. Results are shown to be accurate by comparison with the ideal gas law, while the precision of the measurement is at least as good as the precision of the mass flow controllers that control the gas mixture.

II. EXPERIMENTAL METHODS

A. Optical system and stabilization

The experimental setup is displayed in Fig. 1. The OFC (Menlo Systems FC1500) used to interrogate the gas sample spans approximately 1500–1600 nm, with a repetition rate (f_{rep}) of 250 MHz. The carrier-envelope-offset frequency (f_{CEO}) of the comb is locked to a cesium beam clock (Datum CsIII), while f_{rep} is stabilized by locking the

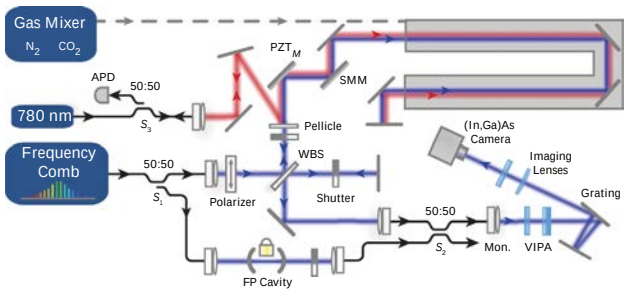

FIG. 1. A simplified diagram of the experiment. APD, avalanche photodetector; S_i, fiber splitter; FP, Fabry-Perot (cavity); WBS, wedged beam splitter; PZT_M, mirror with piezoelectric transducer; SMM, mirror with stepper motor. Fiber-coupled paths are shown in solid black, gas connections in dashed gray, and free-space optical paths in red and blue for the frequency-doubled version of the continuous-wave reference laser (doubled to 780 nm) and optical-frequency comb, respectively.

nearest comb mode to a cavity-stabilized reference laser (NKT Koheras Boostik E15) at 1560 nm (fractional frequency stability below 10^{-14}).

The stabilized comb light is split with a four-port 50:50 fiber coupler (S_1) into two paths. The first path is used for spectroscopy of CO_2 and is split via a wedged beam splitter (WBS) into the reference and sample paths of the experiment. The reference path is used for optical comparison to the sample path that contains a double-passed 3.25-m-long gas cell at room temperature (296 ± 1 K) and atmospheric pressure. The sample cell is connected to a gas mixing system (Environics Series 2000) that mixes CO_2 and N_2 to deliver a set CO_2 concentration while maintaining a constant gas flow rate. N_2 is used as the buffer gas due to its optical transparency in the examined spectral region. Both sample and reference paths are coupled into a single-mode fiber to ensure stable spectrometer alignment.

The 6.5-m path length through the free-space sample cell is sufficiently long to produce deleterious effects from beam-alignment fluctuations, particularly when the CO_2/N_2 concentration ratio is altered. The alignment is thus actively controlled using a mirror equipped with a piezoelectric transducer (PZT_M). The correction of long-term drifts are beyond the range of PZT_M, so the PZT_M actuation is augmented with a mirror mounted on wide-range stepper motors (SMM) to ensure the system stays within range of PZT_M. An alignment error signal is constructed by dithering the angle of PZT_M while synchronously detecting the retroreflected signal on an avalanche photodetector (APD). The alignment system depends on the injection of an additional 780-nm laser that has been chosen so that no alignment light is transmitted into the spectrometer, and that little comb light is detected by the APD.

The second output path of the four-port 50:50 coupler (S_1) is directed through a stabilized low finesse (about 200) Fabry-Perot (FP) cavity with a bandwidth of approximately 50 MHz. The cavity length is stabilized such that every 36th comb mode is transmitted, as seen in Fig. 2(b). This rarefied comb is sufficiently well spaced such that each comb mode may be independently detected by the spectrometer [27,28]. This allows identification and assignment of a relative frequency to every comb mode imaged by the spectrometer camera, granting high-quality calibration of the relative frequency.

All paths are sent to the spectrometer for imaging via a four-port 50:50 coupler (S_2), ensuring colinearity of the three paths at the spectrometer input [27]. A VIPA etalon (Light Machinery) forms the basis of the spectrometer. Automated shutters are used to select light from the sample, reference, and cavity paths. The selected beam then enters a cylindrical lens which line focuses the light into the antireflective-coated input window of the VIPA. The VIPA is an etalon with a finesse of about 100 and free spectral range (FSR) of about 50 GHz that disperses the comb light

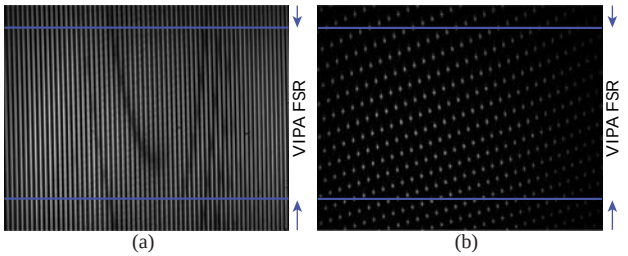

FIG. 2. (a) Typical signal image, showing the 2D fingerprint of $^{12}C^{16}O_2$. The blue horizontal lines mark one VIPA FSR containing unique spectral data. The horizontal separation of adjacent bright vertical stripes is also one VIPA FSR. (b) Typical cavity-rarefied image showing fully resolved comb modes.

vertically as a function of wavelength, as seen in Fig. 2 [29]. The VIPA is used in combination with a 600-lines/mm diffraction grating to remove frequency ambiguity by providing a lower-resolution spatial dispersion in the horizontal plane [30]. The grating is double passed to improve horizontal angular resolution, ensuring the potential cross talk between adjacent VIPA stripes is minimized. The resulting dispersed beam is focused onto an (In,Ga)As camera (Xenics XEVA-1.7-320) to form images as seen in Figs. 2(a) and 2(b) with approximately 2.9-THz (approximately 25-nm) spectral range in the horizontal and just over one VIPA FSR in the vertical direction.

Six VIPA images are required per calibrated spectrum where we use shutters to open one particular path through the optical system at a time: (a) sample, (b) reference, and (c) a rarefied comb path. In addition, we take one associated dark image for each of the three configurations with all shutters closed. These dark images are used for camera background subtraction, with each of these images acquired with an integration time that matches its bright counterpart.

B. Image analysis

The $^{12}C^{16}O_2$ absorption signal is extracted from the six images that are generated by the VIPA spectrometer. First, the three dark images (from each of the three possible optical paths) are used to perform background correction of the three bright images. The nonlinearity of the camera response is then corrected using a calibration based on a set of previously obtained gray images. The VIPA resolution (approximately 1 GHz) is not high enough to resolve the frequency comb modes ($f_{\mathrm{rep}} = 250$ MHz), resulting in the continuous bright vertical stripes seen in Fig. 2(a). Each stripe holds just over one VIPA FSR of spectral information and the horizontal spacing between adjacent stripes is equal to one VIPA FSR.

The reference image is used as the basis for extracting spectral information from each set of three images [28]. The horizontal cross section of each vertical stripe in the reference image is well approximated by a Gaussian profile spanning several pixels. Averaging a large number of these cross sections results in an accurate approximation of the underlying stripe line profile. This profile is used together with stripe center position to produce a set of matched filters. We correlate (pixel-by-pixel products) the entire image using the matched filters along the stripes to produce one representative brightness point for each row along a stripe. The same matched filters are applied to the corresponding sample and cavity images. Division of the processed signal image data by the processed reference image data produces a final transmission spectrum for fitting. The use of matched filtering minimizes the potential effects of cross talk between adjacent stripes to below the measurement noise, while maximizing the available signal-to-noise ratio.

In the final step, the processed rarefied comb image is used to generate an accurate mapping of position on the image to relative optical frequency. Measurements of the cavity FSR, f_{rep} and f_{CEO} allow the frequency of each mode to be identified relative to every other comb mode. An absolute frequency axis may be attained with the use of an appropriate cw laser [28], though for this work the HITRAN spectral positions are used to set the absolute axis.

C. Spectral fitting and number-density extraction

To extract an estimate of the number density we fit each experimental spectrum with a model $^{12}C^{16}O_2$ absorption spectrum [23] built upon parameters from the HITRAN 2012 database [25]. We include an additional third-order polynomial in our model to allow for broad background variations. In this work, the demonstration of $^{12}C^{16}O_2$ concentration retrieval is accomplished via interrogation of the $30012 \leftarrow 00001$ spectral band centered at 6347.880 cm^{-1} (approximately 1575.33 nm or 190.44 THz) [31], along with the smaller $31112 \leftarrow 01101$ hot band that falls within the observed spectral region.

The 126 largest spectral absorption features from the two bands are modeled as Voigt line shapes. The parameters for each peak are extracted from the HITRAN database including: line strength $[S_{\eta\eta'}(T_{\mathrm{ref}})]$, lower state energy of the transition (E_η), line center ($\nu_{\eta\eta'}$), pressure shift, and pressure-broadened line half-widths (both due to air and self-broadening) where η and η' denote the lower and upper states of each transition, respectively. Spectrometer broadening terms are also included, and are measured by observation of the rarefied comb images. This shows a Voigt-like profile for each mode with a Lorentzian half-width-at-half-maximum of 0.01 ± 0.001 cm^{-1} and Gaussian $1/e$ half-width of 0.006 ± 0.001 cm^{-1}. Doppler broadening of each absorption line is also included, and is calculated to be 0.007 cm^{-1} ($1/e$ half-width) at laboratory conditions.

The HITRAN parameters are provided at a reference temperature of $T_{\mathrm{ref}} = 296$ K, which requires a temperature dependence of some parameters, such as $S_{\eta\eta'}(T_{\mathrm{ref}})$, to be included in the fit

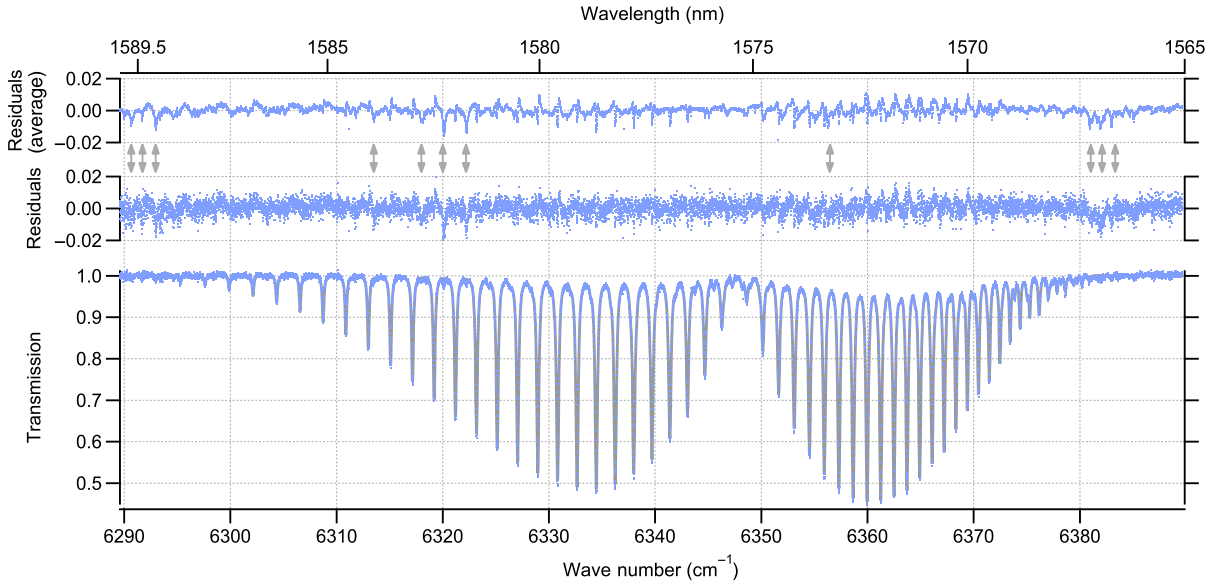

FIG. 3. A typical single-shot experimental 30012 ← 00001 transition spectrum (blue markers) for 100% CO_2, with spectral fit (gray solid line) and fit residuals (middle graph). This fit returns a density of $2.41 \pm 0.09 \times 10^{19}$ molecules/cm^3 and a temperature of 295.9 K. A complete spectrum with fit is acquired in an average of 0.9 s. A video demonstration of fitting to each spectrum at an increased frame rate may be seen in the Supplemental Material [32]. Also included are fit residuals for a 600-measurement average fit (top). Smaller hot-band transitions excluded from the fit appear more clearly in the averaged residuals as symmetric peaks (gray arrows), while asymmetric spectrometer broadening and use of a Voigt line shape results in the remainder of residuals.

$$S_{\eta\eta'}(T) = S_{\eta\eta'}(T_{\mathrm{ref}})\frac{Q(T_{\mathrm{ref}})}{Q(T)}\frac{e^{-c_2E_\eta/T}}{e^{-c_2E_\eta/T_{\mathrm{ref}}}}\frac{1-e^{-c_2\nu_{\eta\eta'}/T}}{1-e^{-c_2\nu_{\eta\eta'}/T_{\mathrm{ref}}}}, \quad (1)$$

where $c_2 = hc/k_B$, h is the Planck constant, c is the speed of light, and k_B is the Boltzmann constant [23]. Furthermore, the temperature dependence of the complex molecular total internal partition function $(Q(T))$ of $^{12}C^{16}O_2$ must be calculated and included in the fit to obtain the correct line intensity in Eq. (1). We use a polynomial approximation to simplify calculation of the partition function [26].

A least-squares fitting routine enables the model spectrum to optimally fit the experimental spectra with only the number density and temperature as free parameters. A representative fitted spectrum may be seen in Fig. 3, with an enlarged portion of the spectrum shown in Fig. 4. Acquisition time of all six VIPA images is typically on the order of 0.1 s. Spectral extraction and fitting take an average time of 0.8 s, with the time required for image analysis and fitting being approximately equal.

Also displayed in Fig. 3 are the residuals for a single shot and 600 sample (1 min) average. The averaged residuals allow resolution of absorption features of less than 0.5% in transmission. The features in both sets of residuals marked with gray arrows are associated with absorption lines not included in the model spectra as they are comparatively small, and have a negligible effect on measurement of concentration. The remaining residual features are associated with subtle effects that are only evident due to the high resolution of the measurements. The majority of these are associated with the use of a Voigt line shape in the fit model which does not take complex collisional dynamics into account [33–36]. These non-Voigt-like residual features appear across the full spectrum in Fig. 3, and are more clearly seen as the M-shaped residuals in Fig. 4.

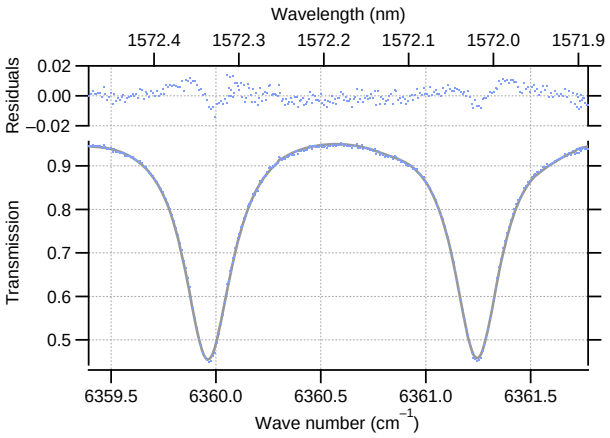

FIG. 4. Close-up of the $R16$ and $R18$ features of the 30012 ← 00001 spectral band of CO_2. Spectrometer broadening asymmetry unaccounted for by the fit and known issues from using a Voigt line shape produces slightly asymmetric M-shaped structures in the residuals.

III. RESULTS

The analysis is applied to extract number density and temperature from a two-hour data set in which the CO_2/N_2 concentration in the flow cell is varied with the gas mixer (see Fig. 5). The initial concentration of CO_2 is 100%, and is decreased incrementally until reaching 0%. A video demonstration of the fitting and concentration extraction from each spectrum may be found in the Supplemental Material [32]. Throughout the experiment the extracted temperatures remain in the range 295.5 ± 1 K, in agreement with laboratory conditions. The extracted number density of absorbers at the 100% CO_2 setting is found to be $2.41 \pm 0.02 \times 10^{19}$ molecules/cm^3. A third-order corrected ideal-gas-law calculation [37] shows a number density of 2.419×10^{19} molecules/cm^3 for the natural isotopic abundance (98.4%) of $^{12}C^{16}O_2$ [38] at the temperature (296 K) and pressure (1010 hPa) [39] of the measurement. This demonstration shows that the accuracy of the measurements is in agreement with the ideal gas law to within 0.6%.

The precision of the single-shot number-density measurements is excellent showing a standard deviation of approximately 0.04% (9.6×10^{14} molecules/cm^3 referenced to the 100% data) during measurements in which the CO_2/N_2 ratio is held constant (the plateaus of Fig. 5). The first plateau (*A*) is excluded from calculations of the precision as purging of remnant N_2 gas created a drift. The precision may be improved by averaging multiple number-density measurements. For example, the precision of a 20-s (20-spectra) average improves to approximately 0.01% (2.4×10^{14} molecules/cm^3).

The experimentally derived $^{12}C^{16}O_2$ number densities are plotted as a function of set values in Fig. 6. A linear fit produces a slope of 1.005 ± 0.003 with an offset of $-2.65 \pm 0.03 \times 10^{16}$ molecules/cm^3, showing close agreement with the expected 1:1 slope. The gas mixer used to create the varying CO_2/N_2 ratios has a stated

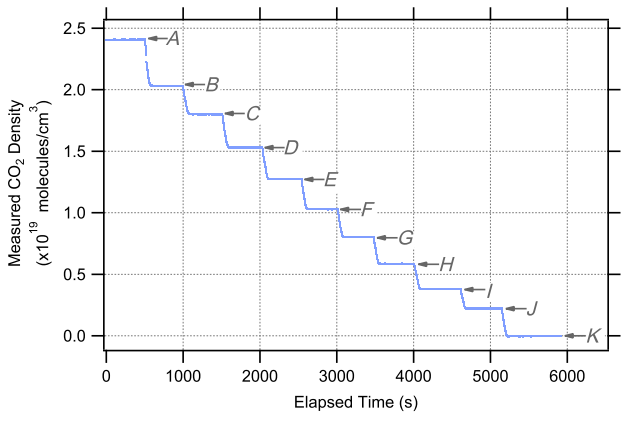

FIG. 5. Extracted $^{12}C^{16}O_2$ density as a function of time. A video demonstration of the density extraction for each spectrum may be seen in the Supplemental Material [32]. Labels correspond to set CO_2 densities listed in Table II. The discontinuity between labels *A* and *B* corresponds to an alignment control servo error.

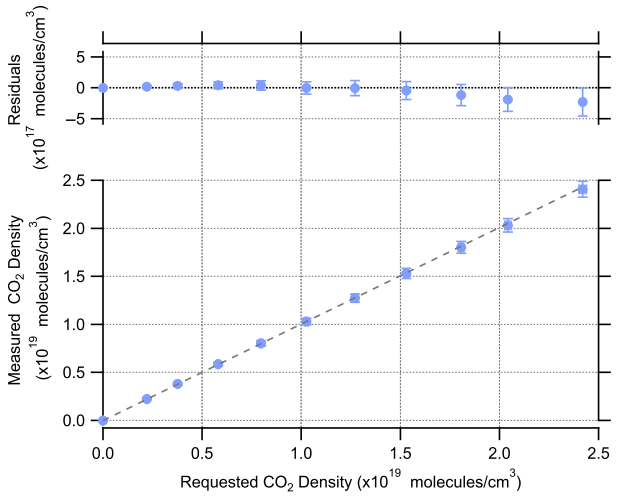

FIG. 6. Absolute $^{12}C^{16}O_2$ number density as extracted from the fits as a function of set density (blue markers) as retrieved from the plateaus of Fig. 5 and listed in Table II. Vertical error bars of both graphs are conservatively estimated as 0.95%, derived from a quadrature combination of uncertainties as summarized in Table I. Residuals are differences from the error-weighted linear fit (gray dashed line) of slope 1.005 ± 0.003 and offset $-2.65 \pm 0.03 \times 10^{16}$.

accuracy of 0.75% of the set concentration of each gas, which is consistent with the deviation of the fitted slope from the expected 1:1 line, and accounts for the majority of residuals in Fig. 6. Other contributors to the vertical error bars in Fig. 6 are the stated uncertainties in the line strengths as provided by HITRAN (see Table I). HITRAN reports the errors derived for each line from the original source. On the assumption that these errors are uncorrelated, we estimate the weighted standard error in the ensemble of $S_{\eta\eta'}$ to be 0.4% [40,41]. Improved error bounds on line strengths provided by HITRAN would thus improve fitting and retrieved number-density accuracy.

An additional uncertainty in the overall accuracy arises from the variation in spectrometer broadening across the spectral range observed. For simplicity, constant values are used in this analysis, although the spectrometer broadening

TABLE I. Sources of uncertainty and their relative effect on number-density measurements.

Effect	Uncertainty (%)[a]
Gas mixer concentration uncertainty	0.75
HITRAN 2012 $S_{\eta\eta'}(T_{\mathrm{ref}})$ uncertainty	0.4
Spectrometer broadening variation	0.3
Spectrometer asymmetry	0.3
Combined uncertainty	0.95

[a]Uncertainties listed are percentages of measured number density at the 1σ level. The combined uncertainty value of 0.95% results from combining the tabulated errors in quadrature. Detailed discussion of the derivation of the above values is found in text. The stated gas-mixer concentration uncertainty dominates as the main source of error.

TABLE II. Requested and measured CO_2 density comparison.

Label	Requested CO_2 density[a]	Measured CO_2 density[a]	Fractional difference ($\times 10^{-3}$)
A	2.419 ± 0.018	2.406 ± 0.023	−5.7
B	2.042 ± 0.015	2.030 ± 0.019	−5.8
C	1.807 ± 0.014	1.801 ± 0.017	−3.1
D	1.530 ± 0.011	1.531 ± 0.015	0.3
E	1.271 ± 0.010	1.274 ± 0.012	2.5
F	1.027 ± 0.008	1.029 ± 0.010	1.9
G	0.797 ± 0.006	0.802 ± 0.008	6.3
H	0.581 ± 0.004	0.585 ± 0.006	7.4
I	0.377 ± 0.003	0.379 ± 0.004	6.3
J	0.221 ± 0.002	0.221 ± 0.002	1.8
K	0.000	-0.002 ± 0.00003	⋯

[a]Units are $\times 10^{19}$ molecules/cm^3. Labels correspond to those seen in Fig. 5. Errors for the set and measured CO_2 densities are dominated by stated gas mixer and $S_{\eta\eta'}$ uncertainties, respectively.

using rarefied comb images [Fig. 2(b)] displays a variation of 6% for both the Gaussian and Lorentzian components across the image. The effect of ignoring these variations in the analysis produces an uncertainty of 0.3% in extracted number densities. This error may be reduced by using frequency-dependent broadening values. We note also that the measured spectrometer broadening is slightly asymmetric. Ignoring this gives rise to some of the residual effects that can be seen on Fig. 3, with the net effect of this on the density estimated at 0.3%. This is estimated by comparison between fits to a selected CO_2 line—one in which the asymmetry is accounted for, and the other the symmetric Voigt line shape used in this paper. It is possible to remove these errors by using the rarefied comb to interrogate the gas. In this case, all spectrometer broadening is eliminated and we are able to reobtain the same spectral sampling by sequentially interrogating the gas with various independent rarefied combs at the cost of a slightly longer integration period [27].

Another potential error in the number-density estimate arises from the use of a Voigt molecular line shape [33,42]. The Voigt line shape is commonly used in fitting high-resolution spectral measurements, but has been shown to lead to underestimates of line intensities [34–36]. However, as we have used HITRAN data designed for use with a Voigt line shape, the effect of this on the overall concentration estimation is minimal.

IV. CONCLUSION

The VIPA-based technique presented in this paper produces number-density measurements that demonstrate high accuracy and precision over the full measurement range. The single-shot measurement precision (approximately 1 s) is 0.04% over the range of measurements, while averaging for 20 s can yield a precision of 0.01%. The current limiting factors and means to further increase precision, if required, have been identified. The accuracy of the measurements is in agreement to within 0.6% of a Virial-corrected ideal gas law, inside the combined measurement uncertainty range of 0.95%. The precision and accuracy of the technique allows its use in applications requiring high sensitivity and low noise, such as in atmospheric monitoring of greenhouse gases. It is also important to note that it is relatively simple to extend the approaches expounded in this paper to measure other molecules, including greenhouse gases such as H_2O and CH_4, and means this technique is highly likely to find numerous real-world applications.

ACKNOWLEDGMENTS

Australian Research Council (ARC) Linkage Project Grants (No. LP120200605 and No. LP140100647); The Government of South Australia (Catalyst Research Grant, The Premiers Science and Research Fund).

[1] L. Zhang and E. Solbraa, Prediction of solubility of n-hexane and other heavy hydrocarbons in LNG processes, *Proceedings of the 90th Annual Convention of the Gas Processors Association, San Antonio, Texas* (2011), p. 698.

[2] K. H. Kim, S. A. Jahan, and E. Kabir, A review of breath analysis for diagnosis of human health, Trends Anal. Chem. **33**, 1 (2012).

[3] A. Amann, G. Poupart, S. Telser, M. Ledochowski, A. Schmid, and S. Mechtcheriakov, Applications of breath gas analysis in medicine, Int. J. Mass Spectrom. **239**, 227 (2004).

[4] W. Cao and Y. Duan, Breath analysis: Potential for clinical diagnosis and exposure assessment, Clin. Chem. (Washington, DC) **52**, 800 (2006).

[5] A. M. Cubillas, J. M. Lazaro, O. M. Conde, M. N. Petrovich, and J. M. Lopez-Higuera, Gas sensor based on photonic crystal fibres in the $2\nu_3$ and $\nu_2 + 2\nu_3$ vibrational bands of methane, Sensors **9**, 6261 (2009).

[6] L. Sun, K. C. Wong, P. Wei, S. Ye, H. Huang, F. Yang, D. Westerdahl, P. K. K. Louie, C. W. Y. Luk, and Z. Ning, Development and application of a next generation air Sensor network for the Hong Kong marathon 2015 air quality monitoring, Sensors **16**, 211 (2016).

[7] G. B. Rieker, F. R. Giorgetta, W. C. Swann, J. Kofler, A. M. Zolot, L. C. Sinclair, E. Baumann, C. Cromer, G. Petron, C. Sweeney, P. P. Tans, I. Coddington, and N. R. Newbury, Frequency-comb-based remote sensing of greenhouse gases over kilometer air paths, Optica **1**, 290 (2014).

[8] K. C. Cossel, E. M. Waxman, F. R. Giorgetta, M. Cermak, I. R. Coddington, D. Hesselius, S. Ruben, W. C. Swann, G.-W. Truong, G. B. Rieker, and N. R. Newbury, Open-path dual-comb spectroscopy to an airborne retroreflector, Optica **4**, 724 (2017).

[9] C. E. Miller, D. Crisp, P. L. DeCola, S. C. Olsen, J. T. Randerson, A. M. Michalak, A. Alkhaled, P. Rayner, D. J. Jacob, P. Suntharalingam *et al.*, Precision requirements for space-based $^{X}CO_2$ data, J. Geophys. Res. **112**, D10314 (2007).

[10] D. R. Thompson, D. Chris Benner, L. R. Brown, D. Crisp, V. M. Devi, Y. Jiang, V. Natraj, F. Oyafuso, K. Sung, D. Wunch, R. Castaño, and C. E. Miller, Atmospheric validation of high accuracy CO_2 absorption coefficients for the OCO-2 mission, J. Quant. Spectrosc. Radiat. Transfer **113**, 2265 (2012).

[11] K. L. Mays, P. B. Shepson, B. H. Stirm, A. Karion, C. Sweeney, and K. R. Gurney, Aircraft-based measurements of the carbon footprint of Indianapolis, Environ. Sci. Technol. **43**, 7816 (2009).

[12] W. Brand, 15th WMO/IAEA meeting on carbon dioxide, other greenhouse gases, and related measurement techniques, GAW Report No. 194, World Meteorological Organization, 2009.

[13] A. M. Zolot, F. R. Giorgetta, E. Baumann, J. W. Nicholson, W. C. Swann, I. Coddington, and N. R. Newbury, Direct-comb molecular spectroscopy with accurate, resolved comb teeth over 43 THz, Opt. Lett. **37**, 638 (2012).

[14] L. Nugent-Glandorf, F. R. Giorgetta, and S. A. Diddams, Open-air, broad-bandwidth trace gas sensing with a mid-infrared optical frequency combs, Appl. Phys. B **119**, 327 (2015).

[15] F. R. Giorgetta, G. B. Rieker, E. Baumann, W. C. Swann, L. C. Sinclair, J. Kofler, I. Coddington, and N. R. Newbury, Broadband Phase Spectroscopy over Turbulent Air Paths, Phys. Rev. Lett. **115**, 103901 (2015).

[16] P. J. Schroeder, R. J. Wright, S. Coburn, B. Sodergren, K. C. Cossel, S. Droste, G. W. Truong, E. Baumann, F. R. Giorgetta, I. Coddington, N. R. Newbury, and G. B. Rieker, Dual frequency comb laser absorption spectroscopy in a 16-MW gas turbine exhaust, Proc. Combust. Inst. **36**, 4565 (2017).

[17] B. Bernhardt, A. Ozawa, P. Jacquet, M. Jacquey, Y. Kobayashi, T. Udem, R. Holzwarth, G. Guelachvili, T. W. Hänsch, and N. Picqué, Cavity-enhanced dual-comb spectroscopy, Nat. Photonics **4**, 55 (2010).

[18] A. M. Zolot, F. R. Giorgetta, E. Baumann, W. C. Swann, I. Coddington, and N. R. Newbury, Broad-band frequency references in the near-infrared: Accurate dual comb spectroscopy of methane and acetylene, J. Quant. Spectrosc. Radiat. Transfer **118**, 26 (2013).

[19] F. Adler, P. Masowski, A. Foltynowicz, K. C. Cossel, T. C. Briles, I. Hartl, and Jun Ye, Mid-infrared Fourier transform spectroscopy with a broadband frequency comb, Opt. Express **18**, 21861 (2010).

[20] A. Klose, G. Ycas, F. C. Cruz, D. L. Maser, and S. A. Diddams, Rapid, broadband spectroscopic temperature measurement of CO_2 using VIPA spectroscopy, Appl. Phys. B **122**, 122 (2016).

[21] H. Haken and H. C. Wolf, *Molecular Physics and Elements of Quantum Chemistry: Introduction to Experiments and Theory*, 2nd ed. (Springer, New York, 2004).

[22] J. M. Hollas, *Modern Spectroscopy*, 4th ed. (Wiley, New York, 2004).

[23] L. S. Rothman, C. P. Rinsland, A. Goldman, S. T. Massie, D. P. Edwards, J.-M. Flaud, A. Perrin, C. Camy-Peyret, V. Dana, J.-Y. Mandin *et al.*, The HITRAN molecular spectroscopic database and HAWKS (HITRAN Atmospheric Workstation): 1996 edition, J. Quant. Spectrosc. Radiat. Transfer **60**, 665 (1998).

[24] F. Adler, M. J. Thorpe, K. C. Cossel, and J. Ye, Cavity-enhanced direct frequency comb spectroscopy: Technology and applications, Annu. Rev. Anal. Chem. **3**, 175 (2010).

[25] L. S. Rothman, I. E. Gordon, Y. Babikov, A. Barbe, D. Chris Benner, P. F. Bernath, M. Birk, L. Bizzocchi, V. Boudon, L. R. Brown *et al.*, The HITRAN 2012 molecular spectroscopic database, J. Quant. Spectrosc. Radiat. Transfer **130**, 4 (2013).

[26] R. R. Gamache, R. L. Hawkins, and L. S. Rothman, Total internal partition sums in the temperature range 70–3000 K: Atmospheric linear molecules, J. Mol. Spectrosc. **142**, 205 (1990).

[27] N. Hébert, S. Scholten, R. White, J. Genest, A. Luiten, and J. Anstie, A quantitative mode-resolved frequency comb spectrometer, Opt. Express **23**, 13991 (2015).

[28] S. K. Scholten, J. D. Anstie, N. Hébert, R. W. White, J. Genest, and A. N. Luiten, Complex direct comb spectroscopy with a virtually imaged phased array, Opt. Lett. **41** (2016).

[29] M. Shirasaki, Large angular dispersion by a virtually imaged phased array and its application to a wavelength demultiplexer, Opt. Lett. **21**, 366 (1996).

[30] S. A. Diddams, L. Hollberg, and V. Mebele, Molecular fingerprinting with the resolved modes of a femtosecond laser frequency comb, Nature (London) **445**, 627 (2007).

[31] L. S. Rothman and W. S. Benedict, Infrared energy levels and intensities of carbon dioxide, Appl. Opt. **17**, 2605 (1978).

[32] See Supplemental Material at http://link.aps.org/supplemental/10.1103/PhysRevApplied.9.054043 for a video demonstration of the fitting and concentration extraction for each spectrum as the carbon dioxide concentration is changed.

[33] J. T. Hodges, J. Tennyson, P. F. Bernath, A. Campargue, A. Csaszar, L. Daumont, R. R. Gamache, D. Lisak, O. Naumenko, L. Rothman *et al.*, Recommended isolated-line profile for representing high-resolution spectroscopic transitions (IUPAC technical report), Pure Appl. Chem. **86**, 1931 (2014).

[34] N. H. Ngo, N. Ibrahim, X. Landsheere, H. Tran, P. Chelin, M. Schwell, and J.-M. Hartmann, Intensities and shapes of H_2O lines in the near infrared by tunable diode laser spectroscopy, J. Quant. Spectrosc. Radiat. Transfer **113**, 870 (2012).

[35] V. P. Kochanov, On systematic errors in spectral line parameters retrieved with the Voigt line profile, J. Quant. Spectrosc. Radiat. Transfer **113**, 1635 (2012).

[36] D. Lisak and J. T. Hodges, Low-uncertainty H_2O line intensities for the 930-nm region, J. Mol. Spectrosc. **249**, 6 (2008).

[37] A. F. Estrada-Alexanders, O. Guzmán, and B. Pérez-Vidal, High-precision virial coefficients of argon and carbon dioxide from integration of speed of sound data in the pressure-temperature domain, Mol. Phys. **110**, 1349 (2012).

[38] P. De Bifwre, M. Gallet, N. E. Holden, and I. L. Barnes, Isotopic abundances and atomic weights of the elements, J. Phys. Chem. Ref. Data **13**, 809 (1984).

[39] Australian Bureau of Meteorology: Adelaide (Kent Town), South Australia November 2016 daily weather observations, accessible via http://www.bom.gov.au/climate/data-services. Last accessed on 14 Aug. 2017.

[40] Richard A. Johnson, *Miller & Freund's Probability and Statistics for Engineers*, 7th ed. (Pearson Prentice Hall, Upper Saddle River, New Jersey, 2005).

[41] Statistics LET subcommands: Weighted standard deviation, NIST Technical Report, National Institute of Standards and Technology, 1996.

[42] I. E. Gordon *et al.*, The HITRAN2016 molecular spectroscopic database, J. Quant. Spectrosc. Radiat. Transfer **203**, 3 (2017).

Isotopic CO_2 Determination

This chapter is based on the submitted article:

S. K. Scholten, C. Perrella, J. D. Anstie, R. T. White, and A. N. Luiten, "Rapid optical measurement of $^{12}CO_2$ and $^{13}CO_2$ number density with direct optical frequency comb spectroscopy" (2019).

11.1 Overview and Motivation

This paper describes extension of the fitting code as seen in Chapter 10 to retrieve the concentrations for the two most common isotopologues of carbon dioxide: $^{12}C^{16}O_2$ and $^{13}C^{16}O_2$. The $^{13}C/^{12}C$ ratio of CO_2 is important to environmental sciences such as paleoclimatology, carbon cylcing studies, oceanography, atmospheric science, and monitoring of greenhouse gas emissions, sequestration and storage integrity [277–283]. Isotopic analysis is additionally used in biomedical applications such as metabolic flux analysis, *Helicobactor pylori* bacterium detection, liver function assessment, and pancreatic function, among others [37,284]. While this isotopic ratio has been measured previously with DFCS and other methods, this is the first verification of isotopologue specificity for this system and the first for such a system without an enhancement cavity [37,273,285].

The architecture of the physical experiment is identical to that seen in Chapter 10, excepting the introduction of the extended comb source as described in Section 5.4. This was required in order to observe absorption features from both isotopologues in the same spectral region. In addition, the large dynamic range of results when comparing the smaller-magnitude $^{13}C^{16}O_2$ absorption features to the much larger $^{12}C^{16}O_2$ features demonstrated a linearity gradient response across the spectrometer camera. This was rectified by moving to a pixel-by-pixel nonlinearity correction as described in Section 6.3.5. This paper aimed to retrieve the natural isotopic abundances from measured spectra. Additionally, by using nitrogen as a buffer gas to change the overall concentration of carbon dioxide in the sample cell, the linearity of the spectrometer system as whole could be examined and was found to be exceptionally linear over three orders of magnitude in concentration.

11.2 Statement of Contribution

11.2.1 Conceptualisation

The concept of isotope-specific detection of carbon dioxide using the VIPA spectrometer system was first conceptualised by James Anstie. The idea to extend the fitting code presented in Chapter 10 to cover both $^{13}CO_2$ and $^{12}CO_2$ and retrieve their individual concentrations simultaneously was that of Sarah Scholten. The idea of comparison to the natural abundance was also that of Sarah Scholten. The need and solution for a more accurate camera non-linearity correction was conceptualised by Sarah Scholten, Christopher Perrella, and Andre Luiten.

11.2.2 Realisation

The experimental apparatus was identical in nature to that presented in Chapter 10, except for the introduction of the spectrally-broadened optical frequency comb by use of a highly nonlinear optical fibre. The implementation of the HNLF and characterisation of the broadened comb was the work of Sarah Scholten with assistance provided by Christopher Perrella. The re-characterisation and implementation of a new non-linearity correction scheme for the camera was implemented by Sarah Scholten. Extension of the fitting code to cover the additional carbon dioxide isotopologue was primarily that of Sarah Scholten with assistance from Christopher Perrella and guidance of Andre Luiten. The data for this paper was acquired and analysed by Sarah Scholten.

11.2.3 Documentation

This paper was primarily written by Sarah Scholten, with assistance from Christopher Perrella and Andre Luiten. Editing support was provided by all other authors.

Candidate overall percentage contribution: 75%.

Sarah K. Scholten

11.2.4 Co-author Contributions

By signing below, each co-author certifies that:

- The candidate's stated contribution to the publication is accurate (as stated above).
- Permission is granted for the candidate to include the publication in the thesis.

Co-author certifications are in order of published authorship unless otherwise specified.

Christopher Perrella

James D. Anstie

Richard T. White

Andre N. Luiten

Accurate optical number density measurement of $^{12}CO_2$ and $^{13}CO_2$ with direct frequency comb spectroscopy

Sarah K. Scholten,[1,*] Christopher Perrella,[1] James D. Anstie,[1] Richard T. White,[1] and Andre N. Luiten[1]

[1] *Institute for Photonics and Advanced Sensing (IPAS), School of Physical Sciences, The University of Adelaide, Adelaide SA 5005, Australia*

(Dated: June 6, 2019)

We report on the use of direct frequency comb spectroscopy to accurately measure the concentrations of $^{12}C^{16}O_2$ and $^{13}C^{16}O_2$ isotopologues within a gas sample. We demonstrate an accuracy of 0.5% and 12% for concentration measurements of $^{12}C^{16}O_2$ and $^{13}C^{16}O_2$ respectively, with the measured isotopic ratio in excellent agreement with that expected from their natural abundances. Precision of the concentration measurements is also high, at 0.03% and 1.24% for $^{12}C^{16}O_2$ and $^{13}C^{16}O_2$ respectively. The measurement technique is also verified to be highly linear for concentrations ranging over three orders of magnitude. Direct frequency comb spectroscopy can be applied to numerous molecular species, and is therefore a promising technique for measurements in environmental monitoring and biomedical sciences.

I. INTRODUCTION

Accurate measurement of the isotopic composition of a gas sample is useful in a wide variety of applications. The $^{13}C/^{12}C$ ratio of CO_2 is particularly important within the environmental sciences including paleoclimatology [1, 2], carbon cycling studies [3–5], oceanography [6], atmospheric science [7], and monitoring of greenhouse gas emissions, sequestration and storage integrity [8, 9]. Isotopic analysis is also used in biomedical applications including metabolic flux analysis [10, 11], detection of *Helicobacter pylori* bacterium (which cause gastric ulcers and gastric cancers) [11], assessment of liver function and disease, gastric emptying, bacterial overgrowth, and pancreatic function [11].

To correctly measure the relative concentrations of isotopologues, techniques with high precision, high accuracy, large dynamic range, and of course isotopologue differentiability are required. A commonly-used technique is mass spectrometry, which fulfills most of these requirements but typically suffers an inability to differentiate between species of similar atomic mass (e.g. $^{13}C^{16}O_2$ and $^{16}O^{12}C^{17}O$). More recently, instruments based on optical spectroscopy have been developed to measure isotopic ratios by exploiting the nuclear-mass dependent frequency shifts of the ro-vibrational absorption peaks [12].

These optical techniques include Cavity Ring-Down Spectroscopy (CRDS) [11–13], Fourier Transform Infrared (FTIR) [14, 15], Dual Comb [16], and Direct Frequency Comb Spectroscopy (DFCS) [17, 18]. While possessing excellent precision and accuracy, CRDS requires many sequential measurements as the interrogation laser frequency is scanned, and makes complex gas analysis cumbersome when it is necessary to have a large scan range. FTIR overcomes this by measuring many chemical absorption signatures at once, however this comes at the expense of long data acquisition times. Without careful calibration, FTIR can yield inaccurate wavelength determination due to imperfections in their mechanical scans. Dual-comb techniques have measured CO_2 molecular spectra for ^{13}C and ^{12}C in open-air paths, however, this technique requires two optical frequency combs, making them relatively costly and complex systems. Nonetheless, recent work on shrinking frequency combs to chip-sized devices might eventually offer a rational way forward in this area [19–21].

In this paper we use direct frequency comb spectroscopy without an enhancement cavity to analyse the $^{12}C^{16}O_2$ and $^{13}C^{16}O_2$ isotopologues of CO_2. We demonstrate accurate, highly precise and linear extraction of the concentration of both isotopologues over a large dynamic range. DFCS has been used for isotopic analysis of CO2 before but only with an enhancement cavity [17]. The spectroscopy method used in this paper operates in the eye-safe NIR spectral band, and has the additional benefits of requiring only a single frequency comb as a light source, which is measured with a fixed and robust spectrometer based on spatial frequency dispersion. This reduction in complexity makes the system appealing for

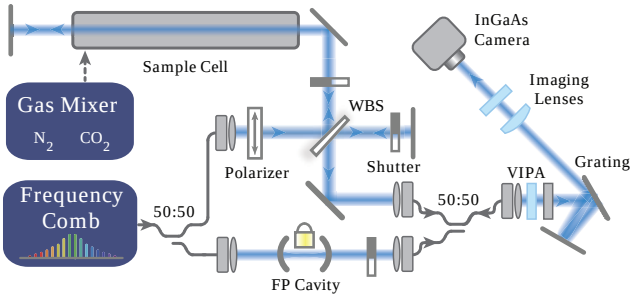

FIG. 1. A simplified diagram of the experiment. FP: Fabry-Perot (Cavity); WBS: Wedged Beam Splitter; Fibre-coupled paths are shown in solid grey, and free space optical paths in blue for the optical frequency comb.

* sarah.scholten@adelaide.edu.au

applications oustide the laboratory.

II. EXPERIMENTAL METHODS

A. Optical Experiment

The experimental setup is shown in Fig. 1. An optical frequency comb (OFC) (Menlo Systems FC1500) was used as the interrogation source which spans ∼1500 - 1600 nm. The carrier-envelope-offset frequency (f_{CEO}) of the comb is locked to a cesium beam clock (Datum CsIII), while the repetition rate, $f_{\mathrm{rep}} \approx 250$ MHz, is stabilised by locking one comb mode to a cavity-stabilized reference laser (NKT Koheras Boostik E15) at 1560 nm. The comb light is split into two paths via a 50:50 fibre coupler. The first path is used for spectroscopy and is further split into two paths, using a wedged beam splitter (WBS), into the reference (for optical comparison) and sample path that contains a double-passed 3.25 m-long sample cell (296 ± 1 K) at atmospheric pressure. A gas mixer (Environics Series 2000) uses N_2 as a buffer gas to adjust the CO_2 concentration within the sample cell, with the CO_2 gas containing a natural abundance of CO_2 isotopologues. The second fibre coupler output is sent to a length-stabilized low finesse (∼200) Fabry-Perot (FP) cavity with bandwidth of ~ 50 MHz that transmits every 36^{th} comb mode. The filtered OFC is sufficiently sparse that the spectrometer can isolate each mode which allows identification and assignment of a relative frequency to each comb mode, allowing calibration of the relative frequency axis (to within an overall frequency offset) [22–24].

Automated shutters select light from the sample, reference and cavity paths, with the co-linearity of all three paths ensured by coupling via a four-port 50:50 coupler. The spectrometer is based on a virtually imaged phased array (VIPA) etalon (Light Machinery), with a finesse of ∼100 and free spectral range (FSR) of ~ 50 GHz, that spreads the comb light vertically as a function of wavelength [25]. The VIPA is followed by a 600-lines/mm diffraction grating to remove frequency ambiguity of the VIPA by dispersing the beam horizontally [26]. This results in a 2D array of comb modes imaged on an InGaAs IR camera (Xenics XEVA-1.7-320), with ~ 2.9 THz (~ 25 nm) spectral range in the horizontal and just over one VIPA FSR in the vertical direction. Two images were acquired for both the reference and sample paths; one bright, followed by a dark image with matched integration time for camera dark field subtraction.

B. Image Analysis

To extract the CO_2 absorption signature from the images taken by the spectrometer [24], the dark frames are first subtracted from each bright image, before a pixel-by-pixel camera non-linearity correction is applied. To reduce noise, 100 measurements of each of the sample and reference images were averaged together. In order to ascertain the accuracy and precision of the measurements, 10 nominally identical sets of 100 images were taken for statistical purposes. The procedure to extract the absorption signature from these averaged images may be found in more detail in Refs. [23] and [24]. As described in Ref [24], we use the optically filtered comb image (with an effective mode spacing of 9 GHz), together with the known repetition rate and offset frequency of the comb, to derive an accurate mapping from position on the detector to relative optical frequency.

C. Spectral Fitting and Number Density Extraction

A concentration measurement of $^{12}C^{16}O_2$ and $^{13}C^{16}O_2$, and hence isotopic ratio, is obtained by fitting the experimental spectrum with a model absorption spectrum based upon parameters from the HITRAN 2012 database [28, 29]. There are differences in the optical transfer function of the signal and reference paths due to effects such as beam divergence, etalons, and polarisation rotation between paths. To remove the broad-scale background variations that are a result of this difference in optical transfer function between paths, the background was measured by filling the sample cell with N_2 to remove any absorption features. This background was well-fitted by an eighth-order Fourier series, which was used as a model for this persistent background. Any slight shot-to-shot variations from this background, originating from alignment fluctuations, were accounted for with an additional third-order polynomial. There are three absorption bands that fall within the observed spectral region: the 30012←00001 overtone band of $^{13}C^{16}O_2$ and the 30013←00001 and 31113←01101 overtone and hot band respectively of $^{12}C^{16}O_2$, totalling 307 ro-vibrational features that are all modelled as Voigt line-shapes. Parameters of each peak are available from the HITRAN database including: line strengths ($S_{\eta\eta'}(T_{\mathrm{ref}})$) where η and η' denote the lower and upper states of the transition respectively, line centres ($\nu_{\eta\eta'}$), lower state energy of the transition (E_η), pressure shifts, and pressure-broadened line half-widths due to both air and self-broadening. The spectrometer imposes an instrumental broadening on the spectrum, the shape of which is close to that of a Voigt function with a Lorentzian half-width-at-half-maximum of $0.01 \pm 0.001\,\mathrm{cm}^{-1}$ and Gaussian $1/e$ half-width of $0.012 \pm 0.001\,\mathrm{cm}^{-1}$. We obtain this through observation of individual comb modes using the optically-filtered frequency comb image. Doppler broadening of $0.06841 \pm 0.00002\,\mathrm{cm}^{-1}$ for each absorption line was also included in the model. We note that HITRAN parameters are provided at a reference temperature of $T_{\mathrm{ref}} = 296$ K. This requires a temperature correction to be included for certain parameters including the

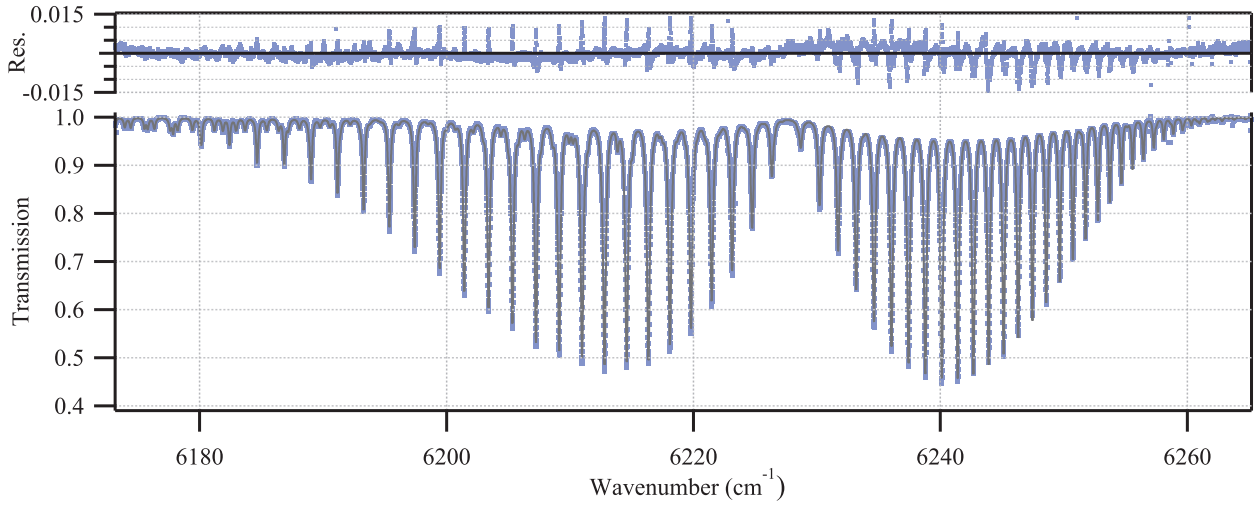

FIG. 2. Data for pure CO_2 gas sample averaged 1000 times (blue markers) showing the $^{13}C^{16}O_2$ 30012←00001 spectral band, and the $^{12}C^{16}O_2$ 30013←00001 and 31113←01101 overtone and hot band respectively. A fit (grey) to the 307 ro-vibrational features is shown. Fit residuals (top) show peak height issues due to the use of the HITRAN-recommended Voigt line-profile and some broad-scale structure as the spectrum and background are not separable during fitting.

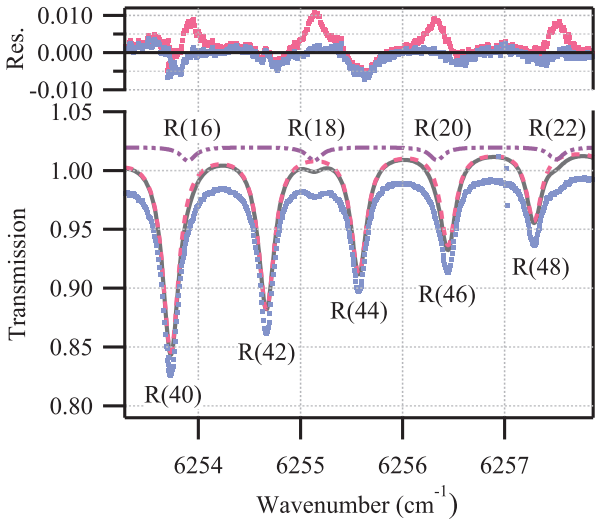

FIG. 3. Close-up of the R16 - R22 features of the 30012←00001 spectral band of $^{13}C^{16}O_2$ amongst the much larger R40 - R46 lines of the 30013←00001 band of $^{12}C^{16}O_2$. Note the odd-numbered transitions are forbidden due to molecular symmetry [27]. Main graph: total fit in solid grey, data in blue markers, $^{13}C^{16}O_2$ fit in purple dot-dashed line, and $^{12}C^{16}O_2$ in pink dashed line. Fits are offset by +0.02. Residuals graph: blue dots are residuals of data from total fit; pink dots are residuals of data from total fit with the $^{13}C^{16}O_2$ contributions omitted.

line strength:

$$S_{\eta\eta'}(T) = S_{\eta\eta'}(T_{\text{ref}}) \frac{Q(T_{\text{ref}})}{Q(T)} \frac{e^{\frac{-c_2 E_\eta}{T}}}{e^{\frac{-c_2 E_\eta}{T_{\text{ref}}}}} \frac{1 - e^{\frac{-c_2 \nu_{\eta\eta'}}{T}}}{1 - e^{\frac{-c_2 \nu_{\eta\eta'}}{T_{\text{ref}}}}} \quad (1)$$

where $c_2 = hc/k_B$, h is the Planck constant, c is the speed of light and k_B is the Boltzmann constant [29]. The total internal partition function ($Q(T)$) of each isotopologue must also be altered for temperature, with the full calculation simplified by use of a polynomial approximation [30].

We performed a least-squares optimised fitting of the model to the experimental spectrum with the only free parameters being the two isotopologue number densities, temperature, and background terms. The fitted and experimental spectrum for a pure sample of CO_2 is shown in Fig. 2 for 1000 averages, with a zoomed portion shown in Fig. 3. Under-estimation of the peak heights is apparent as seen in the blue residuals and is a known problem with using the Voigt line-shape recommended for use by the HITRAN database which does not take into account more complex collisional dynamics [32–36].

III. RESULTS

To demonstrate the spectrometer's ability to accurately measure the ratio of isotopologues over a wide range of absorption strengths (or concentrations), we presented the spectrometer with gas mixtures made up of CO_2 and N_2. Measurements were made at CO_2/N_2 concentration ratios within the sample cell of 100%, 75%, 50%, 25%, and 10%. The analysis was applied to extract

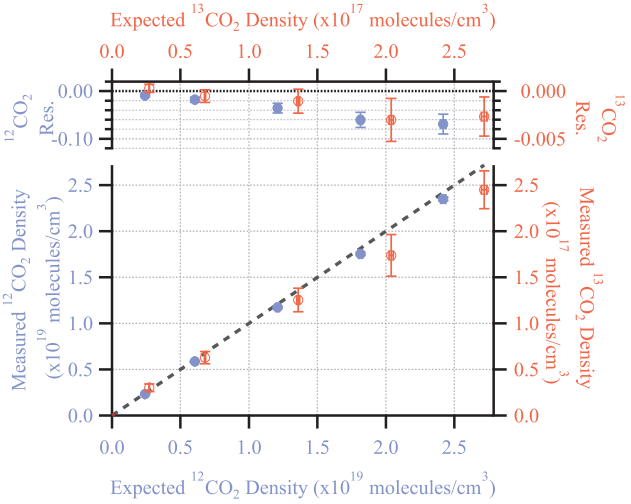

FIG. 4. Average measured densities of $^{13}C^{16}O_2$ (open red markers) and $^{12}C^{16}O_2$ (filled blue markers) for 10 sets (reference and signal) of 100 images against densities predicted by the Virial-corrected Ideal Gas Law. The expected 1:1 density line is shown in dashed grey [31].

the number density of the two targeted isotopologues for the five total CO_2 concentrations examined. Figure 4 shows the measured number density of both isotopologues against those predicted by a third-order corrected Ideal Gas Law calculation (grey dashed line) [31, 37]. Isotopic ratio measurements are shown in Fig. 5 which are in excellent agreement with the natural abundance values of 98.420% and 1.106% for $^{12}C^{16}O_2$ and $^{13}C^{16}O_2$ respectively, with the remaining isotopologues present in trace amounts [31]. The measurements have a precision of 0.03% and 1.24% for the 100% CO_2 measurement for $^{12}C^{16}O_2$ and $^{13}C^{16}O_2$ respectively. The measurement precision is taken to be the standard deviation of 10 concentration measurements, each of which are retrieved from fits to a spectrum containing 100 spectra averaged together.

The accuracy of the $^{12}C^{16}O_2$ density measurements are in agreement with the Virial corrected Ideal Gas Law to within 0.5%, while the $^{13}C^{16}O_2$ measurements agree to within 12%. The discrepancy for $^{13}C^{16}O_2$ arises from the small absorption (only ∼1%) when compared to the $^{12}C^{16}O_2$ peaks, as seen in Fig. 3. The accuracy of our optical concentration measurements, shown in Fig. 4, is limited by four major contributors: the residual background transmission structure, uncertainties in the known absorption strengths and shape of the spectral lines, and spectral broadening from the VIPA. Residual background structure was unable to be adequately fitted as the background and absorption spectra are not completely separable. This contributes uncertainties of 0.2% and 8% to the measured concentrations of $^{12}C^{16}O_2$ and $^{13}C^{16}O_2$ respectively. The uncertainties in the absorption line strengths were taken from HITRAN [36]. Assuming the errors for each peak are uncorrelated, we estimate the weighted standard error in the ensemble of $S_{\eta\eta'}$ to be 0.1% for $^{12}C^{16}O_2$ and 0.3% for $^{13}C^{16}O_2$ [38, 39]. These uncertainties set the ultimate accuracy limit of the spectrometer, and form the limit for all optical spectroscopy isotopologue concentration measurements. Another contributor to the error is the use of the HITRAN-recommended Voigt molecular line-shape, which has been shown to lead to underestimates of line intensities in high resolution spectral measurements [32, 36]. Slight asymmetry and frequency dependence in the VIPA spectrometer broadening is not accounted for when fitting, with the net effect of each on the density estimated at 0.4% for both isotopologues [24]. This issue can be removed by using the rarefied comb to interrogate the gas, which completely eliminates spectrometer broadening [22]. These optical uncertainties, listed in Table I, were combined in quadrature with the measurement precision to yield total uncertainties of 0.5% and 12% for the $^{12}C^{16}O_2$ and $^{13}C^{16}O_2$ absolute number density measurements respectively, which are displayed as the error bars in Fig. 4 and Fig. 5. The gas mixer has a specified accuracy of 0.75% of the requested concentration for both N_2 and CO_2; this is displayed as the horizontal error bars of Fig. 4 for both isotopes.

TABLE I. **Optical uncertainties and their relative effect on number density measurements**

Effect	$^{12}CO_2$ (%)	$^{13}CO_2$ (%)
HITRAN 2012 $S_{\eta\eta'}$ (T_{ref}) uncertainty	0.1	0.3
Spectrometer broadening/asymmetry	0.4	0.4
Residual background structure	0.2	8.0
Combined Optical Uncertainty	0.5	8.0

Uncertainties listed are percentages of measured number density at the 1σ level for $^{12}CO_2$ and $^{13}CO_2$. Detailed discussion of the derivation of the above values are found in-text.

Agreement of the measured isotopic ratio to the natural abundance value (Fig. 5) over the full range of CO_2 concentrations examined demonstrates the excellent linearity of the concentration measurements using the DFCS technique. Deviations from a linear measurement, ΔL, were quantified by taking the ratio of two concentrations u_1 and u_2, scaled by their known CO_2/N_2 ratios, r_1 and r_2:

$$\Delta L = 1 - \frac{u_1}{r_1} \Big/ \frac{u_2}{r_2} \,. \tag{2}$$

If the measurement is linear, each ratio u_1/r_1 and u_2/r_2 should produce the same measured concentration. Taking all possible comparisons such that $r_1 > r_2$, and $u_1 > u_2$, gave a deviation from a linear measurement of $-0.15\pm0.47\%$ for $^{12}C^{16}O_2$ measurements. The $^{13}C^{16}O_2$ concentration measurements gave a deviation from linearity of $-2.6\pm8.6\%$ with increased error due

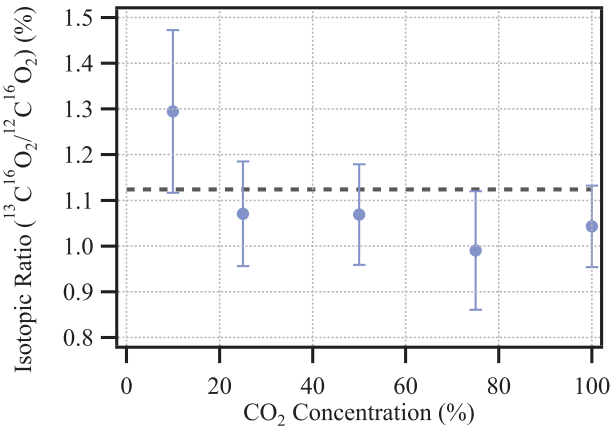

FIG. 5. The measured $^{13}C^{16}O_2/^{12}C^{16}O_2$ isotopic ratio derived from 10 sets (reference and signal) of 100 images for each CO_2 concentration against gas mixer concentration (blue markers). Error bars are a quadrature sum (see main text). The ratio predicted by the HITRAN database is shown in dashed grey for the natural abundances of the isotopologues in question.

to lower signal-to-noise ratio. Comparison between $^{12}C^{16}O_2$ and $^{13}C^{16}O_2$, over a concentration range of three orders of magnitude, gave a deviation of linearity of $-4.9\pm8.5\%$, again limited by the signal-to-noise ratio of the $^{13}C^{16}O_2$ absorption peaks. This demonstrates a large dynamic range of highly-linear concentration measurements, which can be improved upon with more averaging and/or longer absorption path length.

IV. CONCLUSION

We have demonstrated accurate concentration retrieval of the $^{12}C^{16}O_2$ and $^{13}C^{16}O_2$ isotopologues of CO_2. Agreement between concentration measurements and the Virial-corrected Ideal Gas Law is shown to be within 0.5% for $^{12}C^{16}O_2$ and 12% for $^{13}C^{16}O_2$, with the measured ratio in excellent agreement with that expected from the natural abundance of both isotopes. The measurement technique is demonstrated to be highly linear, with deviation from a linear measurement being $-4.9\pm8.5\%$ over a concentration range of three orders of magnitude. These results demonstrate the ability of DFCS to correctly measure the relative concentrations of isotopologues with high precision, accuracy, and large dynamic range, making it a promising technique for measurements for environmental monitoring and biomedical sciences.

ACKNOWLEDGMENTS

This work was supported by: Australian Research Council (ARC) Linkage Project Grants (LP120200605, LP140100647); The Government of South Australia (The Premiers Science and Research Fund).

[1] R. J. Francey, C. E. Allison, D. M. Etheridge, C. M. Trudinger, I. G. Enting, M. Leunberger, R. L. Langenfelds, E. Michel, and L. P. Steele, Tellus B **51**, 170 (1999).
[2] T. K. Bauska, D. Baggenstos, E. J. Brook, A. C. Mix, S. A. Marcott, V. V. Petrenko, H. Schaefer, J. P. Severinghaus, and J. E. Lee, Proceedings of the National Academy of Sciences **113**, 3465 (2016).
[3] M. S. Torn, S. C. Biraud, C. J. Still, W. J. Riley, and J. A. Berry, Tellus B: Chemical and Physical Meteorology **63**, 181 (2011).
[4] D. Yakir and L. d. S. L. Sternberg, Oecologia **123**, 297 (2000), arXiv:arXiv:1011.1669v3.
[5] W. G. Mook, Netherlands Journal of Sea Research **20**, 211 (1986).
[6] A. C. Mix, N. G. Pisias, R. Zahn, W. Rugh, C. Lopez, and K. Nelson, Paleoceanography **6**, 205 (1991).
[7] S. S. Assonov, C. A. Brenninkmeijer, T. J. Schuck, and P. Taylor, Atmospheric Chemistry and Physics **10**, 8575 (2010).
[8] B. Galfond, D. Riemer, and P. Swart, Int. J. Greenhouse Gas Control **42**, 307 (2015).
[9] S. Krevor, J. C. Perrin, A. Esposito, C. Rella, and S. Benson, International Journal of Greenhouse Gas Control **4**, 811 (2010).
[10] T. H. Yang, E. Heinzle, and C. Wittmann, Computational Biology and Chemistry **29**, 121 (2005).
[11] E. R. Crosson, K. N. Ricci, B. A. Richman, F. C. Chilese, T. G. Owano, R. A. Provencal, M. W. Todd, J. Glasser, A. A. Kachanov, B. A. Paldus, T. G. Spence, and R. A. Zare, Anal. Chem. **74**, 2003 (2002).
[12] D. Dickinson, S. Bodé, and P. Boeckx, Rapid Communications in Mass Spectrometry **31**, 1892 (2017).
[13] R. N. Zare, D. S. Kuramoto, C. Haase, S. M. Tan, E. R. Crosson, and N. M. R. Saad, Proceedings of the National Academy of Sciences **106**, 10928 (2009).
[14] J. Mohn, M. J. Zeeman, R. A. Werner, W. Eugster, and L. Emmenegger, Isotopes in Environmental and Health Studies **44**, 241251 (2008).
[15] D. W. T. Griffith, M. B. Esler, and S. R. Wilson, AIP Conference Proceedings AIP Conference Proceedings, **430**, 207 (1998).
[16] G. B. Rieker, F. R. Giorgetta, W. C. Swann, J. Kofler, A. M. Zolot, L. C. Sinclair, E. Baumann, C. Cromer, G. Petron, C. Sweeney, P. P. Tans, I. Coddington, and N. R. Newbury, Optica **1**, 290 (2014).
[17] M. J. Thorpe, D. Balslev-Clausen, M. S. Kirchner, and J. Ye, Optics Express **16**, 2387 (2008).
[18] F. Adler, M. J. Thorpe, K. C. Cossel, and J. Ye, Annu. Rev. Anal. Chem. **3**, 175 (2010).
[19] D. R. Carlson, D. D. Hickstein, A. Lind, S. Droste, D. Westly, N. Nader, I. Coddington, N. R. Newbury, K. Srinivasan, S. A. Diddams, and S. B. Papp, Opt.

Lett. **42**, 2314 (2017).
[20] P. DelHaye, A. Schliesser, O. Arcizet, T. Wilken, R. Holzwarth, and T. J. Kippenberg, Nature **450**, 1214 (2007).
[21] B. Stern, X. Ji, Y. Okawachi, A. L. Gaeta, and M. Lipson, Nature **562**, 401 (2018).
[22] N. Bourbeau Hébert, S. Scholten, R. White, J. Genest, A. Luiten, and J. Anstie, Opt. Express **23**, 13991 (2015).
[23] S. K. Scholten, J. D. Anstie, N. Hébert, R. W. White, J. Genest, and A. N. Luiten, Opt. Lett. **41** (2016).
[24] S. K. Scholten, C. Perrella, J. D. Anstie, R. T. White, W. Al-Ashwal, N. B. Hébert, J. Genest, and A. N. Luiten, Phys. Rev. Applied **9**, 054043 (2018).
[25] M. Shirasaki, Opt. Lett. **21**, 366 (1996).
[26] S. A. Diddams, L. Hollberg, and V. Mebele, Nature **445**, 627 (2007).
[27] R. Kakkar, *Atomic and Molecular Spectroscopy: Basic Concepts and Applications* (Cambridge University Press, 2015).
[28] L. S. Rothman, I. E. Gordon, Y. Babikov, A. Barbe, D. Chris Benner, P. F. Bernath, M. Birk, L. Bizzocchi, V. Boudon, L. R. Brown, A. Campargue, K. Chance, E. A. Cohen, L. H. Coudert, V. M. Devi, B. J. Drouin, A. Fayt, J. M. Flaud, R. R. Gamache, J. J. Harrison, J. M. Hartmann, C. Hill, J. T. Hodges, D. Jacquemart, A. Jolly, J. Lamouroux, R. J. L. Roy, G. Li, D. A. Long, O. M. Lyulin, C. J. Mackie, S. T. Massie, S. Mikhailenko, H.S.P. Müller, O. V. Naumenko, A. V. Nikitin, J. Orphal, V. Perevalov, A. Perrin, E. R. Polovtseva, C. Richard, M. A. H. Smith, E. Starikova, K. Sung, S. Tashkun, J. Tennyson, G. C. Toon, V. G. Tyuterev, and G. Wagner, J. Quant. Spectrosc. Radiat. Transfer **130**, 4 (2013).
[29] L. S. Rothman, C. P. Rinsland, A. Goldman, S. T. Massie, D. P. Edwards, J. -M. Flaud, A. Perrin, C. Camy-Peyret, V. Dana, J. -Y. Mandin, J. Schroeder, A. McCann, R. R. Gamache, R. B. Wattson, K. Yoshino, K. V. Chance, K. W. Jucks, L. R. Brown, V. Nemtchinov, and P. Varanasi, J. Quant. Spectrosc. Radiat. Transfer **60**, 665 (1998).
[30] R. R. Gamache, R. L. Hawkins, and L. S. Rothman, J. Mol. Spectrosc. , 205 (1990).
[31] P. De Biévre, M. Gallet, N. E. Holden, and I. L. Barnes, J. Phys. Chem. Ref. Data **13**, 809 (1984).
[32] J. T. Hodges, J. Tennyson, P. F. Bernath, A. Campargue, A. Csaszar, L. Daumont, R. R. Gamache, D. Lisak, O. Naumenko, L. Rothman, H. Tran, N. Zobov, B. Chris, L. Gianfrani, and J. M. Hartmann, Pure Appl. Chem. **86**, 1931 (2014).
[33] N. Ngo, N. Ibrahim, X. Landsheere, H. Tran, P. Chelin, M. Schwell, and J.-M. Hartmann, J. Quant. Spectrosc. Radiat. Transfer **113**, 870877 (2012).
[34] V. Kochanov, J. Quant. Spectrosc. Radiat. Transfer **113**, 16351641 (2012).
[35] D. Lisak and J. T. Hodges, Journal of Molecular Spectroscopy **249**, 6 (2008).
[36] I. E. Gordon, L. S. Rothman, C. Hill, R. V. Kochanov, Y. Tan, P. F. Bernath, M. Birk, V. Boudon, A. Campargue, K. V. Chance, B. J. Drouin, J. -M. Flaud, R. R. Gamache, J. T. Hodges, D. Jacquemart, V. I. Perevalov, A. Perrin, K. P. Shine, M. -A. H. Smith, J. Tennyson, G. C. Toon, H. Tran, V. G. Tyuterev, A. Barbe, A. G. Császár, V. M. Devi, T. Furtenbacher, J. J. Harrison, J. -M. Hartmann, A. Jolly, T. J. Johnson, T. Karman, I. Kleiner, A. A. Kyuberis, J. Loos, O. M. Lyulin, S. T. Massie, S. N. Mikhailenko, N. Moazzen-Ahmadi, H. S. P. Müller, O. V. Naumenko, A. V. Nikitin, O. L. Polyansky, M.Rey, M. Rotger, S. W. Sharpe, K. Sung, E. Starikova, S. A. Tashkun, J. Vander Auwera, G. Wagner, J. Wilzewski, P. Wcisło, S. Yu, and E. J. Zak, J. Quant. Spectrosc. Radiat. Transfer **203**, 3 (2017).
[37] A. F. Estrada-Alexanders, O. Guzmán, and B. Pérez-Vidal, Mol. Phys. **110**, 13491358 (2012).
[38] R. A. Johnson, *Miller & Freund's Probability and Statistics for Engineers*, 7th ed. (Pearson Prentice Hall, 2005).
[39] *Statistics LET Subcommands: Weighted Standard Deviation*, Tech. Rep. (National Institute of Standards and Technology (NIST), 1996).

High-Resolution Measurements of $^{12}C_2H_2$

This chapter is based on the article under preparation:

F. Karim†, S. K. Scholten†, C. Perrella, and A. N. Luiten, "High-resolution spectroscopy of $^{12}C_2H_2$ with a tunable rarefied optical frequency comb and virtually imaged phased array spectrometer" (2019).

†These authors contributed equally to this work.

12.1 Overview and Motivation

The aim of this paper was to improve the frequency-resolution of the VIPA spectrometer, as demonstrated on the narrow absorption features of low-pressure acetylene ($^{12}C_2H_2$). High-resolution, broad-bandwidth spectroscopy with absolute frequency accuracy is an invaluable tool to provide precision parameters for spectral databases to facilitate models by which future measurements are compared [133,286,287]. In such cases, a lack of or reduced instrumentation broadening is beneficial, removing the need for deconvolution of the resulting spectra from the instrument function of the spectrometer [288,289]. This is particularly true for cases where the molecular spectrum is crowded with an abundance of absorption features or in low pressure scenarios [138,181,290].

This paper describes use of the rarefication cavity as introduced in Chapters 7 & 8. As in Chapter 8 the rarefied comb was used directly to probe the sample in order to fully resolve the modes of the comb. However instead of stepping the cavity through the peaks of the filter-cavity transmission function as described in Chapter 8, the repetition rate of the comb was instead sequentially increased by 10 Hz, with the cavity tracking this new comb. A small change in repetition rate results in a shift at the observed frequency, resulting in new comb slightly offset from the previous. Sequential stepping of the repetition rate then fills in the entirety of the sample spectrum. This manuscript details the first use of this method with an optical frequency comb and VIPA spectrometer to perform high-resolution spectroscopy, as demonstrated on the narrow features of acetylene. The experimental apparatus is similar to that seen in Chapters 10 & 11, excepting the removal of the gas mixer, rarefication of the comb by the FP cavity prior to sample interrogation, a change from the 6.5 m flow cell to a 5 cm double-passed $^{12}C_2H_2$ at 50 Torr, and switching the comb to a radio-frequency locking scheme for repetition rate flexibility. In addition, the image analysis code was changed to a box-summation method as described in the following paper. The model fit discussed in

the paper is the same as that presented in Chapters 10 & 11, as appropriately modified for low-pressure acetylene, and compares favourably with the measured spectrum.

12.2 Statement of Contribution

12.2.1 Conceptualisation

The idea of performing ultra-high resolution spectroscopy of acetylene was a joint effort between Sarah Scholten, Christopher Perrella, and Andre Luiten as a way to extend the applications of the molecular modelling code demonstrated in Chapter 10. The need for and solution to interfacing between the data acquisition code, rarefication cavity, and optical frequency comb was a joint idea between all four authors. The need for change and solution to the analysis code modification to work with the new spectrographs was also a collaborative affair between all four authors.

12.2.2 Realisation

This paper used the extended comb source, model fitting code and rarefication cavity system described in previous papers and as previously attributed. In addition, the data acquisition, model fitting and interfacing code was built upon previous work by Sarah Scholten. Faisal Karim modified the acquisition code to interface with the optical frequency comb and sequentially change its repetition rate to acquire the interleaved spectra under guidance from the remaining authors. In addition, Faisal Karim constructed the optical setup as well as performing data acquisition and analysis on the data that appears in this paper.

12.2.3 Documentation

This paper was primarily written by Faisal Karim with assistance from Sarah Scholten and under the guidance of Christopher Perrella and Andre Luiten. Editorial support was provided by all authors.

Candidate overall percentage contribution: 45%.

Sarah K. Scholten

12.2.4 Co-author Contributions

By signing below, each co-author certifies that:

- The candidate's stated contribution to the publication is accurate (as stated above).
- Permission is granted for the candidate to include the publication in the thesis.

Co-author certifications are in order of published authorship unless otherwise specified. Faisal Karim is joint first-author for this manuscript.

Faisal Karim

Christopher Perrella

Andre N. Luiten

High-resolution spectroscopy of $^{12}C_2H_2$ with a tunable rarefied optical frequency comb and virtually imaged phased array spectrometer

Faisal Karim,[1,*] Sarah K. Scholten,[1,*] Christopher Perrella,[1] and Andre N. Luiten[1]

[1] *Institute for Photonics and Advanced Sensing (IPAS), School of Physical Sciences, The University of Adelaide, Adelaide SA 5005, Australia*

(Dated: July 17, 2019)

Molecular spectra possess a large number of narrow absorption features spread across a relatively wide spectral bandwidth. To obtain correct line shapes and widths of these narrow absorption features, one needs to perform high-resolution spectroscopy that is ideally free from spectrometer instrumentation broadening. Here we demonstrate a technique for acquiring high-resolution spectra of gas molecules with spectral sampling of between a few kHz to a few MHz with 3.3 THz (25 nm) spectral bandwidth. In addition, the acquired spectra are free from spectrometer instrumentation broadening and not limited by the spectrometer resolution. This is achieved via tuning the repetition rate of an optical frequency comb in combination with an optical rarefication cavity that resolves each comb mode individually. The technique is demonstrated with a 7.88 MHz frequency-sampled spectrum of $^{12}C_2H_2$ at 50 Torr with more than 500,000 data points.

I. INTRODUCTION

High-resolution broadband spectroscopy of molecules is vital for performing analytic gas phase research, and has yielded essential information on material structure for physical, chemical and biological sciences [1]. A new and exciting tool for probing molecular systems is the optical frequency comb (OFC), which has enabled real-time detection [2] and identification of gases in mixtures [3], with applications in the oil and gas industry [4], environmental monitoring [5], breath analysis [6], and defence. OFCs are near-ideal interrogation sources for molecular spectroscopy as they deliver a light source with dense spectral sampling over a broad spectral bandwidth, enabling precise, high-resolution spectroscopy with absolute frequency accuracy [7–9].

The development of a broadband and high-resolution OFC-based spectrometer has been the subject of intense interest over recent years. OFCs have previously been used in conjunction with Fourier transform spectroscopy [10], micro-resonator based frequency comb spectroscopy [11, 12], cavity ring-down spectroscopy [13], dual-comb spectroscopy [14], and single-comb heterodyning techniques [15]. However, in all cases the resolution was limited to tens of MHz at best. A key challenge in all of these techniques is unravelling the comb into its component frequencies without negatively affecting the shape of narrow spectral features. Additionally if a dispersive spectrometer is used there is a trade-off between measurable spectral resolution by the spectrometer and density of comb modes and hence spectral sampling [16–19].

In this paper we demonstrate a technique to acquire high-resolution molecular spectra using a cavity-rarefied optical frequency comb and dispersive spectrometer based on a virtually imaged phased array (VIPA). An approximately 25 nm spectrum of isotopically-pure acetylene ($^{12}C_2H_2$) with 7.88 MHz frequency-resolution was acquired, and agrees favourably with a model of the absorption spectrum without spectrometer instrumentation broadening based on parameters from the high-resolution transmission molecular absorption (HITRAN) database.

II. EXPERIMENTAL METHODS

A. Optical Experiment

The experimental setup is shown in Fig. 1. An OFC (Menlo Systems FC1500) is used as the sample interrogation source and spans 1500-1700 nm. It has a tunable repetition rate (f_r) of 250 MHz, with both f_r and the carrier-envelope offset frequency (f_0) stabilised to a Caesium beam clock (Datum CsIII). Comb modes of spacing f_r are unable to be directly resolved by the available spectrometer. To resolve the densely packed comb modes, the light from the OFC is first rarefied by a length-stabilised low-finesse (∼200) Fabry-Pérot (FP) cavity that has a free spectral range (FSR) of 9 GHz ($36 \times f_r$), which allows every 36^{th} comb mode to be transmitted. This generates a new comb with $f_r = 9$ GHz which is sufficiently sparse for complete resolution by the spectrometer [18, 20].

The rarefied comb first passes through a polariser before being split into the reference and sample paths of the experiment via a 50/50 wedged beam splitter (WBS). The reference arm is used for optical comparison while the sample arm contains a double-passed 5 cm $^{12}C_2H_2$ gas cell (50 ± 5 Torr, Wavelength References) at room temperature. Each path is equipped with an automated shutter and both paths are directed to the spectrometer via optical fibre to ensure colinearity at the spectrometer input.

The spectrometer is based upon a Virtually Imaged Phased Array (VIPA) etalon that disperses the beam as a function of frequency in the vertical direction [21]. Light

* These authors contributed equally to this work

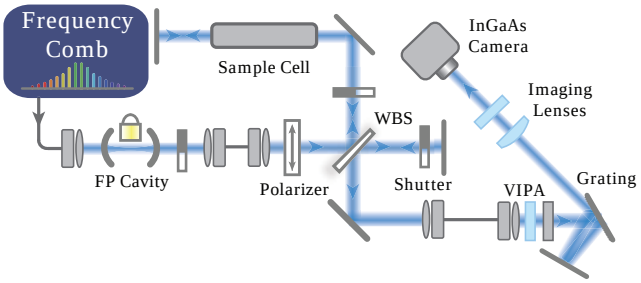

FIG. 1. Diagram of the experimental setup for high-resolution spectroscopy of acetylene. Blue: free-space path of the optical frequency comb; grey: optical fibres; FP: Fabry Pérot (cavity); WBS: wedged beam splitter.

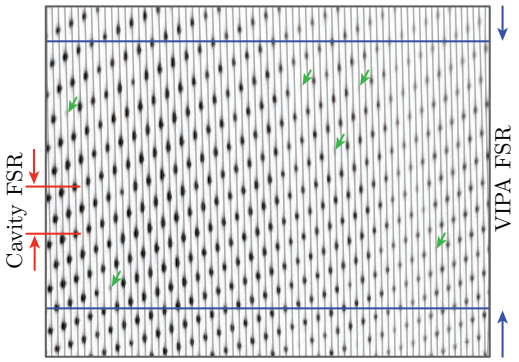

FIG. 2. A typical sample path image showing the rarefied comb (inverted colours). The blue horizontal lines mark one VIPA FSR containing unique spectral data, while the red horizontal lines denote one cavity FSR of $36 \times f_r$. The horizontal separation of adjacent vertical stripes with the centres as mapped from the unrarefied image (overlayed in light grey stripes) is also one VIPA FSR. There are typically five to six comb modes per vertical VIPA stripe. Several comb modes have been absorbed by acetylene (green arrows).

from the reference or sample path is directed through a cylindrical lens which line focuses the light into the antireflective-coated input window of the VIPA. The VIPA has an FSR of about 50 GHz and finesse of approximately 100. When used in isolation the VIPA displays self-wrapping behaviour, sending frequencies separated by multiples of the VIPA FSR to the same spatial location. This creates bright stripes of overlapping comb modes. In order to remove this ambiguity, the VIPA is used in conjunction with a 600 lines/mm diffraction grating arranged orthogonally to disperse the overlapped modes in the horizontal direction [8]. The grating is double passed to improve horizontal angular resolution and ensures potential cross talk between adjacent VIPA stripes is minimized. This results in a 2D array of comb modes that are then focused onto and imaged by an InGaAs camera (Xenics XEVA-1.7-320) [7]. Each image spans approximately 2.9 THz (approximately 25 nm) of spectral range in the horizontal and just over one VIPA FSR in the vertical direction. A typical rarefied-comb sample-path image is shown in Fig. 2.

When considered in the spectral domain, the frequency of the n^{th} comb mode is related to f_r and f_0 through

$$f_n = nf_r + f_0 \tag{1}$$

where n is a large positive integer [7]. In order to acquire high-resolution spectra of acetylene, which at low pressure possesses a crowded absorption spectrum of narrow features, f_r was increased in steps of $\Delta f_r = 10$ Hz, while f_0 was maintained at 20 MHz. At the spectral region of measurement for acetylene (1510 nm – 1540 nm), n is approximately 7.885×10^5. By Eq. 1, a change of $\Delta f_r = 10$ Hz to f_r corresponds to a shift of 7.88 MHz in the observed spectral range. This shift in frequency also defines the effective resolution of the measurement, with greater resolution also increasing measurement times. The rarefication cavity is able to automatically track this change via length adjustment, and produces a new rarefied comb with an effective repetition rate of $36 \times (f_r + \Delta f_r)$ [18]. This is demonstrated for the comb subsets with effective repetition rates of $36 \times f_r$ and $36 \times (f_r + \Delta f_r)$ in Fig. 3. The repetition rate of the comb is sequentially increased by Δf_r until the final frequency shift at the observed frequency range has increased by 9 GHz from the initial comb, forming a complete spectrum.

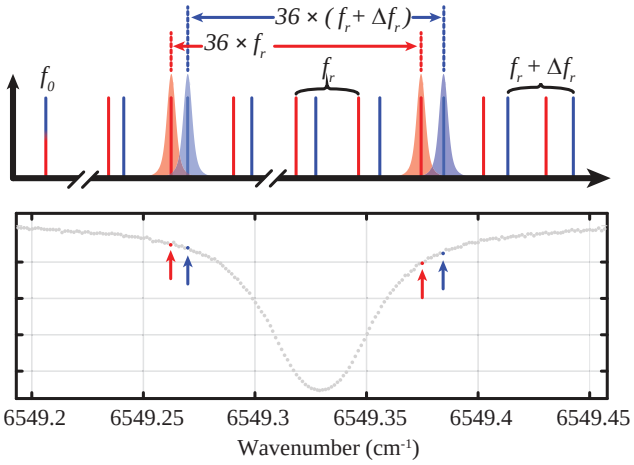

FIG. 3. Interleaving the high-resolution spectrum obtained by stepping f_r while the being tracked by the FP cavity. The original mode spacing subset $36 \times f_r$ is shown in red, while a 'new' comb subset (blue) with repetition rate $36 \times (f_r + \Delta f_r)$ is obtained by shifting the repetition rate by Δf_r. The resulting spectral data points from the comb-cavity system generated by the stepping of f_r are shown in corresponding colours. All comb subsets have the offset frequency $f_0 = 20$ MHz.

B. Image Analysis

A set of four images is taken with matching integration times using the optical shutters: a bright reference image

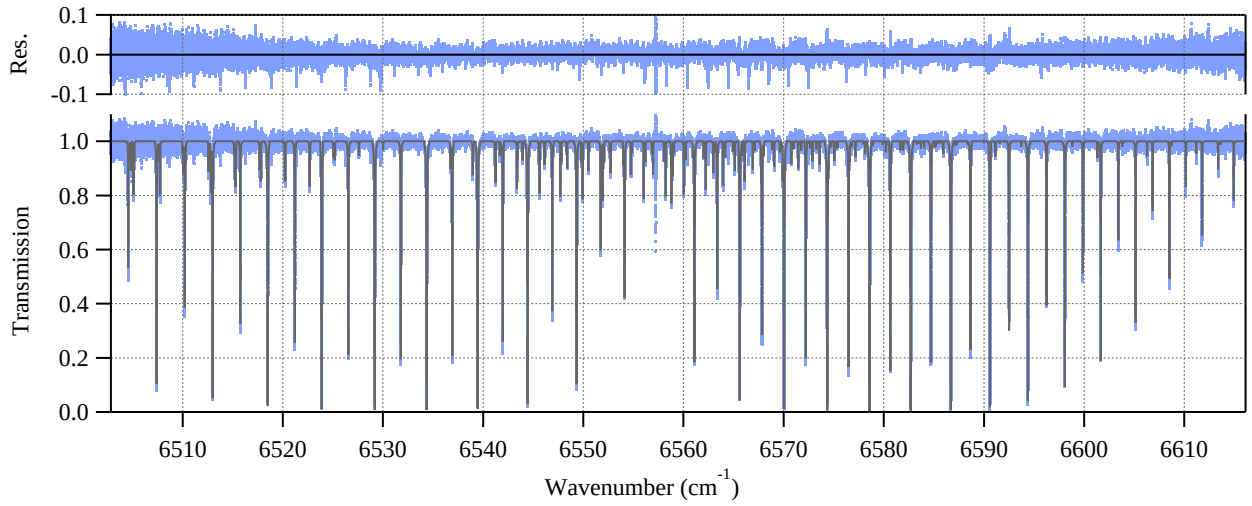

FIG. 4. High-resolution acetylene spectrum (blue markers) with fit results using parameters from the HITRAN database (grey line). The strongest transition (101000 ← 000000, see Ref. [22] for notation) - though saturated - shows the characteristic 3:1 intensity variation that arises due to nuclear spin statistics [23]. Owing to the large number of $^{12}C_2H_2$ absorption lines in this spectral region, only the four strongest vibrational transitions are included in the fit (101000 ← 000000, 101011 ← 000011, 101101 ← 000101, 110110 ← 000000), and some unfitted ro-vibrational transitions appear in the residuals [24].

and sample path image pair, along with a matching dark image for each path. Each dark image is subtracted from the corresponding bright image to remove dark background effects, followed by a pixel-by-pixel camera nonlinearity correction based upon a previously obtained set of grey images. An unrarefied image with the comb bypassing the FP cavity captured during initialisation of the system is used to locate the centres of VIPA stripes, which allows for accurate frequency assignment of each comb mode location on the rarefied reference image and its corresponding sample path image. The power of each mode is calculated using a box-summation approach wherein pixels surrounding each mode are summed to capture all available signal per mode, and collapses each comb mode to a single data point.

The reference and sample data for each comb subset is averaged with 100 like images to improve the signal to noise ratio of the final spectrum. Division of the sample's comb modes by the reference modes yields absorption for that subset of comb modes. This additionally removes irregularities in the power envelop of the comb and any common-mode optical effects. The process is repeated for each comb subset of sequentially differing repetition rate to completely sample the spectrum of C_2H_2. This process is shown in Fig. 3. Finally, the individual absorption spectra from each comb subset are stitched together to obtain the complete high-resolution absorption spectrum of C_2H_2 as seen in Fig. 4.

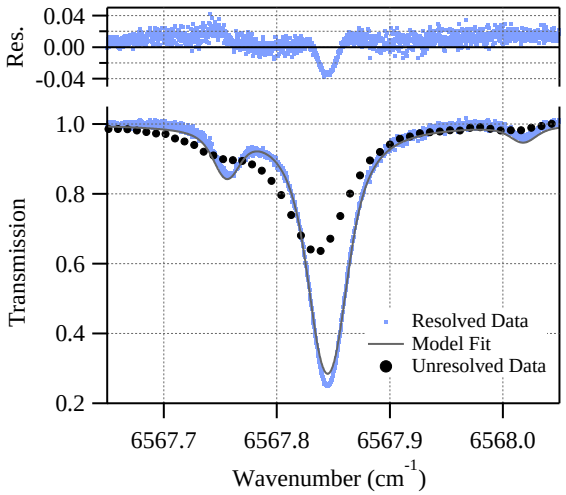

FIG. 5. Zoomed portion of the spectrum (blue markers) with corresponding HITRAN fit (solid grey) and residuals. A spectrum acquired under the same conditions for the unresolved case is shown in black, with the effects of instrumentation broadening apparent [25]. Use of a Voigt line shape during fitting results in structure in the residuals and an underestimate of line strengths [26–29].

III. RESULTS

Fig. 4 demonstrates the technique with a spectrum of sub-10 MHz (7.88 MHz) spectral resolution, much below the 2 GHz resolution limit of the spectrometer [25]. The spectrum is normalised using comb modes with zero ab-

sorption common to all repetition rates. As can be seen more clearly on a zoomed portion of the spectrum shown in Fig. 5, results acquired without the cavity-rarefication process suffer the effects of instrumentation broadening from not individually resolving comb modes. In particular for low pressure acetylene, which possesses a multitude of exceedingly narrow absorption features in this spectral range, instrumentation broadening from the VIPA spectrometer results in the reduction of absorption depths, along with the merging or smearing of adjacent peaks. In addition, the broadening can suppress small transitions into the noise of the measurement as seen in Fig. 5 at $\sim 6568\,\mathrm{cm}^{-1}$, which becomes apparent by comparison with the fully-resolved case.

Obtaining the correct width and strengths of absorption features is crucial for extracting valuable spectroscopic information such as the temperature and pressure of a sample, along with fundamental parameters of the molecule. The width of an individual absorption feature is a combination of the natural linewidth, Doppler broadening, and collisional broadening, and so an accurate width must be used to extract the pressure of a gas sample from each line without requiring knowledge about an instrumentation function [30]. Additionally, the relative heights of the features in an absorption band reflects the population distribution among various rotational states of the molecules, revealing the sample temperature [31, 32]. To this end, the four strongest absorption bands of the spectrum comprising 222 individual ro-vibrational absorption features were simultaneously fit with a model derived from parameters available on the HITRAN database using a Voigt lineshape [25]. The Doppler full-width-at-half-maximum was also included in the fit ($7.167\,\mathrm{cm}^{-1}$). The fit returned a temperature of 19.5° and pressure of 51.8 Torr, in agreement with laboratory conditions and manufacturing tolerances. The signal-to-noise ratio of the rarefied spectra may be improved by increasing the power per comb mode, reducing the need for averaging over multiple spectra for the purposes of noise reduction.

IV. CONCLUSION

The combined tunable comb rarefication and VIPA spectrometer technique as demonstrated in this paper provides a method for broadband, sub-10 MHz frequency resolution while removing the instrumentation broadening of the spectrometer. This method is highly suited to perform high resolution spectroscopy for the purposes of acquiring precision molecular parameters for spectral databases and for acquiring low pressure or densely-packed absorption spectra.

ACKNOWLEDGMENTS

This work was supported by: Australian Research Council (ARC) Linkage Project Grants (LP120200605, LP140100647); The Government of South Australia (The Premiers Science and Research Fund).

[1] S. Kinugawa and H. Sasada, Japanese Journal of Applied Physics **29**, 611 (1990).
[2] P. Weibring, D. Richter, J. G. Walega, and A. Fried, Opt. Express **15**, 13476 (2007).
[3] L. Nugent-Glandorf, T. Neely, F. Adler, A. J. Fleisher, K. C. Cossel, B. Bjork, T. Dinneen, J. Ye, and S. A. Diddams, Optics Letters **37**, 3285 (2012).
[4] S. Coburn, C. B. Alden, R. Wright, K. Cossel, E. Baumann, G.-W. Truong, F. Giorgetta, C. Sweeney, N. R. Newbury, K. Prasad, I. Coddington, and G. B. Rieker, Optica **5**, 320 (2018).
[5] G. B. Rieker, F. R. Giorgetta, W. C. Swann, J. Kofler, A. M. Zolot, L. C. Sinclair, E. Baumann, C. Cromer, G. Petron, C. Sweeney, P. P. Tans, I. Coddington, and N. R. Newbury, Optica **1**, 290 (2014).
[6] M. J. Thorpe, K. D. Moll, R. J. Jones, B. Safdi, and J. Ye, Science **311**, 1595 (2006), https://science.sciencemag.org/content/311/5767/1595.full.pdf.
[7] N. Picqué and T. W. Hänsch, Nature Photonics **13**, 146 (2019).
[8] S. A. Diddams, L. Hollberg, and V. Mebele, Nature **445**, 627 (2007).
[9] B. Bernhardt, A. Ozawa, P. Jacquet, M. Jacquey, Y. Kobayashi, T. Udem, R. Holzwarth, G. Guelachvili, T. W. Hänsch, and N. Picqué, Nat. Photonics **4**, 55 (2009).
[10] P. Maslowski, K. F. Lee, A. C. Johansson, A. Khodabakhsh, G. Kowzan, L. Rutkowski, A. A. Mills, C. Mohr, J. Jiang, M. E. Fermann, and A. Foltynowicz, Physical Review A **93**, 1 (2016).
[11] M. Yu, Y. Okawachi, A. G. Griffith, M. Lipson, and A. L. Gaeta, Opt. Lett. **42**, 4442 (2017).
[12] A. Gambetta, M. Cassinerio, D. Gatti, P. Laporta, and G. Galzerano, Scientific Reports **6**, 35541 (2016).
[13] M. J. Thorpe, K. D. Moll, R. J. Jones, B. Safdi, and J. Ye, Science **311**, 1595 (2006), https://science.sciencemag.org/content/311/5767/1595.full.pdf.
[14] Y. D. Hsieh, Y. Iyonaga, Y. Sakaguchi, S. Yokoyama, H. Inaba, K. Minoshima, F. Hindle, T. Araki, and T. Yasui, Scientific Reports **4**, 1 (2014).
[15] T. Shioda, K. Fujii, K. Kashiwagi, and T. Kurokawa, Optics Communications **284**, 5180 (2011).
[16] I. Coddington, N. Newbury, and W. Swann, Optica **3**, 414 (2016).
[17] G. Ycas, F. R. Giorgetta, K. C. Cossel, E. M. Waxman, E. Baumann, N. R. Newbury, and I. Coddington, Optica **6**, 165 (2019).
[18] N. Hébert, S. Scholten, R. White, J. Genest, A. Luiten, and J. Anstie, Optics Express **23**, 13991 (2015).
[19] S. A. Diddams, L. Hollberg, and V. Mebele, Nature **445**, 627 (2007).

[20] S. K. Scholten, J. D. Anstie, N. Hébert, R. W. White, J. Genest, and A. N. Luiten, Opt. Lett. **41** (2016).
[21] M. Shirasaki, Optics Letters **21**, 366 (1996).
[22] D. Jacquemart, J. -Y. Mandin, V. Dana, C. Claveau, J. Vander Auwera, M. Herman, L. S. Rothman, L. Régalia-Jarlot, and A. Barbe, Journal of Quantitative Spectroscopy and Radiative Transfer **82**, 363 (2003).
[23] G. Herzberg, *Molecular Spectra and Molecular Structure: Infrared and Raman of Polyatomic Molecules*, edited by J. W. T. Spinks, Vol. 2 (Prentice-Hall, 1990).
[24] I. E. Gordon, L. S. Rothman, C. Hill, R. V. Kochanov, Y. Tan, P. F. Bernath, M. Birk, V. Boudon, A. Campargue, K. V. Chance, B. J. Drouin, J. M. Flaud, R. R. Gamache, J. T. Hodges, D. Jacquemart, V. I. Perevalov, A. Perrin, K. P. Shine, M. A. H. Smith, J. Tennyson, G. C. Toon, H. Tran, V. G. Tyuterev, A. Barbe, A. G. Császár, V. M. Devi, T. Furtenbacher, J. J. Harrison, J. M. Hartmann, A. Jolly, T. J. Johnson, T. Karmanav, I. Kleiner, A. A. Kyuberis, J. Loos, O. M. Lyulin, S. T. Massie, S. N. Mikhailenko, N. Moazzen-Ahmadi, H. S. P. Müller, O. V. Naumenko, A. V. Nikitin, O. L. Polyansky, M. Rey, M. Rotger, S. W. Sharpe, K. Sung, E. Starikova, S. A. Tashkun, J. V. Auwera, G. Wagner, J. Wilzewski, P. Wcisło, S. Yuh, and E. J. Zak, Journal of Quantitative Spectroscopy and Radiative Transfer **203**, 3 (2017).
[25] S. K. Scholten, C.Perrella, J. D. Anstie, R. T. White, W. Al-Ashwal, N. B. Hébert, J. Genest, and A. N. Luiten, Physical Review Applied **9**, 054043 (2018).
[26] J. Tennyson, P. Bernath, A. Campargue, *et al.*, Pure Appl. Chem. **86**, 1931 (2014).
[27] N. Ngo, N. Ibrahim, X. Landsheere, H. Tran, P. Chelin, M. Schwell, and J.-M. Hartmann, J. Quant. Spectrosc. Radiat. Transfer **113**, 870877 (2012).
[28] V. Kochanov, J. Quant. Spectrosc. Radiat. Transfer **113**, 16351641 (2012).
[29] D. Lisak and J. T. Hodges, Journal of Molecular Spectroscopy **249**, 6 (2008).
[30] C. J. Foot, *Atomic physics*, Vol. 7 (Oxford University Press, 2005).
[31] R. A. Nyquist, *Interpreting Infrared, Raman, and Nuclear Magnetic Resonance Spectra* (Academic Press, United States of America, 2001).
[32] G. Herzburg, *Molecular Spectra and Molecular Structure: Spectra of Diatomic Molecules*, 2nd ed., Vol. 1 (D. Van Nostrand Company; Prentice-Hall, Princeton, New Jersey, 1950).

Conclusion and Future Work

The goal of this project was the development of a direct frequency comb spectroscopy approach for future applications in biomedical and environmental fields. The system needed to be reliable, rapid, sensitive, accurate, precise, broadband, and have isotopic and species selectivity. Each of these factors has been demonstrated in turn throughout the course of this thesis. A spectrometer was constructed and we developed an initial analysis code to extract broadband absorption spectra from spectrometer images. This was created in the course of preparing the paper described in Chapter 8. In the same chapter, the rarefication cavity that allows both sub-VIPA-resolution measurements and accurate frequency-axis measurements was described. The next chapter marked the improvement of the spectrometer to function with the unrarefied frequency comb and several changes to several optical elements to capture the full optical transfer function of the sample gas. Additionally, Chapter 9 included the introduction of the rapid computation package for Voigt profiles by inclusion of the Faddeeva package.

Chapter 10 saw the introduction of a spectral fitting code to extract parameters of interest from the molecular system. Namely, the concentration and temperature. Importantly, this paper marked the demonstration of a highly robust, accurate, precise, and rapid spectroscopic system. Several changes to the analysis, interfacing, and acquisition codes made this possible, as well as a substantial effort to correct the nonlinear response and backgrounding issues of the spectrometer CCD array. Chapter 11 saw the improvement of the camera corrections further, with the development of a pixel-by-pixel camera correction improving the linearity of the camera over three orders of concentration magnitude. At the same time, isotopic specificity was demonstrated, with the extension of the molecular fitting code to cover multiple species simultaneously. Chapter 12 demonstrated ultra-high resolution spectroscopy of acetylene by combining the rarefication cavity first introduced in Chapter 8 with tuning of the comb's repetition rate and the molecular model initially described in Chapter 10.

While much improvement and characterisation of the spectroscopic system was made during the course of this thesis, there is always more work to be done. Future work is primarily focused on development and demonstrations for more specialised applications, as well as introducing more complex gas samples involving multiple gas species, liquid components and more challenges as would be faced in real-world scenarios. These applications follow two main streams: biomedical and environmental monitoring.

The road to medical breath analysis is a long one and will require several developments to the system, as well as the relevant clinical trials. Development would first focus on accurate quantitative detection of known complex (dry) gas samples in the concentrations present in the human breath. This is a method similar to testing of capnography machines, in which the exhalation of carbon dioxide of a patient is monitored for use during anaesthesia and in intensive care [291–294]. In addition, the human breath contains a significant amount of water vapour that would be hazardous to any optical instrument, necessitating a simultaneous stream of research involving the extraction of water vapour from a sample while leaving the remaining gases intact. A first attempt at this has already been demonstrated with the spectroscopic system presented in this thesis by monitoring the total carbon dioxide respiration product of baker's yeast in a closed system. Preliminary results may be seen in Fig 13.1. This demonstration required the use of a drying column to remove the water vapour from the circulating air, proving the efficacy of the preliminary moisture handling system and represents the first test on a biological sample. Future work still remains however to make moisture handling more robust in the system, potentially by either a removable sample chamber separate to the optical elements and/or by inclusion of a controlled condensation system. In addition to further trials on yeast, additional biological sources should be investigated before moving onto efficacy trials with human subjects.

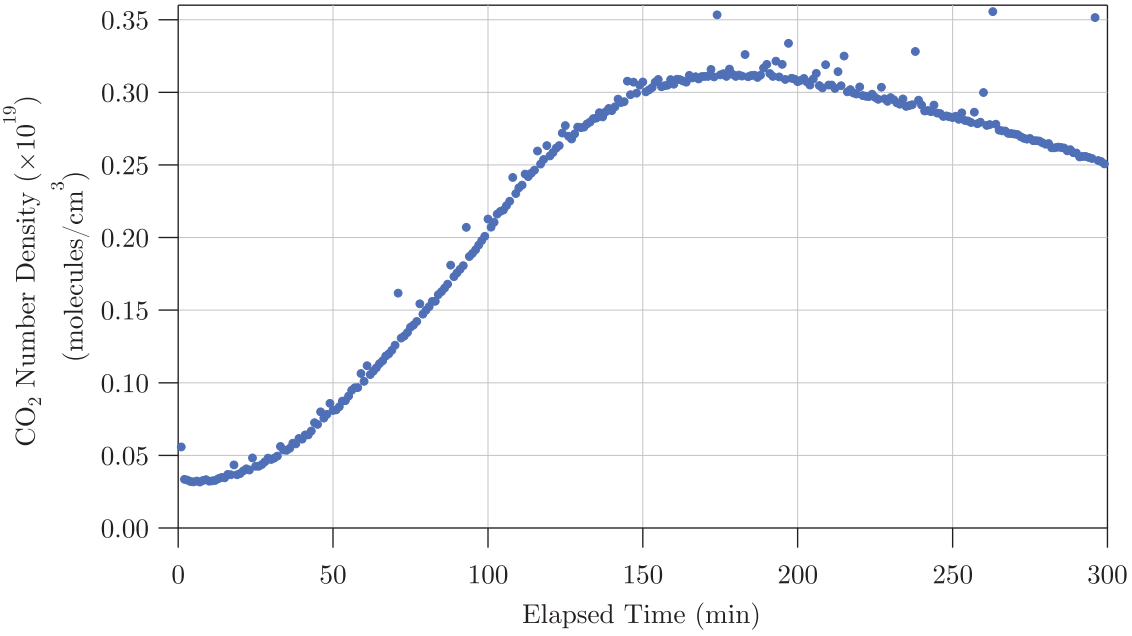

Figure 13.1: Preliminary results of the system measuring the total carbon dioxide released during respiration by Baker's yeast held at 30° over a five hour period.

The second easily-identifiable set of applications and future work is in the field of environmental monitoring. While the system has been used to detect carbon dioxide in a laboratory-based setting, it would be of interest to acquire atmospheric point-to-point measurements of carbon dioxide and other important molecules. This not only has applications to

monitoring of greenhouse gas levels, but to pollution monitoring, air quality monitoring, and in industrial processing environments, which would all benefit from point-to-point sensing. Similar dual-comb systems have been demonstrated recently in such capabilities with great success [132,133,295,296].

For both applications, more complex samples containing gases of multiple species must also be tested and accurate retrieval of concentrations of each component demonstrated. Though the system has demonstrated the ability to differentiate between isotopologues of the same species and it is theoretically a relatively simple extension, it still remains to be demonstrated that this is also true for molecules of different species in practice. In addition, the entire system is not currently portable and requires sizable amounts of miniaturisation work. The miniaturisation of optical frequency combs has come a long way in the years since their invention, with briefcase-sized combs and smaller appearing at time of writing. Additionally, micro-combs based on microresonators and 'combs on a chip' are active fields of study that may provide even smaller comb technologies [129,142,297–300]. The spectrometer and sampling systems are realistically able to be miniaturised to a portable size and is more of an engineering puzzle.

For more complex samples, several factors require additional development and exploration. Rotation of the diffraction grating that forms a part of the spectrometer allows access to a wider spectrum, as the main limitation to the spectral bandwidth is currently the physical size of the camera CCD array, which limits the single-shot optical bandwidth to approximately 25 nm. However, the 200 nm-wide spectral bandwidth of the comb is still present at the output of the spectrometer, but does not land on the CCD array. Rotation of the grating directs a different 25 nm section of the comb light to the camera, and in this way the entire bandwidth of the optical frequency comb may be used for spectroscopy. Alternatively, the spectrometer may be reconstructed based around a camera with a larger CCD array, though the cost could be high.

Another aspect with more complex samples is the increased computation time in fitting to spectra. At present, fitting to the spectrum requires pre-knowledge about the contents of the gas sample, which may not be feasible in out-of-lab applications. Additionally, in a typical 25 nm spectrum of a single molecule it was not uncommon to be fitting 200-300 absorption features simultaneously. As the number of molecular species increases this number will grow drastically, including the need to cope with overlapping of absorption peaks from different species. These factors combine to make the current method of parameter extraction an infeasible long-term solution. A better solution would be to include an element of machine learning to extract the parameters from many training spectra or, at the very least, to identify the molecular species present in the sample to inform the starting parameters of a more traditional fitting code.

In future it may also be beneficial to investigate the absorption of molecules in the mid-infrared, where the fundamental ro-vibrational transitions of these small molecules are typically located. The absorption features are much stronger in this region which allows improved

sensitivity of measurements. Additionally, it reduces the path lengths and hence total gas volumes required. Research using mid-infrared dual-comb spectroscopy has recently demonstrated this to be a viable technique for measurements in the environmental field, with a VIPA spectrometer suitable for the mid-IR also demonstrated in a laboratory setting [144,145,296]. Alternatively, the permanent inclusion of a multi-pass enhancement cell to improve the interaction path length of the sample should be considered.

Part V

Appendices

Harmonic Oscillator Vibrational Selection Rule Addendum

In the interest of space, the full derivation of the vibrational transition selection rule in the harmonic oscillator approximation was not introduced in Section 3.3.1.2. It is presented here for the interested reader in its entirety.

A.1 The Dipole Transition Moment

In order for a transition to occur in a molecular system by way of encountering electromagnetic radiation, two important factors must be considered. Firstly, the incoming radiation must posses an energy - and hence frequency - that corresponds to some energy difference between states of the molecular system. Secondly and most importantly from a transition rule perspective, the dipole transition moment $\langle \boldsymbol{\mu} \rangle_{nm}$ between an initial state ψ_m and a final state ψ_n must be non-zero [153,157,166]:

$$\langle \boldsymbol{\mu} \rangle_{nm} = \int \psi_n^* \mu \psi_m d\tau = \langle \psi_n | \mu | \psi_m \rangle \neq 0. \tag{A.1}$$

Initial and final state wavefunctions ψ_m and ψ_n are associated with energy levels of the system n and m respectively, μ is the dipole operator, and Eq. A.1 is evaluated over all space. The asterisk implies complex conjugation. Equation A.1 is particularly important to ro-vibrational molecular spectroscopy as it gives rise to, amongst other results, the selection rules for allowed vibrational transitions [166,171].

A.2 The Harmonic Oscillator Approximation Vibrational Selection Rule

The selection rules for allowed transitions of the diatomic quantum harmonic oscillator are derivable by application of Eq. A.1. That is, the transition between initial vibrational state ψ_m and final vibrational state ψ_n must produce a nonzero dipole transition moment:

$$\langle \boldsymbol{\mu} \rangle_{nm} = \int \psi_n^* \mu \psi_m d\tau = \langle \psi_n | \mu | \psi_m \rangle \neq 0$$

in order for the transition to be allowed [153,157,171]. Consider the transition moment evaluated for the harmonic oscillator wavefunctions presented in Eq. 3.33:

$$\psi_n(x) = \left(\frac{\alpha}{\pi}\right)^{\frac{1}{4}} H_n\left(\sqrt{\alpha}x\right) e^{-\frac{\alpha x^2}{2}}$$

for Hermite polynomials of order n:

$$\begin{aligned}
\langle \boldsymbol{\mu} \rangle_{nm} &= \int \psi_n^*(x)\, \mu \psi_m(x)\, d\tau && \text{(A.2)}\\
&= \left(\frac{\alpha}{\pi}\right)^{\frac{1}{4}} \left(\frac{\alpha}{\pi}\right)^{\frac{1}{4}} \int H_n\left(\sqrt{\alpha}x\right) e^{-\frac{\alpha x}{2}^2} \mu H_m\left(\sqrt{\alpha}x\right) e^{-\frac{\alpha x}{2}^2} dx && \text{(A.3)}\\
&= \left(\frac{\alpha}{\pi}\right)^{\frac{1}{2}} \int e^{-\alpha x^2} dx \int H_n\left(\sqrt{\alpha}x\right) \mu H_m\left(\sqrt{\alpha}x\right) dx && \text{(A.4)}\\
&= q \int H_n(x)\, x H_m(x)\, dx && \text{(A.5)}
\end{aligned}$$

in which

$$\int_{-\infty}^{\infty} e^{-\alpha x^2} = \left(\frac{\pi}{\alpha}\right)^{\frac{1}{2}},$$

were we have set $\alpha = 1$, and the dipole moment operator for a single charged particle of charge q in one dimension is $\mu = qx$ [301].

At this point it is important to note the parity of the wavefunction components within the integrand and more generally. A function $f(x)$ is called even if $f(-x) = f(x)$ or odd if $f(-x) = -f(x)$ [302]. Multiplication of parity components is straightforward: $even \times even = even$, $odd \times even = odd$, and $odd \times odd = even$ [303]. When a product function within an integrand is odd, integration along the x-axis yields a zero result, while integrands with even parity, such as the Gaussian components of the transition moment integral, integrate to a non-zero value.

Examples of this can be seen graphically in Fig. A.1. Figures A.1(a) and A.1(b) show the products of $\psi_0(x)$ with $\psi_1(x)$ and $\psi_1(x)$ with $\psi_2(x)$ respectively. In both cases an odd function results, leading to a net area of zero when integrated along x due to the orthonormality of the Hermite polynomials and even parity of the Gaussian contributions. Note that Hermite polynomials with $n = 0, 2, 4...$ have even parity, while those with $n = 1, 3, 5...$ have odd parity [304]. Figure A.1(c) shows the first two wavefunctions, along with the dipole moment operator μ. As the dipole moment operator is odd, the product function of the operator with the two wavefunctions is even and positive for both positive and negative values of x, as seen in Fig. A.1 [212]. This leads to a non-zero integration result along the x-axis. As it is the odd functions that can change the parity of an integrand, even components may be effectively ignored qualitatively. This method can be used to check quickly whether a transition moment is zero, and hence whether the transition is allowed. Returning to Eq. A.5 and recalling the recursion relation for Hermite polynomials (Eq. 3.34):

$$zH_m(z) = mH_{m-1}(z) + \frac{1}{2}H_{m+1}(z), \qquad \text{(A.6)}$$

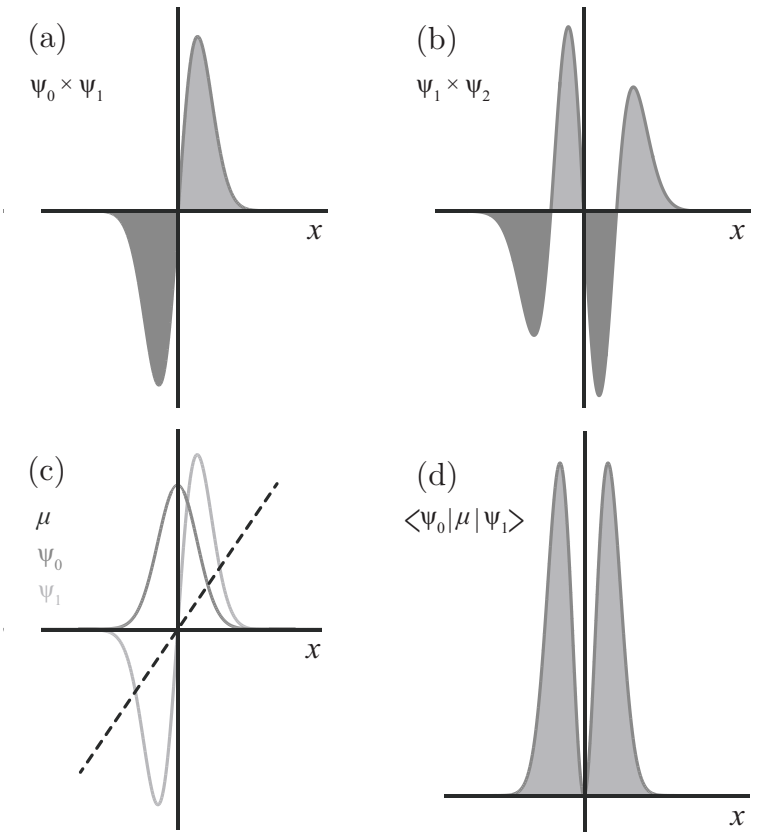

Figure A.1: A graphical representation of the orthonormal properties of the vibrational wavefunctions and transition moment in the harmonic oscillator approximation, as reproduced from Ref. [171]. (a) The product of ψ_0 and ψ_1. The light and dark grey areas under the curves are of equal area, resulting in a zero net area when integrated and confirming the result predicted by Eq. 3.35 of zero as the wavefunctions are orthogonal. (b) The product of ψ_1 and ψ_2 is also zero as the wavefunctions are still orthogonal. (c) Plot of ψ_0 (dark grey), ψ_1 (light grey), and the dipole operator $\mu = ex$ (black dashed line). (d) Integration of $\langle \psi_n | \mu | \psi_m \rangle$ along the x-axis leads to a non-zero net area and transition moment, indicating an allowed transition.

the term $xH_m(x)$ can be substituted into Eq. A.5 to give

$$\langle \boldsymbol{\mu} \rangle_{nm} = \int H_n(x) \left[mH_{m-1}(x) + \frac{1}{2} H_{m+1}(x) \right] dx \tag{A.7}$$

$$= m \int H_n(x) H_{m-1}(x)\, dx + \frac{1}{2} \int H_n(x) H_{m+1}(x)\, dx. \tag{A.8}$$

As mentioned previously, the Hermite polynomials form an orthonormal set (Eq. 3.35), and so the two integrals in Eq. A.8 are nonzero if and only if:

$$\int H_n(x) H_{m-1}(x)\, dx = \delta_{n,m-1} = \begin{cases} 1, & \text{if } n = m-1. \\ 0, & \text{if } n \neq m-1. \end{cases} \tag{A.9}$$

and

$$\int H_n(x) H_{m+1}(x)\, dx = \delta_{n,m+1} = \begin{cases} 1, & \text{if } n = m+1. \\ 0, & \text{if } n \neq m+1. \end{cases} \tag{A.10}$$

Therefore vibrational transitions in the harmonic oscillator approximation are only allowed if the vibrational quantum number changes by one unit ($\Delta n = \pm 1$), that is

$$\Delta v = \pm 1. \tag{A.11}$$

This means only transitions between adjacent vibrational energy levels are allowed in the harmonic oscillator approximation [166,167]. However, higher harmonic transitions ($\Delta v = \pm 2, \pm 3...$) are also observed in practice, and may only be explained by introducing anharmonicity to the vibrational system.

Effects of Parity and Rotational-Vibrational Selection Rules

As briefly discussed in Section 3.5, intra-band intensities may be modified depending on the parity of the molecular species in question. Of particular interest are centrosymmetric molecules such as some of the isotopologues of acetylene and carbon dioxide as examined in this thesis. To understand the effects of nuclear spin statistics and further modifiers such as l-type doubling, along with the origin of ro-vibrational transition selection rules, it is important to first differentiate between the varied types of parity or symmetry a molecule may possess.

B.1 Types of Parity

Extreme care must be taken when defining the parity of diatomic or linear polyatomic molecules. This is because there are several types of parity including $+/-$, e/f, u/g, and a/s, which all depend upon different symmetry operations and in which components of the wavefunction are assessed. In essence, if the Hamiltonian operator $\hat{H}$ commutes with a symmetry operator $\hat{O}_S$, then a set of simultaneous eigenfunctions (wavefunctions) of the two operators may be found [157]. In mathematical terms:

$$\left[\hat{H}, \hat{O}_S\right] = 0 \tag{B.1}$$

implies

$$\hat{H}\psi_{\pm} = E\psi_{\pm} \tag{B.2}$$

and that

$$\hat{O}_S\psi_{\pm} = \pm\psi_{\pm}. \tag{B.3}$$

The effect of the associated symmetry operator may be used to label the wavefunctions and energy levels of a molecule with a particular symmetry. However, both the part of the total Hamiltonian operator and the symmetry operator under consideration must be specified in order to avoid confusion. Each of the types of parity will now be explained explicitly.

B.1.1 Total (+/−) Parity

The total parity of a molecule is obtained when considering the electronic, vibrational, and rotational (but not nuclear spin) components of the total Hamiltonian operator with the inversion symmetry operator, $\hat{E}^*$. The $\hat{E}^*$ operator inverts the coordinates of all nuclei and electrons in the laboratory frame that originates at the centre of mass, and is also known as the reflection symmetry of a molecule. In Cartesian coordinates this would be

$$\hat{E}^*\psi\left(x_i, y_i, z_i\right) = \psi\left(-x_i, -y_i, -z_i\right) \tag{B.4}$$

$$= \pm\psi\left(x_i, y_i, z_i\right). \tag{B.5}$$

The $\hat{E}^*$ symmetry operator is used to divide molecular energy states into two classes:

$$\hat{E}^*\psi = \hat{E}^*\left(\psi_{\text{el}}\psi_{\text{vib}}\psi_{\text{rot}}\right) = \pm\psi \tag{B.6}$$

where energy levels that transform as $+\psi$ have positive (+) total parity, and those that transform as $-\psi$ have negative (-) total parity [157,203]. The effects of $\hat{E}^*$ must be considered on each part of ψ individually. The orbital and nuclear spin parts of the electronic wavefunction ψ_{el} are affected by the application of $\hat{E}^*$, and the $+/-$ superscript on the molecular term symbol for a state indicates the effect of $\hat{E}^*$ on the orbital part of ψ_{el}. For Π states and higher ($\ell > 0$) this superscript is not used as the rotational levels always occur as a $+/-$ pair due to ℓ-type doubling (see Section B.4). The effect on the vibrational wavefunction is also relatively simple as this inversion relation leaves ψ_{vib} unchanged, as ψ_{vib} relies only upon the magnitude of the internuclear separation and not the particular coordinates. The rotational wavefunction ψ_{rot} transforms as

$$\hat{E}^*\psi_{\text{rot}} = (-1)^J\psi_{\text{rot}} \tag{B.7}$$

so that each rotational energy level alternates total parity as J increases [153,157]. This means that for all totally symmetric vibrational species Σ^+ in the electronic ground state, even-J rotational levels are positive parity, while odd-J levels are negative parity [153,159,165]. In Σ^- vibrational states, the opposite is true as the electronic part of the wavefunction is now antisymmetric, with even-J rotational levels having negative parity, and odd-J rotational levels having even parity to compensate [152,153]. In $\Pi, \Delta, ...$ vibrational levels, there are two sublevels for each J of slightly different energy and of differing parity [153]. The parity ordering alternates either as $+-$, $-+$, $+-$, ... or $-+$, $+-$, $-+$,... as can be seen in Fig. B.1(a) [153].

The selection rules for total parity are again derived by the transition moment integral

$$\langle\boldsymbol{\mu}\rangle_{nm} = \int \psi_n^*\mu\psi_m d\tau \tag{B.8}$$

needing a symmetric integrand to be non-zero [160,166]. Noting that the transition moment

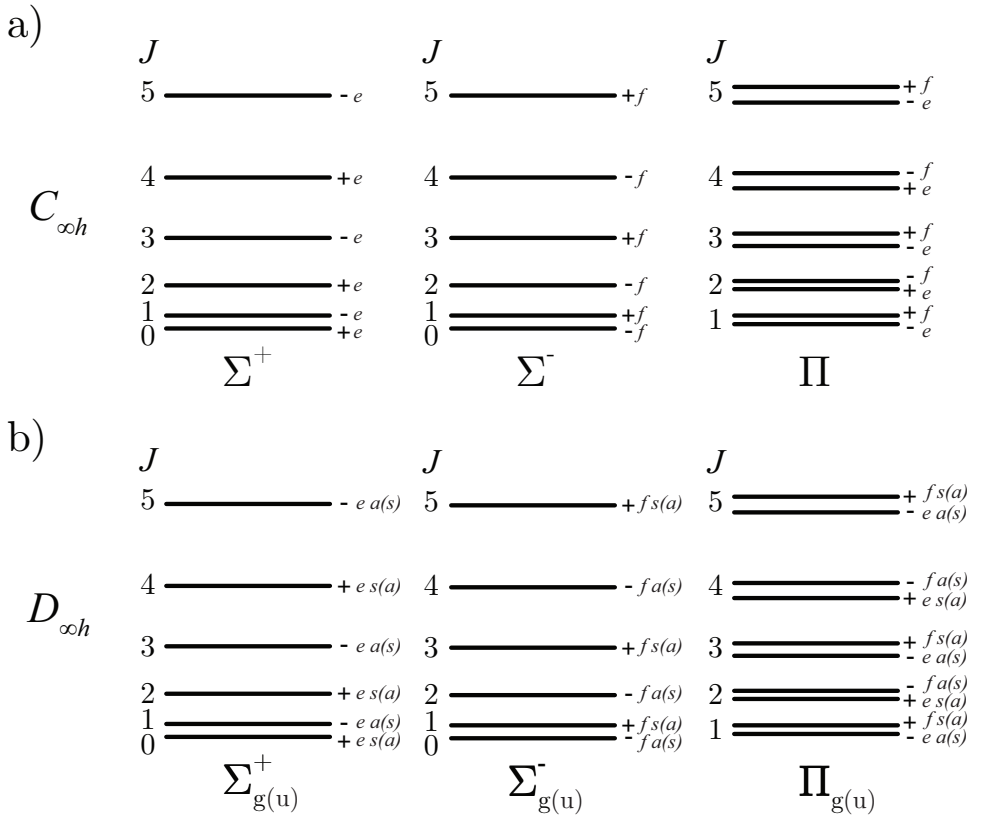

Figure B.1: Summary of the symmetry properties of rotational levels in various species of vibrational levels of linear molecules as seen in this thesis. (a) shows the symmetries for molecules in point group $C_{\infty h}$ for linear molecules that are not centrosymmetric such as HCN, while (b) shows symmetries of point group $D_{\infty h}$ for molecules possessing a centre of inversion symmetry such as CO_2 and C_2H_2 [153]. In (b) the symmetry properties for vibrational levels that are antisymmetric with respect to the centre of symmetry (u) are listed in brackets [153].

operator μ has (-) parity as

$$\hat{E}^* \mu = -\mu \tag{B.9}$$

this implies that only $+ \leftrightarrow -$ transitions are allowed in the case of single-photon electric dipole transitions:

$$+ \leftrightarrow -, \quad + \nleftrightarrow +, \quad - \nleftrightarrow -. \tag{B.10}$$

B.1.2 Rotationless (e/f) Parity

As the total parity always alternates with J, it can be useful to define a new parity with this rotational dependence factored out, with the e and f parities defined for integer J as

$$\hat{E}^* \psi = +(-1)^J \psi \tag{B.11}$$

and

$$\hat{E}^*\psi = -(-1)^J\psi \tag{B.12}$$

respectively. That is, if the total parity is described by Eq. B.11, it is e parity, while if it is described by Eq. B.12, it is f parity [157,162]. In this case, ψ is $\psi_{\text{el}}\psi_{\text{vib}}\psi_{\text{rot}}$. The rotationless parity is sometimes also referred to as *Kronig* parity. All rotational levels associated with a vibration of type $^1\Sigma^+$ have e parity, while all those associated with a $^1\Sigma^-$ type have f parity. $^1\Pi$ vibrational states have rotational energy levels that are split into e/f sublevel pairs due to ℓ-type doubling (see Subsection B.4), which results in an extra term in the ro-vibrational term value. Another effect of $\ell \neq 0$ for Π states (and higher) is the lack of a $J = 0$ rotational state. This is because J actually refers to the *total* angular momentum, and $J \geq |\ell|$ [153]. The $+ \leftrightarrow -$ selection rule for the total parity becomes

$$e \leftrightarrow e, \quad f \leftrightarrow f, \quad e \nleftrightarrow f \quad \text{for } \Delta J = \pm 1 \tag{B.13}$$

and, when not forbidden,

$$e \nleftrightarrow e, \quad f \nleftrightarrow f, \quad e \leftrightarrow f \quad \text{for } \Delta J = 0 \tag{B.14}$$

where these rules are again derived by requiring a symmetric integrand in the transition moment integral as done for the total parity case [157].

B.1.3 Gerade/Ungerade (u/g) Parity

For homonuclear diatomics or other molecules with a centre of inversion symmetry, such as CO_2, there is an additional parity known as g/u parity, where g stands for the german '*gerade*' meaning positive parity; u is '*ungerade*' meaning negative parity [156]. This type of parity relates to the inversion of the molecular electronic orbital part of the wavefunction through the centre of symmetry, a process described by the inversion operator, $\hat{i}$. In contrast to the total parity which is evaluated in the laboratory frame, the effects of $\hat{i}$ are considered in the frame of the molecule. Additionally, $\hat{i}$ acts only on the spatial coordinates of the electrons, leaving the vibrational, rotational, and nuclear spin components of the wavefunction unchanged. If inversion through the centre of symmetry results in a molecular orbital indistinguishable from the original molecular arrangement, then it is symmetric to inversion and the molecular orbital is symmetric (g). Conversely, if the molecule is distinguishable as being in a new state after inversion with respect to the inversion centre, the resulting molecular orbital is antisymmetric (u) [157]. The selection rules are

$$g \leftrightarrow u, \quad g \nleftrightarrow g, \quad u \nleftrightarrow u \tag{B.15}$$

again derived by satisfying the dipole transition moment integral, noting that the transition dipole moment operator μ is of u parity, and [156,157,166]

$$u \times u = g \times g = g, \quad u \times g = g \times u = u. \tag{B.16}$$

As one might expect, if the molecule has no centre of inversion, g/u is not included in the term symbol [157]. Transition diagrams of molecular species then summarise the term symbols for each vibrational state, such as for $^{12}CO_2$ in Fig. B.2.

B.1.4 Antisymmetric/Symmetric (a/s) Parity

The final type of parity relates to the total wavefunction of a centrosymmetric molecule including nuclear spin, separating the rotational levels into antisymmetric (a) or symmetric (s) character [156]. This parity is described with the *pseudo-symmetry operator* $\hat{P}_{12}$ and the selection rules

$$s \leftrightarrow s, \quad a \leftrightarrow a, \quad s \nleftrightarrow a. \tag{B.17}$$

This type of parity arises due to the Pauli exclusion principle, which requires that the total wavefunction be symmetric or antisymmetric with the exchange of two identical nuclei depending if the exchanged nuclei are bosons or fermions respectively [162,190]. If the identical nuclei are bosons, which have integer nuclear spin quantum numbers I, then the total wavefunction is symmetric with respect to the exchange. For fermions, with half-integer I, the total wavefunction must be antisymmetric with respect to exchange of the identical nuclei [162,190]. So we have

$$\hat{P}_{12}\left(\psi_{\mathrm{el}}\psi_{\mathrm{vib}}\psi_{\mathrm{rot}}\psi_{\mathrm{ns}}\right) = +\left(\psi_{\mathrm{el}}\psi_{\mathrm{vib}}\psi_{\mathrm{rot}}\psi_{\mathrm{ns}}\right) \tag{B.18}$$

for bosons and

$$\hat{P}_{12}\left(\psi_{\mathrm{el}}\psi_{\mathrm{vib}}\psi_{\mathrm{rot}}\psi_{\mathrm{ns}}\right) = -\left(\psi_{\mathrm{el}}\psi_{\mathrm{vib}}\psi_{\mathrm{rot}}\psi_{\mathrm{ns}}\right) \tag{B.19}$$

for fermions [157]. Nucleons (protons and neutrons) are fermions, with the total amount of nucleons composing the atomic nucleus being equal to its *mass number* [192,193]. Three scenarios are then possible [194]:

- The mass number is even, with even number of protons and even number of neutrons, results in bosonic nuclei with I= 0 such as for ^{16}O and ^{12}C.
- The mass number is even, with odd number of protons and odd number of neutrons, produces bosonic nuclei with integer spin (I= 1, 2, 3...) such as ^{14}N where I=1.
- The mass number is odd, indicating fermionic nuclei with half-integral nuclear spins (I = 1/2,3/2,5/2...) such as ^{1}H where I = 1/2.

The nuclear spins of some common nuclei are summarised in Table B.1. For molecules with a centre of symmetry, such as those belonging to the $D_{\infty h}$ point group like CO_2 and C_2H_2, the

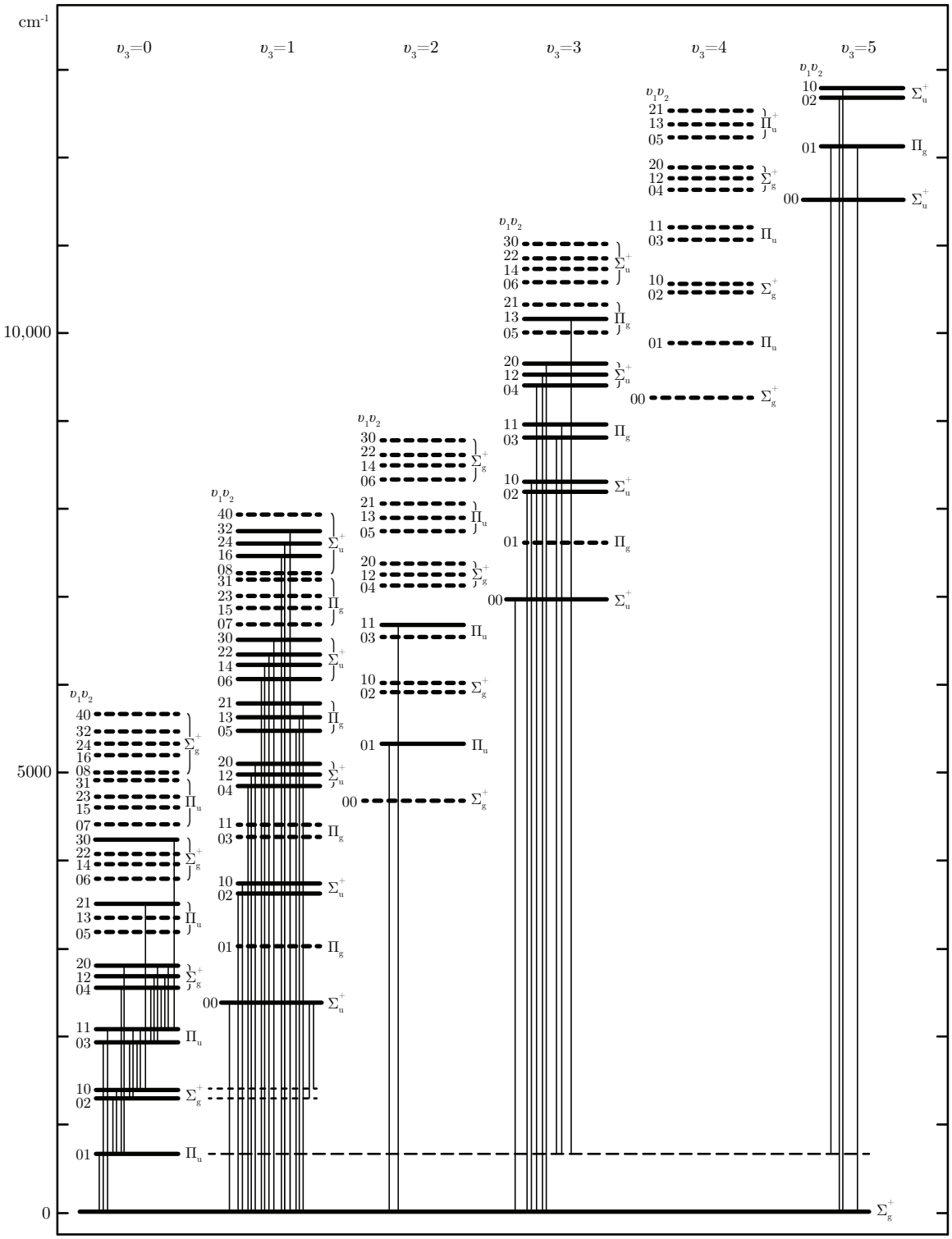

Figure B.2: Reproduction of the vibrational energy level diagram of the centrosymmetric $^{12}CO_2$ molecule as seen in Refs. [153,305]. Only Σ^+ and Π levels are shown. Observed levels are shown by horizontal heavy full lines, predicted levels by broken lines. Observed transitions are indicated by light vertical lines.

positive rotational levels are symmetric, and the negative rotational levels are antisymmetric for vibrational levels of g symmetry (Σ_g^+, Σ_g^-, Π_g,...) [153,159]. The reverse is true for vibrational levels of u symmetry (Σ_u^+, Σ_u^-, Π_u,...) [153]. Examples of this behaviour may be seen in Fig. B.1(b).

Spin I	**Nuclei**	**Statistics**
0	^{12}C, ^{14}C, ^{16}O, ^{18}O, ^{32}S	Bose-Einstein
$\frac{1}{2}$	^{1}H, ^{3}H, ^{13}C, ^{13}N, ^{15}N, ^{15}O, ^{31}P, ^{19}F	Fermi-Dirac
1	^{2}H (D), ^{14}N	Bose-Einstein
$\frac{3}{2}$	^{11}B, ^{33}S, ^{35}Cl, ^{37}Cl	Fermi-Dirac
$\frac{5}{2}$	^{17}O	Fermi-Dirac
3	^{10}B	Bose-Einstein

Table B.1: Some common nuclei, their spin quantum numbers, and statistics classification [154,189].

Consider the exchange of identical nuclei of CO_2 in its vibrational ground state as seen in Fig. B.3. This operation can also be thought of in terms of a 180° rotation about its centre of symmetry (the ^{12}C atom). In the vibrational ground state, this rotation produces a state indistinguishable from the original state prior to rotation, and therefore the vibrational ground state is symmetric. A similar condition occurs when considering any of the excited states of the symmetric stretch, as the two C=O bonds stretch or contract simultaneously.

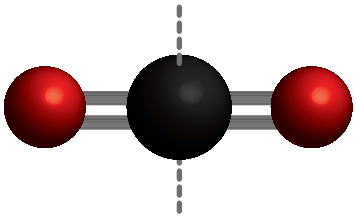

Figure B.3: A diagram of the $^{12}CO_2$ molecule in its vibrational ground state, showing the centre of symmetry (grey dashed line) passing through the ^{12}C atom (dark grey). The identical oxygen atoms are shown in red. The vibrational ground state is symmetric under inversion or the equivalent 180° rotation about its centre of symmetry.

The asymmetric stretching vibration is a different matter. After a 180° rotation, the molecule is not indistinguishable from its starting state, making the final state asymmetric as seen in Fig. B.4.

B.2 Nuclear Spin Statistics: Acetylene

Now consider centrosymmetric acetylene (C_2H_2) as seen in Fig. B.5 and the exchange of identical ^{1}H ($I = \frac{1}{2}$) nuclei. As ^{1}H are fermions, Ψ_{total} must be antisymmetric [188]. The ground electronic state is symmetric, as are most of the vibrational wavefunctions (Σ_g^+ type)

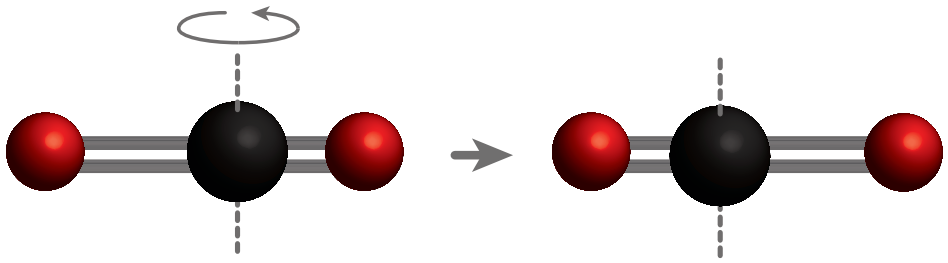

Figure B.4: A diagram of the $^{12}CO_2$ molecule in an excited state of the asymmetric stretch vibration mode. The molecule is asymmetric under exchange of the two identical oxygen nuclei (red) or the equivalent inversion through or 180° rotation about its centre of symmetry (grey dashed line) passing through the ^{12}C atom (dark grey), making this vibrational state asymmetric.

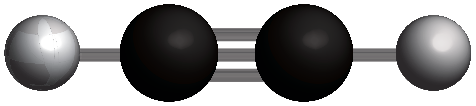

Figure B.5: A diagram of a C_2H_2 molecule in its vibrational ground state. This type of acetylene possesses a centre of symmetry at the midpoint of the triple bond between the two carbon atoms (dark grey), greatly affecting its ro-vibrational spectrum. Hydrogen atoms are light grey.

[154]. By Eq. 3.57 and 3.58, there are three symmetric and one antisymmetric nuclear spin states. In order to make Ψ_{total} antisymmetric, the odd J rotational states must combine with the even nuclear spin states, and the even J with the odd nuclear spin states. So the following situations may occur:

$\Psi_{\textbf{total}}$	=	$\psi_{\textbf{el}}$	×	$\psi_{\textbf{vib}}$	×	$\psi_{\textbf{rot}}$	×	$\psi_{\textbf{ns}}$
ODD	=	EVEN	×	EVEN	×	ODD ($J = 1, 3, 5...$)	×	EVEN
ODD	=	EVEN	×	EVEN	×	EVEN ($J = 0, 2, 4...$)	×	ODD

Table B.2: Summary of the symmetry of each component of the final wavefunction Ψ_{total} of centrosymmetric $^{12}C_2H_2$. As ^1H are fermions, the individual spatial wavefunctions must combine to make Ψ_{total} odd under inversion.

Equation 3.59 predicts a 3:1 symmetric:antisymmetric spin state (3:1 odd:even J) intensity variation as there are three times as many allowed nuclear spin states resulting in Ψ_{total} being odd [152,160,188]. This is indeed what observed in the spectrum of acetylene's $101000 \leftarrow 0000000$ vibrational transition in Fig. B.6.

B.3 Nuclear Spin Statistics: Carbon Dioxide

Now consider the spin statistics of carbon dioxide as seen in Fig. B.3, in particular the $30012 \leftarrow 00001$ vibrational transition. The symmetry of Ψ_{total} must be must be even with respect to exchange of the two bosonic ^{16}O nuclei ($I = 0$) [188,189]. There are no predicted antisymmetric nuclear spin states, and one symmetric nuclear spin state. The electronic

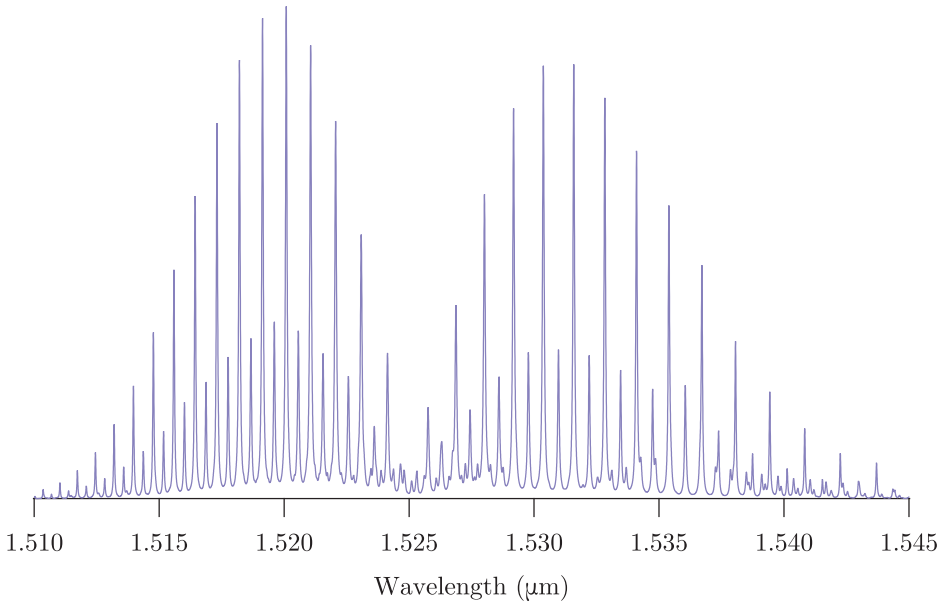

Figure B.6: A simulated ro–vibrational spectrum of $^{12}C_2H_2$ arising from the 101000 ← 0000000 vibrational transition, showing the expected 1:3 (even:odd J) intensity variation due to nuclear spin statistics [306]. Note the existence of additional, smaller-intensity bands at mid-to-higher wavelengths.

ground state and the initial vibrational state (Σ_g^+ type) are symmetric according to Fig. B.2, while the final vibrational state (Σ_u^+ type) is asymmetric [152,154]. The lack of asymmetric nuclear spin states has a profound impact on the spectrum of this transition. In order to make Ψ_{total} even in the ground state, the only allowed nuclear spin state is symmetric, and must combine with only even rotational levels as summarised in Table B.3 [188].

$\Psi_{\textbf{total}}$	=	$\psi_{\textbf{el}}$	×	$\psi_{\textbf{vib}}$	×	$\psi_{\textbf{rot}}$	×	$\psi_{\textbf{ns}}$
EVEN	=	EVEN	×	EVEN	×	EVEN ($J = 0, 2, 4...$)	×	EVEN

Table B.3: Summary of the symmetry of each component of the wavefunction Ψ_{total} of centrosymmetric CO_2. As ^{16}O are bosons, the individual spatial wavefunctions must combine to make the ground state Ψ_{total} even under inversion. The lack of antisymmetric nuclear spin states leads to lines originating from odd-J levels being absent entirely.

That is, only rotational levels that are symmetric (even J) are allowed to exist. This leads to the complete absence of half of the 30012 ← 00001 lines in spectra of centrosymmetric species of CO_2, leading to a spectrum that *appears* free of intensity variations due to nuclear spin statistics as seen in Fig. B.7 [162,166,188]. If the symmetry of the molecule was destroyed, for example by replacing one of the ^{16}O nuclei with any other oxygen isotope, the missing states would be re-instated in the spectrum as oxygen atoms would no longer be subject to the Pauli principle, with $^{18}OC^{16}O$ being observed to retain all its rotational lines [152,153,155,162,189].

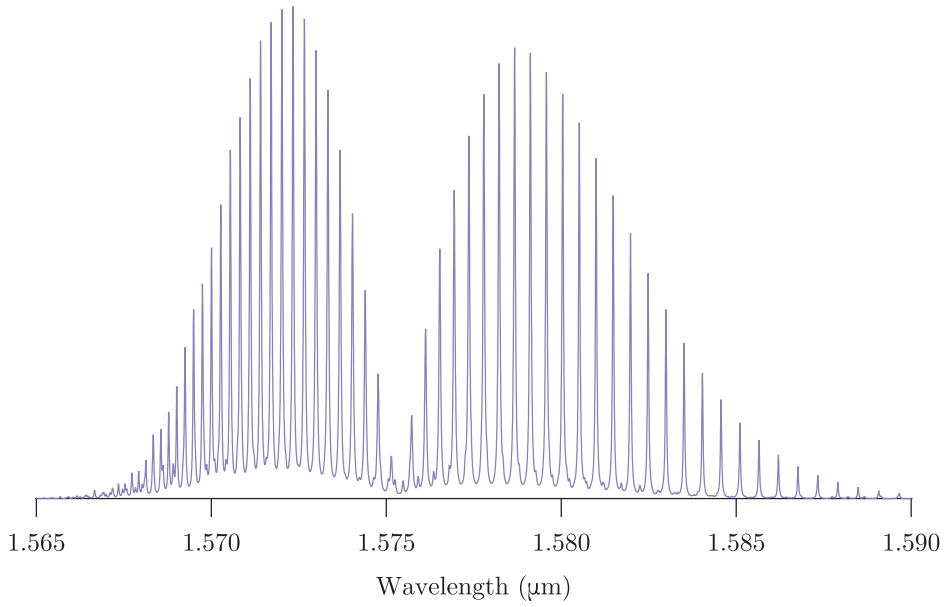

Figure B.7: A simulated ro–vibrational spectrum of $^{12}CO_2$ arising from the $30012 \leftarrow 00001$ vibrational transition. While it appears there is no intensity–variation due to nuclear spin statistics, the transitions originating from odd-J states are missing entirely. Note the existence of additional, smaller-intensity bands at lower-to-mid wavelengths.

B.4 ℓ-type Doubling

One of the final considerations for intra-band intensity modification is that of ℓ-type doubling for Π vibrational states or higher in which $|\ell| > 0$. This additional vibrational angular momentum causes each rotational level to be split into $+/-$ symmetry pairs for each J as $\ell = \pm 1$ [159]. This is because when considering the molecule in a bending vibration without rotation, the bend may occur in two perpendicular planes with the same oscillation frequency, and are exactly degenerate. However once rotation is included, the two bending modes will have slightly different effective moments of inertia about the axis of rotation, and the two bending modes see different Coriolis forces [153,160,307]. This results in the two components for the same J begin to separate in energy as the rotational and vibrational angular momenta interact, leading to a doubling-up of rotational energy levels. This can be seen in the ro-vibrational transition diagram for the $31113 \leftarrow 01101$ hotband transition of centrosymmetric CO_2 in Fig. B.8, which is a $\Pi_u - \Pi_g$ type vibrational transition.

This splitting of the rotational levels is termed ℓ-type doubling. The amount of splitting, $\Delta\nu_{splitting}$, is given by

$$\Delta\nu_{splitting} = q_i J\,(J+1) \tag{B.20}$$

where q_i is the ℓ-type doubling constant [153,155,157]. Therefore, as J increases the magnitude of the splitting will also increase. Another thing to note is that the two components of the Π state will have slightly different rotational constants as these constants are inversely

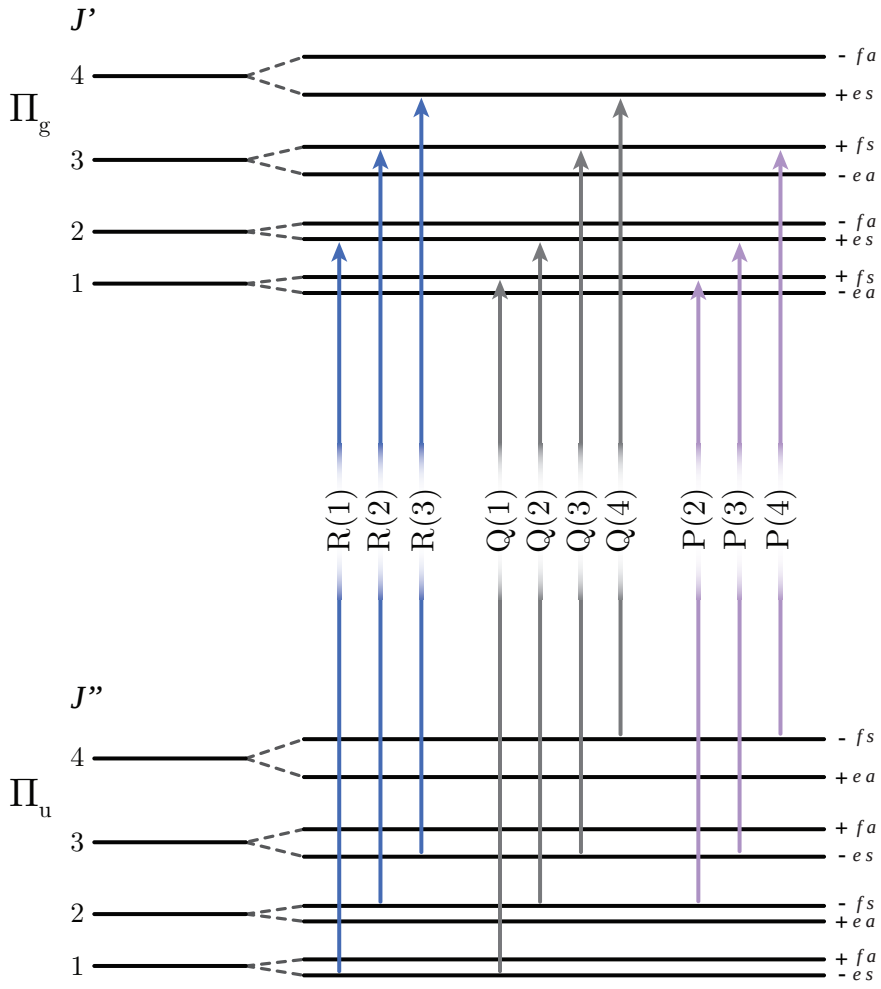

Figure B.8: Some of the rotational levels involved in a $\Pi_u - \Pi_g$ vibrational transition, such at for the $31113 \leftarrow 01101$ hotband transition of centrosymmetric CO_2. This is an example for the $C_{\infty h}$ point group. For a molecule in the $D_{\infty h}$ point group, the u/g and a/s labelling should be dropped. The rotational levels of both the upper and lower vibrational states are split by ℓ-type doubling, and the $J = 0$ rotational states are missing as $\ell = 1$ for Π vibrational levels [153,159]. Not to scale.

proportional to the moment of inertia. This can lead to what looks like aliasing effects in the ro-vibrational spectrum as seen in Fig. B.9 [308]. The different types of parity are then quite useful to differentiate the split rotational levels. Due to the split levels having differing parity values, some interesting spectra with at first unexpected features that may be explained by the symmetry considerations presented.

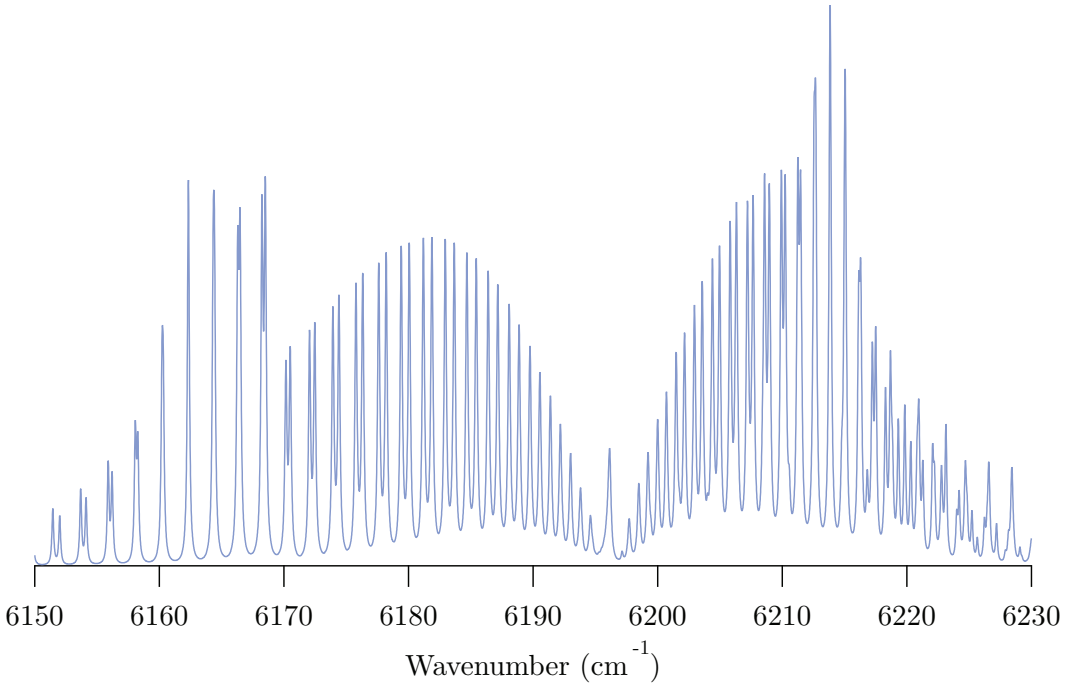

Figure B.9: A simulated ro–vibrational spectrum of centrosymmetric $^{12}CO_2$ arising from the 31113 ← 01101 hotband transition, showing the effects of ℓ-type doubling. Note the existence of a weak Q-branch at the band centre of approximately 6197 cm^{-1}, and the aliasing effect due to the differing rotational constants.

Consider the 31113 ← 01101 hotband transition of centrosymmetric CO_2 depicted in Fig. B.8. Unlike the 30012 ← 00001 transition evaluated in Section B.3, all J-values are represented due to the splitting. According to the transition rules relating to parity derived earlier, the lower vibrational state allows only e parity levels for odd-J, and f parity levels for even-J, while the upper vibrational state allows only e levels for even-J and f levels for odd-J. According to Section 3.4.2, this is a parallel vibrational transition in which $\Delta\ell = 0$ but $\ell \neq 0$, and we see a weak Q-branch accompanying the R and P branches. According to Section B.1, the ro-vibrational transitions must, and do, fulfill the selection rules:

$$+ \leftrightarrow -, \quad u \leftrightarrow g, \quad s \leftrightarrow s, \quad a \leftrightarrow a \tag{B.21}$$

for all transitions, and

$$e \leftrightarrow e, \quad f \leftrightarrow f, \quad e \nleftrightarrow f \quad \text{for } \Delta J = \pm 1 \tag{B.22}$$

for the P and R branches, and

$$e \nleftrightarrow e, \quad f \nleftrightarrow f, \quad e \leftrightarrow f \quad \text{for } \Delta J = 0 \tag{B.23}$$

for the Q branch. This results in a spectrum in which half of the split states are forbidden but all J-values are represented, and the differing rotational constants result in what appears to be aliasing in R and P branches of the final spectrum in Fig. B.9. Finally, the ground rotational state with $J = 0$ does not exist in either Π state, as J actually refers to the *total* angular momentum, and so cannot be less than ℓ, so $J \geq |\ell|$ [159,307].

HITRAN Uncertainty Codes

Uncertainties are provided with each parameter requested from the HITRAN database using defined error codes. The uncertainty codes as used by HITRAN are listed in Ref. [1], and are reproduced here. Two types of uncertainty codes are used corresponding to uncertainty in cm^{-1}, which is used for the line position and air pressure-induced line shift parameters, and relative uncertainty in %, which is used for the line intensity and broadening parameters. The error codes are as follows:

Code	Absolute Uncertainty Range	Code	Relative Uncertainty Range
0	≥ 1 or Unreported	0	Unreported or unavailable
1	≥ 0.1 and < 1	1	Default or constant
2	≥ 0.01 and < 0.1	2	Average or estimate
3	≥ 0.001 and < 0.01	3	$\geq 20\,\%$
4	≥ 0.0001 and < 0.001	4	$\geq 10\,\%$ and $< 20\%$
5	≥ 0.00001 and < 0.0001	5	$\geq 5\,\%$ and $< 10\%$
6	≥ 0.000001 and < 0.00001	6	$\geq 2\,\%$ and $< 5\%$
7	≥ 0.0000001 and < 0.000001	7	$\geq 1\,\%$ and $< 2\%$
8	≥ 0.00000001 and < 0.0000001	8	$< 1\%$
9	≥ 0.000000001 and < 0.00000001		

Table C.1: The uncertainty codes as used by HITRAN as listed in Ref. [1]

Optical Frequency Comb: Mathematical Background

This appendix is intended to provide the mathematical background to the creation and stabilisation of an optical frequency comb as presented in Chapter 5. It is not intended as a comprehensive overview of the complex mathematics behind optical frequency combs, but as an introduction to the controlling equations of comb operation.

D.1 Frequency Spectrum of an Identical Pulse Train

In order to understand the output mode structure of an optical frequency comb based on a femto-second fibre laser, it is useful to consider the case of a pulse circulating within the laser cavity with (angular) carrier frequency ω_c. The output of such a laser is a series of identical pulses separated by the round-trip time (τ) of the cavity:

$$\tau = \frac{2L}{v_g} \tag{D.1}$$

where L is the cavity length and v_g is the mean group velocity of the cavity respectively [224,228,229]. The electric field at a time t of such a pulse, $E_p(t)$, is given by multiplication of the oscillatory carrier signal by the envelope function of the pulse, $\hat{E}(t)$:

$$E_p(t) = \hat{E}(t)\, e^{i(\omega_c t + \phi_{CE})}. \tag{D.2}$$

where ϕ_{CE} is the phase between the carrier and envelope, and the square of the envelope function gives the intensity profile of the pulse [224,239]. If the pulse propagates through a dispersive material (one in which the the refractive index varies as a function of frequency), then ϕ_{CE} will evolve as the group and phase velocities (v_p) are different. The carrier propagates at v_p while the envelope propagates at v_g. This causes the carrier to 'slip' through the envelope, with the slipping causing the evolution of ϕ_{CE} as the pulse circulates within the laser cavity. The phase of the intra-cavity pulse is sampled each time the pulse strikes the partially reflective output coupler of the cavity, leading to ϕ_{CE} evolving on a pulse-to-pulse basis at the output. In the absence of other perturbations to the laser, ϕ_{CE} evolves by a fixed amount $\Delta\phi_{CE}$ between each output pulse [239]. However, only $\Delta\phi_{CE}$ *modulo* 2π matters in terms of the mathematics, which will be designated as simply $\Delta\phi_{CE}$. This means that the output of the laser is a series of pulses - a 'pulse train' - with each successive pulse differing

by $\Delta\phi_{CE}$ from the last, and in the case of an optical frequency comb, $\Delta\phi_{CE}$ must be tightly controlled to a fixed value.

In order to understand the resulting frequency spectrum of this pulse train, it is useful to firstly ignore $\Delta\phi_{CE}$ altogether. This results in all pulses in the pulse train being identical, and the electric field $E(t)$ of a train of n pulses may be written as

$$E(t) = \sum_n E_p(t - n\tau). \tag{D.3}$$

The round trip time of the cavity τ is also the time between output pulses, and is equal to the inverse of the repetition rate f_{rep} ($f_{\text{rep}} = 1/\tau$). It is also assumed that the duration of $E_p(t)$ is less that τ so that the output pulses do not overlap. Such a periodic function may be represented as a Fourier series, as is embodied in the Poisson Sum formula from Fourier analysis:

$$\sum_{m=-\infty}^{\infty} f(x - mp) = \sum_{k=-\infty}^{\infty} \frac{1}{p} F\left(\frac{k}{p}\right) e^{\frac{2\pi i k x}{p}} \tag{D.4}$$

where $F(y)$ is the Fourier transform of $f(x)$. Application of the Poisson Sum formula to Eq. D.3 (with $p = \tau$ and $x = t$) gives:

$$\begin{aligned}
\sum_n E_p(t - n\tau) &= \sum_k \frac{1}{\tau} F\left(\frac{k}{\tau}\right) e^{\frac{2\pi i k t}{\tau}} \\
&= \sum_k f_{\text{rep}} F\left(\frac{k}{\tau}\right) e^{i(2\pi k t f_{\text{rep}})} \\
&= f_{\text{rep}} \sum_k F\left(\frac{k}{\tau}\right) e^{i(2\pi k t f_{\text{rep}})}.
\end{aligned}$$

The spectrum of the periodic train of pulses is therefore a 'comb' of discrete frequencies that are integer multiples of f_{rep}, with the amplitude of each comb line given by the the spectrum of a single pulse [223].

D.2 Frequency Spectrum of a Pulse Train with Varying Phase Shift

If the pulse-to-pulse phase shift $\Delta\phi_{CE}$ is included, the pulses are not all identical and the spectrum of the pulse train becomes more complex. The electric field of the pulse train $E(t)$ may be written in terms of the electric field of a single pulse $E_p(t)$ (Eq. D.2) with the carrier-envelope phase of each pulse given by

$$\phi_{CE} = n\Delta\phi_{CE} + \phi_0$$

for the n^{th} pulse and ϕ_0 is the initial phase offset. The electric field for the pulse train is then given by

$$\begin{aligned} E(t) &= \sum_n E_p(t-n\tau)\, e^{i(\omega_c(t-n\tau)+\phi_{CE})} \\ &= \sum_n E_p(t-n\tau)\, e^{i(\omega_c t - n\omega_c\tau+\phi_{CE})} \\ &= \sum_n E_p(t-n\tau)\, e^{i(\omega_c t - n\omega_c\tau+n\Delta\phi_{CE}+\phi_0)} \\ &= \sum_n E_p(t-n\tau)\, e^{i(\omega_c t+n(\Delta\phi_{CE}-\omega_c\tau)+\phi_0)}. \end{aligned}$$

Recall that the Fourier transform of a function $f(x)$ is given by

$$\mathcal{F}[f(x)] = \int_{-\infty}^{\infty} f(x)\, e^{-i\omega x}\mathrm{d}x \tag{D.5}$$

where the Fourier transform of $f(x)$, $\mathcal{F}[f(x)]$, is also often represented by alternative $F(\omega)$, $\tilde{f}(\omega)$, or $\hat{f}(\omega)$ notations [157,254]. If we take the Fourier transform of the electric field of the train of pulses, $E(t)$, from above:

$$\begin{aligned} E(\omega) &= \int_{-\infty}^{\infty} \sum_n \hat{E}(t-n\tau)\, e^{i(\omega_c t+n(\Delta\phi_{CE}-\omega_c\tau)+\phi_0)} e^{-i\omega t}\mathrm{d}t \\ &= \int_{-\infty}^{\infty} \sum_n \hat{E}(t-n\tau)\, e^{i(\omega_c t+n(\Delta\phi_{CE}-\omega_c\tau)+\phi_0-\omega t)}\mathrm{d}t \\ &= \int_{-\infty}^{\infty} \sum_n \hat{E}(t-n\tau)\, e^{i(n(\Delta\phi_{CE}-\omega_c\tau)+\phi_0)} e^{-i(\omega-\omega_c)t}\mathrm{d}t \\ &= e^{i(n(\Delta\phi_{CE}-\omega_c\tau)+\phi_0)} \int_{-\infty}^{\infty} \sum_n \hat{E}(t-n\tau)\, e^{-i(\omega-\omega_c)t}\mathrm{d}t \end{aligned}$$

where $E(\omega)$ is the Fourier transform of our pulse train $E(t)$. Let the Fourier transform of a single pulse be:

$$\tilde{E}(\omega) = \int_{-\infty}^{\infty} \hat{E}(t)\, e^{-i\omega t}\mathrm{d}t.$$

However the pulses at the cavity output are time-shifted by a constant factor $n\tau$. This time shift can be included by recalling the Fourier transform time-shift property [229]:

$$\int_{-\infty}^{\infty} f(x-a)\, e^{-i\alpha x}\mathrm{d}x = e^{-i\alpha a} \int_{-\infty}^{\infty} f(x)\, e^{-i\alpha x}\mathrm{d}x \tag{D.6}$$

which may be applied to give

$$\begin{aligned} E(\omega) &= \sum_n e^{i(n(\Delta\phi_{CE}-\omega_c\tau)+\phi_0)} e^{-i(\omega-\omega_c)n\tau} \int_{-\infty}^{\infty} \hat{E}(t)\, e^{-i(\omega-\omega_c)t} \mathrm{d}t \\ &= \sum_n e^{i(n(\Delta\phi_{CE}-\omega_c\tau)+\phi_0)} e^{-in\tau(\omega-\omega_c)} \tilde{E}(\omega-\omega_c) \\ &= \sum_n e^{(in\Delta\phi_{CE}-in\omega_c\tau+i\phi_0-in\omega\tau+in\omega_c\tau)} \tilde{E}(\omega-\omega_c) \\ &= \tilde{E}(\omega-\omega_c)\, e^{i\phi_0} \sum_n e^{i(n\Delta\phi_{CE}-n\omega\tau)}. \end{aligned}$$

Now if the Poisson Sum formula is applied in reverse, and noting that the Fourier transform of a delta function ($\delta(t)$) is a constant:

$$E(\omega) = e^{i\phi_0} \tilde{E}(\omega-\omega_c) \sum_{m=-\infty}^{\infty} \delta(\Delta\phi_{CE} - \omega\tau - 2\pi m) \tag{D.7}$$

where in the reverse application of the Poisson Sum formula $p = 2\pi$, $x = \Delta\phi_{CE} - \omega\tau$, and $f(x - mp) = \delta(\Delta\phi_{CE} - \omega\tau - 2\pi m)$. Equation D.2 describes a comb spectrum with frequencies:

$$\omega_m = \frac{2\pi m}{\tau} - \frac{\Delta\phi_{CE}}{\tau}$$

or, converting from angular frequency

$$f_m = m f_{\mathrm{rep}} + f_0$$

where $\delta = f_0 = (-\Delta\phi_{CE} f_{rep}) / (2\pi)$ (noting that it is common to drop the minus sign in this expression, which simply changes the sign in the definition of $\Delta\phi_{CE}$) [223,224,229,254]. Hence we see that the position of the comb is offset from integer multiples of the repetition rate by a frequency f_0, which is determined by the pulse-to-pulse phase shift ($\Delta\phi_{CE}$) [223,224,240]:

$$f_0 = \frac{\Delta\phi_{CE} f_{rep}}{2\pi}.$$

The connection between the time and frequency domain pictures of the frequency comb is summarised in Fig. 5.5. In the absence of active laser stabilisation, f_0 is sensitive to fluctuations of the laser, causing $\Delta\phi_{CE}$ to change on a pulse-to-pulse basis [224,309]. It is the effective stabilisation of this parameter that separates the optical frequency comb from a mode-locked laser.

Rarefication Cavity Addendum

The explanation of the characteristic cavity envelope introduced in Section 7.3 is a simplification of a more complex interaction between the optical frequency comb and the rarefication cavity - the 'walking-off' between the modes of the frequency comb and the cavity transmission function. Additional information is provided in this appendix to explain the details of this interaction, and the resultant effects on imaging.

E.1 Comb-Cavity Walk-Off

The characteristic cavity envelope presented in Section 7.3 is the result of the change in cavity transmission function with respect to the stationary comb modes as the rarefication cavity length is altered. This change to the cavity transmission function may be separated into two related parts: the small change to the cavity FSR and the shift of the cavity passbands. In reality both factors are the result of stretching the passband separation *around DC*, which manifests as a large frequency offset with a small change in cavity FSR at the frequency range of operation.

Firstly, consider the peak of the photodetector envelope as seen in Fig. E.1 (labelled C as seen previously in Section 7.3) which corresponds to a cavity FSR of 9.5 GHz. As the modes of the frequency comb are separated by 250 MHz, this FSR corresponds to the condition in which the the cavity Airy function lines up optimally with integer multiples of f_{rep}, resulting in the largest possible cavity transmission signal being observed on the photodetector. This corresponds to every 38^{th} comb mode being transmitted, across a large span of comb modes. Now consider a slight shrinking of the cavity length by just enough to move to the adjacent fine structure peak 250 MHz away in Fig. E.1. This corresponds to a slight increase to the cavity FSR and resonance with a new subset of comb modes shifted 250 MHz away from the previous subset, as seen in Fig. E.2.

This explains the fine structure of the cavity envelope: as the cavity length is changed, the cavity FSR is altered and so too is the alignment between the cavity transmission function and the modes of the comb. Good alignment will result in a maximum in the fine structure within the envelope, while poor alignment between the passbands will result in a minimum. However, as changing the cavity length causes a change to the cavity FSR, there is an additional offset of $m\delta$ (m =1,2,3... is an integer) on top of the 250MHz shift intended - a stretch around the optimally-tracking cavity mode. This additional offset may be seen in Fig. E.3 for the cases

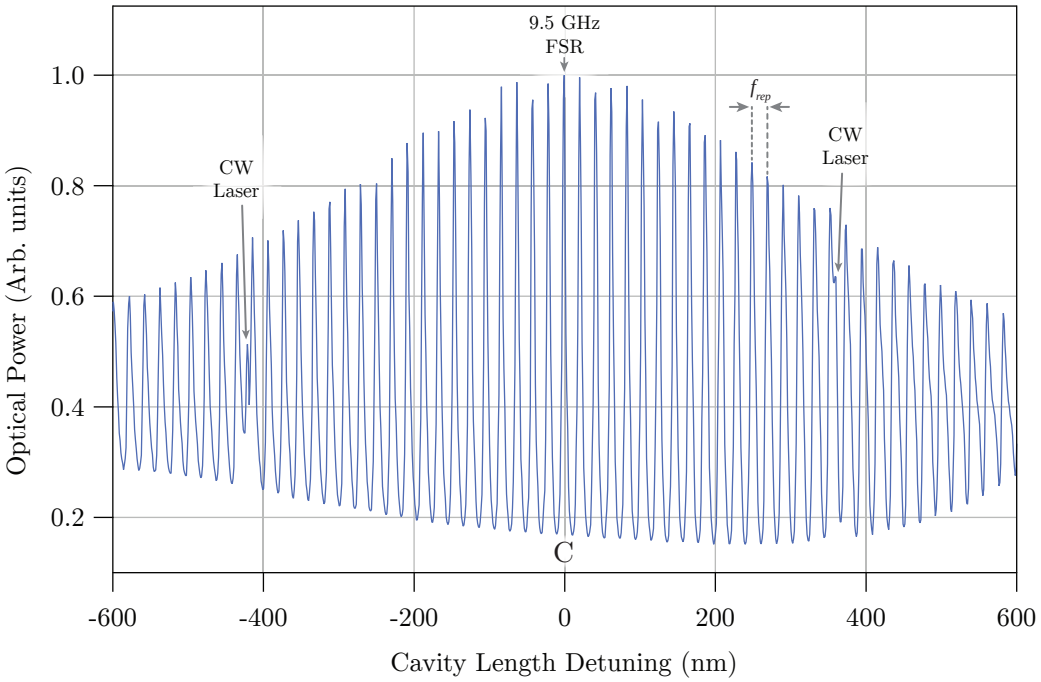

Figure E.1: The characteristic cavity envelope as the cavity length is altered. The envelope peak (C), fine structure peak spacing and CW laser deformations of the fine structure may be seen.

of $m = 0$, 1, and 2.

Note that there will exist an 'optimally-tracking' mode (denoted with mode index q) which, in the transition between the central maximum and the adjacent maximum, maps perfectly onto the adjacent comb mode without additional offset ($m = 0$). This perfectly-tracking mode is in actuality the result of many thousands of δ factors, such that they have accumulated to push the cavity filter mode exactly on top of its nearest neighbour. From this it may be seen that the shift of the blue cavity modes in Fig. E.3 is in fact many thousands of cumulative green shifts. The next filter cavity mode in sequence (the $q + 1$ mode) will be offset by δ, $q + 2$ by 2δ and so on as shown.

Although δ is small, the cumulative effect is to cause the cavity filter modes to align increasingly poorly with the corresponding modes of the comb, until there is no overlap and the cavity loses resonance with the next comb mode in sequence. Furthermore, the cumulative factors of δ ensure that there is no longer optimised alignment of cavity and comb modes across the whole range of comb modes, leading to a drop in the total amplitude of the envelope. This explains the tailing-off of the envelope in Fig. E.1 to the left of 9.5 GHz central maximum. Note that lengthening of the cavity or moving to the comb mode to the right of the central maximum, and the tailing off of the envelope on this side, is due to the same mechanism with the exception that the δ shift is in the opposing direction.

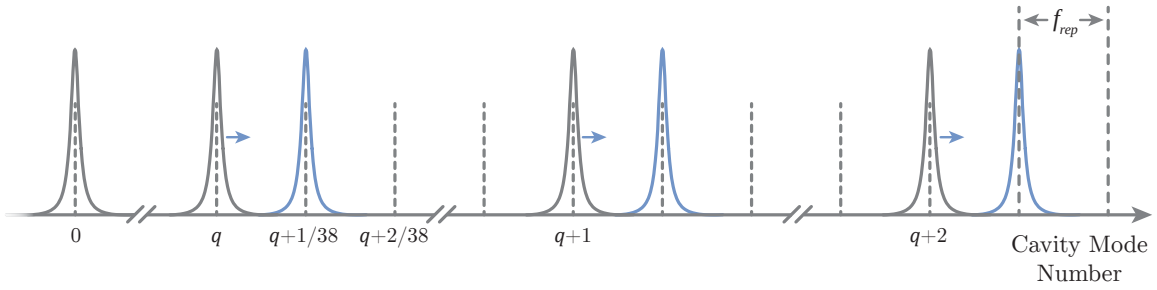

Figure E.2: A slight cavity length change (shortening) results corresponds to moving the cavity transmission Airy functions to a subset of comb modes (grey dashed lines) offset by $f_{\text{rep}} = 250\,\text{MHz}$. The grey Airy function is the cavity passband prior to alteration of the cavity length, while the blue Airy function is the passband after length adjustment. The cavity mode number is denoted by q.

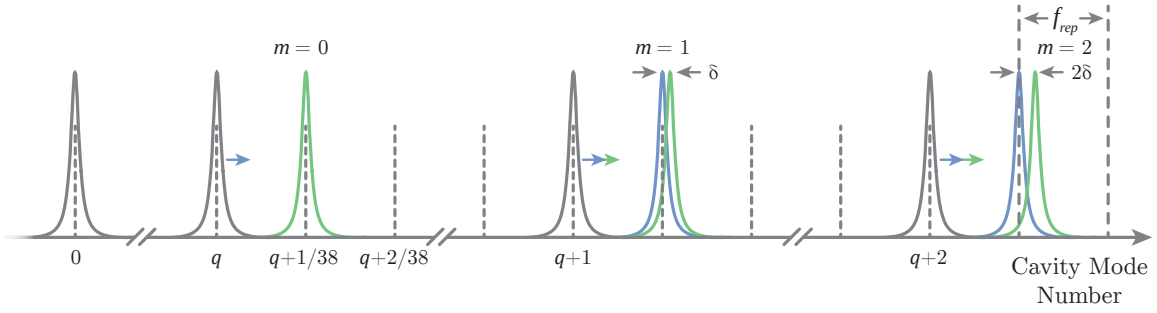

Figure E.3: The cavity Airy function showing the full effects of stretching around DC (green). The optimally-tracking mode of index q is shown.

E.2 Effects on Imaging

The tailing-off of the characteristic envelope on either side of the central maximum has an effect on the output images of the cavity filter system, as the resulting images display a sequentially reduced number of comb modes efficiently transmitted by the optical cavity. In applications where the cavity-filtered image is used for calibration of the frequency axis only, and not as the laser interrogation source, this is not too problematic. Care must be taken to ensure the cavity is locked to the global maximum of the envelope, where the cavity FSR is exactly 9.5 MHz and is easily discernible. This results in uniform illumination of the cavity-rarefied VIPA image and corresponds to the highest signal of the photodetector.

However, in applications where summation of the 38 (or 36) individual subsets is required such as in Chapter 8, this tailing-off manifests as a horizontal gradient across VIPA images, with the central region being the brightest and a reduction in brightness to either side. While a horizontal gradient is removed from final transmission data by division of the sample path image by that of the reference path, this gradient will have a detrimental effect on the signal to noise ratio of the outer parts of the images for the affected comb subsets.

E.2.1 Proportion of Frequency Comb Subsets Affected

To understand when the tail-off becomes detrimental, the amount by which the FSR changes in moving between adjacent maxima of the characteristic fine structure must be found. Consider Eq. 7.4 re-arranged to give the periodic resonant frequencies of the cavity [221]:

$$f_q = \frac{qc}{2nL} = q\text{FSR}. \tag{E.1}$$

for cavity mode number q. From this it may be seen that the amount the FSR changes between adjacent maxima is δFSR. For simplicity, assume that the optimally-tracking cavity mode q is the cavity mode that corresponds to the centre of the comb output at 1560 nm (192 THz). Therefore $q = 192\,\text{THz}/9.5\,\text{GHz} \approx 20000$, which will give an order-of-magnitude indication. Now let Δf be the change in frequency experienced by the optimally-tracking mode when the cavity length is changed to move to an adjacent fine structure maximum. This may be expressed in terms of the change in FSR between adjacent maxima: $\Delta f = q\,(\text{FSR} + \delta\text{FSR}) - q\,(\text{FSR}) = q\delta\text{FSR}$. As we have defined the optimally-tracking mode q as the mode which almost perfectly maps to the adjacent comb mode with this change, it can be seen that $\Delta f = 250\,\text{MHz}$. Thus $\delta\text{FSR} = \Delta f/q = 250\,\text{MHz}/20000 = 12.5\,\text{kHz} = \delta$.

This means that every time the cavity length is tuned to change the optimally-tracking cavity mode's frequency by one 38^{th} of an FSR (250 MHz), equivalent to moving to the adjacent fine structure maximum to the right in the photodetector envelope, an additional shift of 12.5 kHz per cavity mode is acquired along with the one 38^{th} of an FSR shift. I.e. $m\delta$ worth of detuning around the optimally-tracking cavity mode. With this knowledge the point at which the dimming of the sides of images for certain subsets becomes detrimental may be found. Recall Eq. 7.5:

$$\text{FWHM} = \frac{\text{FSR}}{\mathcal{F}}.$$

Knowing that the cavity finesse and FSR are ~ 200 and 9.5 GHz respectively, this results in a FWHM of ~ 50 MHz. This can be converted into a change of cavity mode index Δq by dividing the FWHM value by δ: $\Delta q = 50\,\text{MHz}/\,(m \times 12.5\,\text{kHz}) = 4000$ for $m = 1$. This corresponds to the width in cavity passband mode index before the transmission of a comb mode falls to its half-maximum value due to accumulated δ factors.

This may be converted into the bandwidth of comb modes transmitted by the cavity when the cavity length is tuned to any fine structure maximum adjacent to the central fine structure peak via $\Delta q \times (9.5\,\text{GHz} + m\delta)$. For the peak directly adjacent to the central maximum this is 38 THz, compared to the ~ 3 THz of comb modes able to be imaged in a single frame by the camera. This results in the entirety of the camera image being filled with bright comb modes. however, when $m = 12$ (12 maxima away from the centre of the envelope), the width of the transmitted comb modes is ~ 3 THz. For maxima further out ($m > 12$), the brightness of the comb modes is reduced to half-power or less at the horizontal edges of the images, producing reduced signal-to-noise ratios for the comb modes on the outer edges of

these distant maxima. In the very furthest maxima, the proportion of the screen that is filled with bright comb modes may be so small as to preclude its use within a stitched spectrum.

VIPA Extended Mathematical Treatment

F.1 VIPA Dispersion Relation

The dispersive properties of a VIPA etalon are most easily understood by first considering the phase matching conditions for a tilted air-spaced etalon of thickness t. As the etalon is air-spaced, light rays do not undergo refraction at interfaces unlike when an interface between two materials of differing refractive index is considered. This greatly simplifies the mathematics and is a good starting point.

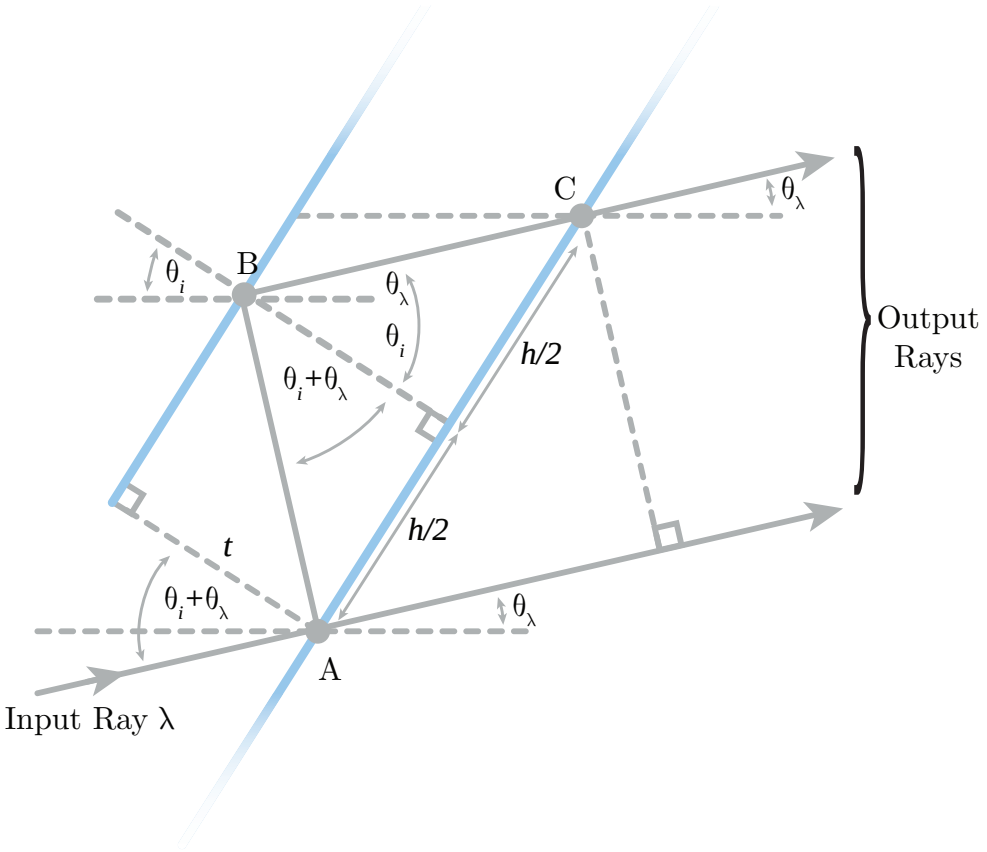

Figure F.1: A diagram of an air-spaced VIPA of thickness t, showing the geometry for a single incident ray of wavelength λ [258].

For a ray incident upon the back face of the VIPA at an angle $(\theta_i + \theta_\lambda)$, it can be seen from Fig. F.1 that

$$\cos(\theta_i + \theta_\lambda) = \frac{t}{\overline{AB}}$$

where θ_λ, the transmission angle for wavelength λ, and θ_i - the angle the incident ray makes

with the VIPA normal (i.e. the VIPA tilt angle) - are as shown in Fig. F.1. Note that over-lining indicates a distance between the over-lined points. Additionally, it can be seen that the lengths $\overline{AB}$ and $\overline{BC}$ are equal, and so the total distance $\overline{ABC} = \overline{AB} + \overline{BC}$ is given by

$$\overline{ABC} = \frac{2t}{\cos(\theta_i + \theta_\lambda)}. \tag{F.1}$$

It may also be seen that

$$\tan(\theta_\lambda + \theta_i) = \frac{h}{2t}$$

where $h = \overline{AC}$. Rearrangement for h yields

$$h = 2t\tan(\theta_i + \theta_\lambda) \tag{F.2}$$

and from Fig. F.1 it can also seen that

$$\sin(\theta_i + \theta_\lambda) = \frac{\overline{AD}}{h}.$$

After rearranging this expression for $\overline{AD}$, it may be combined with Eq. F.2 to give

$$\overline{AD} = 2t\sin(\theta_i + \theta_\lambda)\tan(\theta_\lambda + \theta_i). \tag{F.3}$$

In order for the two transmitted beams shown in Fig. F.1 to constructively interfere, it is a requirement that the path length difference between the two adjacent beams $\overline{AD}$ is equal to an integer multiple of the incident wavelength λ. That is, the two adjacent beams are required to be in phase with one another to prevent destructive interference. This is stated mathematically as

$$\overline{ABC} = \overline{AD} + m\lambda \quad \text{for } m = 1, 2, 3... \tag{F.4}$$

Substitution of Eqs. F.1 and F.3 into Eq. F.4 gives

$$\frac{2t}{\cos(\theta_t)} = 2t\sin(\theta_t)\tan(\theta_t) + m\lambda \tag{F.5}$$

where $\theta_t = \theta_i + \theta_\lambda$. After further rearrangement and using the definition of the angular wavenumber, $k = (2\pi)/\lambda$, Eq. F.5 may be written as

$$2t\left(\frac{1}{\cos(\theta_t)} - \sin(\theta_t)\tan(\theta_t)\right) = \frac{2\pi m}{k}. \tag{F.6}$$

Using the definition of the tangent function and a common trigonometric identity:

$$\begin{aligned} \tan(\theta_t) &= \frac{\sin(\theta_t)}{\cos(\theta_t)} \\ 1 - \sin^2(\theta_t) &= \cos^2(\theta_t), \end{aligned}$$

Eq. F.6 may be written

$$2kt\cos(\theta_t) = 2kt\cos(\theta_i + \theta_\lambda) = 2\pi m. \tag{F.7}$$

In the case of an air-spaced etalon, the ray does not experience refraction at either of the entrance or exit faces, that is, only $\theta_t = 0$ is physically allowed [310]. In such a case the dispersion relation is that given by Eq. F.7 for a standard Fabry-Pérot etalon. However, in the case of a VIPA etalon the beam is focused by a semi-cylindrical lens, and so is presented with input rays of many angles. Following the approach set by Xiao *et al.* in Ref. [259], the angle of the central ray in the input beam with respect to the VIPA normal is denoted θ_i and $\theta_i + \theta_\lambda$ as the angle of the ray elsewhere in the focused beam with respect to the VIPA normal as seen in Fig. F.2.

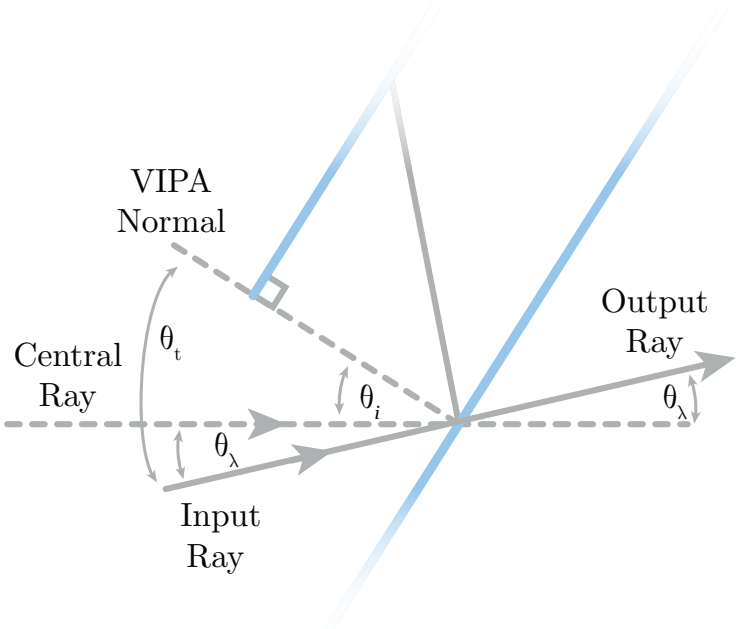

Figure F.2: Geometry of the air-spaced VIPA etalon, showing the angular definitions of important rays with respect to the VIPA normal [258].

Rays within the focused input beam are selectively transmitted by the VIPA provided they satisfy the dispersion relation, the mathematical description of the etalon's resonance condition. In the case of the air-spaced etalon, the input angle is equal to that of the output angle for such rays. Again following the work of Xiao *et al.*, now consider a Taylor expansion about $\theta_\lambda = 0$ of Eq. F.7 to second order in θ_λ. This yields the approximate dispersion relation for the air-spaced etalon of:

$$2kt\left(\cos(\theta_i) - \sin(\theta_i)\,\theta_\lambda - \frac{1}{2}\cos(\theta_i)\,{\theta_\lambda}^2\right) = 2\pi m.$$

Though this derivation was based on an air-spaced etalon, Xiao *et al.* have shown in Ref. [259] that this result is applicable to a solid etalon with minor modifications. The dispersion

relation for a solid VIPA etalon of refractive index n_r is given by

$$2kt\left(n_r\cos\left(\theta_{in}\right)-\tan\left(\theta_{in}\right)\cos\left(\theta_i\right)\theta_\lambda-\frac{1}{2n_r}\cos\left(\theta_{in}\right)\theta_\lambda{}^2\right)=2\pi m \tag{F.8}$$

where $n_r\sin\left(\theta_{in}\right)=\sin\left(\theta_i\right)$ (Snell's Law) and θ_{in} is the internal angle inside the solid etalon resulting from the refraction as seen in Fig. 6.5. The dispersion relation in Eq. F.8 describes the phase criterion for a specific wavelength to be transmitted by the VIPA etalon, and thus describes the spectral dispersion of the VIPA as a function of angle.

F.2 VIPA Free Spectral Range

The FSR of a solid VIPA may again be derived following the example set by Xiao *et al.* for an air-spaced VIPA in Ref. [259]. Again considering a solid etalon of refractive index n_r, the angular wavenumber may be rewritten in terms of frequency as

$$k=\frac{2\pi}{\lambda}=\frac{2\pi f}{c}$$

where c is the speed of light in vacuum. This expression for k may then be substituted into the dispersion relation derived for a solid etalon (Eq. F.8) to give:

$$2t\left(\frac{2\pi f}{c}\right)\left(n_r\cos\left(\theta_{in}\right)-\tan\left(\theta_{in}\right)\cos\left(\theta_i\right)\theta_\lambda-\frac{1}{2n_r}\cos\left(\theta_{in}\right)\theta_\lambda{}^2\right)=2\pi m. \tag{F.9}$$

After cancellation of common factors, Eq. F.9 may be rearranged for f to give

$$f=\frac{mc}{2t\left(n_r\cos\left(\theta_{in}\right)-\tan\left(\theta_{in}\right)\cos\left(\theta_i\right)\theta_\lambda-\frac{1}{2n_r}\cos\left(\theta_{in}\right)\theta_\lambda{}^2\right)}.$$

The VIPA FSR is defined as the frequency interval between two adjacent transmission modes of the tilted etalon, i.e. $\Delta m=1$. Thought of another way, the VIPA FSR can also be defined as the distance in frequency that must be moved before a new wavelength satisfies the dispersion relation for the same set of input and output angles as the original wavelength. Note that this is distinct from the spatial FSR which describes the distance or angle between two adjacent transmission modes on an imaging plane placed at some distance from the output of the etalon. Using the definition of FSR in frequency, the final expression for the VIPA FSR may be derived from Eq. F.9 to be

$$\mathrm{FSR}=\frac{c}{2t\left(n_r\cos\left(\theta_{in}\right)-\tan\left(\theta_{in}\right)\cos\left(\theta_i\right)\theta_\lambda-\frac{1}{2n_r}\cos\left(\theta_{in}\right)\theta_\lambda{}^2\right)}$$

in which Δm has been set to one in keeping with the definition for the FSR. This expression defines the FSR of a solid VIPA etalon in accordance with paraxial wave theory.

Rarefication Cavity Arduino Code

The rarefication or decimation optical cavity used in this thesis to calibrate the relative frequency axis of acquired spectra is stabilised using an Arduino Due microcontroller board programmed with the following code. The output of the optical cavity is monitored by a photodetector which is interpreted by the Arduino system as per Chapter 8, maintaining the high cavity output. It is important to note that this code and the stabilisation system incorporating the microcontroller was produced by visiting student Nicolas Bourbeau Hébert, but it presented here for completeness.

```
// All inputs and outputs operate in the 0-3.3V range for the
// Arduino Due (digital and analog) When using a 12-bit
// resolution, values are restrained between 0-4095.

//Load a useful library for time management (uses interrupts)
#include <DueTimer.h>

//*************************************************************
//Declare variables

//Hardware settings
int PinServo = 42; //Pin which turns the servo ON or OFF.
int PinModulation = 52; //Modulation output
int sampleFreq = 20000; // Update rate [Hz]
int DCLevel = 2048; // DC level to center all the values within
    the PI loop around 0
int errorLevel = 0; // Latest error level (0-4095)
int PIoutLevel = DCLevel; // Current output level of the PI
   controller (0-4095)
int statePinServo = LOW; //Current state of the Servo Pin
bool recenter = 0; //When recenter==1, the coarse output is
   incremented until the fine output comes back within its range
float coarseValue = 2048; //Current value for the coarse
   adjustment

//PI algorithm
```

```
float PIout = 0; // Current output value of the PI controller
float error = 0; // Latest error value

float sum = 0; // Holds the sum of all error values (integral
   of the error signal)

//PI parameters
float fPI = 600; //PI corner frequency [Hz]
float Gp = -0.085; //Proportional gain [-]
float Gi = Gp * 2 * 3.141593 * fPI / sampleFreq; //Integral
        // gain [-]

//Define a vector for square modulation
int square[2] = {LOW, HIGH}; //Square wave obtained from
        // flipping a bit
int i = 0; //Index to pick a value in vector "square"

// Variable to store the past inputs and use them for filtering
float x[2] = {0, 0};

//************************************************************
//Initialization
void setup() {
Timer0.attachInterrupt(PIiteration).setFrequency(sampleFreq).
   start(); // Set the timer
analogWriteResolution(12);  // Set the analog output resolution
    to 12 bit (4096 levels)
analogReadResolution(12);  // Set the analog input resolution
   to 12 bit (4096 levels)
pinMode(PinServo, INPUT_PULLUP); // Acts as a switch to turn
   the Servo ON.
pinMode(PinModulation, OUTPUT); // Square modulation will come
   from that digital pin (filtered later on by a RC low-pass
   filter)

}
//************************************************************
void loop() {
//Useless here I guess...
}
//************************************************************
```

```
void PIiteration() { // Function to be called every 1/
   sampleFreq (each time Timer0 "rings").

//Read the current errorLevel and convert it to float and
   remove DCLevel
delayMicroseconds(0); //Adjust the delay to sample on top of
   the sine wave. It is important because we sample exactly at
   Nyquist
errorLevel = analogRead(A0) - DCLevel;
error = (float)(errorLevel);

//Square demodulation
if (i == 0) {
error = -1 * error;
}

// Low-pass filter the demodulated error signal (simple
   averaging 2-tap filter)
x[0] = x[1];
x[1] = error;
error = 0.5 * x[1] + 0.5 * x[0];

//Increment index for modulation
i++;
if (i == 2) {
i = 0;
}
//************************************************************

statePinServo = digitalRead(PinServo); //Checks if the Servo
   Switch is on.

if (statePinServo == LOW) { //If Servo Switch is turned off,
   outputs the DCLevel
PIoutLevel = DCLevel;
coarseValue = 2048;
sum = 0; //Reset sum value while the servo is turned off
}

else if (statePinServo == HIGH) { //If Servo Switch if turned
```

```
   on, outputs the calculated control value


// Recenter the fine control ouput by modifying the coarse
   output, to prevent it to go out of range.
if (recenter == 1) {

if (PIoutLevel > (DCLevel + 500)) {
coarseValue = coarseValue + 0.05; //Fractional increments to
   let time for the PI to adjust between each integer step
}
else if (PIoutLevel < (DCLevel - 500)) {
coarseValue = coarseValue - 0.05; //Fractional increments to
   let time for the PI to adjust between each integer step
}
else {
recenter = 0;
}
}

//Update the error sum only if output is within bounds.  Avoids
    integrator windup.
if (PIout > -2048 && PIout < 2047)
{
sum = sum + error;
}

//Compute the PI output (float)
PIout = (Gp * error) + (Gi * sum);

// Put min and max limits on the output
if (PIout > 2047)
{
PIout = 2047;
recenter = 1; //Turn on the coarse control.
}
if (PIout < -2048)
{
PIout = -2048;
recenter = 1; //Turn on the coarse control.
}
```

```
//Make sure that PIoutLevel is an integer.
//Casting from float to integer truncates instead of rounding
PIoutLevel = (int)(PIout);

//Add the DCLevel
PIoutLevel = PIoutLevel + DCLevel;
}

//*************************************************************
//Write the PI output level on DAC0
analogWrite(DAC0, PIoutLevel);

//Write the coarse value on DAC1
if (coarseValue > 4095) { //Set the maximum value for
   coarseValue (comes from the limited number of voltage levels)
coarseValue = 4095;
}
analogWrite(DAC1, (int)(coarseValue));

//Square modulation for the Fabry-Perot cavity. Gets low-pass
   filtered with a simple RC circuit at output for a smoother
   modulation
digitalWrite(PinModulation, square[i]);

}
```

Long-path Cell Alignment Servo Code

The 6.5 m sample cell used in Chapter 10 is of sufficient length to suffer from beam wander due to turbulence effects as gas is injected into the cell. Additionally, as the output is coupled into optical fibre, the magnitude of beam wander required to completely lose signal is relatively small. To maintain output power, the cell path is actively corrected via the use of a mirror connected to a piezo-electric transducer for rapid correction. Additionally, a stepper-motor mirror - known as *PicoMotor* in the upcoming code - is used for coarse correction of alignment and to keep the system within range of the piezo mirror. In order to not interfere with the spectroscopic measurement, an additional 780 nm laser is introduced collinear to the sample path, with the retro-reflected 780 nm light detected upon return by an avalanche photodetector that is the input to Fig. H.1. This signal is then fed to a lock-in amplifier, and the system attempts to maintain the photodetector signal at its maximum value corresponding to good alignment. The photodetector output is continuously monitored and then interpreted by the following code, with the stepper motor mirror activated to keep the applied voltage within range of the piezo-controlled mirror. This is mentioned very briefly in the article forming Chapter 10, and the full correction code is presented here for completeness.

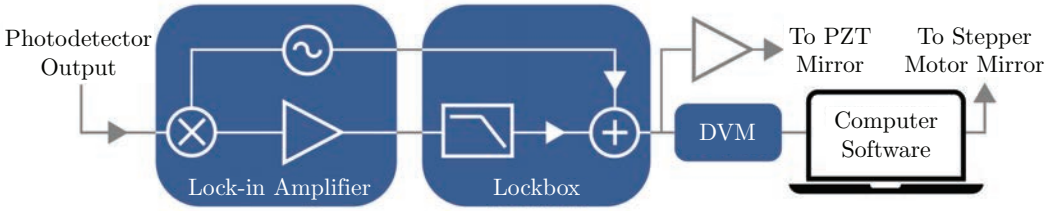

Figure H.1: Schematic of the stepper motor and PZT-controlled mirrors as presented in Chapter 10. The 780 nm beam collinear to the frequency comb beam is detected by an avalanche photodetector and is the input to the stabilisation loop.

RELATE TO THE DIAGRAM

```
using System;
using System.Collections.Generic;
using System.Linq;
using System.Text;
using System.Threading.Tasks;
using System.Threading;
using InterfaceSystem;
using System.Diagnostics;
```

```
using System.IO;

namespace PicomotorControl
{
  class Program
  {
    static void Main(string[] args)
    {
      InterfaceManager im = new InterfaceManager();
      //            im.ShowLogWindow();

      // Find the DVM (and confirm by displaying id to console)
      im.SearchForInstruments();
      Agilent344xxA dvm =
          (Agilent344xxA)im.GetInstrumentsByDriver(typeof(
          Agilent344xxA))[0];
      Console.WriteLine("DVM id:");
      Console.WriteLine(dvm.Identification);

      // Find + setup the Picomotor (and confirm by displaying the
          firmware version to console)
      NewFocusPicomotor875x pico = new
          NewFocusPicomotor875x("10.32.98.116");
      Console.WriteLine("Picomoter Firmware Version:");
      Console.WriteLine(pico.FirmwareVersion());
      pico.LoadDefaultsParameters();
      pico.DisableAllDrivers();
      pico.SetJoystickMode(NewFocusPicomotor875x.JoystickMode.Off);
      pico.EnableDriver(NewFocusPicomotor875x.Driver.a1);
      pico.EnableMotor(NewFocusPicomotor875x.Motor.m0,
          NewFocusPicomotor875x.Driver.a1);
      int Position =
          pico.GetPosition(NewFocusPicomotor875x.Driver.a1);
      Console.WriteLine("Position");
      Console.WriteLine(Position);

      // Definitions
      double errorVoltage = dvm.Voltage;
      double Integratorgain = -0.0004;
      double ProportionalGain = -4;
      double Offset = 5; // Offset of the DVM (point we aim for)
      int dt = 75; // In ms
      double correctionPosition = 0;// What we want the picomotor to
          do
      double Integrator = 0;
      int absolutePosition =
          pico.GetPosition(NewFocusPicomotor875x.Driver.a1);
```

```
int relativePosition = absolutePosition;// What pico motor
    reports it has done
long loopTime = 75; // Keeps track of the time the loop takes
long absoluteTime = 0; // Keeps track of the total time the
    program has been running
long startTime = 0;
Stopwatch loopTimer = new Stopwatch(); // Initialise the timer
loopTimer.Start();

// Commence loop
Console.WriteLine("DVM Error Voltage (V), Correction Position,
    Relative Position, Absolute Position, Absolute Time (ms),
    Loop Time (ms)");
StreamWriter fileSave = new
    StreamWriter(@"C:\Users\Optical.pmg\Desktop\Sarah\Programs\
    PicomotorControl\LogFiles\Log2.txt", true);
fileSave.WriteLine("DVM Error Voltage (V), Correction Position,
    Relative Position, Absolute Position, Absolute Time (ms),
    Loop Time (ms)");

while (Console.KeyAvailable == false)
{
  startTime = loopTimer.ElapsedMilliseconds;
  errorVoltage = dvm.Voltage - Offset;
  Integrator = Integrator +
     errorVoltage*loopTime*Integratorgain;
  correctionPosition = Integrator + errorVoltage *
     ProportionalGain;
  pico.SetPosition(NewFocusPicomotor875x.Driver.a1, (int)
     correctionPosition);
  relativePosition =
     pico.GetPosition(NewFocusPicomotor875x.Driver.a1);

  while (relativePosition != (int) correctionPosition)
  {
    relativePosition =
       pico.GetPosition(NewFocusPicomotor875x.Driver.a1);
    Thread.Sleep(1);
  }

  absolutePosition = absolutePosition + relativePosition;
  loopTime = loopTimer.ElapsedMilliseconds - startTime;
  absoluteTime = loopTimer.ElapsedMilliseconds;

  //Debugging and logging
  string errorVoltage1 = errorVoltage.ToString("f6");
  string correctionPosition1 =
```

```
            correctionPosition.ToString("f6");
        string relativePosition1 = relativePosition.ToString();
        string absolutePosition1 = absolutePosition.ToString();
        string absoluteTime1 = absoluteTime.ToString();
        string loopTime1 = loopTime.ToString();

        Console.WriteLine("{0},\t{1},\t{2},\t{3},\t{4},\t{5}",
            errorVoltage1,correctionPosition1,relativePosition1,
            absolutePosition1,absoluteTime1, loopTime1);
        fileSave.WriteLine("{0},\t{1},\t{2},\t{3},\t{4},\t{5}",
            errorVoltage1, correctionPosition1, relativePosition1,
            absolutePosition1, absoluteTime1, loopTime1);
      }

      //Shutdown
      loopTimer.Stop();
      fileSave.Close();
      Console.ReadLine();
      im.Shutdown();
    }
  }
}
```

Conference Publications and Awards

Conference Papers

Presenting author is highlighted in **bold**, and all papers are presented in chronological order.

J. Anstie, R. White, S. Scholten, R. Yazbek, R. Butler, and A. Luiten,"*Cavity Enhanced Frequency Comb Spectrometer for Breath Analysis Applications*", The International Association of Breath Researchers (IABR) Summit, 2015.

S. Scholten, J. Anstie, N. Bourbeau Hébert, R. White, J. Genest, and A. Luiten, "*Broadband phase-sensitive frequency-comb spectroscopy using a virtually imaged phased array*", International OSA Network of Students Conference on Optics, Atoms, and Laser Applications (IONS KOALA), 2015.

S. Scholten, J. Anstie, N. Bourbeau Hébert, R. White, J. Genest, and A. Luiten, "*Broadband phase-sensitive frequency-comb spectroscopy using a virtually imaged phased array*", Australian and New Zealand Conference on Optics and Photonics (ANZCOP) Congress, 2015.

S. Scholten, C. Perrella, J. Anstie, R. White, S. Afshar, G. Moffa, N. Bourbeau Hébert, W. Al-Ashwal, J. Genest, and A. Luiten,"*Real-time Concentration Measurements of CO_2 with an Optical Frequency Comb*", Australian Institute of Physics (AIP) Congress, 2016.

S. Scholten, **C. Perrella**, J. Anstie, R. White, N. Bourbeau Hébert, W. Al-Ashwal, J. Genest, and A. Luiten, "*Real-time accurate optical measurements of CO_2 number density*", Atmospheric Composition and Chemistry Observations and Modelling Conference (ACCOMC), 2017.

S. Scholten, C. Perrella, J. Anstie, R. White, N. Bourbeau Hébert, W. Al-Ashwal, and **A. Luiten**, "*Real-time and Precise Concentration Measurements of CO_2*", Australian and New Zealand Conference on Optics and Photonics (ANZCOP) Congress, 2017.

S. Scholten, C. Perrella, J. Anstie, R. White, N. Bourbeau Hébert, W. Al-Ashwal, J. Genest, and A. Luiten, "*Real-time accurate optical measurements of CO_2 number density*", Australian Institute of Physics (AIP) Summer Meeting, 2017.

G. -W. Troung, S. Scholten, F. Karim, J. D. Anstie, C. Perrella, P. Light, Dong Wei, E. F. May, T. M. Stace, and **A. N. Luiten**, "*Measuring Temperature with Atoms and Molecules*", Conference on Lasers and Electro-Optics (CLEO), In Proceedings of the CLEO: Science and Innovations 2018 Vol. Part F94-CLEO_SI 2018 (pp. 1-2), 2018.

S. Scholten, C. Perrella, J. Anstie, R. White, N. Bourbeau Hébert, F. Karim, W. Al-Ashwal, J. Genest, and A. Luiten, "*Rapid Optical Measurement of* $^{13}CO_2$ *and* $^{12}CO_2$ *Number Density*", Emerging Sensing Technologies Summit (ESTS), 2018.

S. Scholten, C. Perrella, J. Anstie, R. White, N. Bourbeau Hébert, F. Karim, W. Al-Ashwal, J. Genest, and A. Luiten, "*Rapid Optical Measurement of* $^{13}CO_2$ *and* $^{12}CO_2$ *Number Density*" (Invited), Australian Institute of Physics (AIP) Congress, 2018.

A. Luiten, S. Scholten, C. Perrella, J. Anstie, R. White, N. Bourbeau Hébert, F. Karim, W. Al-Ashwal and J. Genest, "*Measuring gas thermodynamic properties with an optical frequency comb*" (Invited), SPIE Photonics West, 2019.

Conference Posters

S. Scholten, C. Perrella, J. Anstie, R. White, N. Bourbeau Hébert, F. Karim, W. Al-Ashwal, J. Genest, and A. Luiten,"*Rapid Optical Measurement of* $^{13}CO_2$ *and* $^{12}CO_2$ *Number Density*", Australian Institute of Physics (AIP) Congress, 2018.

Awards

The Merry Wickes Transdisciplinary Award, Awarded by the Institute for Photonics and Advanced Sensing (IPAS), 2017.

Warsash Science Communications Prize in Optics, Awarded by the Australian Optical Society (AOS), 2018.

IPAS Best Student Paper (2018), Awarded by the Institute for Photonics and Advanced Sensing (IPAS), 2019.

References

[1] L. S. Rothman, D. Jacquemart, A. Barbe, D. C. Benner, M. Birk, L. R. Brown, M. R. Carleer, C. Chackerian Jr., K. Chance, L. H. Coudert, V. Dana, V. M. Devi, J. -M. Flaud, R. R. Gamache, A. Goldman, J. -M. Hartmann, K. W. Jucks, A. G. Maki, J. -Y. Mandin, S. T. Massie, J. Orphal, A. Perrin, C. P. Rinsland, M. A. H. Smith, J. Tennyson, R. N. Tolchenov, R. A. Toth, J. Vander Auwera, P. Varanasi, and G. Wagner. The HITRAN 2004 molecular spectroscopic database. *Journal of Quantitative Spectroscopy and Radiative Transfer*, 96:139–204, 2005.

[2] A. Amann and D. Smith. *Volatile Biomarkers: Non-Invasive Diagnosis in Physiology and Medicine*. Elsevier, Oxford, United Kingdom, 2013.

[3] S. Das, S. Pal, and M. Mitra. Significance of exhaled breath test in clinical diagnosis: A special focus on the detection of diabetes mellitus. *Journal of Medical and Biological Engineering*, 36(5):605–624, 2016.

[4] F. S. Cikach and R. A. Dweik. Cardiovascular biomarkers in exhaled breath. *Progress in Cardiovascular Disease*, 55(1):34–43, 2012.

[5] K. Strimbu and J. A. Tave. What are biomarkers? *Current opinion in HIV and AIDS*, 5(6):463–466, 2010.

[6] A. Ghorani-Azam, B. Riahi-Zanjani, and M. Balali-Mood. Effects of air pollution on human health and practical measures for prevention in Iran. *Journal of Research in Medical Sciences*, 21(65), 2016.

[7] R. G. Williams, V. Roussenov, P. Goodwin, L. Resplandy, and L. Bopp. Sensitivity of global warming to carbon emissions: Effects of heat and carbon uptake in a suite of earth system models. *Journal of Climate*, 30:9343–9363, 2017.

[8] G. Santos. Road transport and CO_2 emissions: What are the challenges? *Transport Policy*, 59:71–74, 2017.

[9] P. C. Jain. Greenhouse effect and climate change: scientific basis and overview. *Renewable Energy*, 2(4-5):403–420, 1993.

[10] B. Buszewski, M. Kesy, T. Ligor, and A. Amann. Human exhaled air analytics: biomarkers of diseases. *Biomedical Chromatography*, 21(6):553–566, 2007.

[11] W. Ma, X. Liu, and J. Pawliszyn. Analysis of human breath with microextraction techniques and continuous monitoring of carbon dioxide concentration. *Analytical and Bioanalytical Chemistry*, 385(8):1398–1408, 2006.

[12] M. Phillips. Breath tests in medicine. *Scientific American*, 267(1):74–79, 1992.

[13] F. Di Francesco, R. Fuoco, M. G. Trivella, and A. Ceccarini. Breath analysis: trends in techniques and clinical applications. *Microchemical Journal*, 79(1-2):405–410, 2005.

[14] M. Libardoni, P. T. Stevens, J. Hunter Waite, and R. Sacks. Analysis of human breath samples with a multi-bed sorption trap and comprehensive two-dimensional gas chromatography (gc x gc). *Journal of Chromatography B*, 842(1):13–21, 2006.

[15] M. Asif. The prevention and control the type-2 diabetes by changing lifestyle and dietary pattern. *Journal of Education and Health Promotion*, 3(1), 2014.

[16] C. Lourenço and C. Turner. Breath analysis in disease diagnosis: Methodological considerations and applications. *Metabolites*, 4(2):465–498, 2014.

[17] K. Rogers, editor. *The Respiratory System*. The Rosen Publishing Group, 2010.

[18] S. Whittemore. *The Respiratory System*. Infobase Publishing, 2009.

[19] C. M. Ionescu. *The Human Respiratory System: An Analysis of the Interplay between Anatomy, Structure, Breathing and Fractal Dynamics*. Springer, 2013.

[20] V. C. Broaddus, R. J. Mason, J. D. Ernst, T. E. King Jr., S. T. Lazarus, J. F. Murray, J. A. Nadel, A. S. Slutsky, and M. B. Gotway, editors. *Murray and Nadel's Textbook of Respiratory Medicine*, volume 1. Elsevier, 6th edition, 2016.

[21] J. Tinker and M. Rapin, editors. *Care of the Critically Ill Patient*. Springer, 1983.

[22] V. Saasa, T. Malwela, M. Beukes, M. Mokgotho, C. P. Liu, and B. Mwakikunga. Sensing technologies for detection of acetone in human breath for diabetes diagnosis and monitoring. *Diagnostics*, 8(1), 2018.

[23] R. Schnabel, R. Fijten, A. Smolinska, J. Dallinga, M. L. Boumans, E. Stobberingh, A. Boots, P. Roekaerts, D. Bergmans, and F. Jan van Schooten. Analysis of volatile organic compounds in exhaled breath to diagnose ventilator-associated pneumonia. *Scientific Reports*, 5:17179, 2015.

[24] I. Khurana. *Textbook Of Medical Physiology*. Elsevier India, India, 2005.

[25] G. K. Pal, P. Pal, and N. Nanda. *Comprehensive Textbook of Medical Physiology - Two Volume Set*. JP Medical Ltd, Bangladesh, 2016.

[26] L. Shaw. *Anatomy and Physiology*. Nelson Thornes, United Kingdom, 2005.

[27] K. K. Chow, M. Short, and H. Zeng. A comparison of spectroscopic techniques for human breath analysis. *Biomedical Spectroscopy and Imaging*, 1(4):339–353, 2012.

[28] M. Ferwana, I. Abdulmajeed, A. Alhajiahmed, W. Madani, B. Firwana, R. Hasan, O. Altayar, P. J. Limburg, M. H. Murad, and B. Knawy. Accuracy of urea breath test in *Helicobacter pylori* infection: Meta-analysis. *World Journal of Gastroenterology: WJG*, 21(4):1305–1314, 2015.

[29] M. Peeters. Urea breath test: a diagnostic tool in the management of *Helicobacter pylori*-related gastrointestinal diseases. *Acta Gastro-enterologica Belgica*, 61(3):332–335, 1998.

[30] D. Y. Graham and M. Miftahussurur. *Helicobacter pylori* urease for diagnosis of *Helicobacter pylori* infection: A mini review. *Journal of Advanced Research*, 13:51–57, 2018.

[31] J. P. Gisbert and J. M. Pajares. Review article: ^{13}C-urea breath test in the diagnosis of *Helicobacter pylori* infection - a critical review. *Alimentary Pharmacology & Therapeutics*, 20(10), 2004.

[32] Y. A. Bakhirkin, A. A. Kosterev, R. F. Curl, F. K. Tittel, D. A. Yarekha, L. Hvozdara, M. Giovannini, and J. Faist. Subpppbv nitric oxide concentration measurements using cw thermoelectrically cooled quantum cascade laser-based integrated cavity output spectroscopy. *Applied Physics B - Lasers and Optics*, 82(1):149–154, 2006.

[33] K. Namjou, C. B. Roller, and G. McMillen. Breath-analysis using mid-infrared tunable laser spectroscopy. *in: Sensors, 2007 IEEE*, pages 1337–1340, 2007.

[34] K. Namjou, C. B. Roller, T. E. Reich, J. D. Jeffers, G. L. McMillen, P. J. McCann, and M. A. Camp. Determination of exhaled nitric oxide distributions in a diverse sample population using tunable diode laser absorption spectroscopy. *Applied Physics B - Lasers and Optics*, 85(2-3):427–435, 2006.

[35] W. Lee and P. S. Thomas. Oxidative stress in COPD and its measurement through exhaled breath condensate. *Clinical and Translational Science*, 2(2):150–155, 2009.

[36] R. Ghorbani, A. Blomberg, and F. M. Schmidt. Modeling pulmonary gas exchange and single-exhalation profiles of carbon monoxide. *Frontiers in Physiology*, 9(927), 2018.

[37] E. R. Crosson, K. N. Ricci, B. A. Richman, F. C. Chilese, T. G. Owano, R. A. Provencal, M. W. Todd, J. Glasser, A. A. Kachanov, B. A. Paldus, T. G. Spence, and R. N. Zare. Stable isotope ratios using cavity ring-down spectroscopy: Determination of C-13/C-12 for carbon dioxide in human breath. *Analytical Chemistry*, 74(9):2003–2007, 2002.

[38] V. Savarino, S. Vigneri, and G. Celle. The C-13 urea breath test in the diagnosis of *Helicobacter pylori* infection. *Gut*, 45:I18I22, 1999.

[39] A. Bajtarevic, C. Ager, M. Pienz, M. Klieber, K. Schwarz, M. Ligor, T. Ligor, W. Filipiak, H. Denz, M. Fiegl, W. Hilbe, W. Weiss, P. Lukas, H. Jamnig, M. Hackl, A. Haidenberger, B. Buszewski, W. Miekisch, J. Schubert, and A. Amann. Noninvasive detection of lung cancer by analysis of exhaled breath. *BMC Cancer*, 9:348–364, 2009.

[40] P. J. Mazzone. Exhaled breath volatile organic compound biomarkers in lung cancer. *Journal of Breath Research*, 6(2):027106, 2012.

[41] K. D. Skeldon, L. C. McMillan, C. A. Wyse, S. D. Monk, G. Gibson, C. Patterson, T. France, C. Longbottom, and M. J. Padgett. Application of laser spectroscopy for measurement of exhaled ethane in patients with lung cancer. *Respiratory Medicine*, 100(2):300–306, 2006.

[42] G. Song, T. Qin, H. Liu, G. B. Xu, Y. Y. Pan, F. X. Xiong, K. S. Gu, G. P. Sun, and Z. D. Chen. Quantitative breath analysis of volatile organic compounds of lung cancer patients. *Lung Cancer*, 67(2):227–231, 2010.

[43] A. Wehinger, A. Schmid, S. Mechtcheriakov, M. Ledochowski, C. Grabmer, G. A. Gastl, and A. Amann. Lung cancer detection by proton transfer reaction mass-spectrometric analysis of human breath gas. *International Journal of Mass Spectrometry*, 265(1):49–59, 2007.

[44] S. Davies, P. Spanel, and D. Smith. Quantitative analysis of ammonia on the breath of patients in end-stage renal failure. *Kidney International*, 52(1):223–228, 1997.

[45] S. Davies, P. Spanel, and D. Smith. A new online method to measure increased exhaled isoprene in end-stage renal failure. *Nephrology Dialysis Transplantation*, 16(4):836–839, 2001.

[46] P. Lirk, F. Bodrogi, H. Raifer, K. Greiner, H. Ulmer, and J. Rieder. Elective haemodialysis increases exhaled isoprene. *Nephrology Dialysis Transplantation*, 18(5):937–941, 2003.

[47] L. R. Narasimhan, W. Goodman, and C. K. N. Patel. Correlation of breath ammonia with blood urea nitrogen and creatinine during hemodialysis. *Proceedings of the National Academy of Sciences of the United States of America*, 98(8):4617–4621, 2001.

[48] C. H. Deng, J. Zhang, X. F. Yu, W. Zhang, and X. M. Zhang. Determination of acetone in human breath by gas chromatography-mass spectrometry and solid-phase microextraction with on-fiber derivatization. *Journal of Chromatography B Analytical Technologies in the Biomedical and Life Sciences*, 810(2):269–275, 2004.

[49] C. J. Wang, A. Mbi, and M. Shepherd. A study on breath acetone in diabetic patients using a cavity ringdown breath analyzer: Exploring correlations of breath acetone with blood glucose and glycohemoglobin A1C. *IEEE Sensors Journal*, 10(1):54–63, 2010.

[50] R. Yazbeck, S. E. Jaenisch, and D. I. Watson. From blood to breath: New horizons for esophageal cancer biomarkers. *World Journal of Gastroenterology*, 22(46):10077–10083, 2016.

[51] S. Kumar, J. Huang, N. Abbassi-Ghadi, P. Španěl, D. Smith, and G. B. Hanna. Selected ion flow tube mass spectrometry analysis of exhaled breath for volatile organic compound profiling of esophago-gastric cancer. *Analytical Chemistry*, 85(12):6121–6128, 2013.

[52] S. Kumar, J. Huang, N. Abbassi-Ghadi, H. A. Mackenzie, K. A. Veselkov, J. M. Hoare, L. B. Lovat, P. Španěl, D. Smith, and G. B. Hanna. Mass spectrometric analysis of exhaled breath for the identification of volatile organic compound biomarkers in esophageal and gastric adenocarcinoma. *Annals of Surgery*, 262(6):981–990, 2015.

[53] R. Fernández del Río, M. E. O'Hara, A. Holt, P. Pemberton, T. Shah, T. Whitehouse, and C. A. Mayhew. Volatile biomarkers in breath associated with liver cirrhosis comparisons of pre- and post-liver transplant breath samples. *EBioMedicine*, 2(9):1243–1250, 2015.

[54] F. Morisco, E. Aprea, V. Lembo, V. Fogliano, P. Vitaglione, G. Mazzone, L. Cappellin, F. Gasperi, S. Masone, G. Domenico De Palma, R. Marmo, N. Caporaso, and F. Biasioli. Rapid breath-print of liver cirrhosis by proton transfer reaction time-of-flight mass spectrometry. A pilot study. *PloS One*, 8(4):e59658, 2013.

[55] J. Dadamioa, S. Van den Velde, W. Laleman, P. Van Hee, W. Coucke, F. Nevens, and M. Quirynen. Breath biomarkers of liver cirrhosis. *Journal of Chromatography B*, 905:17–22, 2012.

[56] M. I. Friedman, G. Preti, R. O. Deems, L. S. Friedman, S. J. Munoz, and W. C. Maddrey. Limonene in expired lung air of patients with liver disease. *Digestive Diseases and Sciences*, 39(8):1672–1676, 1994.

[57] N. B. Minkoff. Analysis of the current care model of the COPD patient: a health outcomes assessment and economic evaluation. *Journal of Managed Care Pharmacy*, 11(6):S3–7, 2005.

[58] P. M. P. van Oort, S. de Bruin, H. Weda, H. H. Knobel, M. J. Schultz, and L. D. Bos. Exhaled breath metabolomics for the diagnosis of pneumonia in intubated and mechanically-ventilated intensive care unit (icu)-patients. *International Journal of Molecular Sciences*, 18(2):449, 2017.

[59] T. Hüppe, D. Lorenz, M. Wachowiak, F. Maurer, A. Meiser, H. Groesdonk, T. Fink, D. I. Sessler, and S. Kreuer. Volatile organic compounds in ventilated critical care patients: a systematic evaluation of cofactors. *BMC Pulmonary Medicine*, 17:116, 2017.

[60] W. Cao and Y. Duan. Breath analysis: Potential for clinical diagnosis and exposure assessment. *Clinical Chemistry*, 52(5):800–811, 2006.

[61] L. Pauling, A. B. Robinson, R. Teranishi, and P. Cary. Quantitative analysis of urine vapor and breath by gas-liquid partition chromatography. *Proceedings of the National Academy of Sciences of the United States of America*, 68(10):2374–2376, 1971.

[62] D. Smith and P. Španěl. Application of ion chemistry and the sift technique to the quantitative analysis of trace gases in air and on breath. *International Reviews in Physical Chemistry*, 15(1):231–271, 1996.

[63] M. Phillips, K. Gleeson, J. M. B. Hughes, J. Greenberg, R. N. Cataneo, L. Baker, and P. McVay. Volatile organic compounds in breath as markers of lung cancer: a cross-sectional study. *The Lancet*, 353(9168):1930–1933, 1999.

[64] J. Obermeier, P. Trefz, K. Wex, B. Sabel, J. K. Schubert, and W. Miekisch. Electrochemical sensor system for breath analysis of aldehydes, CO and NO. *Journal of Breath Research*, 9(1):016008, 2015.

[65] C. Di Natale, R. Paolesse, E. Martinelli, and R. Capuano. Solid-state gas sensors for breath analysis: A review. *Analytica Chimica Acta*, 824:1–17, 2014.

[66] T. Kuretake, S. Kawahara, M. Motooka, and S. Uno. An electrochemical gas biosensor based on enzymes immobilized on chromatography paper for ethanol vapor detection. *Sensors*, 17(281), 2017.

[67] M. Phillips, V. Basa-Dalay, J. Blais, G. Bothamley, A. Chaturvedi, K. D. Modi, M. Pandya, M. P. Natividad, U. Patel, N. N. Ramraje, P. Schmitt, and Z. F. Udwadia. Point-of-care breath test for biomarkers of active pulmonary tuberculosis. *Tuberculosis*, 92(4):314–320, 2012.

[68] D. W. Dockery. Health effects of particulate air pollution. *Annals of Epidemiology*, 19(4):257–263, 2009.

[69] F. J. Kelly and J. C. Fussell. Air pollution and public health: emerging hazards and improved understanding of risk. *Environmental Geochemistry and Health*, 37(4):631–649, 2015.

[70] A. L. Power, R. K. Tennant, R. T. Jones, Y. Tang, J. Du, A. T. Worsley, and J. Love. Monitoring impacts of urbanisation and industrialisation on air quality in the anthropocene using urban pond sediments. *Frontiers in Earth Science*, 6:131, 2018.

[71] C. A. Mgbemene, C. C. Nnaji, and C. Nwozor. Industrialization and its backlash: Focus on climate change and its consequences. *Journal of Environmental Science and Technology*, 9(4):301–316, 2016.

[72] H. S. Rumana, R. C. Sharma, V. Beniwal, and A. K. Sharma. A retrospective approach to assess human health risks associated with growing air pollution in urbanized area of Thar Desert, Western Rajasthan, India. *Journal of Environmental Health Science and Engineering*, 12(23), 2014.

[73] S. S. Yamamoto, R. Phalkey, and A. A. Malik. A systematic review of air pollution as a risk factor for cardiovascular disease in South Asia: Limited evidence from India and Pakistan. *International Journal of Hygiene and Environmental Health*, 217(2-3):133–144, 2014.

[74] W. Zhang, C. N. Qian, and Y. X. Zeng. Air pollution: A smoking gun for cancer. *Chinese Journal of Cancer*, 33(4):173–175, 2014.

[75] N. Brucker, M. F. Charão, A. M. Moro, P. Ferrari, G. Bubols, E. Sauer, R. Fracasso, J. Durgante, F. V. Thiesen, M. M. Duarte, A. Gioda, I. Castro, P. H. Saldiva, and S. C. Garcia. Atherosclerotic process in taxi drivers occupationally exposed to air pollution and co-morbidities. *Environmental Research*, 131:131–138, 2014.

[76] A. Biggeri, P. Bellini, and B. Terracini. Meta-analysis of the italian studies on short-term effects of air pollution–MISA 1996-2002. *Epidemiologia e prevenzione*, 28:4–100, 2004.

[77] K. Vermaelen and G. Brusselle. Exposing a deadly alliance: novel insights into the biological links between COPD and lung cancer. *Pulmonary Pharmacology and Therapeutics*, 26(5):544–554, 2013.

[78] G. M. Lovett, T. H. Tear, D. C. Evers, S. E. Findlay, B. J. Cosby, J. K. Dunscomb, C. T. Driscoll, and K. C. Weathers. Effects of air pollution on ecosystems and biological diversity in the eastern United States. *Annals of the New York Academy of Sciences*, 1162(1):99–135, 2009.

[79] R.-H. Shie and C.-C. Chan. Tracking hazardous air pollutants from a refinery fire by applying on-line and off-line air monitoring and back trajectory modeling. *Journal of Hazardous Materials*, 261(15):72–82, 2013.

[80] R. B. Jackson, A. Down, N. G. Phillips, R. C. Ackley, C. W. Cook, D. L. Plata, and K. Zhao. Natural gas pipeline leaks across Washington, DC. *Environmental Science and Technology*, 48:2051–2058, 2014.

[81] L. E. Mitchell, E. T. Crosman, A. A. Jacques, B. Fasoli, L. Leclair-Marzolf, J. Horel, D. R. Bowling, J. R. Ehleringer, and J. C. Lina. Monitoring of greenhouse gases and pollutants across an urban area using a light-rail public transit platform. *Atmospheric Environment*, 187:9–23, 2018.

[82] F. Perera. Pollution from fossil-fuel combustion is the leading environmental threat to global pediatric health and equity: Solutions exist. *International Journal of Environmental Research and Public Health*, 15(1):16, 2018.

[83] D. Huisingh, Z. Zhang, J. C. Moore, Q. Qiao, and Q. Li. Recent advances in carbon emissions reduction: policies, technologies, monitoring, assessment and modeling. *Journal of Cleaner Production*, 103:1–12, 2015.

[84] I. Andrić, N. Jamali-Zghal, M. Santarelli, B. Lacarriére, and O. Le Corre. Environmental performance assessment of retrofitting existing coal fired power plants to co-firing with biomass: carbon footprint and emergy approach. *Journal of Cleaner Production*, 103:13–27, 2015.

[85] R. Khalilpour, K. Mumford, H. Zhai, A. Abbas, G. Stevens, and E. S. Rubin. Membrane-based carbon capture from flue gas: a review. *Journal of Cleaner Production*, 103:286–300, 2015.

[86] S. H. Schneider. The greenhouse effect: Science and policy. *Science*, 243(4892):771–781, 1989.

[87] J. T. Hardy. *Climate Change: Causes, Effects, and Solutions*. John Wiley & Sons, Chichester, England, 2003.

[88] M. D. H. Jones and A. Henderson-Sellers. History of the greenhouse effect. *Progress in Physical Geography: Earth and Environment*, 14(1):1–18, 1990.

[89] D. W. Kweku, O. Bismark, A. Maxwell, K. A. Desmond, K. B. Danso, E. A. Oti-Mensah, A. T. Quachie, and B. B. Adormaa. Greenhouse effect: Greenhouse gases and their impact on global warming. *Journal of Scientific Research and Reports*, 17(6):1–9, 2017.

[90] T. R. Anderson, E. Hawkins, and P. D. Jones. CO_2, the greenhouse effect and global warming: from the pioneering work of arrhenius and callendar to today's earth system models. *Endeavour*, 40(3):178–187, 2016.

[91] G. Luber and N. Prudent. Climate change and human health. *Transactions of the American Clinical and Climatological Association*, 120:113–117, 2009.

[92] G. Luber and M. McGeehin. Climate change and extreme heat events. *American Journal of Preventative Medicine*, 35(5):429–435, 2008.

[93] B. Bronselaer, M. Winton, S. M. Griffies, W. J. Hurlin, K. B. Rodgers, O. V. Sergienko, R. J. Stouffer, and J. L. Russell. Change in future climate due to antarctic meltwater. *Nature*, 564:53–58, 2018.

[94] C. Mora, D. Spirandelli, E. C. Franklin, J. Lynham, M. B. Kantar, W. Miles, C. Z. Smith, K. Freel, J. Moy, L. V. Louis, E. W. Barba, K. Bettinger, A. G. Frazier, J. F. Colburn IX, N. Hanasaki, E. Hawkins, Y. Hirabayashi, W. Knorr, C. M. Little, K. Emanuel, J. Sheffield, J. A. Patz, and C. L. Hunter. Broad threat to humanity from cumulative climate hazards intensified by greenhouse gas emissions. *Nature Climate Change*, 8:1062–1071, 2018.

[95] J. Hjort, O. Karjalainen, J. Aalto, S. Westermann, V. E. Romanovsky, F. E. Nelson, B. Etzelmüller, and M. Luoto. Degrading permafrost puts arctic infrastructure at risk by mid-century. *Nature Communications*, 9:1–9, 2018.

[96] B. K. Biskaborn, S. L. Smith, J. Noetzli, et al. Permafrost is warming at a global scale. *Nature Communications*, 10:1–11, 2019.

[97] C. B. Fields et al., editors. *IPCC Climate Change 2014: Impacts, Adaptation, and Vulnerability*. Cambridge Univ. Press, 2014.

[98] K. E. Trenberth. Framing the way to relate climate extremes to climate change. *Climatic Change*, 115:283–290, 2012.

[99] J. Liang. *Chemical Modeling for Air Resources: Fundamentals, Applications, and Corroborative Analysis*. Elsevier, 2013.

[100] S. Solomon, G. K. Plattner, R. Knutti, and P. Friedlingstein. Irreversible climate change due to carbon dioxide emissions. *Proceedings of the National Academy of Sciences of the United States of America*, 106(6):1704–1709, 2009.

[101] B. Ioan and L. Amelitta. Carbon dioxide significant emission sources and decreasing solutions. *Procedia - Social and Behavioral Sciences*, 180:1122–1128, 2015.

[102] C. Le Quéré, R. M. Andrew, P. Friedlingstein, et al. Global carbon budget 2018. *Earth System Science Data*, 10(4):2141–2194, 2018.

[103] D. K. Benbi. Greenhouse gas emissions from agricultural soils: Sources and mitigation potential. *Journal of Crop Improvement*, 27(6):752–772, 2013.

[104] E. Bakker and Y. Qin. Electrochemical sensors. *Analytical Chemistry*, 78(12):3965–3984, 2006.

[105] I. Coddington, N. Newbury, and W. Swann. Dual-comb spectroscopy. *Optica*, 3(4):414–426, 2016.

[106] G. Berden R. Peeters and G. Meijer. Cavity ring-down spectroscopy: Experimental schemes and applications. *International Reviews in Physical Chemistry*, 19(4):565–607, 2010.

[107] N. Picqué and T. W. Hänsch. Frequency comb spectroscopy. *Nature Photonics*, 13:146–157, 2019.

[108] D. Ficai and A. M. Grumezescu, editors. *Nanostructures for Novel Therapy: Synthesis, Characterization and Applications*. Elsevier, 2017.

[109] S. Li, Y. Ge, S. A. Piletsky, and J. Lunec, editors. *Molecularly Imprinted Sensors*. Elsevier, 2012.

[110] E. Bakker and M. Telting-Diaz. Electrochemical sensors. *Analytical Chemistry*, 74(12):2781–2800, 2002.

[111] A. Mugweru, B. L. Clark, and M. V. Pishko. Electrochemical sensor array for glucose monitoring fabricated by rapid immobilization of active glucose oxidase within photochemically polymerized hydrogels. *Journal of diabetes science and technology*, 1(3):366–371, 2007.

[112] D. Bruen, C. Delaney, L. Florea, and D. Diamond. Glucose sensing for diabetes monitoring: Recent developments. *Sensors*, 17(8):1866, 2017.

[113] D. Grieshaber, R. MacKenzie, J. Vörös, and E. Reimhult. Electrochemical biosensors - sensor principles and architectures. *Sensors*, 8(3):1400–1458, 2008.

[114] B. J. Privett, J. H. Shin, and M. H. Schoenfisch. Electrochemical sensors. *Analytical Chemistry*, 80(12):4499–4517, 2008.

[115] C. C. Austin, B. Roberge, and N. Goyer. Cross-sensitivities of electrochemical detectors used to monitor worker exposures to airborne contaminants: False positive responses in the absence of target analytes. *Journal of Environmental Monitoring*, 8(1):161–166, 2005.

[116] M. I. Mead, O. A. M. Popoola, G. B. Stewart, P. Landshoff, M. Calleja, M. Hayes, J. J. Baldovi, M. W. McLeod, T. F. Hodgson, J. Dicks, A. Lewis, J. Cohen, R. Baron, J. R. Saffell, and R. L. Jones. The use of electrochemical sensors for monitoring urban air quality in low-cost, high-density networks. *Atmospheric Environment*, 70:186–203, 2013.

[117] H. S. Hong, J. W. Kim, S. J. Jung, and C. O. Park. Suppression of NO and SO_2 cross-sensitivity in electrochemical CO_2 sensors with filter layers. *Sensors and Actuators B: Chemical*, 113(7):71–79, 2006.

[118] R. L. Grob and E. F. Barry, editors. *Modern Practice of Gas Chromatography*. John Wiley & Sons, 4th edition, 2004.

[119] A. B. Littlewood. *Gas Chromatography: Principles, Techniques, and Applications*. Elsevier, 2nd edition, 2013.

[120] G. Gauglitz and T. Vo-Dinh, editors. *Handbook of Spectroscopy*. Wiley-VCH Verlag GmbH & Co, Weinheim, 2003.

[121] E. de Hoffmann and V. Stroobant. *Mass Spectrometry: Prinicples and Applications*. Wiley, England, 3rd edition, 2007.

[122] N. Forsgard, M. Salehpour, and G. Possnert. Accelerator mass spectrometry in the attomolar concentration range for ^{14}C-labelled biologically active compounds in complex matrices. *Journal of Analytical Atomic Spectrometry*, 25:74–78, 2009.

[123] G. Nikolic, editor. *Fourier Transforms - New Analytical Approaches and FTIR Strategies*. InTech, 2011.

[124] F. L. Pedrotti, S. J., L. S. Pedrotti, and L. M. Pedrotti. *Introduction To Optics*. Pearson Prentice Hall, Upper Saddle River, New Jersey, USA, 3rd edition, 2007.

[125] B. C. Smith. *Fundamentals of Fourier Transform Infrared Spectroscopy*. CRC Press, United States of America, 1996.

[126] M. D. Wheeler, S. M. Newman, A. J. Orr-Ewing, and M. N. R. Ashfold. Cavity ring-down spectroscopy. *Journal of the Chemical Society, Faraday Transactions*, 94(3):337–351, 1998.

[127] P. Zalicki and R. N. Zare. Cavity ring-down spectroscopy for quantitative absorption measurements. *The Journal of Chemical Physics*, 102(7):2708–2717, 1994.

[128] D. Romanini, A. A. Kachanov, N. Sadeghi, and F. Stoeckel. Cavity ringdown spectroscopy: broadband absolute absorption measurements. *Chemical Physics Letters*, 270(5-6):546–550, 1997.

[129] G-W. Truong, E. M. Waxman, K. C. Cossel, E. Baumann, A. Klose, F. R. Giorgetta, W. C. Swann, N. R. Newbury, and I. Coddington. Accurate frequency referencing for fieldable dual-comb spectroscopy. *Optics Express*, 24(26):30495–30504, 2016.

[130] B. Bernhardt, A. Ozawa, P. Jacquet, M. Jacquey, Y. Kobayashi, T. Udem, R. Holzwarth, G. Guelachvili, T. W. Hänsch, and N. Picqué. Cavity-enhanced dual-comb spectroscopy. *Nature Photonics*, 4:55–57, 2009.

[131] T. Ideguchi, A. Poissonand G. Guelachvili, N. Picqué, and T. W. Hänsch. Adaptive real-time dual-comb spectroscopy. *Nature Communications*, 5:3375, 2014.

[132] G. B. Rieker, F. R. Giorgetta, W. C. Swann, J. Kofler, A. M. Zolot, L. C. Sinclair, E. Baumann, C. Cromer, G. Petron, C. Sweeney, P. P. Tans, I. Coddington, and N. R. Newbury. Frequency-comb-based remote sensing of greenhouse gases over kilometer air paths. *Optica*, 1(5):290–298, 2014.

[133] K. C. Cossel, E. M. Waxman, F. R. Giorgetta, M. Cermak, I. R. Coddington, D. Hesselius, S. Ruben, W. C. Swann, G-W. Truong, G. B. Rieker, and N. R. Newbury. Open-path dual-comb spectroscopy to an airborne retroreflector. *Optica*, 4(7):724–728, 2017.

[134] A. M. Zolot, F. R. Giorgetta, E. Baumann, J. W. Nicholson, W. C. Swann, I. Coddington, and N. R. Newbury. Direct-comb molecular spectroscopy with accurate, resolved comb teeth over 43 THz. *Optics Letters*, 37(4):638–640, 2012.

[135] L. Nugent-Glandorf, F. R. Giorgetta, and S. A. Diddams. Open-air, broad-bandwidth trace gas sensing with a mid-infrared optical frequency combs. *Applied Physics B: Lasers and Optics*, 119(2):327–338, 2015.

[136] F. R. Giorgetta, G. B. Rieker, E. Baumann, W. C. Swann, L. C. Sinclair, J. Kofler, I. Coddington, and N. R. Newbury. Broadband Phase Spectroscopy over Turbulent Air Paths. *Physical Review Letters*, 115(10):103901–103905, 2015.

[137] P. J. Schroeder, R. J. Wright, S. Coburn, B. Sodergren, K. C. Cossel, S. Droste, G.W. Truong, E. Baumann, F. R. Giorgetta, I. Coddington, N. R. Newbury, and G. B. Rieker. Dual frequency comb laser absorption spectroscopy in a 16 MW gas turbine exhaust. *Proceedings of the Combustion Institute*, 36:4565–4573, 2017.

[138] A. M. Zolot, F. R. Giorgetta, E. Baumann, W. C. Swann, I. Coddington, and N. R. Newbury. Broad-band frequency references in the near-infrared: Accurate dual comb spectroscopy of methane and acetylene. *Journal of Quantitative Spectroscopy and Radiative Transfer*, 118:26–39, 2013.

[139] F. Adler, M. J. Thorpe, C. K. Cossel, and J. Ye. Cavity-enhanced direct frequency comb spectroscopy: technology and applications. *Annual Review of Analytical Chemistry*, 3:175–205, 2010.

[140] S. Schiller. Spectrometry with frequency combs. *Optics Letters*, 27(9):766–768, 2002.

[141] I. Coddington, W. C. Swann, and N. R. Newbury. Coherent multiheterodyne spectroscopy using stabilized optical frequency combs. *Physical Review Letters*, 101(4):049901, 2008.

[142] A. L. Gaeta, M. Lipson, and T. J. Kippenberg. Photonic-chip-based frequency combs. *Nature Photonics*, 13:158–169, 2019.

[143] M. J. Thorpe and J. Ye. Cavity-enhanced direct frequency comb spectroscopy. *Applied Physics B: Lasers and Optics*, 91(3-4):397–414, 2008.

[144] L. Nugent-Glandorf, T. Neely, F. Adler, A. J. Fleisher, K. C. Cossel, B. Bjork, T. Dinneen, J. Ye, and S. A. Diddams. Mid-infrared virtually imaged phased array spectrometer for rapid and broadband trace gas detection. *Optics Letters*, 37(15):3285–3287, 2012.

[145] A. Foltynowicz, P. Masłowski, A. J. Fleisher, B. J. Bjork, and J. Ye. Cavity-enhanced optical frequency comb spectroscopy in the mid-infrared application to trace detection of hydrogen peroxide. *Applied Physics B: Lasers and Optics*, 110(2):163–175, 2013.

[146] C. Gohle, B. Stein, A. Schliesser, T. Udem, and T. W. Hänsch. Frequency comb vernier spectroscopy for broadband, high-resolution, high-sensitivity absorption and dispersion spectra. *Physical Review Letters*, 99(26):263902, 2007.

[147] R. Grilli, G. Méjean, C. Abd Alrahman, I. Ventrillard, S. Kassi, and D. Romanini. Cavity-enhanced multiplexed comb spectroscopy down to the photon shot noise. *Physical Review A*, 85(5):051804, 2012.

[148] K. V. Reddy. *Symmetry And Spectroscopy Of Molecules*. New Age International, Daryaganj, New Delhi, 1998.

[149] D. N. Sathyanarayana. *Vibrational Spectroscopy: Theory and Applications*. New Age International, Daryaganj, New Delhi, 2015.

[150] C. J. H. Schutte, J. E. Bertie, P. R. Bunker, J. T. Hougen, I. M. Mills, J. K. G. Watson, and B. P. Winnewisser. Notation and conventions in molecular spectroscopy: Part 1. general spectroscopic notation. *Pure and Applied Chemistry*, 69(8):1633–1639, 1997.

[151] J. M. Hollas. *Modern Spectroscopy*. Wiley, Chichester, England, 4th edition, 2004.

[152] R. Kakkar. *Atomic and Molecular Spectroscopy: Basic Concepts and Applications*. Cambridge University Press, Daryaganj, Delhi, India, 2015.

[153] G. Herzberg. *Molecular Spectra and Molecular Structure: Infrared and Raman of Polyatomic Molecules*, volume 2. Prentice-Hall, 1990.

[154] R K. Hanson, R. M. Spearrin, and C. S. Goldenstein. *Spectroscopy and Optical Diagnostics for Gases*. Springer, 2015.

[155] H. Haken and H. C. Wolf. *Molecular Physics and Elements of Quantum Chemistry*. Springer, Stuttgart, Germany, 2nd edition, 2004.

[156] R. S. Mulliken. Report on notation for the spectra of polyatomic molecules. *Journal of Chemical Physics*, 23(11):1997–2011, 1955.

[157] P. F. Bernath. *Spectra of Atoms and Molecules*. Oxford University Press, New York, 2nd edition, 2005.

[158] J. M. Hollas. *High Resolution Spectroscopy*. Butterworth-Heinemann, London, England, 2013.

[159] D. Williams. *Molecular Physics: Methods of Experimental Physics*. Academic Press, New York, New York, 2013.

[160] C. Di Lauro. *Rotational Structure in Molecular Infrared Spectra*. Elsevier, 2013.

[161] H. K. Moudgil. *Textbook of Physical Chemistry*. PHI Learning Pvt. Ltd, New Delhi, 2010.

[162] W. J. Witteman. *The CO_2 Laser*, volume 53 of *Springer Series in Optical Sciences*. Springer-Verlag Berlin Heidelberg GmbH, 1987.

[163] H. J. Eichler, J. Eichler, and O. Lux. *Lasers: Basics, Advances and Applications*. Springer, 2018.

[164] S. T. Thornton and A. Rex. *Modern Physics For Scientists and Engineers*. Brooks/Cole, Boston, Massachusetts, 4th edition, 2013.

[165] J. E. Wollrab. *Rotational Spectra and Molecular Structure*. Academic Press, New York, New York, 2016.

[166] P. Atkins and R. Friedman. *Molecular Quantum Mechanics*. Oxford University Press, New York, 4th edition, 2005.

[167] A. Beiser. *Concepts of Modern Physics*. McGraw-Hill, New York, New York, 6th edition, 2003.

[168] F. Gatti, B. Lasorne, H. D. Meyer, and A. Nauts. *Applications of Quantum Dynamics in Chemistry*. Springer, 2017.

[169] R. A. Newing. Uncertainty principle and the zero-point energy of the harmonic oscillator. *Nature*, 136:395, 1935.

[170] G. Arfken. *Special Functions*. Cambridge University Press, Orlando, Florida, 3rd edition, 1985.

[171] M. Diem. *Modern Vibrational Spectroscopy and Micro-Spectroscopy: Theory, Instrumentation and Biomedical Applications*. John Wiley & Sons, 2015.

[172] J. W. Ellis. The molecular spectrum of carbon dioxide. *Nature*, 118(2959):82–83, 1926.

[173] S. Califano. *Vibrational States*. Wiley, 1976.

[174] T. G. Charles. *Foundations of Wave Phenomena*. Open Textbooks, Utah, 2016.

[175] W. Greiner. *Quantum Mechanics: An Introduction*. Springer, Berlin, 4th edition, 2000.

[176] P. M. Morse. Diatomic molecules according to the wave mechanics. II. Vibrational levels. *Phys. Rev.*, 34(1):57–64, 1929.

[177] S. H. Dong. *Factorization Method in Quantum Mechanics*. Springer, Dordrecht, The Netherlands, 2007.

[178] L. D. Landau and E. M. Lifshitz. *Mechanics*. Pergamon Press, Oxford; New York, 1976.

[179] L. S. Rothman, A. Barbe, D. C. Benner, L. R. Brown, C. Camy-Peyret, M. R. Carleer, K. Chance, C. Clerbaux, V. Dana, V. M. Devi, A. Fayt, J. -M. Flaud, R. R. Gamache, A. Goldman, D. Jacquemart, K. W. Jucks, W. J Lafferty, J. -Y. Mandin, S. T. Massie, V. Nemtchinov, D. A. Newham, A Perrin, C. P. Rinsland, J. Schroeder, K. M. Smith, M. A. H. Smith, K. Tang, R. A. Toth, J. Vander Auwera, P. Varanasi, and K. Yoshino. The HITRAN molecular spectroscopic database: edition of 2000 including updates through 2001. *Journal of Quantitative Spectroscopy and Radiative Transfer*, 82:5–44, 2003.

[180] L. S. Rothman and L. D. G. Young. Infrared energy levels and intensities of carbon dioxide -II. *Journal of Quantitative Spectroscopy and Radiative Transfer*, 25:505–524, 1981.

[181] D. Jacquemart, J. -Y. Mandin, V. Dana, C. Claveau, J. Vander Auwera, M. Herman, L. S. Rothman, L. Régalia-Jarlot, and A. Barbe. The IR acetylene spectrum in HITRAN: update and new results. *Journal of Quantitative Spectroscopy and Radiative Transfer*, 82:363–382, 2003.

[182] E. R. Cohen, T. Cvitaš, J. G. Frey, B. Holmström, K. Kuchitsu, R. Marquardt, I. Mills, F. Pavese, M. Quack, J. Stohner, H. L. Strauss, M. Takami, and A. J. Thor. *Quantities, Units and Symbols in Physical Chemistry*. The Royal Society of Chemistry, Cambridge, UK, 3rd edition, 2007.

[183] R. N. Compton and M. A. Duncan. *Laser Experiments for Chemistry and Physics*. Oxford University Press, Oxford, United Kingdom, 2016.

[184] D. W. Ball. *Physical Chemistry*. Cengage Learning, Stamford, Connecticut, 2nd edition, 2014.

[185] J. M. Hollas. *Basic Atomic and Molecular Spectroscopy*. Royal Society of Chemistry, Cambridge, 2002.

[186] Y. Ozaki, W. F. McClure, and A. A. Christy, editors. *Near-Infrared Spectroscopy in Food Science and Technology*. John Wiley & Sons, United States of America, 2006.

[187] K. A. Mohamed. *High Resolution Fourier Transform Spectroscopy of Linear Molecules*. Nova Publishers, 2005.

[188] B. P. Straughan and S. Walker. *Spectroscopy*, volume 2. Chapman & Hall, 1976.

[189] M. L. Myrick, P. E. Colavita, A. E. Greer, B. Long, and D. Andreatta. Use of molecular symmetry to describe pauli principle effects on the vibration-rotation spectroscopy of CO_2 (g). *Journal of Chemical Education*, 81(3):379–382, 2004.

[190] K. S. Krane. *Introductory Nuclear Physics*. John Wiley & Sons, United States of America, 1988.

[191] P. C. H. Mitchell, S. F. PArker, A. J. Ramirez-Cuesta, and J. Tomkinson. *Vibrational Spectroscopy with Neutrons: With Applications in Chemistry, Biology, Materials Science and Catalysis*. World Scientific, 2005.

[192] I. S. Hughes. *Elementary Particles*. Cambridge Univeristy Press, 3rd edition, 1972.

[193] R. Myers. *The Basics of Chemistry*. Greenwood Publishing Group, 2003.

[194] M. N. Avadhanulu and P. G. Kshirsagar. *A Textbook of Engineering Physics*. S. Chand & Company, 1992.

[195] X. Huang and Y. L. Yung. A Common Misunderstanding About the Voigt Line Profile. *Journal of the Atmospheric Sciences*, 61:1630–1632, 2004.

[196] V. Parthasarathi, S. Ganapathy, and C. A. McDowell. The evaluation and characterization of Voigt lineshape. *Journal of Molecular Structure.*, 64:29–38, 1980.

[197] K. S. Seshadri and R. N. Jones. The shapes and intensities of infrared absorption bands - a review. *Spectrochimica Acta*, 19(6):1013–1085, 1963.

[198] G. K. Wertheim, M. A. Butler, K. W. West, and D. N. E. Buchanan. Determination of the Gaussian and Lorentzian content of experimental line shapes. *Review of Scientific Instruments*, 45(11):1369–1371, 1974.

[199] J. Humlíček. Optimized computation of the Voigt and complex probability functions. *Journal of Quantitative Spectroscopy and Radiative Transfer*, 27(4):437–444, 1982.

[200] S. M. Abrarov and B. M. Quine. Accurate approximations for the complex error function with small imaginary argument. *Journal of Mathematics Research*, 7(1):44–53, 2015.

[201] J. J. Olivero and R. L. Longbottom. Emperical Fits To The Voigt Line Width: A Brief Review. *Journal of Quantitative Spectroscopy and Radiative Transfer*, 17:233–236, 1977.

[202] A. E. Seigman. *Lasers*. University Science Books, 1986.

[203] C. J. Foot. *Atomic physics*, volume 7. Oxford University Press, 2005.

[204] M. Bass, editor. *Handbook of Optics: Fundamentals, Techniques, & Design*, volume 1. McGraw-Hill, United States Of America, 1995.

[205] R. W. Parsons., V. I. Metchnik, and R. J. Dyne. The collision broadening of spectral lines. *Australian Journal of Physics*, 21:13, 1968.

[206] G. W. Ewing, editor. *Analytical Instrumentation Handbook*. Marcel Dekker, New York, New York, 2nd edition, 1997.

[207] R. A. Nyquist. *Interpreting Infrared, Raman, and Nuclear Magnetic Resonance Spectra*. Academic Press, United States of America, 2001.

[208] H. M. Foley. The pressure broademna of spectral lines. *Physical Review*, 69(11-12):616–628, 1946.

[209] W. Demtröder. *Laser Spectroscopy: Basic Concepts and Instrumentation*. Springer, 3rd edition, 2003.

[210] H. Haken and H. C. Wolf. *The Physics of Atoms and Quanta*. Springer-Verlag London, 1996.

[211] G. Herzburg. *Molecular Spectra and Molecular Structure: Spectra of Diatomic Molecules*, volume 1. D. Van Nostrand Company; Prentice-Hall, Princeton, New Jersey, 2nd edition, 1950.

[212] G. W. F. Drake. *Spinger Handbook of Atomic, Molecular, and Optical Physics*. Springer, Berlin, 2nd edition, 2006.

[213] L. S. Rothman, C. P. Rinsland, A. Goldman, S. T. Massie, D. P. Edwards, J.-M. Flaud, A. Perrin, C. Camy-Peyret, V. Dana, J.-Y. Mandinand J. Schroeder, A. McCann, R. R. Gamache, R. B. Wattson, K. Yoshino, K. V. Chance, K. W. Jucks, L. R. Brown, V. Nemtchinov, and P. Varanasi. The HITRAN Molecular Spectroscopic Database and HAWKS (HITRAN Atmospheric Workstation): 1996 Edition. *Journal of Quantitative Spectroscopy and Radiative Transfer*, 60(5):665–710, 1998.

[214] P. De Biévre, N. E. Holden, and I. L. Barnes. Isotopic abundances and atomic weights of the elements. *Journal of Physical and Chemical Reference Data*, 13:809–891, 1984.

[215] F. F. Mazda, editor. *Electronics Engineer's Reference Book*. Butterworth & Co. Ltd, London, England, 6th edition, 1989.

[216] R. R. Gamache, R. L. Hawkins, and L. S. Rothman. Total internal partition sums in the temperature range 70-3000 K: Atmospheric linear molecules. *Journal of Molecular Spectroscopy*, 142(2):205–219, 1990.

[217] D. L. Woolard, W. R. Loerop, and M. S. Shur, editors. *Terahertz Sensing Technology: Emerging Scientific Applications & Novel Device Concepts*, volume 2. World Scientific Publishing, Singapore, 2003.

[218] J. Tennyson, P. F. Bernath, A. Campargue, A. G. Csaszar, L. Daumont, R. R. Gamache, J. T. Hodges, D. Lisak, O. V. Naumenko, L. S. Rothman, H. Tran, N. F. Zobov, J. Buldyreva, C. D. Boone, M. D. De Vizia, L. Gianfrani, J.-M. Hartmann, R. McPheat, J. Murray, N. H. Ngo, O. L. Polyansky, and D. Weidmann. Recommended isolated-line profile for representing high-resolution spectroscopic transitions (IUPAC Technical Report). *Pure and Applied Chemistry*, 86:1931–1943, 2014.

[219] N. H. Ngo, D. Lisak, H. Tran, and J. M. Hartmann. An isolated line-shape model to go beyond the Voigt profile in spectroscopic databases and radiative transfer codes. *Journal of Quantitative Spectroscopy and Radiative Transfer*, 129:89–100, 2013.

[220] H. I. Schiff, G. I. Mackay, and J. Bechara. The use of tunable diode laser absorption spectroscopy for atmospheric measurements. *Research on Chemical Intermediates*, 20(3-5):525–556, 1994.

[221] B. E. A. Saleh and M. C. Teich. *Fundamentals of photonics*, volume 22. Wiley New York, 1991.

[222] O. Svelto. *Principles of Lasers*. Plenum Press, New York, 4th edition, 1998.

[223] J. Ye and S. T. Cundiff. *Femtosecond Optical Frequency Comb: Principle, Operation, and Applications*. Springer US, 2005.

[224] J. C. Diels and W. Rudolph. *Ultrashort Laser Pulse Phenomena: Fundamentals, Techniques, and Applications on a Femtosecond Time Scale*. Academic Press, San Diego, 1996.

[225] T. W Hänch. Nobel lecture: Passion for precision. *Reviews of Modern Physics*, 78:1297, 2006.

[226] J. L. Hall. Nobel lecture: Defining and measuring optical frequencies. *Reviews of Modern Physics*, 78(1279), 2006.

[227] N. Hodgson and H. Weber. *Optical Resonators: Fundamentals, Advanced Concepts and Applications*. Springer-Verlag London, 1997.

[228] J. Liu. *Principles of Photonics*. Cambridge University Press, 2016.

[229] I. V. Hertel and C. P. Schulz. *Atoms, Molecules and Optical Physics 2: Molecules and Photons - Spectroscopy and Collisions*. Springer, 2014.

[230] N. Hodgson and H. Weber. *Laser Resonators and Beam Propagation: Fundamentals, Advanced Concepts and Applications*. Springer, 2nd edition, 2005.

[231] D. Kuizenga and A. Siegman. FM and AM mode locking of the homogeneous laser - Part I: Theory. *IEEE Journal of Quantum Electronics*, 6(11):694 – 708, 1970.

[232] R. Paschotta. *Field Guide to Laser Pulse Generation*. SPIE Press, Bellingham, WA, 2008.

[233] M. E. Fermann, M. J. Andrejco, Y. Silberberg, and M. L. Stock. Passive mode locking by using nonlinear polarization evolution in a polarization-maintaining erbium-doped fiber. *Optics Letters*, 18(11):894–896, 1993.

[234] M. Hofer, M. H. Ober, F. Haberl, and M. E. Fermann. Characterization of ultrashort pulse formation in passively mode-locked fiber lasers. *IEEE Journal of Quantum Electronics*, 28(3):720 – 728, 1992.

[235] Patent: Generation of stabilised, ultra-short light pulses and the use of thereof for synthesising optical frequencies. number EP 1161782 B1, 2002.

[236] F. Doutre, D. Pagnoux, V. Couderc, A. Tonello, B. Vergne, and A. Jalocha. Large temporal narrowing of subnanosecond pulses in a low-birefringence optical fiber. *Optics Letters*, 33(16):1789–1791, 2008.

[237] V. J. Matsas, T. P. Newson, D. J. Richardson, and D. N. Payne. Selfstarting passively mode-locked fibre ring soliton laser exploiting nonlinear polarisation rotation. *Electronics Letters*, 28(15):1391 – 1393, 1992.

[238] K. Tamura, H. A. Haus, and E. P. Ippen. Self-starting additive pulse mode-locked erbium fibre ring laser. *Electronics Letters*, 28(24):2226 – 2228, 1992.

[239] F. W. Helbing, G. Steinmeyer, and U. Keller. Carrier-envelope offset phase-locking with attosecond timing jitter. *IEEE Journal of Selected Topics in Quantum Electronics*, 9(4):1030–1040, 2003.

[240] T. Brabec and F. Krausz. Intense few-cycle laser fields: Frontiers of nonlinear optics. *Reviews of Modern Physics*, 72(2):545–591, 2000.

[241] R. N. Bracewell. *The Fourier transform and its applications*. McGraw-Hill, 1986.

[242] R. Holzwarth, T. Udem, T. W. Hänsch, J. C. Knight, W. J. Wadsworth, and P. St. J. Russell. Optical frequency synthesizer for precision spectroscopy. *Physical Review Letters*, 85(11):2264–2267, 2000.

[243] R. Ell, U. Morgner, F. X. Kärtner, J. G. Fujimoto, E. P. Ippen, V. Scheuer, G. Angelow, T. Tschudi, M. J. Lederer, A. Boiko, and B. Luther-Davies. Generation of 5-fs pulses and octave-spanning spectra directly from a Ti:sapphire laser. *Optics Letters*, 26(6):373–375, 2001.

[244] D. J. Jones, S. A. Diddams, J. K. Ranka, A. Stentz, R. S. Windeler, J. L. Hall, and S. T. Cundiff. Carrier-envelope phase control of femtosecond mode-locked lasers and direct optical frequency synthesis. *Science*, 288(5466):635–639, 2000.

[245] S. A. Diddams, D. J. Jones, J. Ye, S. T. Cundiff, J. L. Hall, J. K. Ranka, R. S. Windeler, R. Holzwarth, T. Udem, and T. W. Hänsch. Direct link between microwave and optical frequencies with a 300 THz femtosecond laser comb. *Physical Review Letters*, 84(22):5102–5105, 2000.

[246] A. Bartels, C. W. Oates, L. Hollberg, and S. A. Diddams. Stabilization of femtosecond laser frequency combs with subhertz residual linewidths. *Optics Letters*, 29(10):1081–1083, 2004.

[247] S. V. Smirnov, J. D. Ania-Castanon, T. J. Ellingham, S. M. Kobtsev, S. Kukarin, and S. K. Turitsyn. Optical spectral broadening and supercontinuum generation in telecom applications. *Optical Fiber Technology*, 12:122–147, 2006.

[248] J. Takayanagi, N. Nishizawa, H. Nagai, M. Yoshid, and T. Goto. Generation of high-power femtosecond pulse and octave-spanning ultrabroad supercontinuum using all-fiber system. *IEEE Photonics Technology Letters*, 17(1):37–39, 2005.

[249] J. W. Nicholson, M. F. Yan, P. Wisk, J. Fleming, F. DiMarcello, E. Monberg, A. Yablon, C. Jørgensen, and T. Veng. All-fiber octave-spanning supercontinuum. *Optics Letters*, 28(8):643–645, 2003.

[250] J. M. Dudley and J. R. Taylor. Ten years of nonlinear optics in photonic crystal fibre. *Nature Photonics*, 3:85–90, 2009.

[251] E. G. Loewen and E. Popov. *Diffraction Gratings and Applications*. Marcel Dekker, New York, New York, 1997.

[252] W. Neumann. *Fundamentals of Dispersive Optical Spectroscopy Systems*. SPIE Press, Bellingham, Washington, 2014.

[253] C. Palmer and E. Loewen. *Diffraction Grating Handbook*. Thermo RGL, Rochester, New York, 2014.

[254] E. Hecht. *Optics*. Addison Wesley, 4th edition, 2002.

[255] M. Shirasaki. Large angular dispersion by a virtually imaged phased array and its applications to a wavelength demultiplexer. *Optics Letters*, 21:366–368, 1996.

[256] M. Shirasaki. Virtually imaged phased array. *FUJITSU Scientific and Technical Journal*, 35:113–125, 1999.

[257] S. Xiao and A. M. Weiner. 2-D wavelength demultiplexer with potential for $\geq$ 1000 channels in the C-band. *Optics Express*, 12(13):2895–2902, 2004.

[258] X. Hu, Q. Sun, J. Li, C. Li, Y. Liu, and J. Zhang. Spectral dispersion modeling of virtually imaged phased array by using angular spectrum of plane waves. *Optics Express*, 23(1):1–12, 2015.

[259] S. Xiao, A. M. Weiner, and C. Lin. A dispersion law for virtually imaged phased array spectral dispersers based on paraxial wave theory. *IEEE Journal of Quantum Electronics*, 40:420–426, 2004.

[260] S. A. Diddams, L. Hollberg, and V. Mbele. Molecular fingerprinting with the resolved modes of a femtosecond laser frequency comb. *Nature*, 445(8):627–630, 2007.

[261] Xenics, Leuven, Belgium. *Xeva-1.7-320*, 2008.

[262] I. S. McLean. *Electronic Imaging in Astronomy: Detectors and Instrumentation*. Springer-Praxis, Chichester, United Kingdom, 2nd edition, 2008.

[263] R. Poggiani. *Optical, Infrared and Radio Astronomy*. Springer International Publishing, Switzerland, 2017.

[264] S. B. Howell. *Handbook of CCD Astronomy*. Cambridge University Press, 2nd edition, 2006.

[265] C. D. Mackay. Charge-coupled devices in astronomy. *Annual Review of Astronomy and Astrophysics*, 24:255–283, 1986.

[266] M. Ferdjallah. *Introduction to Digital Systems: Modeling, Synthesis, and Simulation Using VHDL*. John Wiley & Sons, Hoboken, New Jersey, 2011.

[267] William F. van Altena, editor. *Astrometry for Astrophysics: Methods, Models, and Applications*. Cambridge University Press, New York, 2012.

[268] Xenics, Leuven, Belgium. *User Manual: Xeneth v2.5*, 2014.

[269] T. Steinmetz, T. Wilken, Araujo-Hauck C, R. Holzwarth, T. W. Hänsch, and T. Udem. FabryPérot filter cavities for wide-spaced frequency combs with large spectral bandwidth. *Applied Physics B*, 96(2-3):251–256, 2009.

[270] Layertec. Datasheet for article 103672 (plano-concave high reflectivity mirror). Technical report, 2011.

[271] J. S. Rollett and L. A. Higgs. Correction of spectroscopic line profiles for instrumental broadening by a fourier analysis method. *Proceedings of the Physical Society*, 79(87):87–93, 1962.

[272] E. N. Dulov and D. M. Khripunov. Instrumental broadening of spectral line profiles due to discrete representation of a continuous physical quantity. *Journal of Quantitative Spectroscopy and Radiative Transfer*, 109(10):1922–1930, 2008.

[273] M. J. Thorpe, D. Balslev-Clausen, M. S. Kirchner, and J. Ye. Cavity-enhanced optical frequency comb spectroscopy: application to human breath analysis. *Optics Express*, 16(4):2387–2397, 2008.

[274] G. Kowzan, K. F. Lee, M. Paradowska, M. Borkowski, P. Ablewski, S. Wójtewicz, K. Stec, D. Lisak, M. E. Fermann, R. S. Trawiński, and P. Masłowski. Self-referenced, accurate and sensitive optical frequency comb spectroscopy with a virtually imaged phased array spectrometer. *Optics Letters*, 41(5):974–977, 2016.

[275] I. Coddington, W. C. Swann, and N. R. Newbury. Coherent dual-comb spectroscopy at high signal-to-noise ratio. *Physical Review A*, 82(4):043817, 2010.

[276] L. S. Rothman, I. E. Gordon, Y. Babikov, A. Barbe, D. C. Benner, P. F. Bernath, M. Birk, L. Bizzocchi, V. Boudon, L. R. Brown, A. Campargue, K. Chance, E. A. Cohen, L. H. Coudert, V. M. Devi, B. J. Drouin, A. Faytl, J. M. Flaud, R. R. Gamache, J. J. Harrison, J. M. Hartmann, C. Hill, J. T. Hodges, D. Jacquemart, A. Jolly, J. Lamouroux, R. J. Le Roy, G. Li, D. A. Long, O. M. Lyulin, C. J. Mackie, S. T. Massie, S. Mikhailenko, H. S. P. Müller, O. V. Naumenko, A. V. Nikitin, J. Orphal, V. Perevalov, A. Perrin, E. R. Polovtseva, C. Richard, M. A. H. Smith, E. Starikova, K. Sung, S. Tashkun, J. Tennyson, G. C. Toon, Vl. G. Tyuterev, and G. Wagner. The HITRAN2012 molecular spectroscopic database. *Journal of Quantitative Spectroscopy & Radiative Transfer*, 130:4–50, 2013.

[277] R. J. Francey, C. E. Allison, D. M. Etheridge, C. M. Trudinger, I. G. Enting, M. Leunberger, R. L. Langenfelds, E. Michel, and L. P. Steele. A 1000-year high precision record of delta13C in atmospheric CO_2. *Tellus B*, 51(2):170–193, 1999.

[278] T. K. Bauska, D. Baggenstos, E. J. Brook, A. C. Mix, S. A. Marcott, V. V. Petrenko, H. Schaefer, J. P. Severinghaus, and J. E. Lee. Carbon isotopes characterize rapid changes in atmospheric carbon dioxide during the last deglaciation. *Proceedings of the National Academy of Sciences*, 113(13):3465–3470, 2016.

[279] D. Yakir and L. da S. L. Sternberg. The use of stable isotopes to study ecosystem gas exchange. *Acta Oecologia*, 123(3):297–311, 2000.

[280] W. G. Mook. 13C in atmospheric CO_2. *Netherlands Journal of Sea Research*, 20(2-3):211–223, 1986.

[281] A. C. Mix, N. G. Pisias, R. Zahn, W. Rugh, C. Lopez, and K. Nelson. Carbon 13 in pacific deep and intermediate waters, 0-370 ka: Implications for ocean circulation and pleistocene CO_2. *Paleoceanography*, 6(2):205–226, 1991.

[282] S. S. Assonov, C. A.M. Brenninkmeijer, T. J. Schuck, and P. Taylor. Analysis of 13C and 18O isotope data of CO_2 in CARIBIC aircraft samples as tracers of upper troposphere/lower stratosphere mixing and the global carbon cycle. *Atmospheric Chemistry and Physics*, 10(17):8575–8599, 2010.

[283] B. Galfond, D. Riemer, and P. Swart. Analysis of signal-to-noise ratio of δ 13 C-CO_2 measurements at carbon capture, utilization and storage injection sites. *International Journal of Greenhouse Gas Control*, 42:307–318, 2015.

[284] T. H. Yang, E. Heinzle, and C. Wittmann. Theoretical aspects of 13c metabolic flux analysis with sole quantification of carbon dioxide labeling. *Computational Biology and Chemistry*, 29(2):121–133, 2005.

[285] D. Dickinson, S. Bodé, and P. Boeckx. Measuring ^{13}C-enriched CO_2 in air with a cavity ring-down spectroscopy gas analyser: Evaluation and calibration. *Rapid Communications in Mass Spectrometry*, 31:1892–1902, 2017.

[286] L. Rutkowski, P. Masłowski, A. C. Johansson, A. Khodabakhsh, and A. Foltynowicz. Optical frequency comb Fourier transform spectroscopy with sub-nominal resolution and precision beyond the voigt profile. *Journal of Quantitative Spectroscopy and Radiative Transfer*, 204:63–73, 2018.

[287] N. Hoghooghi, R. J. Wright, A. S. Makowiecki, W. C. Swann, E. M. Waxman, I. Coddington, and G. B. Rieker. Broadband coherent cavity-enhanced dual-comb spectroscopy. *Optica*, 6(1):2019, 2019.

[288] I. E. Gordon, L. S. Rothman, C. Hill, R. V. Kochanov, Y. Tan, P. F. Bernath, M. Birk, V. Boudon, A. Campargue, K. V. Chance, B. J. Drouin, J. M. Flaud, R. R. Gamache, J. T. Hodges, D. Jacquemart, V. I. Perevalov, A. Perrin, K. P. Shine, M. A. H. Smith, J. Tennyson, G. C. Toon, H. Tran, V. G. Tyuterev, A. Barbe, A. G. Császár, V. M. Devi, T. Furtenbacher, J. J. Harrison, J. M. Hartmann, A. Jolly, T. J. Johnson, T. Karmanav, I. Kleiner, A. A. Kyuberis, J. Loos, O. M. Lyulin, S. T. Massie, S. N. Mikhailenko, N. Moazzen-Ahmadi, H. S. P. Müller, O. V. Naumenko, A. V. Nikitin, O. L. Polyansky, M. Rey, M. Rotger, S. W. Sharpe, K. Sung, E. Starikova, S. A. Tashkun, J. Vander Auwera, G. Wagner, J. Wilzewski, P. Wcisło, S. Yuh, and E. J. Zak. The HITRAN2016 molecular spectroscopic database. *Journal of Quantitative Spectroscopy and Radiative Transfer*, 203:3–69, 2017.

[289] F. Hase. Improved instrumental line shape monitoring for the ground-based, high-resolution FTIR spectrometers of the network for the detection of atmospheric composition change. *Atmospheric Measurement Techniques*, 5:603–610, 2012.

[290] Y. Shimizu, S. Okubo, A. Onae, K. M. T. Yamada, and H. Inaba. Molecular gas thermometry on acetylene using dual-comb spectroscopy: analysis of rotational energy distribution. *Applied Physics B: Lasers and Optics*, 124:71, 2018.

[291] O. Goetza, N. Selzner, H. Fruehauf, M. Fried, T. Gerlach, and B. Mullhaupt. ^{13}C-methacetin breath test as a quantitative liver function test in patients with chronic hepatitis C infection: continuous automatic molecular correlation spectroscopy compared to isotopic ratio mass spectrometry. *Alimentary Pharmacology and Therapeutics*, 26:305–311, 2007.

[292] F. J. Cereceda-Sánchez and J. Molina-Mula. Capnography as a tool to detect metabolic changes in patients cared for in the emergency setting. *Revista latino-americana de enfermagem*, 25:e2885, 2017.

[293] G. Tusman, M. Areta, C. Climente, R. Plit, F. Suarez-Sipmann, M. J. Rodríguez-Nieto, G. Peces-Barba, E. Turchetto, and S. H. Böhm. Effect of pulmonary perfusion on the slopes of single-breath test of CO_2. *Journal of Applied Physiology*, 99:650–655, 2005.

[294] J. Yang, B. Chen, J. Zhou, and Z. Lv. A low-power and portable biomedical device for respiratory monitoring with a stable power source. *Sensors*, 15:19618–19632, 2015.

[295] K. C. Cossel, E. M. Waxman, I. A. Finneran, G. A. Blake, J. Ye, and N. R. Newbury. Gas-phase broadband spectroscopy using active sources: progress, status, and applications. *Journal of the Optical Society of America B*, 34(1):104–129, 2017.

[296] G. Ycas, F. R. Giorgetta, K. C. Cossel, E. M. Waxman, E. Baumann, N. R. Newbury, and I. Coddington. Mid-infrared dual-comb spectroscopy of volatile organic compounds across long open-air paths. *Optica*, 6(2):165–168, 2019.

[297] A. S. Raja, A. S. Voloshin, H. Guo, S. E. Agafonova, J. Liu, A. S. Gorodnitskiy, M. Karpov, N. G. Pavlov, E. Lucas, R. R. Galiev, A. E. Shitikov, J. D. Jost, M. L. Gorodetsky, and T. J. Kippenberg. Electrically pumped photonic integrated soliton microcomb. *Nature Communications*, 10:680, 2019.

[298] P. Del'Haye, A. Schliesser, O. Arcizet, T. Wilken, R. Holzwarth, and T. J. Kippenberg. Optical frequency comb generation from a monolithic microresonator. *Nature*, 450(7173):1214–1217, 2007.

[299] T. J. Kippenberg, R. Holzwarth, and S. A. Diddams. Microresonator-based optical frequency combs. *ACS Biomaterials Science & Engineering*, 332(6029):555, 2011.

[300] V. Brasch, Q. F. Chen, S. Schiller, and T. J. Kippenberg. Radiation hardness of high-Q silicon nitride microresonators for space compatible integrated optics. *Optics Express*, 22(25):30786, 2014.

[301] G. C. Schatz and M. A. Ratner. *Quantum Mechanics in Chemistry*. Courier Corporation, 2012.

[302] J. N. Sharma and R. K. Gupta. *Mathematical Methods*. Krishna Prakashan Media, Meerut, India, 1990.

[303] K. B. Howell. *Principles of Fourier Analysis*. CRC Press, 2001.

[304] G. Dattoli, C. Chiccoli, S. Lorenzutta, G. Miano, and A. Torre. Theory of generalized Hermite polynomials. *Computers and Mathematics with Applications*, 28(4):71–83, 1994.

[305] G. Herzburg and L. Herzburg. Rotation-Vibration Spectra of Diatomic and Simple Polyatomic Molecules with Long Absorbing Paths XI. The Spectrum of Carbon Dioxide Below 1.25μm. *Journal of the Optical Society of America*, 43:1037–1044, 1953.

[306] J. Krooswyk and M. Trenary. *Molecular Spectroscopy of Acetylene*. University of Illinois at Chicago.

[307] C. H. Townes and A. L. Schawlow. *Microwave Spectroscopy*. Courier Corporation, 2013.

[308] G. Herzburg. l-type doubling in linear polyatomic molecules. *Reviews of Modern Physics*, 14:219–223, 1942.

[309] S. T. Cundiff and J. Ye. Colloquium: Femtosecond optical frequency combs. *Reviews of Modern Physics*, 75(1):325–342, 2003.

[310] D. J. Gauthier. Comment on 'generalised grating equation for virtually imaged phased-array spectral dispersers'. *Applied Optics*, 51:8184–8186, 2012.